University of Science and Technology of China

A Dissertation for Doctor's Degree

The Application of Therapeutic Nanoreactors and Novel Treatment Strategies to Overcome Multi-Drug Resistance in Cancer Therapy

Author： Jean Felix Mukerabigwi

Specialty： Chemistry and Physics of Polymers

Supervisor： Assoc. Prof. Zhishen Ge

Finished time: 4th June, 2020

中国科学技术大学

博士学位论文

癌症治疗中纳米反应器的应用和克服肿瘤多药耐药性的新策略

作者姓名： Jean Felix Mukerabigwi

学科专业： 高分子化学与物理

导师姓名： 葛治伸副教授

完成时间： 2020 年 06 月 04 日

中国科学技术大学学位论文原创性声明

本人声明所呈交的学位论文,是本人在导师指导下进行研究工作所取得的成果。除已特别加以标注和致谢的地方外，论文中不包含任何他人已经发表或撰写过的研究成果。与我一同工作的同志对本研究所做的贡献均已在论文中作了明确的说明。

作者签名：Jean Felix Mukerabigwi　　签字日期：2020.06.09

中国科学技术大学学位论文授权使用声明

作为申请学位的条件之一，学位论文著作权拥有者授权中国科学技术大学拥有学位论文的部分使用权，即：学校有权按有关规定向国家有关部门或机构送交论文的复印件和电子版，允许论文被查阅和借阅，可以将学位论文编入《中国学位论文全文数据库》等有关数据库进行检索，可以采用影印、缩印或扫描等复制手段保存、汇编学位论文。本人提交的电子文档的内容和纸质论文的内容相一致。

保密的学位论文在解密后也遵守此规定。

☑公开　□保密（____年）

作者签名：Jean Felix Mukerabigwi　　导师签名：

签字日期：2020.06.09　　签字日期：2020.06.09

摘　要

癌症这种疾病在人类中持续且剧烈地增长。跟以往相比，目前更加需要高超的治疗策略来实现有效的治疗。本论文的题目为“癌症治疗中纳米反应器的应用和克服肿瘤多药耐药性的新策略”。论文由四章组成，并都基于个人的相关工作。论文侧重于癌症治疗性纳米反应器的设计和逆转肿瘤耐药性新策略的开发。以下是各章节工作的摘要：

第一章

癌症作为人类日益严重的健康问题，在导致全球每年重大死亡的严重疾病中排名第二。尽管化学疗法是大多数癌症的主要治疗选择，但由于多药耐药性和严重的副作用，其在临床上的应用受到严重限制。在已报道的增强的癌症治疗效果的同时减轻副作用的各种方法中，可包被外源性治疗酶的纳米反应器的应用是一种非常有前途的癌症治疗策略。尽管如此，仍需要进一步的努力来克服领域中的一些阻碍，例如复杂的制备工序，纳米反应器固有的膜渗透性，脱靶，应用治疗性纳米反应器所需的多个步骤等等。在本章中，我们着重介绍了用于癌症治疗和诊断的治疗性纳米反应器的当前进展和局限性，其中包括一些非常新颖的治疗方法和纳米反应器在开发过程中的阻碍。此外，我们提出了两种新型治疗策略来克服常规化学疗法中经常遇到的多药耐药性。总体而言，本论文的研究有望为现下的癌症治疗做出贡献，特别是为之后研究人员开发先进的治疗性纳米反应器提供新思路，在实现增强治疗效果的同时，将不良反应显着降至最低，克服多药耐药性以实现纳米反应器在癌症治疗中的临床应用。

第二章

治疗性纳米反应器目前正在通过将惰性前药原位转化为活性药物，从而作为一种有前途的纳米平台出现。然而，设计具有平衡的关键特征的纳米反应器仍然具有挑战性，这些关键特征包括具有可调节的选择性膜渗透性和结构稳定性，以用于在疾病组织中进行前药递送和活化。本文中，我们提出了一种简便的策略来设计具有肿瘤特异性可调膜通透性的囊泡纳米反应器，从而分别将疏水性苯硼酸酯笼蔽的抗癌前药（例如喜树碱或紫杉醇前药）和亲水性葡萄糖氧化酶（GOD）加载到膜和腔中。纳米反应器在血液循环和正常组织中保持惰性。在肿瘤中积累后，温和的酸性微环境会触发选择性的膜通透性，从而允许小分子（葡萄糖和 O_2）在整个膜上扩散并在 GOD 的催化下发生反应。大量生成的 H_2O_2 通过可降解基团的裂解触发无毒前药原位转化为有毒的药物。所开发的系统通过产生 H_2O_2 以及通过联合氧化化学疗法激活前药而显示出显着增强的抗肿瘤功效。设计精巧的聚合物囊泡纳米反应器具有可调节 pH 值的肿瘤膜通透性，以共同装载 H_2O_2 响应前药和 GOD，是实现前药递送和激活以增强治疗效果且副作用低的新颖策略。

第三章

顺铂的耐药性极大地限制了其在临床上对多种癌症的治疗功效。除了引起细胞内 DNA 损伤和线粒体凋亡外，氧化应激还在顺铂诱导的细胞凋亡机理中起着关键性的作用。本章中，我们构建了一种新型的囊泡纳米反应器，能同时运载顺铂和产生 H_2O_2，放大细胞内的氧化应激水平，进而逆转人肺癌细胞（A549R）的耐药性。该纳米反应器由双亲性的聚乙二醇-聚（甲基丙烯酸苄酯-甲基丙烯酸

2-（哌啶-1-基）乙酯）聚合物自组装而成。同时装载葡萄糖氧化酶（GOD）和顺铂（Cis）的纳米反应器（Cis/GOD@Bz-V）在血液循环过程中能保持结构的完整。当进入肿瘤组织时（pH 6.5-6.8），弱酸性的环境能增加分子量选择性膜的通透性，释放包裹的顺铂。通过膜释放的小分子，譬如氧气和葡萄糖，能在原位产生过量的 H_2O_2，提高细胞内的氧化应激水平，促使耐药的 A549R 细胞凋亡。实验证明，Cis/GOD@Bz-V 纳米反应器能有效的促进 A549R 细胞凋亡，抑制肿瘤的生长。因此，我们设计的酸敏感纳米反应器，在利用顺铂治疗耐药性肿瘤中具有广泛的应用前景。

第四章

多药耐药性（MDR）逐渐成为阻碍实现临床化学疗法的主要威胁之一。许多报道已证实在癌症治疗中诱导 MDR 是由多方面因素造成的，其中多种压力下线粒体介导的通路的在癌细胞产生 ADR 过程中担任着十分重要的作用。因此，靶向线粒体是一个克服 MDR 的理想策略。在本文中，我们报道了一种合理设计的双重靶向聚合物前药纳米颗粒，该纳米颗粒可以通过叶酸（FA）和三苯基膦（TPP）两种靶向物分别靶向癌细胞和线粒体，并通过线粒体氧化应激和 DNA 损伤克服 MDR。简言之，合成了包含肉桂醛（CNM）和阿霉素（DOX）药物部分的二嵌段共聚物，表示为 FA&TPP-PEOGMA$_{18}$-*b*-P(CNM$_{17}$-*co*-DOX$_{15}$)，并用于制备称为 PCD 的纳米颗粒。当 PCD 纳米颗粒在癌细胞中富集后，内涵体的酸性环境（∽pH 5–6.5）可以触发 CNM 在细胞质的释放，致使线粒体中 ROS 增加，继而可以增强氧化应激并触发 DOX 在细胞质中的释放，同时所释放的 DOX 能够对线粒体 DNA 造成损害。这种治疗策略显示出在体内和体外杀死和抑制

DOX 耐药的 MCF-7 ADR 肿瘤细胞的潜力，同时没有明显的副作用。

关键词：纳米反应器，酶前药治疗，药物递送，聚合物囊泡，顺铂，耐药性，线粒体

Abstract

Cancer disease persists to dramatically increase in humankind and sophisticated therapeutic strategies are urgently needed to achieve efficacious therapeutic effect than ever before. This thesis entitled “the application of therapeutic nanoreactors as *in vivo* nanoplatforms and novel treatment strategies to overcome multi-drug resistance in cancer therapy” is composed of four chapters based on individual and yet related works that mainly focus on the engineering of therapeutic nanoreactors that can be used in cancer treatment and development of different treatment strategies to reverse drug resistance in cancer therapy. The following is the abstract of work presented in each chapter:

Chapter I

Cancer is a growing burden to mankind and ranked the second among serious diseases leading to major deaths worldwide annually. Although chemotherapy is the main treatment option for most of cancer types, its successful application in clinics is critically limited by less effectiveness mostly due to multidrug resistance and severe side effects. Among various current approaches reported to achieve enhanced cancer treatment effect with mitigated side effects, the application of therapeutic nanoreactor suggested promising strategies for cancer treatment which also allow the application of exogenous therapeutic enzymes. Nevertheless, further efforts are required to address several limitations in that field such as the complex engineering procedures, intrinsic

membrane permeability, off-target activation of the nanoreactors, required multiple steps required to apply therapeutic nanoreactors and so on. In this chapter, we highlighted the general background about the current progress and limitations of therapeutic nanoreactors designed for cancer treatment and diagnosis by also showing some of the proposed approaches to address these limitations towards the development of ideal therapeutic nanoreactors. Furthermore, we presented two more proposed strategies to overcome multidrug resistance often encountered in the conventional chemotherapy. In overall, the study conducted in this thesis is expected to contribute a lot to the existing literature especially through the inspiring the next generation of researchers to develop advanced therapeutic nanoreactor and with novel treatment approaches to achieve enhanced therapeutic effect and with remarkably minimized adverse effect as well as to overcome multi-drug resistance and ready for clinical translation in cancer therapy.

Chapter II

Therapeutic nanoreactors are currently emerging as promising nanoplatforms to *in situ* transform inert prodrugs into active drugs. Nevertheless, it is still challenging to engineer a nanoreactor with balanced key features of tunable selective membrane permeability and structural stability for prodrug delivery and activation in diseased tissues. Herein, we present a facile strategy to engineer a polymersome nanoreactor with tumor-specific tunable membrane permeability to load both hydrophobic

phenylboronic ester-caged anticancer prodrugs (e.g., camptothecin or paclitaxel prodrug) and hydrophilic glucose oxidase (GOD) in the membranes and cavities, respectively. The nanoreactors maintain inactive during blood circulation and in normal tissues. Upon accumulation in tumors, the mild acidic microenvironment triggers selective membrane permeability to allow small molecules (glucose and O_2) to diffuse across the membrane and react under the catalysis of GOD. The massively generated H_2O_2 triggers *in situ* transformation of innocuous prodrugs into toxic parental drugs through cleavage of the self-immolative degradable caging groups. The developed system showed significantly enhanced antitumor efficacy by H_2O_2 production and prodrug activation *via* combined oxidation-chemotherapy. The well-devised polymersome nanoreactors with tumor-pH-tunable membrane permeability to coload H_2O_2-responsive prodrug and GOD represent a novel strategy to realize prodrug delivery and activation for enhanced therapeutic efficacy with low side toxicity.

Chapter III

Drug resistance of cisplatin significantly limited its therapeutic efficacy in clinical applications against a variety of cancers. In addition to DNA damage and mitochondria apoptosis, oxidative stress is deemed to play a pivotal role in underlying mechanisms of cisplatin-induced cytotoxicity. Herein, we develop a novel strategy to overcome cisplatin drug resistance through sensitizing cisplatin-resistant human lung cancer cells (A549R) under amplified oxidative stress by a vesicular nanoreactor for cisplatin

delivery and H_2O_2 generation. We engineered the nanoreactors from self-assembly of the amphiphilic diblock copolymers consisting of poly(ethylene glycol) and a copolymerized segment of benzyl methacrylate and 2-(piperidin-1-yl) ethyl methacrylate, which co-deliver both glucose oxidase (GOD) and cisplatin (Cis) and were denoted as Cis/GOD@Bz-V. Cis/GOD@Bz-V was rationally designed to stay impermeable during blood circulation until it reaches tumor parenchyma where the mild acidity (pH 6.5-6.8) can activate its molecular-weight selective membrane permeability and release cisplatin locally. The subsequent diffusion of small molecules such as oxygen and glucose across the membrane can induce the *in-situ* generation of superfluous H_2O_2 to promote cellular oxidative stress and sensitize cisplatin-resistant cells A549R *via* activation of pro-apoptotic pathways. The results showed that Cis/GOD@Bz-V nanoreactors can effectively kill A549R cells and significantly inhibits the growth of A549R xenograft tumors. Accordingly, the tumor acidity-activable nanoreactors show great potentials as drug delivery nanocarriers of cisplatin to enhance the therapeutic efficacy of cisplatin-resistant cancers.

Chapter IV

Multidrug resistance (MDR) continues to become one of the major menaces that obstruct chemotherapy success in clinics. In addition to the reported many factors that induce MDR in cancer therapy, the role of mitochondria mediated pathways that generate cancer cell survival mechanisms under various stress is obvious. Therefore,

targeting mitochondria can be an ideal strategy to overcome MDR. Herein, we report a rationally designed dual targeting polymer prodrug nanoparticle that can simultaneously target cancer cell and mitochondria by folic acid (FA) and tetraphenylphosphonium (TPP) targeting species, respectively, to overcome MDR through amplification of mitochondrial oxidative stress and DNA damage. Briefly, a diblock copolymer containing cinnamaldehyde (CNM) and doxorubicin (DOX) drug moieties denoted as FA&TPP-PEOGMA$_{18}$-*b*-P(CNM$_{17}$-*co*-DOX$_{15}$) was synthesized and used to prepare nanoparticles mentioned as PCD. Upon the accumulation of PCD nanoparticles in cancer cells, the endosomal acidity (~pH 5–6.5) can trigger the release of CNM in the cytoplasm followed by amplification of mitochondria ROS production that can subsequently enhance oxidative stress and trigger the release of DOX in the mitochondria for DNA damage. This treatment strategy showed enhanced potential to kill and inhibit DOX resistant MCF-7 ADR tumor cells both *in vitro* and *in vivo* without observable side effect.

Keywords: nanoreactor, enzyme-prodrug therapy, drug delivery, cancer therapy, oxidative stress, drug resistance, mitochondria

Table of Content

Chapter I: General Introduction about Therapeutic Nanoreactors and Cancer Treatment

1.1. Overview about cancer disease

Cancer is a growing burden to mankind and ranked the second among serious diseases leading to major deaths as 1 in 6 deaths is due to cancer Worldwide **(Figure 1.1)**.[1-3] According to the World Health Organization (WHO) current report, more than 9.6 million people are projected to die each year globally due to various type of cancer.[1, 4, 5]

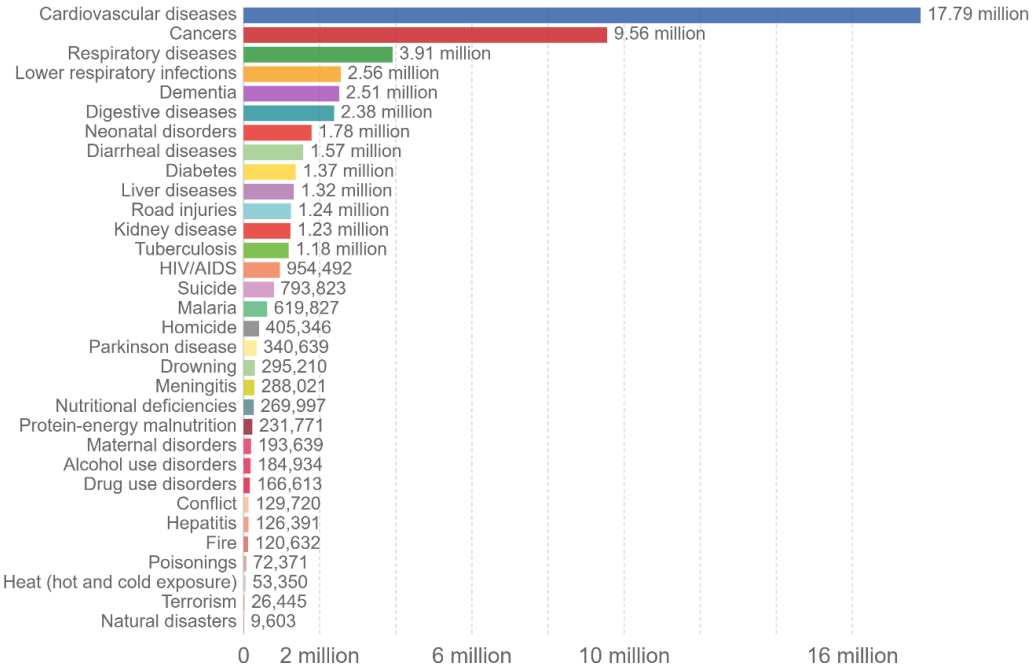

Figure 1. 1. Global death number by cause in 2017. Source: IHME Global Burden of Disease.[2]

Among which, lung cancer is the leading cancer type to claim many lives each year followed by other type of cancers including breast, colorectum, prostate, stomach, liver, esophagus, cervix uteri, thyroid, bladder cancers and so on, respectively.[6] It is also reported that 1 in 5 persons will develop at least one type of cancer during his/her lifetime Worldwide. Particularly, the absolute number for new cancer incident of estimated or diagnosed in 2018 was 18.1 million people and 9.6 million patients died from the disease Worldwide **(Figure 1.2)**.[1, 4]

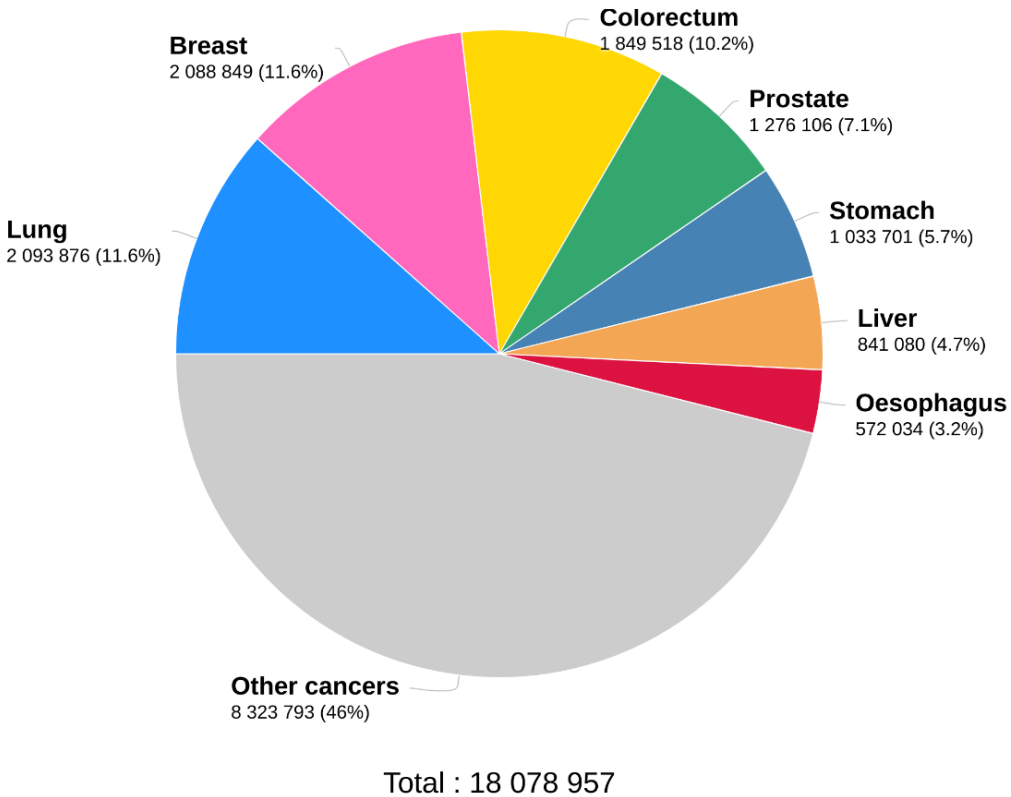

Figure 1. 2. Estimated or diagnosed cancer new incidents in 2018 Worldwide, all cancers, all sex and all ages by WHO. © International agency for research on cancer 2020 [1].

1.2. Cancer therapy and treatment approaches

Concerning treatment, chemotherapy, surgery and radiation have been the most common practice in clinics to cure cancer patients.[7] Moreover, various modern treatment concepts including hormonal therapy, bioimaging, targeted therapies such as immunotherapy, etc., have been introduced for earlier and efficient cancer treatment and diagnosis.[8, 9] Over the years, the evolution of cancer treatment can be evidenced by the remarkably increasing number of cancer survival patients.[10, 11] However, as the new cancer incidents are rapidly increasing overtime worldwide mostly due the population increasing and various facts linked with socioeconomic development,[3-5] there is urgently increasing demand for development of ideal treatment concepts for cancer eradication to save many lives as possible.[3, 12]

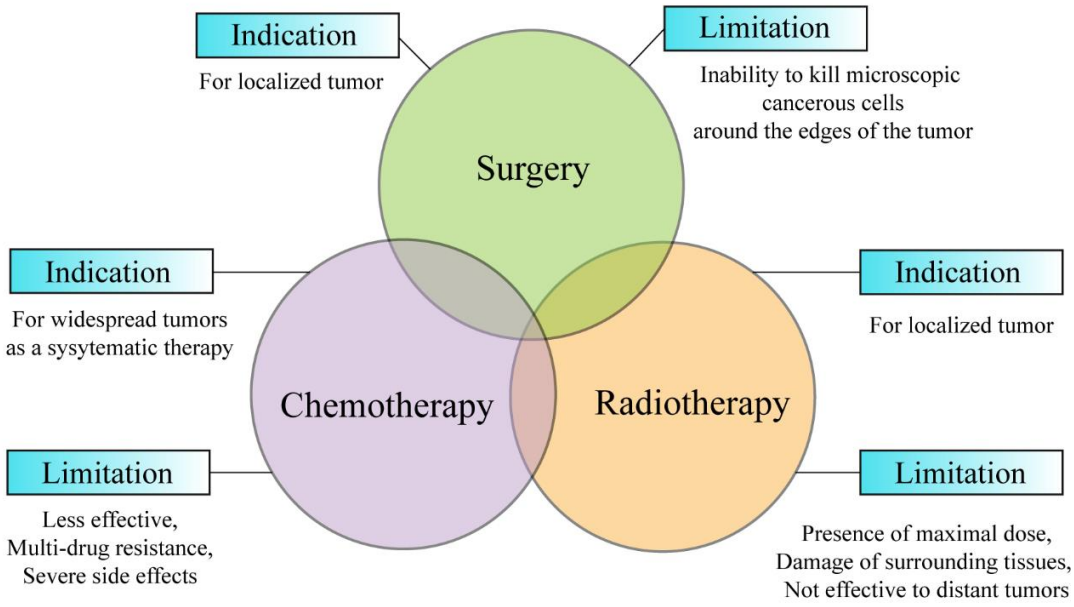

Figure 1. 3. Three general treatment approaches for cancer with their indications and

limitations.

1.3. Nanotechnology for cancer treatment

Chemotherapy is widely still the major treatment approach for various type of cancers in clinics. Nevertheless, the conventional chemotherapy treatment is hampered with multiple drawback effects such as low solubility in aqueous media for most of anticancer drugs, multiple life-threatening adverse effects, off-target cytotoxicity, low bioavailability due to faster systemic clearance, increased multidrug resistance and so on, which consequently lead to inadequate treatment effect against cancer treatment **(Figure 1.3)**. Therefore, the is an increasing demand to develop a significant and effective treatment techniques to cure cancer in the clinics.[13-15]

To address the above-mentioned challenges related to conventional chemotherapy, various researchers from different background have been working hard to find the ideal cancer treatment strategies that can achieve enhanced treatment efficacy and without side effect. For example, many researches showed a tremendous and increasing interest in the application of nanomedicine into cancer therapy and the field has been rapidly growing at great pace since the last several decades.[16, 17] In this scenario various nanoparticles including micelles, polymersomes, liposomes, dendrimers, and so on have been extensively studied and showed a promising potential in various applications including drug delivery, imaging, and so on for cancer treatment and diagnosis **(Figure 1.4)**.[18-20] Since then, there has been a strong perspective that the introduction of

nanomedicine could offer versatile opportunities to develop various personalized treatment concepts for earlier detection and treatment as well as diagnosis for effective cancer treatment.[17, 21]

Compared to their small molecular drug counterparts, nanoparticles showed several interesting properties and benefits in modern medicines such drastically increased systemic circulation half-life, feasibility to achieve smart and novel therapeutic techniques. Preferably, nanoparticles with various size ranging from ~200 to 10 nm can engineered and be used as delivering vehicles for a wide range of materials of interest from small molecular weight such as anticancer drugs to macromolecular payloads such as enzymes and proteins for cancer treatment. [22, 23]

Moreover, nanoparticles can pass through into the leaky vasculature fenestration of the blood vessels to reach the tumor site in what is commonly known as enhanced permeability and retention (EPR) effect.[24] By taking advantage of various extensively studied triggering stimuli such as external and internal environment stimuli (pH, enzyme, ionic strength, temperature, reactive oxygen species (ROS), irradiation, etc.), it is feasible to control the nanoparticle payloads release at the pathological site such as at tumor region.[25, 26] In this respect, a great number of reports about the development of targeted nanoparticles designed for on-demand release of their therapeutic payloads to the site of interest to achieve enhanced therapeutic effect with minimized side effect have been extensively reported.[27, 28]

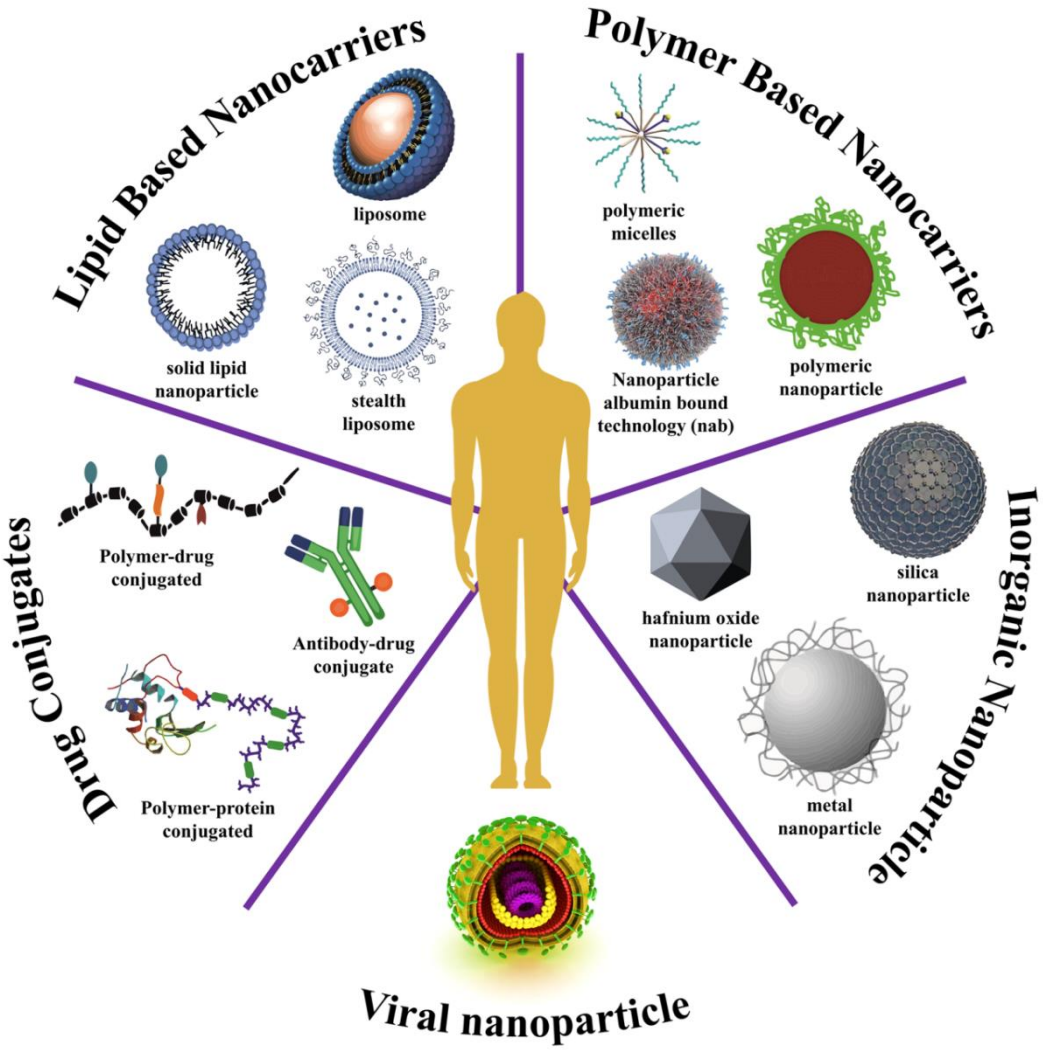

Figure 1. 4. Various representative nanoplatforms used for nanoparticle applications in clinical researches. Reprinted with permission from ref. [18].

1.4. Perspectives for therapeutic nanoreactors in cancer treatment

The application of exogenous enzymes and proteins have showed desirable potential to treat various diseases including cancer.[29-32] Nevertheless, their activity is severely limited by their fragility as they are vulnerable to various proteolytic attacks

and immunogenicity during systemic circulation. In this scenario, various enzyme prodrug therapy (EPT) approaches including antibody-directed enzyme prodrug therapy (ADEPT), gene-directed enzyme-prodrug therapy (GDEPT), substrate mediated enzyme prodrug therapy (SMEPT), and virus-directed enzyme prodrug therapy (VDEPT), have been developed to maintain the activity of the enzymes while working *in vivo*.[33-37] Typically, the EPT involves the immobilization of activating agents into the matrices of synthetic platforms that can *in situ* convert less or no-toxic prodrugs into parent toxic drugs. In a practical manner, the EPT is achieved *via* two steps which are the prior delivery of the immobilized activating enzymes at the treatment location, and the subsequent separate administration of non-toxic prodrug which is then activated after reaching the desired site in the presence of the previously delivered activating enzyme. [38, 39]

Recently, inspired by nature such as the complex biosynthetic pathways of eukaryotic cell, there is a growing interest toward the development and improvement of nanoplatforms that can immobilize various therapeutic fragile biomaterials with integrated diverse functionalities for desired application in precise nanomedicine including cancer treatment.[40, 41] These nanoplatforms here and after referred to as therapeutic nanoreactor are defined as nanocompartments characterized with confined reaction space containing immobilized catalysts such as enzymes, proteins, enzyme-mimics, etc. and able to produce functional therapeutic products *via* various cascade reactions locally **(Figure 1.5)**.

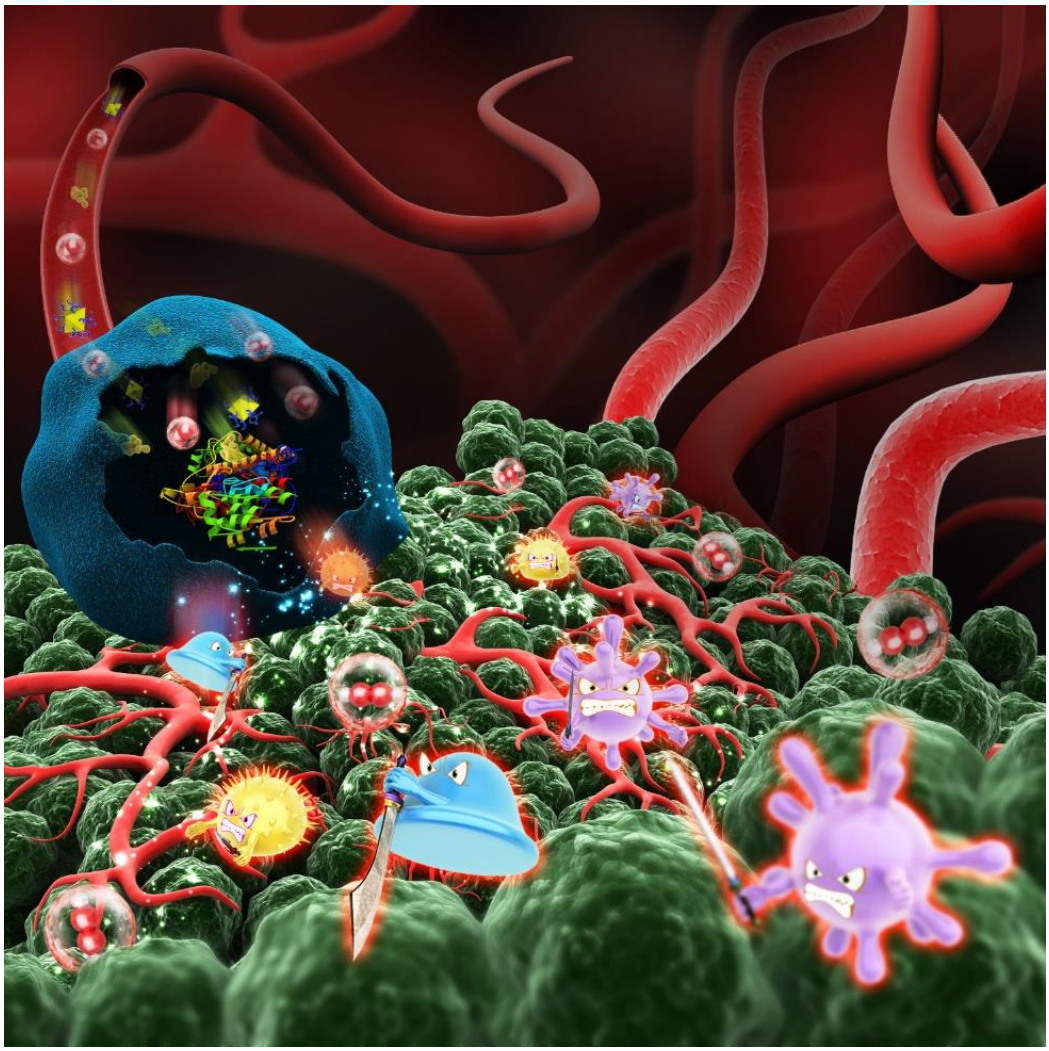

Figure 1. 5. Schematic illustration of therapeutic nanoreactors working as *in vivo* nanoplatforms particularly for cancer therapy. Reprinted with permission from ref.[40].

1.5. The problem statement of this study

Typically, the work presented in this thesis mainly focuses on the improvement of therapeutic nanoreactors designed for *in vivo* application and the reversal of multi-drug resistance that is still the among the major limitations in cancer treatment. Briefly, the application of therapeutic nanoreactors suggested promising approaches to develop

various novel treatment concepts in cancer treatment and diagnosis especially by using various therapeutic enzymes.[42] Nevertheless, this field is still underdeveloped and there are still several major challenges that need to be addressed as mentioned below:

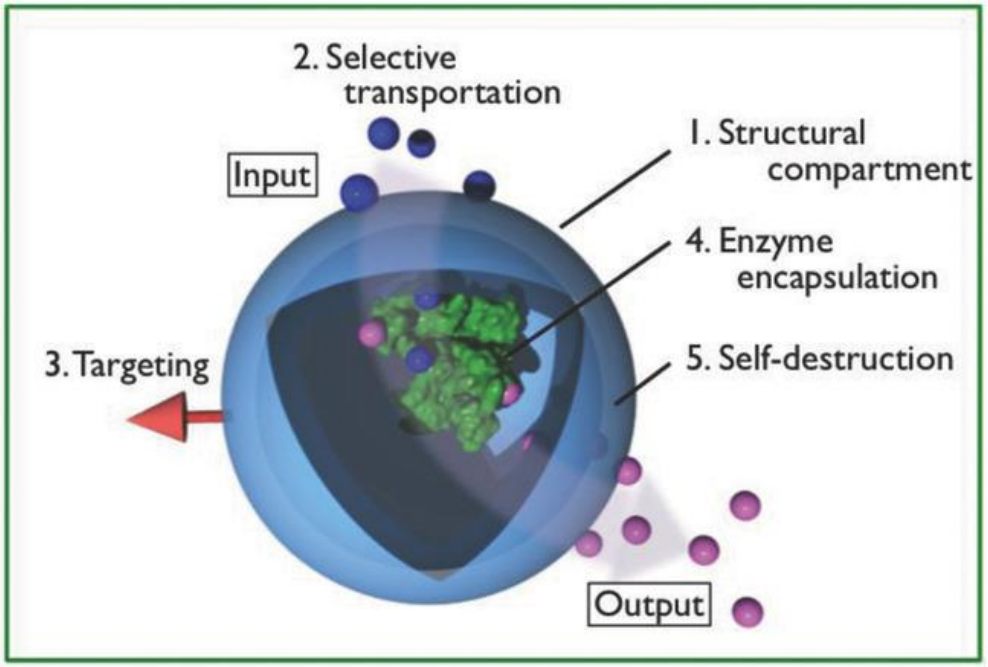

Figure 1. 6. Basic required features for a therapeutic nanoreactor. Adapted with permission from ref.[43].

First, the tunable and controllable membrane permeability to allow the release or retention of a wide range of loaded materials as well as the structure integrity are among the minimum required parameters for promising nanoreactor designed for *in vivo* application **(Figure 1.6)**.[44, 45] Nevertheless, it is still challenging to engineer a nanoreactor with balanced key features such as tunable, selective, controllable membrane permeability and structural stability for payloads delivery and activation in

diseased tissues.

Second, considering EPT as one of the widely reported strategies to deliver activating enzymes, the required administration interval between the activating enzyme and prodrug to minimize off target prodrug activation lead to the frequent different biodistribution and bioavailability between the prodrug and their activating enzymes at the treatment site, which therefore strictly limit the EPT treatment efficacy.[35]

Third, most of the previously reported nanoreactors possess intrinsic membrane semi-permeability/permeability that would cause some unavoidable limitations while considered for *in vivo* applications [46]. For example, given the fact that their distribution in normal tissues can also catalyze the reaction inside normal tissues, this may cause unavoidable adverse side effects. Moreover, although some strategies such as the incorporation of bio-valve macromolecules into the nanoreactor membranes to generate various nanoreactor with controllable membrane permeability have been reported, their required cumbersome engineering process strictly limit their progress [47].

In addition, multi-drug resistance is one of critical challenge in cancer therapy.[48, 49] Particularly, the drug resistance is continuing to be a persistent problem for chemotherapy in clinics. It was reported that altered drug transport mechanism, genetic responses, increased DNA repair, alteration of cancer cell metabolic effects and growth factors are the major causes for the development of drug resistance during treatment.[50] In attempt to minimize the multidrug resistance, the application of various combination therapies has widely reported by several researches. Interestingly, it was revealed that

the application of nanoparticles as vehicles of various drug for cancer treatment can have effect about the relief of multidrug resistance of cancer cells.[51, 52] Therefore, the ideal approach to develop an effective cancer treatment strategy that can also overcome the multi-drug resistance is of great interest.

1.6. The hypothesis of this study

With the aim to address the vigorous and time-consuming requirements to engineer nanoreactor with balanced key features such as tunable selective membrane permeability and structural stability for payloads delivery, we hypothesized that the development of fast-forward strategy to engineer such therapeutic nanoreactor cannot only provide the possibilities to immobilize various materials of interest in the reaction vessels but also enable the controlled entry and exit of various reactants and products across the nanoreactor membrane especially at the diseased tissues as described in the 2nd chapter of this thesis.

Moreover, given the fact that most of the previously reported enzyme prodrug therapies, if not all, are achieved through multiple step strategies, we supposed that the development of a single step enzyme prodrug therapy can possibly enhance the drug bioavailability to improve therapeutic effect compared to previously reported multiple step-based enzyme prodrug therapies in cancer therapy as described in the 2nd chapter of this thesis.

Next, to address the drug resistance limitation often encountered by applying cisplatin as the of widely used chemotherapeutic agent to treat a broad spectrum of human malignant solid tumors including ovarian, prostate, lung, bladder, colorectal and esophageal cancers in clinics, we anticipated that the development of a rationally designed nanoreactor able to induce oxidative stress locally in the presence of cisplatin cannot only enhance the therapeutic effect but also overcome cancer cell drug resistance to cisplatin described in the 3rd chapter of this thesis.

Furthermore, with continuous improvement in understanding of several mechanisms involved in cancer cell biology including the adaptation of resistant to various chemotherapeutic drugs, it is reported that the mitochondria can mediate various metabolic pathways that induce cancer cell survival mechanisms under various stress such as in the presence of various chemotherapeutic drug.[53, 54] Therefore, we hypothesized that the development of a treatment concept that can particularly target mitochondria activities such as through the amplification of mitochondrial oxidative stress and DNA damage can contribute the reverse of multi-drug resistance in the cancer cell as described in the 4th chapter of this thesis.

1.7. The significance of this study

In this thesis that is focusing on the applications of therapeutic nanoreactors as *in vivo* nanoplatforms and the reversal of multi-drug resistance particularly in cancer

therapy, we highlighted the nanoreactors' recent advances and also elucidated the existing current challenges to be addressed as well as recommendations toward further development and translation into clinical applications in cancer therapy. Moreover, in addition to the presented facile strategy to engineer a polymersome nanoreactor with tumor-specific tunable membrane permeability, we showed one of possibilities to achieve a single step enzyme prodrug therapy simply by coloading both hydrophobic phenylboronic ester-caged anticancer prodrugs such as camptothecin or paclitaxel prodrug and hydrophilic glucose oxidase (GOD) in the membranes and cavities of the prepared nanoreactors, respectively. Our proposed strategy showed enhanced tumor treatment efficacy without observable side effect.

Furthermore, the results of our novel developed strategies to reverse multi-drug resistance either through the engineering of nanoreactor that can the *in-situ* generate of superfluous amount of H_2O_2 to promote cellular oxidative stress and sensitize cisplatin-resistant cells to cisplatin chemotherapeutic drug, or targeting mitochondria metabolic activities with a rationally designed polymer prodrug nanoparticles showed promising achievement towards the reversal of multi-drug resistance in cancer treatment. Collectively, the study conducted in this thesis is expected to contribute a lot to the existing literature especially through the inspiring the next generation of researchers to develop advanced therapeutic nanoreactor and with novel treatment approaches to achieve enhanced therapeutic effect and with remarkably minimized adverse effect as well as to overcome multi-drug resistance and ready for clinical translation in cancer therapy.

1.8. References

[1] http://gco.iarc.fr/, International Agency for Research on Cancer, Latest global cancer data, in, 150 Cours Albert Thomas, 69372 Lyon CEDEX 08, France. (visited on 21st April 2020).

[2] H. Ritchie, M. Roser, Causes of Death, Our World in Data, (2020) https://ourworldindata.org/causes-of-death (Accessed on 21st April 2020).

[3] R.L. Siegel, K.D. Miller, A. Jemal, Cancer statistics, 2020, CA: A Cancer Journal for Clinicians, 70 (2020) 7-30.

[4] F. Bray, J. Ferlay, I. Soerjomataram, R.L. Siegel, L.A. Torre, A. Jemal, Global cancer statistics 2018: GLOBOCAN estimates of incidence and mortality worldwide for 36 cancers in 185 countries, CA: A Cancer Journal for Clinicians, 68 (2018) 394-424.

[5] S. Pilleron, D. Sarfati, M. Janssen-Heijnen, J. Vignat, J. Ferlay, F. Bray, I. Soerjomataram, Global cancer incidence in older adults, 2012 and 2035: A population-based study, International Journal of Cancer, 144 (2019) 49-58.

[6] J.A. Barta, C.A. Powell, J.P. Wisnivesky, Global Epidemiology of Lung Cancer, Ann Glob Health, 85 (2019) 8.

[7] M. Arruebo, N. Vilaboa, B. Sáez-Gutierrez, J. Lambea, A. Tres, M. Valladares, A. González-Fernández, Assessment of the evolution of cancer treatment therapies, Cancers (Basel), 3 (2011) 3279-3330.

[8] P.E. Hughes, S. Caenepeel, L.C. Wu, Targeted Therapy and Checkpoint Immunotherapy Combinations for the Treatment of Cancer, Trends in Immunology, 37 (2016) 462-476.

[9] F.J. Esteva, V.M. Hubbard-Lucey, J. Tang, L. Pusztai, Immunotherapy and targeted therapy combinations in metastatic breast cancer, The Lancet Oncology, 20 (2019) e175-e186.

[10] N.E. Davidson, Incident Cancer in Cancer Survivors—When Cancer Lurks in the Background, JAMA Oncology, 4 (2018) 836-837.

[11] P.M. Webb, M.C. Cummings, C.J. Bain, C.M. Furnival, Changes in survival after breast cancer: improvements in diagnosis or treatment?, The Breast, 13 (2004) 7-14.

[12] A.S. Quante, C. Ming, M. Rottmann, J. Engel, S. Boeck, V. Heinemann, C.B. Westphalen, K. Strauch, Projections of cancer incidence and cancer-related deaths in Germany by 2020 and 2030, Cancer Medicine, 5 (2016) 2649-2656.

[13] V. Schirrmacher, From chemotherapy to biological therapy: A review of novel concepts to reduce the side effects of systemic cancer treatment (Review), Int J Oncol, 54 (2019) 407-419.

[14] C.-Y. Huang, D.-T. Ju, C.-F. Chang, P. Muralidhar Reddy, B.K. Velmurugan, A review on the effects of current chemotherapy drugs and natural agents in treating non-small cell lung cancer, Biomedicine (Taipei), 7 (2017) 23-23.

[15] B.A. Chabner, T.G. Roberts, Chemotherapy and the war on cancer, Nature Reviews Cancer, 5 (2005) 65-72.

[16] C.-Y. Zhao, R. Cheng, Z. Yang, Z.-M. Tian, Nanotechnology for Cancer Therapy Based on Chemotherapy, Molecules, 23 (2018) 826.

[17] C.T. Hagan, Y.B. Medik, A.Z. Wang, Chapter Two - Nanotechnology Approaches to Improving Cancer Immunotherapy, in: A.-M. Broome (Ed.) Advances in Cancer Research, Academic Press, 2018, pp. 35-56.

[18] A. Aghebati-Maleki, S. Dolati, M. Ahmadi, A. Baghbanzhadeh, M. Asadi, A. Fotouhi, M. Yousefi, L. Aghebati-Maleki, Nanoparticles and cancer therapy: Perspectives for application of nanoparticles in the treatment of cancers, Journal of Cellular Physiology, 235 (2020) 1962-1972.

[19] A. Rajendra, R. Ariane, H. Philip Michael, R. Michael John, D. Kamal, B. Mary, Nanoparticles in Cancer Treatment: Opportunities and Obstacles, Current Drug Targets, 19 (2018) 1696-1709.

[20] S. Tran, P.-J. DeGiovanni, B. Piel, P. Rai, Cancer nanomedicine: a review of recent success in drug delivery, Clin Transl Med, 6 (2017) 44-44.

[21] S. Parvanian, S.M. Mostafavi, M. Aghashiri, Multifunctional nanoparticle developments in cancer diagnosis and treatment, Sensing and Bio-Sensing Research, 13 (2017) 81-87.

[22] C. Pucci, C. Martinelli, G. Ciofani, Innovative approaches for cancer treatment: current perspectives and new challenges, Ecancermedicalscience, 13 (2019) 961-961.

[23] P. Tran, S.-E. Lee, D.-H. Kim, Y.-C. Pyo, J.-S. Park, Recent advances of nanotechnology for the delivery of anticancer drugs for breast cancer treatment, Journal of Pharmaceutical Investigation, 50 (2019) 261–270.

[24] H. Maeda, Toward a full understanding of the EPR effect in primary and metastatic tumors as well as issues related to its heterogeneity, Advanced Drug Delivery Reviews, 91 (2015) 3-6.

[25] S.R. MacEwan, D.J. Callahan, A. Chilkoti, Stimulus-responsive macromolecules and nanoparticles for cancer drug delivery, Nanomedicine, 5 (2010) 793-806.

[26] A. Raza, T. Rasheed, F. Nabeel, U. Hayat, M. Bilal, H.M.N. Iqbal, Endogenous and Exogenous Stimuli-Responsive Drug Delivery Systems for Programmed Site-Specific Release, Molecules, 24 (2019) 1117.

[27] R. Shukla, M. Handa, S.B. Lokesh, M. Ruwali, K. Kohli, P. Kesharwani, Chapter 18 - Conclusion and Future Prospective of Polymeric Nanoparticles for Cancer Therapy, in: P. Kesharwani, K.M. Paknikar, V. Gajbhiye (Eds.) Polymeric Nanoparticles as a Promising Tool for Anti-cancer Therapeutics, Academic Press, 2019, pp. 389-408.

[28] Z. He, K. Liu, H.J. Byrne, P.J. Cullen, F. Tian, J.F. Curtin, Chapter 8 - Combination Strategies for Targeted Delivery of Nanoparticles for Cancer Therapy, in: S.S. Mohapatra, S. Ranjan, N. Dasgupta, R.K. Mishra, S. Thomas (Eds.) Applications of Targeted Nano Drugs and Delivery Systems, Elsevier, 2019, pp. 191-219.

[29] C. Riess, F. Shokraie, C.F. Classen, B. Kreikemeyer, T. Fiedler, C. Junghanss, C. Maletzki, Arginine-Depleting Enzymes – An Increasingly Recognized Treatment Strategy for Therapy-Refractory Malignancies, Cellular Physiology and Biochemistry, 51 (2018) 854-870.

[30] E. Cellarier, X. Durando, M.P. Vasson, M.C. Farges, A. Demiden, J.C. Maurizis, J.C. Madelmont, P. Chollet, Methionine dependency and cancer treatment, Cancer Treatment Reviews, 29 (2003) 489-499.

[31] M. Vellard, The enzyme as drug: application of enzymes as pharmaceuticals, Current Opinion in Biotechnology, 14 (2003) 444-450.

[32] A.N. Zelikin, Unique enzymatic repertoire reveals the tumour, Nature Chemistry, 12 (2020) 11-12.

[33] O.M. Malekshah, X. Chen, A. Nomani, S. Sarkar, A. Hatefi, Enzyme/Prodrug Systems for Cancer Gene Therapy, Curr Pharmacol Rep, 2 (2016) 299-308.

[34] K.D. Bagshawe, Antibody-directed enzyme prodrug therapy (ADEPT) for cancer, Expert Review of Anticancer Therapy, 6 (2006) 1421-1431.

[35] S.K. Sharma, K.D. Bagshawe, Antibody Directed Enzyme Prodrug Therapy (ADEPT): Trials and tribulations, Advanced Drug Delivery Reviews, 118 (2017) 2-7.

[36] C. Christie, A. Pomeroy, R. Nair, K. Berg, H. Hirschberg, Photodynamic therapy enhances the efficacy of gene-directed enzyme prodrug therapy, Photodiagnosis and Photodynamic Therapy, 18 (2017) 140-148.

[37] B. Fejerskov, A.N. Zelikin, Substrate mediated enzyme prodrug therapy, PLoS One, 7 (2012) e49619-e49619.

[38] G. Xu, H.L. McLeod, Strategies for Enzyme/Prodrug Cancer Therapy, Clinical Cancer Research, 7 (2001) 3314-3324.

[39] R. Walther, J. Rautio, A.N. Zelikin, Prodrugs in medicinal chemistry and enzyme prodrug therapies, Advanced Drug Delivery Reviews, 118 (2017) 65-77.

[40] J.F. Mukerabigwi, Z. Ge, K. Kataoka, Therapeutic Nanoreactors as In Vivo Nanoplatforms for Cancer Therapy, Chemistry – A European Journal, 24 (2018) 15706-15724.

[41] V.S. Madamsetty, A. Mukherjee, S. Mukherjee, Recent Trends of the Bio-Inspired Nanoparticles in Cancer Theranostics, Frontiers in Pharmacology, 10 (2019) 1-12.

[42] I.-C. Sun, H.Y. Yoon, D.-K. Lim, K. Kim, Recent Trends in In Situ Enzyme-Activatable Prodrugs for Targeted Cancer Therapy, Bioconjugate Chemistry, 31 (2020) 1012-1024.

[43] T. Nishimura, K. Akiyoshi, Biotransporting Biocatalytic Reactors toward Therapeutic Nanofactories, Advanced Science, 5 (2018) 1800801.

[44] P. Broz, S. Driamov, J. Ziegler, N. Ben-Haim, S. Marsch, W. Meier, P. Hunziker, Toward Intelligent Nanosize Bioreactors: A pH-Switchable, Channel-Equipped, Functional Polymer Nanocontainer, Nano Letters, 6 (2006) 2349-2353.

[45] K.T. Kim, J.J.L.M. Cornelissen, R.J.M. Nolte, J.C.M. van Hest, A Polymersome Nanoreactor with Controllable Permeability Induced by Stimuli-Responsive Block Copolymers, Advanced Materials, 21 (2009) 2787-2791.

[46] T. Nishimura, Y. Sasaki, K. Akiyoshi, Biotransporting Self-Assembled Nanofactories Using Polymer Vesicles with Molecular Permeability for Enzyme Prodrug Cancer Therapy, Advanced Materials, 29 (2017) 1702406.

[47] C. Edlinger, T. Einfalt, M. Spulber, A. Car, W. Meier, C.G. Palivan, Biomimetic Strategy To Reversibly Trigger Functionality of Catalytic Nanocompartments by the Insertion of pH-Responsive Biovalves, Nano Letters, 17 (2017) 5790-5798.

[48] A. Persidis, Cancer multidrug resistance, Nature Biotechnology, 17 (1999) 94-95.

[49] K.O. Alfarouk, C.-M. Stock, S. Taylor, M. Walsh, A.K. Muddathir, D. Verduzco, A.H.H. Bashir, O.Y. Mohammed, G.O. Elhassan, S. Harguindey, S.J. Reshkin, M.E. Ibrahim, C. Rauch, Resistance to cancer chemotherapy: failure in drug response from ADME to P-gp, Cancer Cell International, 15 (2015) 1-13.

[50] J.-P. Gillet, M.M. Gottesman, Mechanisms of Multidrug Resistance in Cancer, in: J. Zhou (Ed.) Multi-Drug Resistance in Cancer, Humana Press, Totowa, NJ, 2010, pp. 47-76.

[51] M. Majidinia, M. Mirza-Aghazadeh-Attari, M. Rahimi, A. Mihanfar, A. Karimian, A. Safa, B. Yousefi, Overcoming multidrug resistance in cancer: Recent progress in nanotechnology and new horizons, IUBMB Life, 72 (2020) 855-871.

[52] L. Zhou, H. Wang, Y. Li, Stimuli-Responsive Nanomedicines for Overcoming Cancer Multidrug Resistance, Theranostics, 8 (2018) 1059-1074.

[53] V. Cocetta, E. Ragazzi, M. Montopoli, Mitochondrial Involvement in Cisplatin Resistance, Int J Mol Sci, 20 (2019) 3384.

[54] F. Guerra, A.A. Arbini, L. Moro, Mitochondria and cancer chemoresistance, Biochimica et Biophysica Acta (BBA) - Bioenergetics, 1858 (2017) 686-699.

Chapter II: Polymersome Nanoreactors with Tumor pH-Triggered Selective Membrane Permeability for Prodrug Delivery, Activation, and Combined Oxidation-Chemotherapy

2.1. Introduction

Biosynthetic pathways in nature for *in situ* producing and releasing products in the confined compartments have given the inspiration to develop novel therapeutic nanoreactors in the field of precise nanomedicine [1-3]. Typically, therapeutic nanoreactors are defined as synthetic reaction vessels, which can deliver and immobilize fragile catalysts (e.g., enzymes) for *in situ* conversion toxic substances into safe molecules, or production of toxic products from inert prodrugs to kill cells or bacteria [2, 4-6]. Note that the therapeutic nanoreactor strategy for chemotherapy of cancers have recently attracted particular interest, because *in situ* production of toxic drugs from inert prodrugs for cancer cell killing at tumor sites is significantly advantageous to reduce the side toxic effects [4]. The nanoreactors loading therapeutic enzymes can not only shield the activating enzymes from proteolytic attack, but also provide a confined reaction space for various cascade reactions locally at the tumor site [7-9]. In general, the majority of therapeutic nanoreactors for cancer therapy are accomplished *via* a two-step method involving prior delivery of activating enzymes to the tumor region and consecutive systemic administration of prodrugs for activation in the presence of the enzymes [7, 8, 10-12]. Apparently, this strategy has intrinsic shortcomings with the possibility of off-target prodrug activation and thus causing

unwanted toxicity to normal tissues. Different pharmacokinetics between the nanoreactors and prodrugs drastically reduced prodrug activation efficiency. Therefore, more efficient approaches to perform therapeutic nanoreactor strategy are still needed.

A variety of organic and inorganic nanomaterials have been applied to engineer therapeutic nanoreactors for treatment and diagnosis of cancers [4]. Among them, polymersomes possess some distinct advantages for construction of nanoreactors including simultaneous loading hydrophilic and hydrophobic molecules, high structural stability, and facile modulation of the physicochemical properties such as sizes and surface structures [13-16]. Moreover, the tunable membrane permeability may further achieve controllable catalyzed reactions inside polymersome nanoreactors [17]. In addition to the intrinsic membrane permeability of the nanoreactors [7, 8], the techniques such as insertion of protein channels [18, 19] or incorporation of stimuli-responsive segments in the membranes [20-24], have been widely exploited to control the membrane permeability by the external stimuli. The robust properties of polymersomes provide the possibility to construct a nanoreactor that integrates prodrugs and enzymes into one system, and activate the prodrugs specifically at tumor sites for overcoming the disadvantages of the abovementioned two-step prodrug activation strategy on the basis of therapeutic nanoreactors.

Herein we present a general strategy to design a simple polymersome nanoreactor with tunable membrane permeability from the diblock copolymers, PEG-*b*-P(BzMA-*co*-MPE), composed of poly(ethylene glycol) (PEG) and copolymerized segment of benzyl methacrylate (BzMA) and 2-(1-piperidinyl)ethyl methacrylate (MPE) for encapsulation of glucose oxidase (GOD) and hydrophobic H_2O_2-responsive prodrugs,

4-(hydroxymethyl)phenylboronic acid pinacol ester-modified model anticancer drugs (camptothecin prodrug (ProCPT) or paclitaxel prodrug (ProPTX)), in the inner aqueous cavities and membranes, respectively **(Figure 2.1)**.

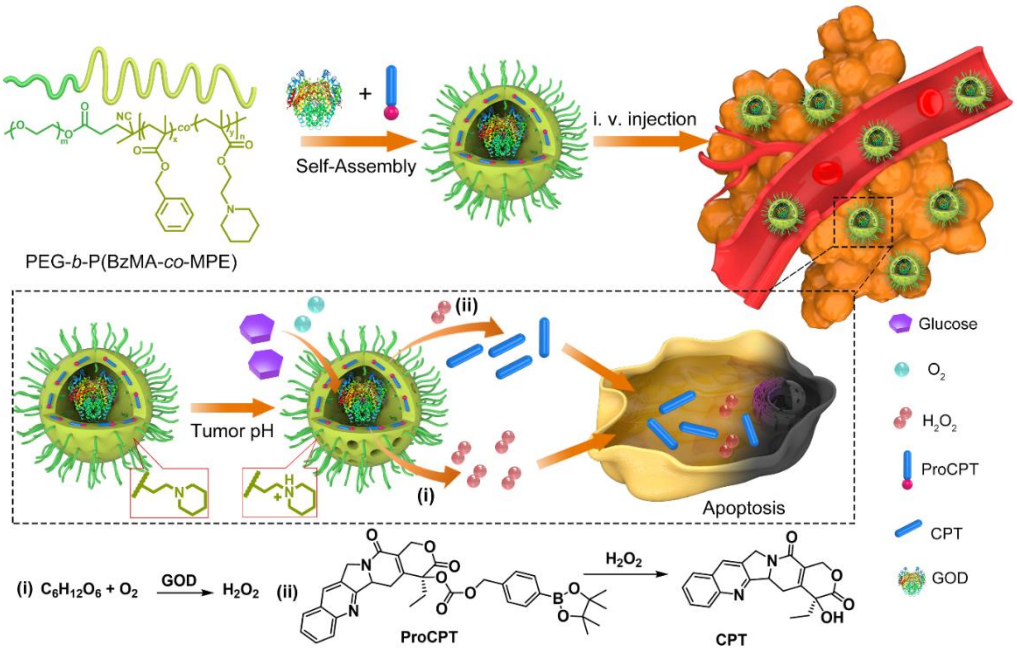

Figure 2. 1. Schematic illustration for preparation of GOD&ProCPT@Bz-MPE nanoreactor and its proposed antitumor mechanism. **(i)** the nanoreactor can respond to tumor acidity and activate its molecular weight-selective membrane permeability to allow small molecule cross the membrane and produce H_2O_2; **(ii)** the produced H_2O_2 can further activates the embedded ProCPT prodrugs to produce toxic drugs locally.

The GOD and prodrug-coloaded polymersomes nanoreactor maintain inactive state during blood circulation and in normal tissues. Once they arrive at the tumor site, the tumoral pH (pH 6.5-6.8) can trigger the molecular weight-selective membrane permeability to allow the diffusion of small molecules such as glucose and O_2 across

the membranes. Sequentially, the *in situ* produced H_2O_2 can facilitate conversion of H_2O_2-responsive prodrugs into toxic drugs *via* cleavage of the cage groups. H_2O_2 generation and activation of prodrugs can significantly enhance tumor eradication to achieve efficacious therapeutic results. Both *in vitro* and *in vivo* findings notably suggested a strong synergism between GOD and chemotherapeutic drug with remarkably enhanced tumor-cell killing capability through oxidation-chemotherapy with low adverse side effect. The facile synthetic method of phenylboronic ester-caged prodrugs presented herein can be extended to other anticancer drugs containing amine or hydroxyl functional groups. This formulation of therapeutic nanoreactors with tunable membrane permeability to coload GOD and H_2O_2-responsive prodrug represents a novel and efficient method of prodrug delivery and activation.

2.2. Materials and methods

2.2.1. Materials

Glucose oxidase from *Aspergillus niger* (GOD, 200 U/mg), 4-(hydroxymethyl) phenylboronic acid, pinacol (98%), anhydrous *N*,*N*-dimethylformamide (DMF), 2-(1-piperidino) ethanol (PE), 4-dimethylaminopyridine (DMAP, 98%), fluorescein isothiocyanate (FITC), bovine serum albumin (BSA), and poly(ethylene glycol) methyl ether (M_n = 2000 Da and 5000 Da) were purchased from Sigma-Aldrich and used as received. Benzyl methacrylate (BzMA, 98%) obtained from Shanghai Aladdin Bio-Chem Technology Co., Ltd (Shanghai, China) was passed through a silica column before use to remove the inhibitor. 2-(1-Piperidinyl)ethyl methacrylate (MPE) was

synthesized according to the previously reported method (**Figure 2.2** and **2.3**) [25]. Horseradish peroxidase (HRP, 250 U/mg) was obtained from klamar® (Shanghai, China). *β*-D-Glucose was purchased from TCI development Co., Ltd (Shanghai, China). Paclitaxel (PTX, > 95.0%) and (S)-(+)-camptothecin (CPT, > 95.0%) was both bought from Jiangyuan Natural Products Co. Ltd. (Chengdu, China) and used as received. Azobisisobutyronitrile (AIBN) obtained from Sigma-Aldrich was purified by recrystallization twice from methanol prior to use. Dichloromethane (DCM), triethylamine (TEA), and tetrahydrofuran (THF) were refluxed and dried over CaH_2 and sodium/benzophenone, respectively, and collected by distillation before being used. PEG_{114}-based macroRAFT agent were prepared according to the previously procedures reported elsewhere [26]. FITC-labelled molecules (FITC-GOD, FITC-BSA, FITC-PEG_{46}, and FITC-PEG_{114}) were synthesized. Fetal bovine serum (FBS), DMEM Medium, DMEM Medium without glucose and trypsin were purchased from GIBCO. Catalase, propidium iodide (PI, 94%), fluorescein diacetate (FDA), hematoxylin and eosin (H&E) staining kit, Cell Counting Kit-8 (CCK-8), 3,3′,5,5′-tetramethylbenzidine (TMB) and reactive oxygen species (ROS) Assay Kit (2',7'-dichlorofluorescin diacetate, DCFH-DA) were purchased from Beyotime Institute of Biotechnology (Shanghai, China). Human non-small cell lung cancer A549 cells and the murine hepatic cancer cell line H22 were kindly provided by Shanghai Institute of Cell Biology (Shanghai, China). 5-Week-old ICR mice were purchased from Beijing Vital River Laboratory Animal Technology Co., Ltd. (Beijing, China). 6'-O-pentafluorobenzene sulfonyl-2',7'-difluorofluorescein (BES-H_2O_2) was purchased from Wako Pure Chemical Industries, Co. Ltd. Unless otherwise stated, all other reagents used were obtained from Sinopharm

Chemical Reagent Co. Ltd and used as received. The animal studies were carried out according to the Regulations for the Administration of Affairs Concerning Experimental Animals (Hefei, revised in June 2013).

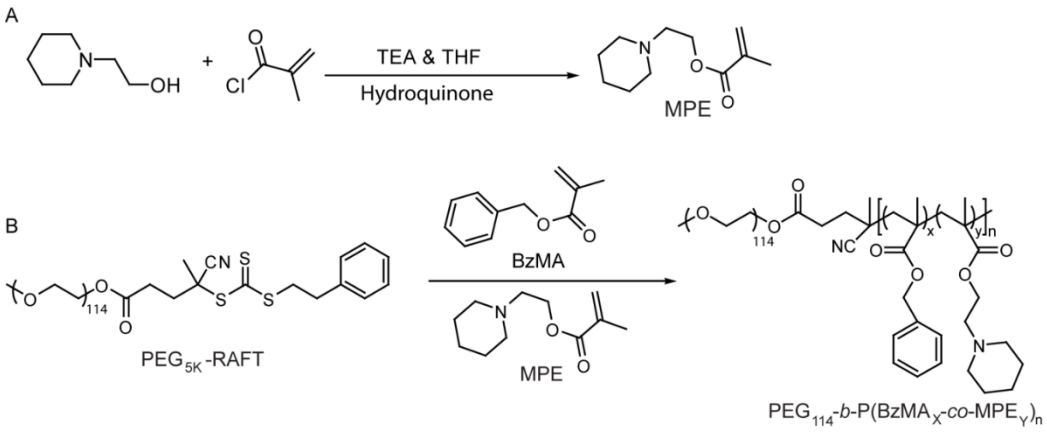

Scheme 2. 1. Synthetic routes to prepare 2-methyl-acrylic acid 2-piperidin-1-yl-ethyl ester (MPE) monomer (A) and PEG_{114}-*b*-$P(BzMA_x$-*co*-$MPE_y)_n$ amphiphilic block copolymers.

2.2.2. Characterization

The chemical structures of all synthesized chemicals were characterized by ^1H NMR spectra on a Bruker AV300 NMR 400 MHz spectrometer using $CDCl_3$ or DMSO-d6 as the solvent. The molecular weight (M_w) and molecular weight distribution (M_w/M_n) of the prepared amphiphilic block copolymers were evaluated by gel permeation chromatography (GPC) equipped with a G1310B Iso. pump, a G1316A PL gel column, and a G1362A differential refractive index detector. The eluent was DMF with 1 g/L LiBr at a flow rate of 1.0 mL/min. A series of low-polydispersity PEG

standards were employed for calibration. The morphology of self-assembled structures was examined by dropping 10 μL of sample on a copper grid placed on filter paper to remove excess solution, followed by drying process at room temperature before being examined by a JEOL-2100F Transmission Electron Microscope (TEM). The sample particle sizes, particle size distributions and zeta potentials were determined on a zeta-potential analyzer with dynamic laser light scattering (DLS) equipped a Malvern Zetasizer Nano ZS90, a He-Ne laser (633 nm), and 173^{o} collecting optics, For zeta potential evaluation, was applied and before polymersomes suspension were diluted and dispersed into ultrapure water at a final concentration of NaCl of 10 mM before being tested either at pH 7.4 or pH 6.8 by phase analysis light scattering (PALS) zeta potential mode, and all data were averaged over three measurements. UV-vis spectroscopy and fluorescence spectroscopy were recorded by UV-2401PC UV-VIS Spectrophotometer (Sahimadzu Corporation, Japan) and F-4600 Fluorescence Spectrophotometer (Hitachi, Japan), respectively. Reversed-phase high performance liquid chromatography (RP-HPLC) analysis was conducted on a Shimadzu HPLC system equipped with a LC-20AP binary pump, a C18 column, and an SPD-20A UV-Vis detector. A Xenogen IVIS Spectrum optical imaging device (PerkinElmer) was used to study the sample bio-distribution *in vivo*

2.2.3. Synthesis of FITC Conjugates

FITC-GOD or FITC-BSA conjugates were prepared according previous literature procedure [27]. Typically, to a solution made of 1 mL GOD or BSA in 100 mM sodium carbonate, 25 μL FITC in DMSO (10 mg/mL) was added and the mixture

was allowed to react for 12 h at 4 °C in the dark. Thereafter, the solution was subjected to dialysis (MWCO = 3500) against PBS (pH 7.4) in the dark until there was no detectable free FITC in the dialysate before being freeze dried to collect the product. To prepare FITC-PEG conjugate such as FITC-PEG_{2K} conjugate: Freeze-dried PEG_{2K}-NH_2 (100 mg, 0.05 mmol) and FITC (19.5 mg, 0.05 mmol), 0.2 µL dry TEA were dissolved in 3 mL dry DMF and incubated in the dark place at 25 °C for 16 h under nitrogen flow. Next, the excess FITC was removed by dialysis (MWCO =3500) against distilled water in the dark before being freeze dried to collect the product. By using the same procedure, FITC-PEG_{5K} was also prepared.

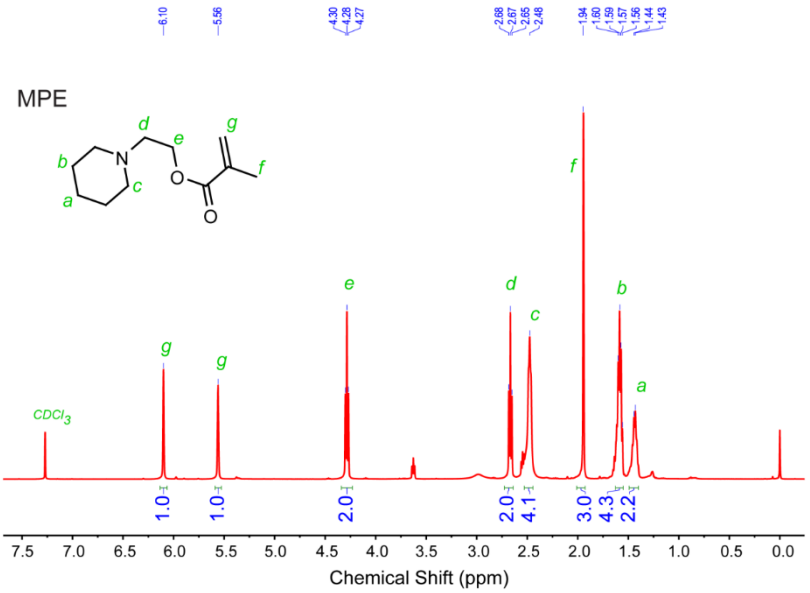

Figure 2. 2. ^{1}H NMR spectrum recorded 2-(1-piperidinyl)ethyl methacrylate (MPE).

2.2.4. Critical aggregation concentration of Bz-MPE Polymersomes

The critical aggregation concentration (CAC) of polymersomes self-assembled from

PEG_{114}-*b*-P($BzMA_{126}$-*co*-MPE_{39}) di-block copolymer was evaluated using pyrene fluorescence probe procedure as previously reported with minor modification.[28, 29] Briefly, after self-assembly, the polymersome solution was diluted from 1 mg/mL to 10^{-6} mg/mL. Thereafter, 50 µL pyrene dissolved in acetone at a concentration of 1.21 $x10^{-2}$ mg/mL was dropped into 5 mL of each polymersome solution. The mixture was then subjected to sonication at room temperature for 2 h, followed by evaporation of acetone under reduced pressure. Finally, the excitation spectrum of each solution was recorded by F-4600 fluorescence spectrophotometer from 290 nm to 370 nm wavelength by setting the fluorescence emission at 374 nm. The polymersome CAC value was determined by plotting excitation intensity ratio at a wavelength 340 nm and 325 nm (I_{340}/I_{325}) against the concentration of polymersome solution.

2.2.5. Determination of Protonation Degree of PEG_{114}-*b*-P($BzMA_{126}$-*co*-MPE_{39}) Polymersomes

Initially, 5 mL of the polymersome made of PEG_{114}-*b*-P($BzMA_{126}$-*co*-MPE_{39}) polymer at a concentration of 0.4 mg/mL was prepared and the pH was adjusted to 12 by 1 M NaOH, and then back titrated against 0.1 M HCl, while recording the pH by a pH-meter at 25 °C. Thereafter, the titration curve was plotted with pH as a function of HCl volume to determine the pK_a. Finally, the degree of protonation "θ(pH)" was calculated according to the following formula:

Equation 2.1:

$$\theta(\mathrm{p}H) = \frac{1}{1 + e^{-\ln 10\,(\mathrm{p}K_a - \mathrm{p}H)}}$$

2.2.6. pH-triggered membrane permeability of Bz-MPE Polymersomes

The pH-responsive membrane permeability behavior of Bz-MPE polymersomes at pH 6.8 or 7.4 was evaluated *via* colorimetric cascade reaction by encapsulation GOD in the inner cavity of GOD to obtain GOD@Bz-MPE. Briefly, 2 mL GOD@Bz-MPE (100 mU/mL GOD**)** was incubated with glucose (1 mg/mL) at 37 °C and pH 6.8 or 7.4, followed by addition of TMB (100 μM) and HRP (150 mU/mL) outside the polymersomes membrane. At a predetermined time interval, the absorbance was recorded by UV-vis spectrophotometer from the wavelength range of 500 to 750 nm for 1 h.

2.2.7. *In Vitro* Observation of Live/Dead Cells after Different Treatments

A549 cells were seeded into several 12-well plates at a density of 1 x 10^5 cells/well in 500 μL DMEM media with 10% FBS and then cultured for 24 h at 37 °C under 5% CO_2 humidified atmosphere. Then the media was changed with pH 6.8 fresh media containing 1 mg/mL glucose, followed by addition of 50 μL PBS, free CPT, GOD@Bz-MPE, or GOD&ProCPT@Bz-MPE and incubation for 48 h, with the GOD equivalent concentration of 100 mU/mL or 0.26 μg/mL ProCPT or CPT. Thereafter, the media was aspirated and followed by staining live cells by FDA and dead cells by PI. Briefly, FDA solution (1 μL, 1 mg/mL in DMSO) was added to each well and incubated for 20 min for staining live cells. Subsequently, each well was washed with PBS twice, followed by addition of 100 μL PBS. PI solution (2 μL, 1 mg/mL in DMSO) was added

to each well followed by 10 min incubation for staining dead cells. Finally, each well was washed with PBS twice and then transferred for observation under Olympus FV1000 fluorescent microscope.

2.2.8. Fluorophore loaded polymersomes preparation (DiR@Bz-MPE)

PEG_{114}-*b*-P($BzMA_{126}$-*co*-MPE_{39}) polymer (2 mg) and 1,1′-dioctadecyl-3,3,3′,3′-tetramethylindotricarbocyanine iodide (DiR) dye mixture with molar ratio 10:1, respectively, were dissolved in THF and DMSO co-solvent (500 μL, v/v 4:1), followed by slowly adding PBS (5 mL) *via* an infusion pump at a constant rate of 1 mL/h and at room temperature in the dark place. Thereafter, the organic solvent solution and unencapsulated DiR dye were removed by dialysis (MWCO = 3500) against PBS at pH 7.4 until there was no detectable DiR fluorescence in the dialysate solution.

2.2.9. Synthesis of PEG_{114}-b-P($BzMA_x$-co-MPE_y)$_n$ amphiphilic block copolymers

The amphiphilic block copolymers were synthesized *via* reversible addition-fragmentation chain transfer (RAFT) copolymerization of BzMA and MPE monomers that were prepared using PEG-based macroRAFT agent as the chain transfer agent (**Scheme 2.2**). In a typical procedure, PEG-based RAFT agent (0.22 g, 0.041 mmol), Bz-MA (1 g, 5.6 mmol), MPE (0.28 mg, 1.418 mmol), and AIBN (0.66 mg, 0.004 mmol) were dissolved in 1,4-dioxane (5 mL) and put into a 10 mL-ampoule equipped with a magnetic stirring bar. The mixture was degassed by three freeze-pump-thaw cycles and sealed under vacuum. The ampoule was subsequently placed into a preheated oil bath

at 75 °C and allowed to polymerize for 12 h. Thereafter, the reaction was stopped by freezing in liquid nitrogen followed by precipitation in cold ether. The precipitate was dissolved in DCM (3 mL) and precipitated in cold ether again. The process was repeated twice. Finally, the product was dried in a vacuum oven, yielding 1.14 g of pale-yellow solid (M_n = 36.2 KDa, M_w/M_n = 1.09, **Figure 2.3**). The actual degree of polymerization of BzMA and MPE segments determined by ^{1}H NMR (300 MHz, $CDCl_3$) was found to be 126 and 39, corresponding to conversion degree of 92.7% and 98%, respectively (**Figure 2.4**). According to the similar procedure, a series of block copolymers including PEG_{114}-*b*-$PBzMA_{162}$, PEG_{114}-*b*-P($BzMA_{154}$-*co*-MPE_9), and PEG_{114}-*b*-P($BzMA_{126}$-*co*-MPE_{49}) were synthesized (**Table 2.1**).

Table 2. 1. Block Copolymers Characterization and the Self-assembled Nanoparticles.

Polymer Name	**MPE ratio[a] (%)**	**M_n[b] (kDa)**	**M_w/M_n[b]**	**D_h[c] (nm)**	**Morphology[d]**
PEG_{114}-*b*-$BzMA_{162}$	0	33.1	1.15	186	Vesicle
PEG_{114}-*b*-P($BzMA_{154}$-*co*-MPE_9)	5.5	34.7	1.08	207	Vesicle
PEG_{114}-*b*-P($BzMA_{126}$-*co*-MPE_{39})	23.6	36.2	1.09	220	Vesicle
PEG_{114}-*b*-P($BzMA_{116}$-*co*-MPE_{49})	29.6	39.1	1.10	170	Vesicle

[a]: determined by ^{1}H NMR, [b]: determined by GPC, [c]: determined by DLS, [d]: determined by TEM.

2.2.10. Synthesis of phenylboronic pinacol ester-caged CPT prodrugs

CPT prodrug (ProCPT) were synthesized according the synthetic routes as shown in **Scheme 2.2.** Briefly, CPT (0.52 g, 1.5 mmol) and DMAP (4.3 mmol) were suspended in dry DCM (15 mL) under nitrogen atmosphere in a 150 mL flask. Subsequently, triphosgene (0.15 g, 0.5 mmol) was added and the mixture was stirred for 30 min at room temperature. 4-(Hydroxymethyl)phenylboronic acid pinacol ester (0.7 g, 3 mmol) in dry THF (10 mL) was added dropwise *via* a constant pressure funnel. The reaction mixture was stirred overnight. After evaporating all the solvents, the crude product was purified by column chromatography using ethyl acetate as eluent (100% EtOAc) to give CPT prodrug (ProCPT) as a pale-yellow solid powder (0.45 g, yield: 49.2%). ^{1}H NMR (400 MHz, DMSO-d6) δ (ppm): 8.70 (s, 1H), 8.22 (d, *J* = 8.5 Hz, 1H), 8.15 (d, *J* = 8.0 Hz, 1H), 7.89 (t, *J* = 7.1 Hz, 1H), 7.74 (t, *J* = 7.8 Hz, 1H), 7.62 (d, *J* = 7.9 Hz, 2H), 7.35 (d, *J* = 7.9 Hz, 2H), 7.08 (s, 1H), 5.58 – 5.46 (m, 2H), 5.29 (s, 2H), 5.22 (s, 2H), 2.25 – 2.13 (m, 2H), 1.22 (d, *J* = 8.4 Hz, 12H), 0.93 (t, *J* = 7.4 Hz, 3H) (**Figure 2.5**). ^{13}C NMR ($CDCl_3$) δ (ppm): 166.30, 156.26, 152.61, 151.29, 147.90, 145.44, 144.62, 136.34, 134.03, 130.13, 129.69, 128.75, 127.41, 127.15, 127.04, 126.00, 125.04, 119.29, 94.99, 82.78, 76.91, 76.21, 69.29, 66.05, 48.95, 30.91, 23.80, 6.62 **(Figure 2.6)**. ESI-MS: Calculated: $[C_{34}H_{33}BN_2O_8+H]^+$ 609.46, found: $[C_{34}H_{33}BN_2O_8+H]^+$ 609.24 **(Figure 2.9A)**.

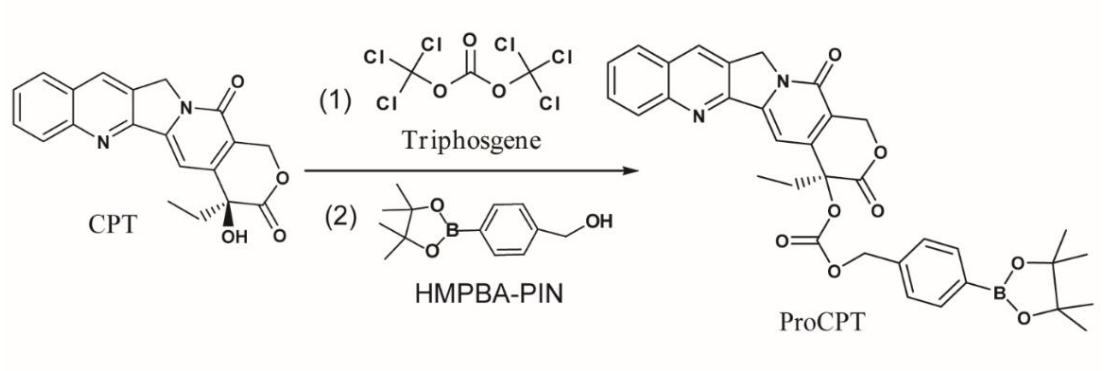

Scheme 2. 2. Synthesis of CPT prodrug (ProCPT).

2.2.11. Synthesis of Phenylboronic Pinacol Ester-Caged PTX (ProPTX)

As shown in **Scheme 2.3**, 4-(Hydroxymethyl)phenylboronic acid pinacol ester (HMPBA-PIN) (85 mg, 0.36 mmol), and DMAP (108 mg, 0.83 mmol) were dissolved in 5 mL dry DCM under nitrogen atmosphere, and triphosgene (27.5 mg, 0.09 mmol) was added and the mixture was stirred for 30 min at room temperature. Then, paclitaxel (PTX) (237 mg, 0.27 mmol) previously dissolved in 2 mL dry acetonitrile was added dropwise *via* a constant pressure dropping funnel, and the reaction mixture was stirred overnight. After evaporating all the solvents, the crude product was purified by column chromatography using ethyl acetate and hexane as eluent (3/2 ratio, respectively) to give a PTX prodrug (ProPTX) as a pure white solid powder (128 mg). ^{1}H NMR (400 MHz, $CDCl_3$) δ (ppm) 8.14 (d, J = 7.7 Hz, 2H), 7.81 (d, J = 7.3 Hz, 2H), 7.73 (d, J = 7.7 Hz, 2H), 7.61 (t, J = 7.2 Hz, 1H), 7.50 (dd, J = 14.5, 7.2 Hz, 3H), 7.44 – 7.32 (m, 9H), 6.93 (d, J = 9.3 Hz, 1H), 6.33 – 6.25 (m, 2H), 5.98 (d, J = 9.3 Hz, 1H), 5.69 (d, J = 6.9 Hz, 1H), 5.44 (s, 1H), 5.18 (q, J = 12.3 Hz, 2H), 4.98 (d, J = 9.4 Hz, 1H), 4.44(s, 1H), 4.32 (d, J = 8.4 Hz, 1H), 4.21 (d, J = 8.5 Hz, 1H), 4.12 (q, J = 7.1 Hz, 1H), 3.82 (d, J = 6.9 Hz, 1H), 2.46 (s, 3H), 2.23 (s, 3H), 2.04 (s, 2H), 1.96 – 1.85 (m, 1H), 1.80

(s, 1H), 1.74 (s, 1H), 1.69 (s, 2H), 1.34 (s,12H), 1.26 (d, J = 10.9 Hz, 6H), 1.14 (s, 3H) (**Figure 2.7**). ^{13}C NMR ($CDCl_3$) δ (ppm) 203.87, 171.32, 169.87, 167.85, 167.12, 167.06, 154.14, 142.74, 137.25, 136.71, 135.15, 133.72, 133.50, 132.80, 132.06, 130.26, 129.18, 129.15, 128.78, 128.73, 128.57, 127.36, 127.18, 126.61, 84.48, 84.00, 81.07, 79.17, 77.27, 76.90, 76.48, 75.62, 75.11, 72.17, 72.11, 70.55, 60.44, 58.54, 52.78, 45.57, 43.21, 35.61, 35.54, 26.86, 24.89, 22.74, 22.20, 21.10, 20.88, 14.87, 14.23, 9.63 (**Figure 2.8**). ESI-MS: Calculated $[C_{61}H_{68}BNO_{17}+K]^+$ 1137.098, found $[C_{61}H_{68}BNO_{17}+K]^+$ 1136.443 (**Figure 2.9B**).

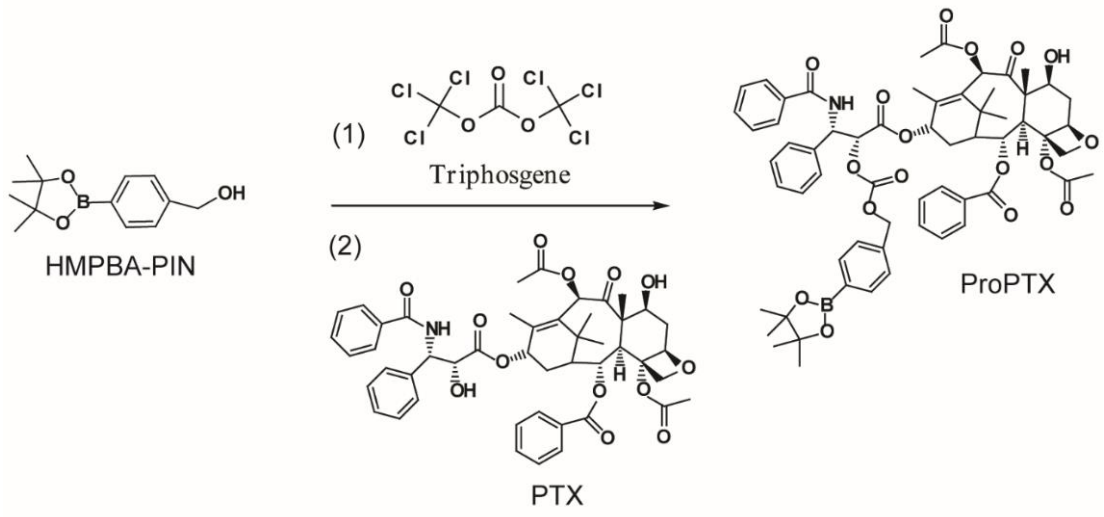

Scheme 2. 3. Synthesis of PTX prodrug (ProPTX).

2.2.12. Preparation of GOD and prodrug-loading nanoreactors

GOD and prodrug coloaded polymersome nanoreactors were prepared via solvent replacement approach. Typically, PEG_{114}-*b*-P($BzMA_{126}$-*co*-MPE_{39}) (1 mg) and ProCPT (0.2 mg) were dissolved in THF and DMSO co-solvent (500 μL, v/v 4:1), followed by

first adding GOD PBS solution (1 mL, 1 mg/mL). Subsequently, PBS (8 mL) were added *via* an infusion pump at a constant rate of 1 mL/h. The organic solvent solution was removed by dialysis (MWCO = 3500) against PBS at pH 7.4, followed by subjecting the solution to filtration and centrifugal ultrafiltration membrane. After washing many times with PBS (pH 7.4), the final nanoreactor solution was collected and dispersed into PBS (5 mL, pH 7.4). This nanoreactor solution was denoted as GOD&ProCPT@Bz-MPE. To quantify the loading capacity of the nanoreactor, FITC-labelled GOD (GOD-FITC) enzymes were used. After removal of unencapsulated GOD-FITC and ProCPT until there was no detectable FITC or ProCPT fluorescence in the solution, the loading capacities (DLCs) and loading efficiency (DLE) of GOD&ProCPT@Bz-MPE polymersomes towards GOD-FITC and ProCPT were measured by fluorescence spectrophotometer and high performance liquid chromatography (HPLC), respectively. DLCs (%) = [(weight of loaded drug)/(weight of total polymersomes)] × 100. DLE (%) = [(weight of loaded drug in polymersomes)/(weight of total drug in feed)] × 100 DLCs for GOD&ProCPT@Bz-MPE were calculated to be 6.04 wt% and 3.46 wt% for GOD and ProCPT, respectively. DLE (%) for GOD&ProCPT@Bz-MPE were determined to be 12.86% and 34.63% for GOD and ProCPT, respectively.

According to the similar procedures, empty PEG_{114}-*b*-P($BzMA_{126}$-*co*-MPE_{39}) polymersomes (Bz-MPE) and GOD-loaded PEG_{114}-*b*-P($BzMA_{126}$-*co*-MPE_{39}) polymersome (GOD@Bz-MPE) were also prepared. Moreover, similar protocol was also applied to encapsulate FITC, FITC-PEG_{46}, FITC-PEG_{114}, or FITC-BSA into PEG_{114}-*b*-$PBzMA_{162}$, PEG_{114}-*b*-P($BzMA_{154}$-*co*-MPE_{9}), PEG_{114}-*b*-P($BzMA_{126}$-*co*-

MPE_{39}), and PEG_{114}-*b*-P($BzMA_{126}$-*co*-MPE_{49}) polymersomes. PEG_{114}-*b*-$PBzMA_{162}$ block copolymer was also used to encapsulate GOD and ProCPT with DLCs of 5.26 wt% and 4.15 wt% for GOD and ProCPT, respectively, which was denoted as GOD&ProCPT@Bz.

2.2.13. Molecular weight-selective membrane permeability

A series of PEG-*b*-P(BzMA-*co*-MPE) polymersomes with the similar length of hydrophobic segments (n) but various ratios of pH-responsive monomer *i.e*. with MPE ratios of 0%, 5.5%, 23.6%, and 29.6% (**Table 2.1**) were prepared. Consecutively, various molecules with different molecular weights which are FITC (0.38 kDa), FITC-PEG_{46} (2.3 kDa), FITC-PEG_{114} (5.3 kDa), or FITC-BSA (66.3 kDa) were separately loaded in each block copolymer polymersome during self-assembly. Subsequently, polymersome solution (2 mL) was sealed into dialyzing bag (MWCO = 7 kDa or 100 kDa) and placed into 50 mL falcon tube filled with 20 mL PBS (pH 6.8) at 25 °C for dialysis with moderate stirring in dark place. At a given time interval, dialysate solution (1 mL) was withdrawn for fluorescence test and taken back into the falcon tube immediately after the fluorescence test. Finally, the release rate of the encapsulated material was evaluated through quantification of FITC fluorescence intensity at emission wavelength of 520 nm at various time intervals.

2.2.14. Quantification of H_2O_2 production

The amount of produced H_2O_2 by the GOD@Bz-MPE (100 mU/mL**)** was

evaluated *via* a colorimetric detection. Briefly, GOD@Bz-MPE (2 mL) were incubated with glucose (1 mg/mL) at 37 °C and pH 6.8 or 7.4, followed by addition of TMB (100 μM) and HRP (150 mU/mL). At a predetermined time interval, the absorbance was recorded by UV-vis spectrophotometer from the wavelength range of 500 to 750 nm. Finally, the produced H_2O_2 concentration at various time points was quantified by the absorbance at 650 nm based on the standard curve of H_2O_2 concentrations.

2.2.15. Drug release profiles

The drug release profiles from GOD&ProCPT@Bz-MPE nanoreactors were monitored by HPLC. Typically, GOD&ProCPT@Bz-MPE solution (1 mL) was sealed in a dialysis bag and incubated in PBS (9 mL, pH 6.8 or 7.4) containing glucose (1 mg/mL) at 37 °C. At predetermined time intervals, aliquot samples were collected and replaced by the same volume for quantification of released CPT by HPLC (mobile phase: methanol/H_2O (9:1, v/v), 1 mL/min, UV-vis detection-wavelength at 365 nm).

2.2.16. *In vitro* cytotoxicity

A549 cells were seeded in 96-well plates at a density of 1×10^4 cells per well in 100 μL DMEM with 10% FBS at 37 °C with 5% CO_2 humidified atmosphere for 24 h. Subsequently, the medium was replaced by fresh pH 7.4 or 6.8 DMEM with or without glucose (1 mg/mL), followed by addition of desired concentrations of free GOD, free CPT, GOD@Bz-MPE, or GOD&ProCPT@Bz-MPE and incubated for another 48 h. Thereafter, the medium was changed with 150 μL fresh media containing 10% Cell

Counting Kit-8 (CCK-8) reagent and incubated for another 3 h before being subjected to a microplate reader for absorbance measurement at the wavelength of 450 nm. Finally, the cell viability was assessed based on colorimetric value of each well compared to the control groups. At each concentration, four individual experiments were carried out.

At a given fraction affected (*f*a) determined based on results of cell viability assay, the corresponding drug synergy combination index (CI) between GOD and CPT against A549 cells was determined *via* Chou-Talalay's isobolographic method [30], as shown from the following **Equation 2.2**:

$$CI=\frac{C_{ProCPT\&GOD@BzMPE}}{C_{CPT}}+\frac{C_{GOD\&ProCPT@BzMPE}}{C_{GOD}}+\alpha\frac{\left(C_{ProCPT\&GOD@BzMPE}\right)\left(C_{GOD\&ProCPT@BzMPE}\right)}{(C_{CPT})(C_{GOD})}$$

Where $C_{ProCPT\&GOD@BzMPE}$ and $C_{GOD\&ProCPT@BzMPE}$ stand for the concentration of ProCPT and GOD, respectively, used in combination to achieve a certain *f*a value. C_{CPT} and C_{GOD} stand for the concentration of CPT and GOD, respectively, used as a single agent to achieve the same *f*a value, and $\boldsymbol{\alpha} = 0$ as the more conservative assumption of mutual exclusivity was adopted. A CI range between >1.3, 1.1 to 1.3, 0.9 to 1.1, 0.8 to 0.9, 0.6 to 0.8, 0.4 to 0.6, and 0.2 to 0.4 indicates antagonism, moderate antagonism, additive effect, slight synergism, moderate synergism, synergism, and strong synergism, respectively.

2.2.17. Intratumorally H_2O_2 level detection

H22 cells (2×10^6 cells) were subcutaneously implanted into 6 weeks old female ICR mice. When the tumors in mice reached ~100 mm^3, they were used for the *in vivo* investigation. The tumor-bearing mice were intravenously administered with PBS (150 μL), free GOD (10 U in 150 μL PBS per mouse), free CPT (26 μg ProCPT in 150 μL PBS per mouse), GOD@Bz-MPE (10 U in 150 μL PBS per mouse), GOD&ProCPT@Bz-MPE (10 U GOD with corresponding 26 μg ProCPT in 150 μL PBS per mouse). After 24 h, H_2O_2-specific probe BES-H_2O_2 (25 μL) was injected intratumorally and after 30 min, the mice were sacrificed to collect the tumors followed by slicing into 10 μm thick sections and stained with DAPI before being observed under fluorescent microscopy. Integrated density of fluorescence was quantified by subtraction of the background using ImageJ software.

2.2.18. *In vivo* ProCPT activation in liver and tumor evaluation

H22 tumor-bearing mice were intravenously administered with GOD&ProCPT@Bz-MPE (150 μL, 10 U GOD with corresponding 26 μg ProCPT per mouse) and the concentrations of CPT or ProCPT were evaluated in liver and tumor at varying time points of 2 h, 12 h, 24 h, and 48 h post intravenous injection according to the reported procedure with minor modifications [31]. Briefly, at a given time point, the mice were excised and tumor and liver organs were harvested and homogenized in saline solution, followed by subsequent CPT and ProCPT extraction with chloroform and methanol cosolvent (ratio 4:1 v/v) through centrifugation at 15 000 g for 5 min. Next, the organic layer was collected and immediately evaporated under reduced

pressure. The obtained residues were re-dissolved in methanol and subjected to UV-vis HPLC for measurement (mobile phase: Methanol/H_2O (9:1, v/v), 1 mL/min, UV-vis detection mode at a wavelength of 365 nm). The concentrations of CPT and ProCPT were determined by analyzing their corresponding peaks at 2.47 min and 3.56 min, respectively, from the sample HPLC spectra. The results were reported as the percentage of the injected dose per gram organ (%ID/g).

2.2.19. Antitumor efficacy and systemic toxicity

The H22 tumor-bearing mice were randomly divided into five treatment groups where each group contained 5 mice. The *in vivo* therapy experiments were initiated. Since day 0, three consecutive doses were intravenously given at day 0, 3, and 6, respectively. For each dose administered, the first group which was the control group received PBS (150 μL), the second group was injected with free GOD (10 U in 150 μL PBS per mouse), the third group received free CPT (26 μg in 150 μL per mouse), the fourth group was injected with GOD@Bz-MPE (10 U in 150 μL PBS per mouse), the last group received GOD&ProCPT@Bz-MPE (10 U GOD with corresponding 26 μg ProCPT in 150 μL PBS per mouse). During 22 days of treatment, the body weight and tumor size of each mouse were recorded each and every two day. The tumor volume was calculated by the following equation: $V = L \times W^2/2$. Where "L" is the length and "W" is the width of the tumor. After treatment, tumors and the major organs (heart, liver, spleen, lung, and kidney) were harvested and sectioned into 10 μm thick slices with a cryostat and stained with H&E for histological analysis.

2.2.20. Statistical analysis

All the results were expressed as mean ± standard deviation (SD). The significance of the results was analyzed by Student's t-test and the differences between two groups were judged statistically significant when the two-tailed P-Value is lower than 0.05.

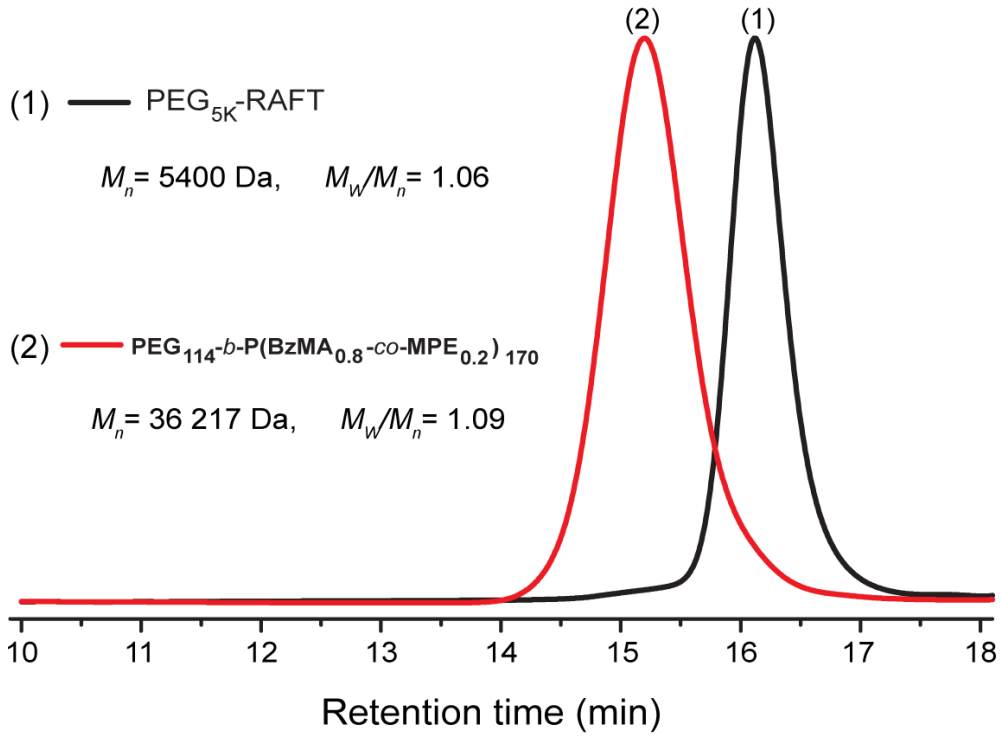

Figure 2. 3. GPC traces for PEG_{114}-based macroRAFT agent and PEG_{114}-*b*-$P(BzMA_{126}$-*co*-$MPE_{39})$ polymer.

2.3. Results

2.3.1. Synthesis of block copolymers and prodrugs for preparation of polymersome nanoreactors

The amphiphilic diblock copolymers were readily synthesized through RAFT copolymerization of BzMA and MPE by using PEG_{114}-based macroRAFT as a chain transfer agent, which were abbreviated as PEG-*b*-P(BzMA-*co*-MPE) (**Figure 2.2**). The final total degree of polymerization of BzMA and MPE was designed to be 170 and the ratios of them were adjusted by changing the feeding ratios.

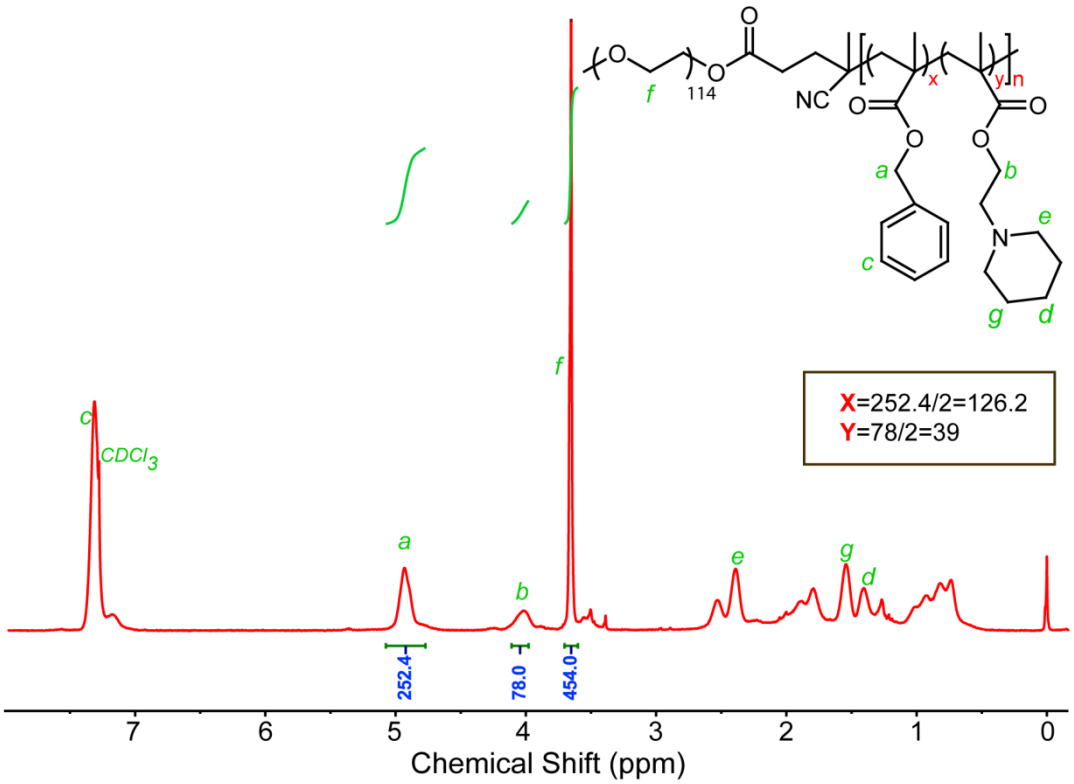

Figure 2. 4. ^{1}H NMR spectrum recorded for PEG_{114}-*b*-P($BzMA_{126}$-*co*-MPE_{39}) in $CDCl_3$.

A series of block copolymers, PEG_{114}-*b*-P($BzMA_x$-*co*-MPE_y)$_{170}$, with varying x and y values were synthesized. Typically, GPC and ^{1}H NMR characterization confirmed successful synthesis of PEG_{114}-*b*-P($BzMA_{126}$-*co*-MPE_{39}) with a relatively narrow molecular weight distribution (M_n = 36.2 kDa, and M_w/M_n = 1.09), and a conversion higher than 90% for all monomers (**Figure 2.2, 2.3,** and **2.4**). In addition, a series of block copolymers were synthesized with the molar ratios of MPE ranging from 0% to 30% according to the similar polymerization procedure (**Table 2.1**).

The application of self-immolative spacer has been demonstrated to hold great potential to engineer caged molecules that can undergo programmable activation through a chemical or enzymatic reaction process [32-35]. In this regard, we used a H_2O_2-responsive moiety, 4-(hydroxymethyl)phenylboronic acid pinacol ester, to cage the anticancer drugs through a self-immolative linker, which was obtained *via* a facile one-pot reaction procedure (**Scheme 2.2** and **Scheme 2.3**).

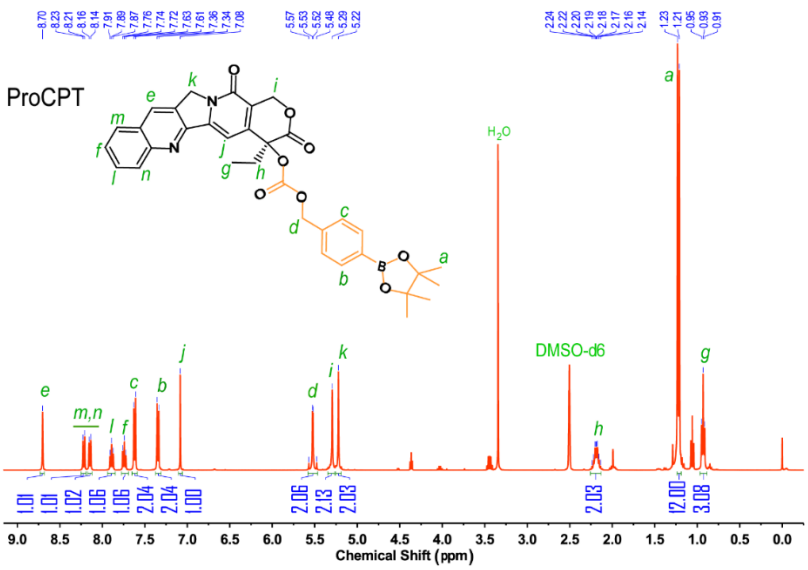

Figure 2. 5. ^{1}H NMR spectrum for ProCPT in DMSO-d6.

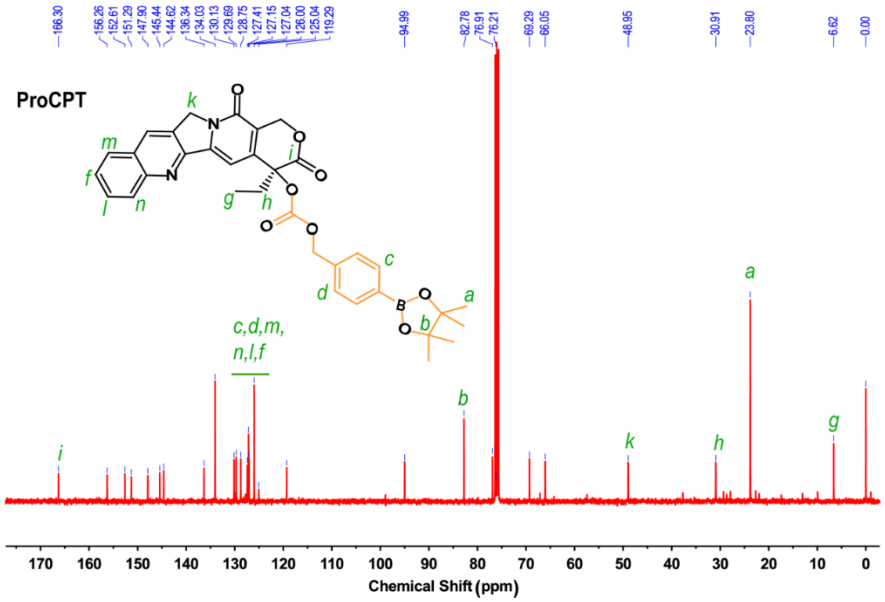

Figure 2. 6. ^{13}C NMR spectrum for ProCPT in $CDCl_3$.

Fascinatingly, this method is feasible to engineer various prodrugs based on different drugs commonly used in chemotherapy containing hydroxyl or amino functional groups. As the representative examples, we prepared CPT and PTX-based prodrugs, which were denoted as ProCPT and ProPTX, respectively. The prepared prodrugs were fully characterized by ^{1}H and ^{13}C NMR (**Figure 2.5, 2.6, 2.7,** and **2.8**). Moreover, ESI-MS characterization also confirmed the successful preparation of ProCPT and ProPTX (**Figure 2.9A,B**). In the following sections, we used ProCPT as the model prodrug to perform the investigation.

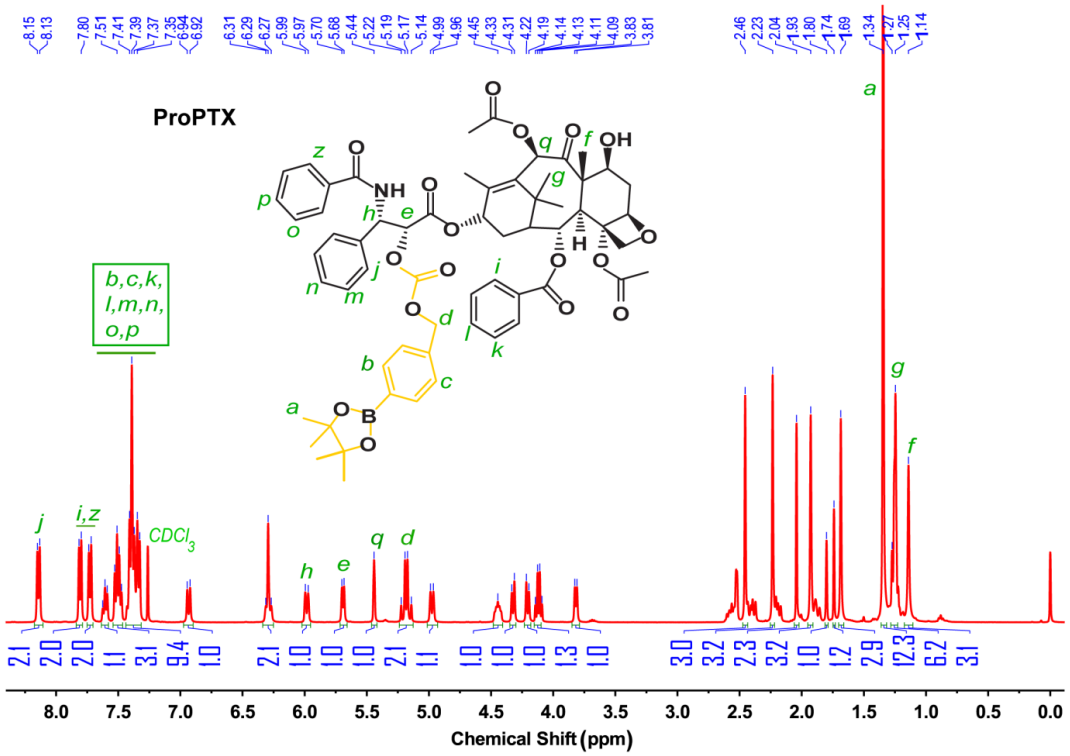

Figure 2. 7. ^{1}H NMR spectrum for ProPTX in $CDCl_3$.

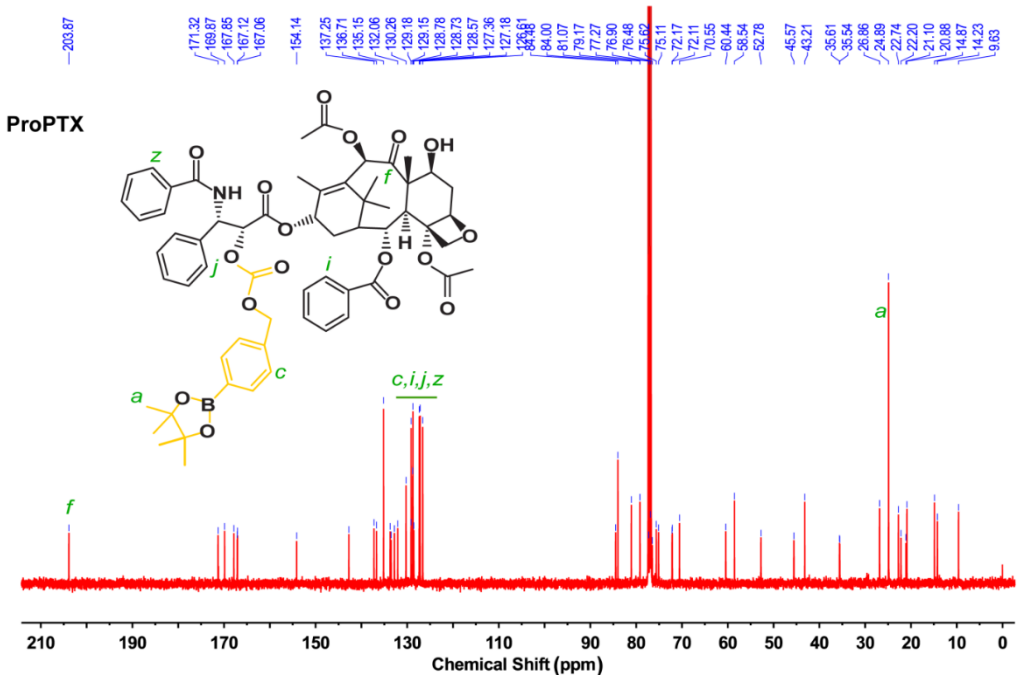

Figure 2. 8. ^{13}C NMR spectrum for ProPTX in $CDCl_3$

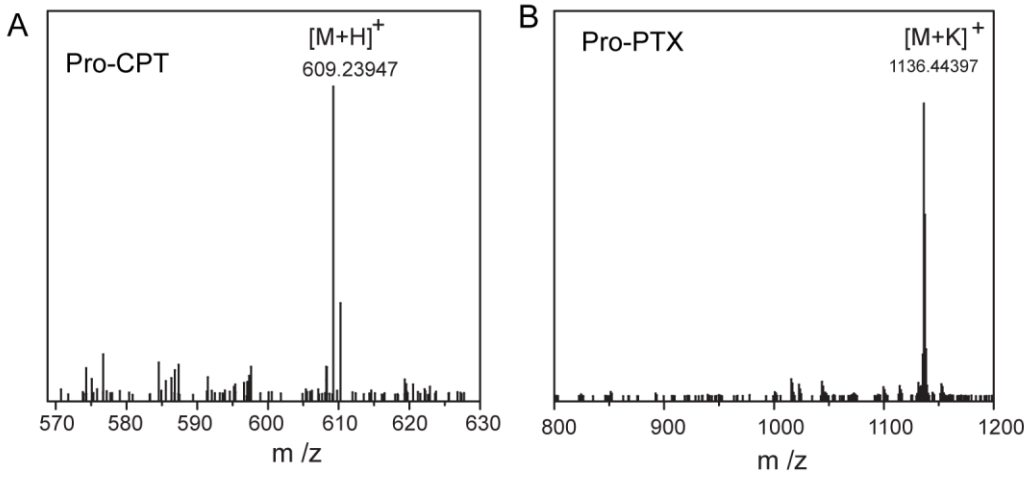

Figure 2. 9. (A) ESI-MS spectrum for ProCPT. **(B)** ESI-MS spectrum for ProPTX.

The well-defined amphiphilic block copolymers, PEG_{114}-*b*-P($BzMA_x$-*co*-MPE_y)$_{170}$, can spontaneously self-assemble into vesicular structures *via* a solvent replacement method at pH 7.4 due to the suitable length ratios of the hydrophilic to hydrophobic segments (**Table 2.1**) [15]. As a representative example, the block copolymer, PEG_{114}-*b*-P($BzMA_{126}$-*co*-MPE_{39}), has a critical aggregation concentration (CAC) of 1.49 × 10^{-3} mg/mL (**Figure 2.10**).

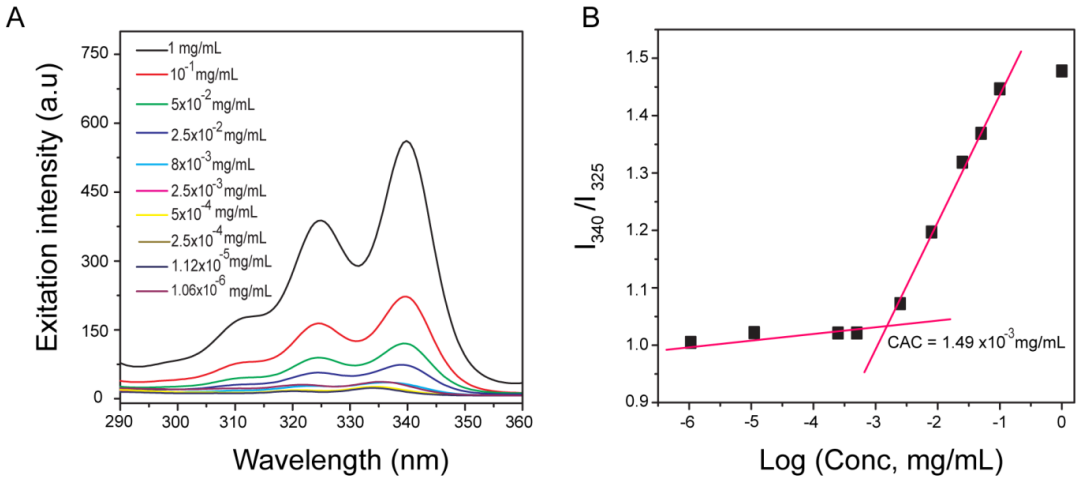

Figure 2. 10. Critical aggregation concentration (CAC) evaluation for polymersome

solutions self-assembled from PEG_{114}-*b*-P($BzMA_{126}$-*co*-MPE_{39} copolymer. **(A)** Pyrene-based fluorescence excitation intensity spectra of polymersomes solution with various concentrations. **(B)** CAC calculation by plotting excitation intensity ratio at a wavelength 340 nm and 325 nm (I_{340}/I_{325}) against the concentration of polymersome solution.

After self-assembly into nanoparticles, cryogenic transmission electron microscopy (cryo-TEM) characterization depicted a typical spherical hollow structure with high contrast between the periphery and center of the self-assembled morphologies, which suggested successful formation of well-organized vesicular structure with a diameter size of ~190 nm at both pH 6.8 and pH 7.4 (**Figure 2.11A,B)**.

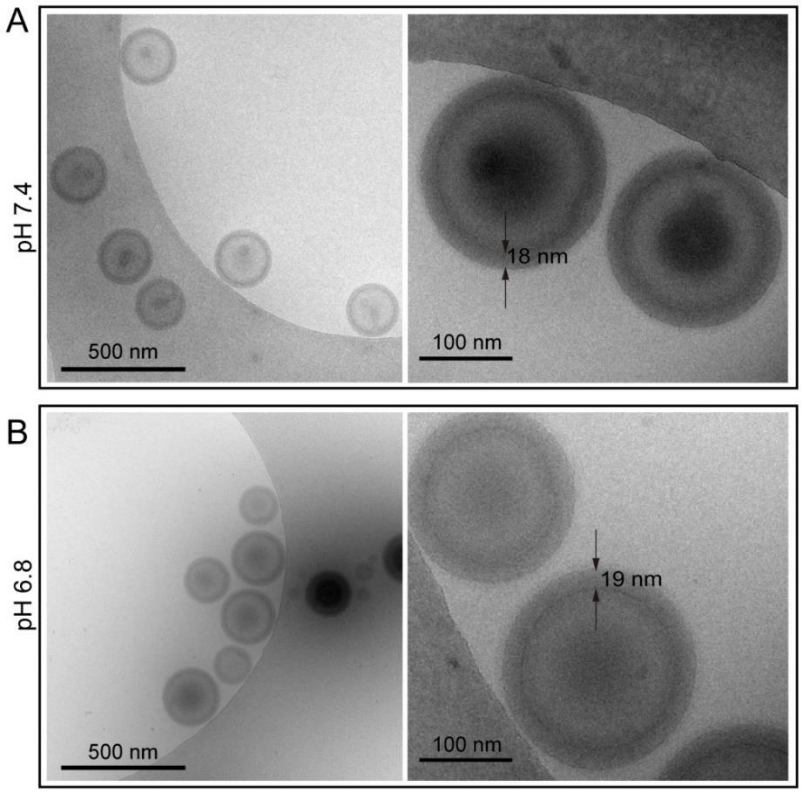

Figure 2. 11. Representative cryo-TEM images of PEG_{114}-*b*-P($BzMA_{126}$-*co*-MPE_{39}) polymersomes. **(A)** at pH 7.4 and **(B)** at pH 6.8 after 48 h incubation in PBS at room

temperature.

The average membrane thickness was determined to be 18 nm at pH 7.4 and 19 nm at pH 6.8. Dynamic light scattering (DLS) measurements in PBS showed well-dispersed particle sizes with a mean hydrodynamic size of 219 nm at pH 7.4 and 227 nm at pH 6.8, respectively (**Figure 2.12A**). In particular, due to the presence of a pH-responsive segment, the *zeta*-potentials of PEG$_{114}$-*b*-P(BzMA$_{126}$-*co*-MPE$_{39}$) polymersomes were found to increase from - 4.83 mV at pH 7.4 to + 0.43 mV at pH 6.8 likely due to the protonation of MPE segments. The slight negatively charged *zeta*-potential of the polymersomes at pH 7.4 should be attributed to the PEG surface [36].

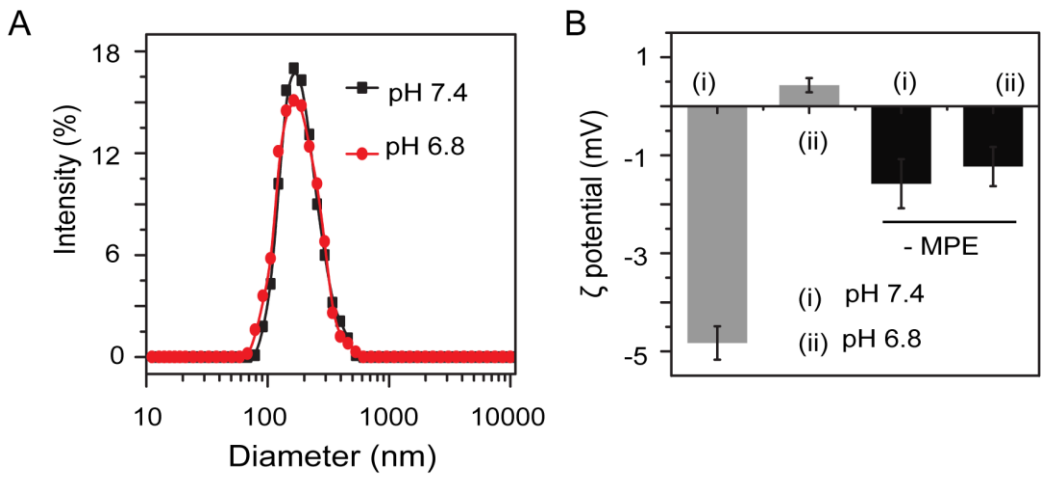

Figure 2. 12. Nanoparticle size and surface charge characterization for PEG$_{114}$-*b*-P(BzMA$_{126}$-*co*-MPE$_{39}$) polymersomes. **(A)** DLS particle size and distribution for PEG$_{114}$-*b*-P(BzMA$_{126}$-*co*-MPE$_{39}$) polymersomes at pH 7.4 and 6.8. **(B)** *Zeta* potentials of PEG$_{114}$-*b*-P(BzMA$_{126}$-*co*-MPE$_{39}$) polymersomes at (i) pH 7.4 and (ii) pH 6.8, and PEG$_{114}$-*b*-PBzMA$_{162}$ polymersome at (iii) pH 7.4 and (iv) pH 6.8. Mean ± SD, n = 3.

This empty pH-responsive PEG_{114}-*b*-P($BzMA_{126}$-*co*-MPE_{39}) polymersomes were denoted as Bz-MPE. On the other hand, the polymersomes self-assembled from PEG_{114}-*b*-$PBzMA_{162}$ without the pH-responsive moiety showed nearly similar negative zeta potentials of -1.58 and -1.23 mV at pH 7.4 and 6.8, respectively (**Figure 2.12B**).

Notably, PEG-*b*-P(BzMA-*co*-MPE) polymersomes with the molar ratios of MPE ranging from 0% to 30% maintained high stability without significantly morphology change after pH was changed from 7.4 to 6.8 and protonation of MPE moieties, which was presumably attributed to the fact that the relatively low ratio of MPE segments randomly distributed in the membranes.

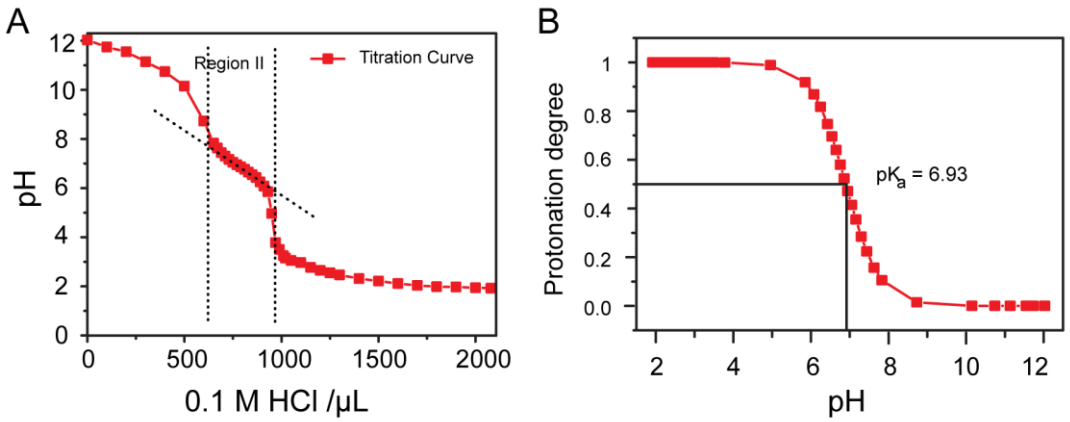

Figure 2. 13. pKa value determination for PEG_{114}-*b*-P($BzMA_{126}$-*co*-MPE_{39}) polymersome. **(A)** Titration curve upon addition of 0.1 M HCl into 0.4 mg/mL PEG_{114}-*b*-P($BzMA_{126}$-*co*-MPE_{39}) polymersome solution at pH 12. **(B)** Protonation degree as a function of pH values after acid-base titration by 0.1 M HCl into 0.4 mg/mL PEG_{114}-*b*-P($BzMA_{126}$-*co*-MPE_{39}) polymersome solution at pH 12.

2.3.2. Tunable selective membrane permeability

With increasing interest to engineer controllable membrane permeability of synthetic assembled capsules such as polymersomes, numerous approaches have been prosperously developed as recently reviewed by Pandit et al. [17]. Among them, the incorporation of stimuli-responsive segments into the block copolymer during polymerization is recently attracting much attention due to simplicity and versatility for smart nanoparticle engineering [21, 24, 37-39]. In this respect, our synthesized amphiphilic block copolymers were rationally designed to contain an ultra pH-sensitive MPE segment that is amenable to control the membrane permeability [25, 40].

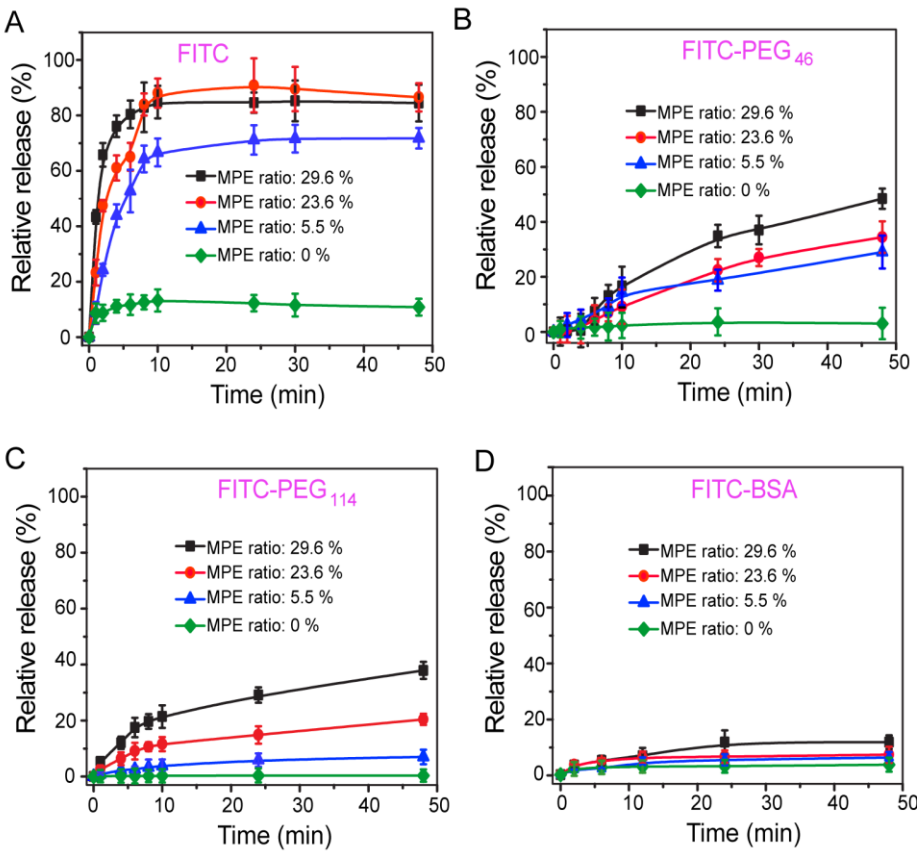

Figure 2. 14. Evaluation of tunable membrane permeability of PEG-*b*-P(BzMA-*co*-

MPE) polymersomes. The effect of various pH-responsive segment ratios (MPE ratio: 0%, 5.5%, 23.6%, or 29.6%) on membrane permeability of PEG-*b*-P(BzMA-*co*-MPE) polymersomes loading various materials with different molecular weights at pH 6.8 and 25 °C. Release profiles of **(A)** FITC, **(B)** FITC-PEG_{46}, **(C)** FITC-PEG_{114}, or **(D)** FITC-BSA from the different polymersomes.

Given that the pK_a value (equal to the pH at the protonation degree α of 0.5) of PEG_{114}-*b*-P($BzMA_{126}$-*co*-MPE_{39}) block copolymer was found to be 6.93 by acid-base titration approach in aqueous solution **(Figure 2.13A,B)**, the MPE segments can become hydrophilic and trigger the membrane permeability of the polymersomes upon decreasing the pH values lower than its pK_a.

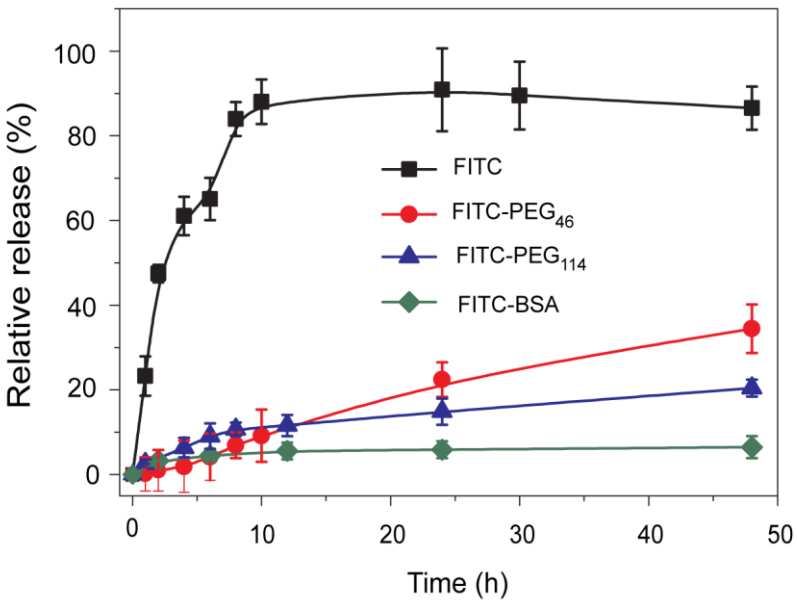

Figure 2. 15. Time-dependent release profiles of FITC and FITC-conjugates of various molecular weights from PEG_{114}-*b*-P($BzMA_{126}$-*co*-MPE_{39}) polymersomes in PBS buffer

(pH 6.8) at 25 °C.

To study the effect of various ratios of MPE segments on the membrane permeability behavior of the polymersomes, a series of PEG_{114}-*b*-P($BzMA_x$-*co*-MPE_y)$_{170}$ block copolymer polymersomes with the comparable hydrophobic segments but various MPE ratios of 0%, 5.5%, 23.6%, and 29.6% were used (**Table 2.1**). Subsequently, the release rates from each polymersome were evaluated by loading various hydrophilic materials with different molecular weights that are FITC (0.38 kDa), FITC-PEG_{46} (2.3 kDa), FITC-PEG_{114} (5.3 kDa), or FITC-BSA (66.3 kDa) through dialysis against PBS at pH 6.8. The release rates of the pH-responsive polymersomes loading FITC, FITC-PEG_{46}, and FITC-PEG_{114} were apparently dependent on MPE ratios (**Figure 2.14A,C**). However, when a high molecular weight molecule, FITC-BSA, was encapsulated, all polymersomes with various MPE ratios showed less than 10% release of FITC-BSA within 48 h incubation **(Figure 2.14D)**. Intriguingly, **Figure 2.14A,D** also demonstrated that the membranes of polymersomes without the pH responsive segments can remain impermeable to all various loaded materials. In particular, PEG_{114}-*b*-P($BzMA_{126}$-*co*-MPE_{39}) polymersomes consisting of 23.6% MPE showed 6.5%, 20.4%, 34.5%, and 86.6% release for FITC-BSA, FITC-PEG_{114}, FITC-PEG_{46}, and FITC, respectively, after 48 h **(Figure 2.15)**.

To further confirm the pH-responsive membrane permeability of our constructed polymersomes from PEG_{114}-*b*-P($BzMA_{126}$-*co*-MPE_{39}) diblock copolymers at both pH 6.8 and 7.4, we used the colorimetric cascade reaction of GOD and glucose in the presence of O_2 to generate H_2O_2 which can further oxidize TMB in the presence of

HRP [22, 41]. Briefly, GOD was encapsulated in the aqueous inner cavities of Bz-MPE polymersomes to obtain GOD@Bz-MPE and the rest of reactants were placed outside at pH 6.8 or 7.4 to monitor pH-responsive membrane permeability behavior. Interestingly, significantly weak absorbance intensity was observed over the course of 1 h at pH 7.4 **(Figure 2.16A,C)**.

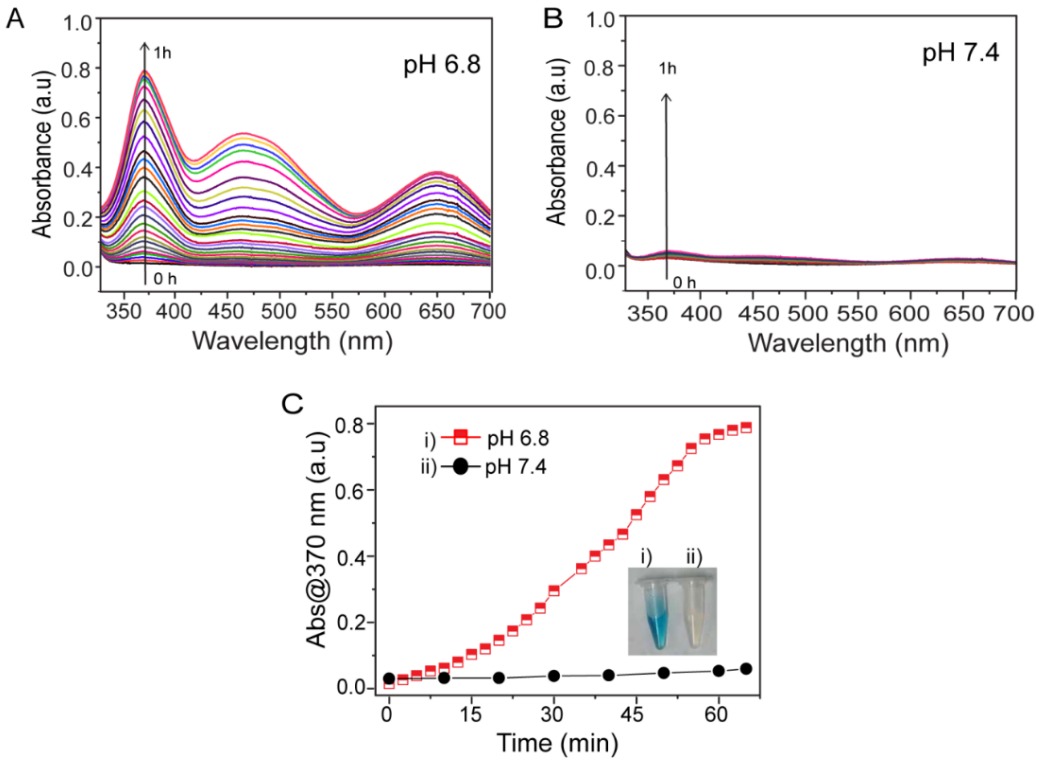

Figure 2. 16. Characterization of pH-responsive membrane permeability. Based on oxidative TMB product through the absorbance at 370 nm after incubation of GOD@Bz-MPE in the presence of 1 mg/mL glucose, 100 μM TMB, and 150 mU/mL HRP outside the polymersomes at **(A)** pH 6.8 or **(B)** 7.4. **(C)** Their time dependence absorbance intensity at 370 nm after incubation at pH 6.8 or pH 7.8. The inset digital images show the solution colors at pH 6.8 (i) or 7.4 (ii) after 1 h incubation.

In a sharp contrast, when the incubation media was adjusted to pH 6.8 in a parallel experiment, the solution color turned into blue with the maximum absorbance peak at a wavelength of 370 nm by UV-vis and the time-dependent absorbance increase was observed revealing pH-triggered membrane permeability and the potential for construction of polymersome nanoreactors with responsive reaction initiation. Collectively, the engineered polymersomes can offer an indispensable feature of tunable membrane permeability towards various materials with different molecular weights readily by altering the ratios of pH-responsive segments. For subsequent studies, we optimized to use PEG_{114}-*b*-P($BzMA_{126}$-*co*-MPE_{39}) polymersomes as they exhibited the membrane permeability with a moderate release rate of small molecules and properties to hinder high molecular weight molecules from crossing the membranes.

2.3.3. Polymersome nanoreactor preparation and characterization

The polymersomes can exhibit distinctive advantages to simultaneously accommodate both hydrophilic and hydrophobic molecules due to the existence of hydrophobic membranes and aqueous inner cavities. To construct therapeutic nanoreactors, we encapsulated GOD in the inner aqueous cavity of PEG_{114}-*b*-P($BzMA_{126}$-*co*-MPE_{39}) polymersome and embedded ProCPT in the hydrophobic membrane *via* π-π stacking and hydrophobic interactions to form GOD and ProCPT-coloaded polymersomes that were denoted as GOD&ProCPT@Bz-MPE. After removal of unencapsulated GOD and ProCPT through Millipore membrane ultrafiltration, DLCs of GOD and ProCPT in GOD&ProCPT@Bz-MPE were determined to be 6.04 wt% and 3.46 wt%, respectively.

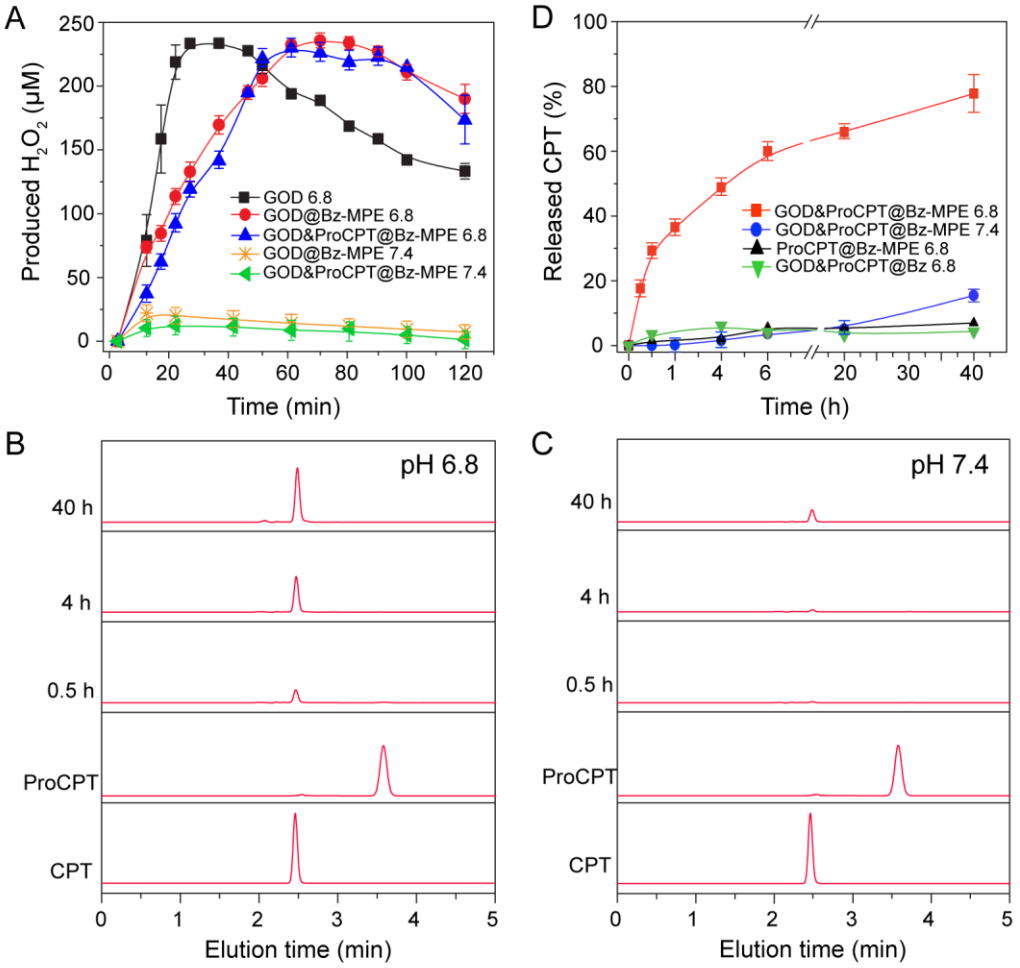

Figure 2. 17. H_2O_2 production and Time-dependent quantitative CPT release profiles.

(A) H_2O_2 production of free GOD, GOD@Bz-MPE, and GOD&ProCPT@Bz-MPE (100 mU/mL GOD) in the presence of 1 mg/mL glucose at pH 7.4 or pH 6.8. Mean ± SD, n =3. HPLC curves of CPT release at **(B)** pH 6.8 and **(C)** pH 7.4. **(D)** Time-dependent quantitative CPT release profiles from GOD&ProCPT@Bz-MPE at 37 °C in the presence of 1 mg/mL glucose at pH 7.4 or pH 6.8, determined by HPLC results. Mean ± SD, n = 3.

For comparison, PEG_{114}-*b*-$PBzMA_{162}$ polymersomes were also used to construct non-responsive nanoreactors *via* encapsulation of GOD and ProCPT with DLCs of 5.26 wt% and 4.15 wt%, respectively, which were denoted as GOD&ProCPT@Bz. It should be noted that GOD&ProCPT@Bz-MPE showed a stable vesicular morphology and size of ~200 nm at both pH 6.8 and 7.4. In fact, as the membrane of GOD&ProCPT@Bz-MPE was comprised of hydrophobic moieties and relatively low ratio of MPE content, the vesicular stability of GOD&ProCPT@Bz-MPE after membrane permeability improvement at pH 6.8 can be maintained. Therefore, once the loaded therapeutic nanoreactor was placed under acidic conditions to activate its membrane permeability, the small molecules such as glucose and oxygen can diffuse into the cavity to react under the catalysis of GOD for *in situ* generation of H_2O_2 that will further activate the embedded H_2O_2-responsive prodrugs to release toxic parental drugs.

To investigate H_2O_2 production, GOD&ProCPT@Bz-MPE nanoreactors were incubated in PBS at pH 6.8 or 7.4 in the presence of 1 mg/mL glucose. The generated H_2O_2 was monitored *via* colorimetric detection in the presence of TMB and HRP on the basis of the fact that H_2O_2 can serve as oxidative donors and react with TMB under the catalysis of HRP. Apparently, GOD&ProCPT@Bz-MPE and GOD@Bz-MPE can produce H_2O_2 quickly with 100 mU/mL GOD at pH 6.8 within 120 min (**Figure 2.17A**). The maximum H_2O_2 generation for GOD&ProCPT@Bz-MPE and GOD@Bz-MPE was reached at ~ 60 min. For comparison, faster H_2O_2 generation by free GOD compared with GOD&ProCPT@Bz-MPE and GOD@Bz-MPE at pH 6.8 can be likely attributed to the fact that free GOD was in close vicinity of all the other reactants in the incubation media. The delayed maximum H_2O_2 generation of GOD&ProCPT@Bz-

MPE and GOD@Bz-MPE at pH 6.8 was due to the fact that the transmembrane diffusion of reactants and products is required for H_2O_2 generation and oxidation of TMB. In sharp contrast, nearly no H_2O_2 production was detected for GOD&ProCPT@Bz-MPE and GOD@Bz-MPE samples at pH 7.4.

To further assess time-dependent CPT release profiles from GOD&ProCPT@Bz-MPE at pH 6.8 and 7.4 in the presence of 1 mg/mL glucose, quantification analysis of parental CPT release was performed by HPLC. The chromatogram peak of each compound can be separately detected at different retention times from HPLC curves. The chromatogram peaks of CPT and ProCPT were detectable at the retention times of 2.46 min and 3.58 min, respectively. Intriguingly, after 30 min incubation of GOD&ProCPT@Bz-MPE at pH 6.8, the peak at 2.46 min increased gradually revealing that the active CPT drugs were produced and released as a function of time **(Figure 2.17**B**)**. However, the peak at 2.46 min was significantly lower than that at pH 7.4 after 40 h incubation **(Figure 2.17**C**)**. Further quantification of CPT release from GOD&ProCPT@Bz-MPE showed that less than 10% CPT was released at pH 7.4 within 40 h, whereas the release ratio reached to more than 80 % at the same time point at pH 6.8 (**Figure 2.17**D). For comparison, ProCPT@Bz-MPE without GOD and GOD&ProCPT@Bz without the pH responsive moiety in the membrane at pH 6.8 showed significantly slow release rates of CPT. Presumably, in addition to the pH-responsive protonation of MPE segments, the prodrug activation by H_2O_2 can further induce membrane disturbance and accelerate release of active drugs. Collectively, the engineered GOD&ProCPT@Bz-MPE nanoreactors were demonstrated to be selectively activated at pH 6.8, and produce massive H_2O_2 that

transformed phenylboronic ester-modified anticancer prodrugs into parental drugs efficiently.

2.3.4. *In vitro* cytotoxicity

Oxidative stress is a common physiological state which can occur particularly when there is excessive generation of reactive oxygen species (ROS) inside cells to interrupt the redox balance and induce the cell apoptosis through mitochondria dysfunction and disturbed cellular signaling pathways [42, 43].

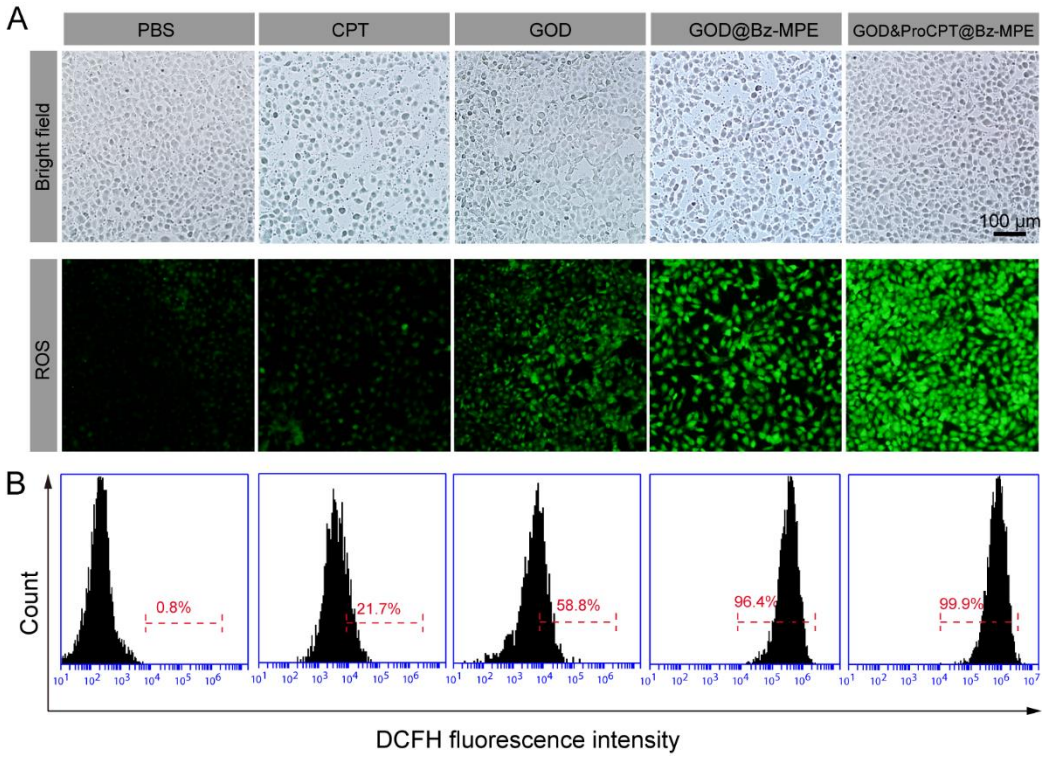

Figure 2. 18. Intracellular ROS quantification.

(A) Intracellular ROS observation in A549 cells using DCFH-DA after incubation with PBS, CPT, GOD, GOD@Bz-MPE, or GOD&ProCPT@Bz-MPE, with the equivalent

concentration of 100 mU/mL GOD and corresponding concentration of 0.83 µM ProCPT or CPT for 12 h in the presence of 1 mg/mL glucose at pH 6.8. **(B)** Intracellular DCFH fluorescent intensity quantification by flow cytometry.

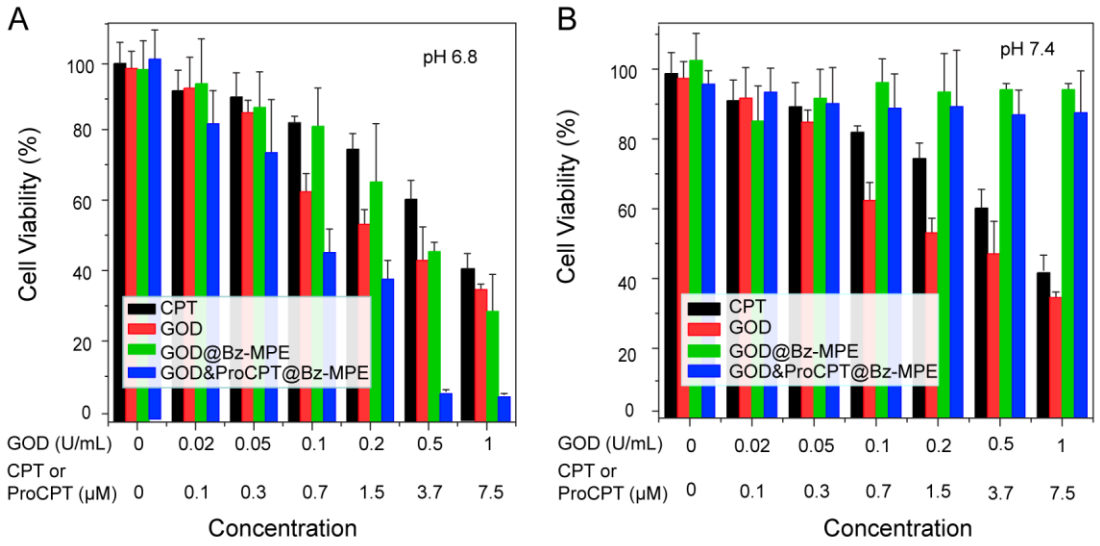

Figure 2. 19. Cytotoxicity evaluation on A549 cells at pH 6.8 and pH 7.4. A549 cells were treated with CPT, GOD, GOD@Bz-MPE or GOD&ProCPT@Bz-MPE for 48 h in the presence of 1 mg/mL glucose at **(A)** pH 6.8 or **(B)** pH 7.4. Mean ± SD, n= 4.

As GOD&ProCPT@Bz-MPE can massively generate H_2O_2 through oxidation of glucose, we thus first assessed the intracellular ROS level by incubating A549 cells with PBS as a negative control, CPT, GOD, GOD@Bz-MPE, or GOD&ProCPT@Bz-MPE at the equivalent GOD concentration of 100 mU/mL or CPT concentration of 0.83 µM for 12 h in the presence of glucose at pH 6.8 using the commercially available ROS probe, DCFH-DA [44]. Obviously, GOD@Bz-MPE and GOD&ProCPT@Bz-MPE-treated groups showed a comparable and stronger green fluorescence intensity, which

suggested higher level of intracellular ROS than the other groups **(Figure 2.18**A**).** Consistently, the flow cytometry results showed that DCFH fluorescence-positive ratios were 0.8%, 21.7%, 58.8%, 96.4%, and 99.9% for PBS, CPT, GOD, GOD@Bz-MPE, and GOD&ProCPT@Bz-MPE groups, respectively **(Figure 2.18**B**)**.

To further evaluate the cytotoxicity, different treatment formulations including PBS, CPT, GOD, GOD@Bz-MPE, GOD&ProCPT@Bz-MPE, and GOD&ProCPT@Bz at various concentrations were incubated with A549 cancer cells in DMEM media containing 10% FBS and 1 mg/mL glucose at pH 6.8 or 7.4 for 48 h. Notably, the results showed that free CPT and GOD displayed half maximal inhibitory concentration (IC_{50}) of 5.8 μM and 406.09 mU/mL, respectively, at both pH 6.8 and 7.4 (**Figure 2.19**A,B**)** which were comparable to the previous reports [20, 22, 45]. GOD@Bz-MPE showed a moderate cell killing efficacy with IC_{50} of 443.89 mU/mL GOD at pH 6.8 which was comparable to the cell cytotoxicity efficacy of free GOD.

Interestingly, the combined treatment by GOD&ProCPT@Bz-MPE exhibited a remarkably enhanced cell killing effect with IC_{50} as low as 92.64 mU/mL GOD and corresponding 0.54 μM ProCPT against A549 cells at pH 6.8 (**Figure 2.19**A). In sharp contrast, GOD@Bz-MPE and GOD&ProCPT@Bz-MPE showed significantly lower cell cytotoxicity when the treatment was performed at pH 7.4 even at a high dose of 1000 mU/mL GOD (**Figure 2.19**B).

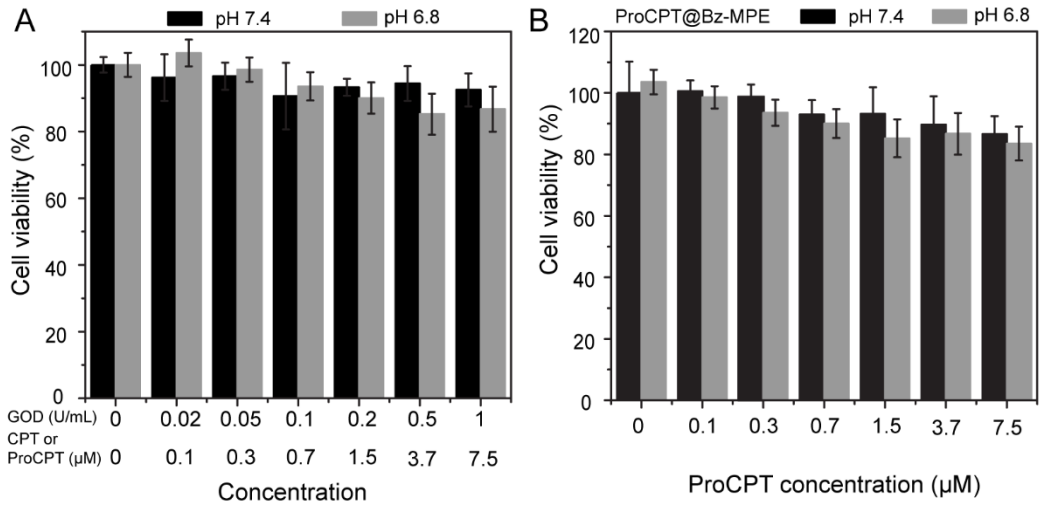

Figure 2. 20. GOD&ProCPT@Bz and ProCPT@Bz-MPE cytotoxicity profile. **(A)** Cell viability profile for A549 cells after treatment with GOD&ProCPT@Bz for 48 h in the presence of 1 mg/mL glucose at pH 6.8 or pH 7.4. Mean ± SD, n= 4. **(B)** Cell viability profile for A549 cells after treatment with ProCPT@Bz-MPE for 48 h in the presence of 1 mg/mL glucose at pH 6.8 or pH 7.4. Mean ± SD, n= 4.

Moreover, GOD&ProCPT@Bz (*i.e.* without pH responsive moiety) and ProCPT@Bz-MPE (*i.e.* without encapsulation of GOD) showed negligible toxicity against A549 cells at both pH 6.8 and 7.4 within the incubation time (**Figure 2.20A,B**). To investigate the synergism behavior of GOD and ProCPT in GOD&ProCPT@Bz-MPE, we comprehensively calculated the GOD and CPT synergy combination index (CI) against by Chou-Talalay's isobolographic method according to the **Equation2.2** [30, 46]. The CI values decreased as a function of fractions affected (f_a), which are in the range of 0.5 and 0.2 indicating a strong synergism degree of GOD and CPT (**Figure 2.21**A).

Next, after treating A549 cells with PBS, CPT, GOD, GOD@Bz-MPE, and GOD&ProCPT@Bz-MPE containing 100 mU/mL GOD and 0.83 μM ProCPT or CPT at pH 6.8 or 7.4, we sequentially performed FDA and PI-staining to differentiate live (green fluorescence) and dead (red fluorescence) cells. As shown in **Figure 2.21B,C**, 49% and ~ 100% of cells after treatment with GOD@Bz-MPE and GOD&ProCPT@Bz-MPE, respectively, at pH 6.8 showed PI-positive images, which suggested that they were either apoptotic or necrotic cells. On the other hand, a relatively lower percentage of cells (< 10%) was determined to be PI positive when the cells were treated with either GOD@Bz-MPE or GOD&ProCPT@Bz-MPE at pH 7.4.

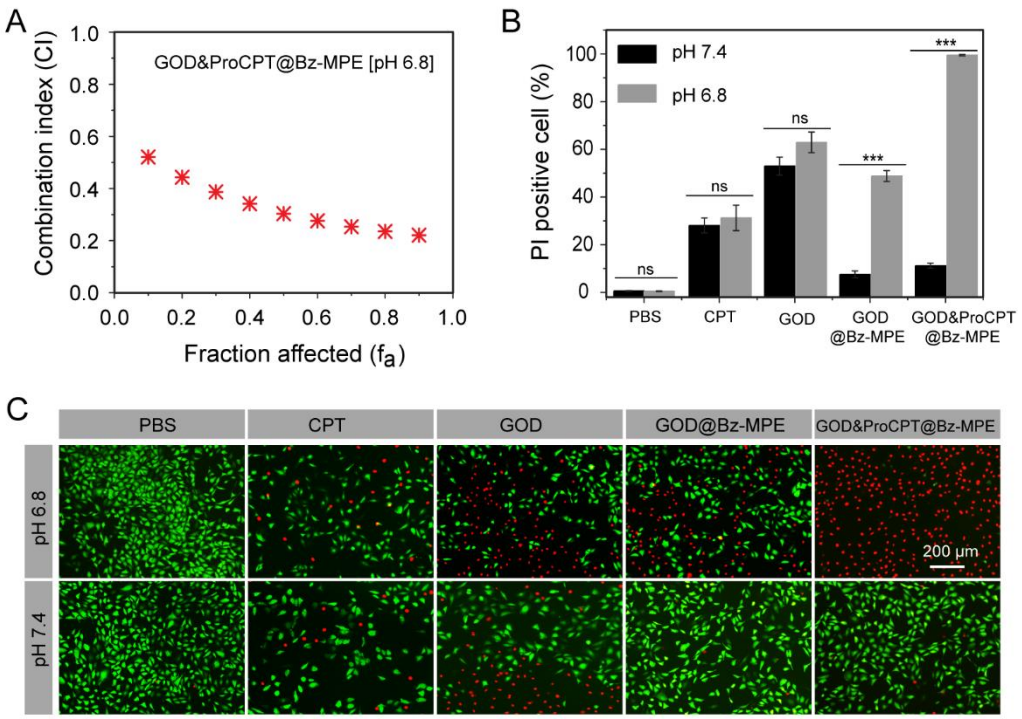

Figure 2. 21. Combination index calculation and live and dead assay. **(A)** Combination index (CI) for GOD&ProCPT@Bz-MPE against A549 at pH 6.8. **(B)** Fluorescence images of live and dead assay for A549 cells stained with PI (red) and FDA (green)

after treatment with PBS, CPT, GOD, GOD@Bz-MPE, or GOD&ProCPT@Bz-MPE for 48 h, at the equivalent concentration of 100 mU/mL GOD and corresponding concentration of 0.26 μg/mL ProCPT or CPT at pH 6.8 or 7.4 in the presence of 1 mg/mL glucose. **(C)** Quantification of dead cells (PI positive cells) at pH 6.8 or 7.4. Mean ± SD, n = 3. ***P< 0.005 (t-test), ns= not significant.

In general, the pronounced detrimental effect of GOD&ProCPT@Bz-MPE against A549 cells at pH 6.8 in the presence of glucose compared to other formulations can be interpreted reasonably. It is well-known that glucose plays a key role as the main source of nutrients to support rapid growth and proliferation of cancer cells [47]. In this regard, the presence of GOD can deplete the cellular glucose supply along with the generation of cytotoxic H_2O_2, which can inhibit cell growth *via* starvation and oxidative stress. Though the application of glucose deprivation to treat cancerous cells *via* starvation has attracted great attention in recent years [48], there is a consensus that the malignant cells can possibly generate alternative metabolic adaptation to sustain growth and survival [49]. To this end, a number of recent reports showed that the therapeutic efficacy of starvation can be improved through combination with other treatment modalities including photodynamic therapy [50, 51], photothermal therapy [52], gas therapy [53, 54], metal ion therapy [55-57], and chemotherapy [20, 58, 59]. In GOD&ProCPT@Bz-MPE, GOD can not only deplete the cell energy supply and induce high level of intracellular H_2O_2, but activate ProCPT prodrugs. The active CPT drugs further eradicate the already weakened cells *via* the blocking of cellular replication and transcription by the inhibition of DNA topoisomerase type 1 in cancer

[60]. Therefore, the synergistic effect of GOD&ProCPT@Bz-MPE can realize significantly higher tumor cell killing potency relative to any single treatment formulation.

2.3.5. *In vivo* pharmacokinetics and biodistribution

To evaluate the *in vivo* performance of GOD&ProCPT@Bz-MPE nanoreactor, we further conducted the *in vivo* study. Note that tumor microenvironment tends to be more acidic than normal tissues mainly due to the high lactate secretion from anaerobic glycolysis *via* a well-validated "Warburg effect" [61]. Considering the acidity gradient in tumor tissues, GOD&ProCPT@Bz-MPE was expected to remain inactive during circulation and in normal tissues at pH 7.4 until it reached the acidic tumor microenvironment (pH 6.5-6.8) where the membrane can become selectively permeable to small molecules. Moreover, given the fact that the shell of GOD&ProCPT@Bz-MPE is covered with hydrophilic PEG shells and significantly low CAC value of the block copolymers, it can be assumed to increase the biosafety and prolong circulation time in blood stream for enhanced tumor accumulation *via* enhanced permeability and retention (EPR) effect [62].

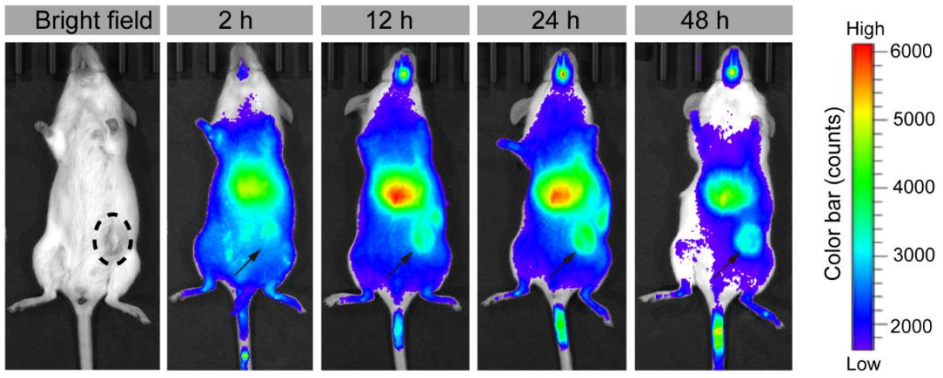

Figure 2. 22. Whole body *in vivo* imaging of tumor-bearing mice at various time points post intravenous injection of DiR@Bz-MPE. The tumor position is highlighted in a dashed line cycle and arrows.

H22 tumor models (~100 mm^3) were established based on ICR mice considering the facile establishment of this tumor model with uniform tumor sizes. By using Bz-MPE polymersomes loading 1,1′-dioctadecyl-3,3,3′,3′-tetramethylindotricarbocyanine iodide (DiR) dye (DiR@Bz-MPE), we assessed the biodistribution in the H22-tumor bearing mice through the *in vivo* imaging system at varying time points of 2 h, 12 h, 24 h, and 48 h post intravenous injection. As shown in **Figure 2.22**, the fluorescence intensity at the tumor site was time-dependent and the maximum was reached at ~ 24 h post intravenous injection. Moreover, an appreciable amount of the injected dose can be localized at the tumor site even after 48 h, which suggested an enhanced accumulation and elongated retention of DiR@Bz-MPE polymersomes in tumor tissues.

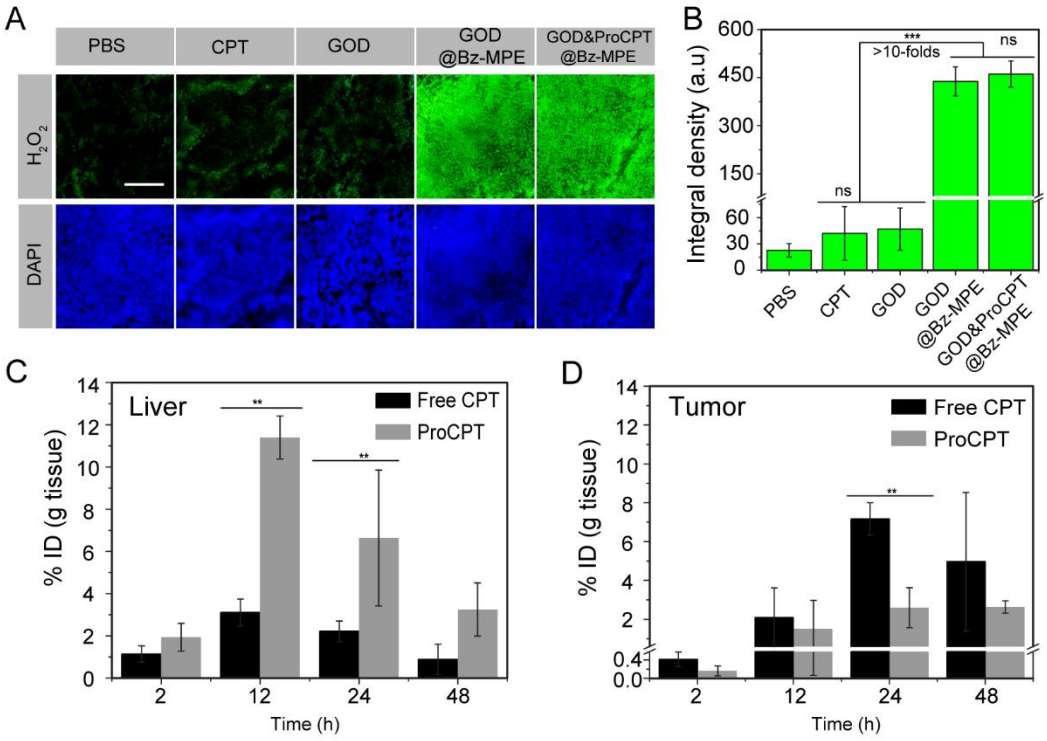

Figure 2. 23. Intratumor H_2O_2 quantification and Time-dependent free CPT and ProCPT concentrations in liver and tumor. **(A)** and **(B)** *Ex vivo* fluorescence images for intratumor H_2O_2 and the corresponding integrated density in H22 tumor tissues at 24 h post intravenous administration of PBS, CPT, GOD, GOD@Bz-MPE, and GOD&ProCPT@Bz-MPE, followed by intratumor injection of BES-H_2O_2 probe, Mean ± SD, n = 3. ***P< 0.005 (t-test), ns = not significant. Scale bar = 200 μm. **(C)** and **(D)** Time-dependent free CPT and ProCPT concentrations in liver and tumor post intravenous injection of GOD&ProCPT@Bz-MPE at the equivalent dose of 10 U GOD and corresponding ProCPT of 26 μg. Mean ± SD, n = 3. **P < 0.01 (t-test).

Next, we investigated the intratumor H_2O_2 production by a H_2O_2-specific probe, BES-H_2O_2, at 24 h post intravenous administration of PBS, CPT, GOD, GOD, GOD@Bz-MPE, and GOD&ProCPT@Bz-MPE, respectively. GOD@Bz-MPE and

GOD&ProCPT@Bz-MPE groups showed significantly stronger fluorescence and higher H_2O_2 levels while the weakly and randomly distributed BES green fluorescence was detectable for free CPT and GOD-treated groups that were similar to the control group (**Figure 2.23**A,B). Therefore, the presence of high intratumor H_2O_2 levels for the mice treated by GOD&ProCPT@Bz-MPE can guarantee the maximum conversion efficiency of loaded ProCPT prodrugs into toxic CPT drugs.

Nevertheless, as it was found that high amounts of the nanoreactors were distributed in the liver, particularly before 24 h post intravenous injection (**Figure 2.22**), we next endeavored to monitor the relative concentrations of CPT and ProCPT in liver and tumor. Interestingly, the results showed that for all time points tested, ProCPT concentrations were remarkably much higher than free CPT in the liver. Specifically, at 12 h post intravenous injection which marked the highest peak of accumulation in livers among the examined time points, the extracted ProCPT concentration in livers was 12.2 %ID/g which was almost 4 folds higher than the free CPT concentration (**Figure 2.23**C). In contrast, at 24 h post intravenous injection in tumors, free CPT concentration was still gradually increasing and higher than the ProCPT concentration. Particularly at 24 h post intravenous injection, free CPT concentration was quantified to be 7.2 %ID/g which was nearly 3 folds higher than ProCPT concentration (**Figure 2.23**D). Reasonably, it can be concluded that our designed nanosystem was relatively inactive in liver but indeed active at the tumor sites due to tumor acidic microenvironment (pH 6.5-6.8)-activated reaction to produce H_2O_2 and transform ProCPT into CPT.

2.3.6. Antitumor efficacy

To evaluate antitumor efficacy, H22 tumor-bearing mice (~ 100 mm^3) were divided into five treatment groups including PBS, CPT, GOD, GOD@Bz-MPE, and GOD&ProCPT@Bz-MPE. After intravenous administration of different formulation, as shown in **Figure 2.24**A, the tumor volumes of PBS and GOD groups rapidly increased. Meanwhile, the mice treated with CPT and GOD@Bz-MPE formulations showed comparable and moderate tumor growth suppression. Remarkably, GOD&ProCPT@Bz-MPE group showed an enhanced tumor ablation efficacy with significantly smaller average tumor weights which were around 9.5 and 4-fold lower compared with CPT and GOD@Bz-MPE groups at day 22 after treatment, respectively (**Figure 2.24**B, C).

Notably, there was no obvious body weight loss remarked during treatment by using the engineered nanoreactor groups while the CPT group showed some body weight loss especially during administration stage of treatment (**Figure 2.24**D). Furthermore, H&E staining images of major organs including spleen, heart, liver, lung, and kidney showed no noticeable tissue damage for GOD&ProCPT@Bz-MPE group while free CPT exhibited obvious damage to liver and kidney **(Figure 2.26)**.

At the end of treatment, H&E staining of tumor tissues, GOD&ProCPT@Bz-MPE group showed tremendously damaged tumor tissues compared to other treatment groups (**Figure 2.25**). Therefore, the antitumor efficacy demonstrated that GOD&ProCPT@Bz-MPE can achieve drastically enhanced therapeutic efficacy against aggressive tumors with relatively no observable side toxicity.

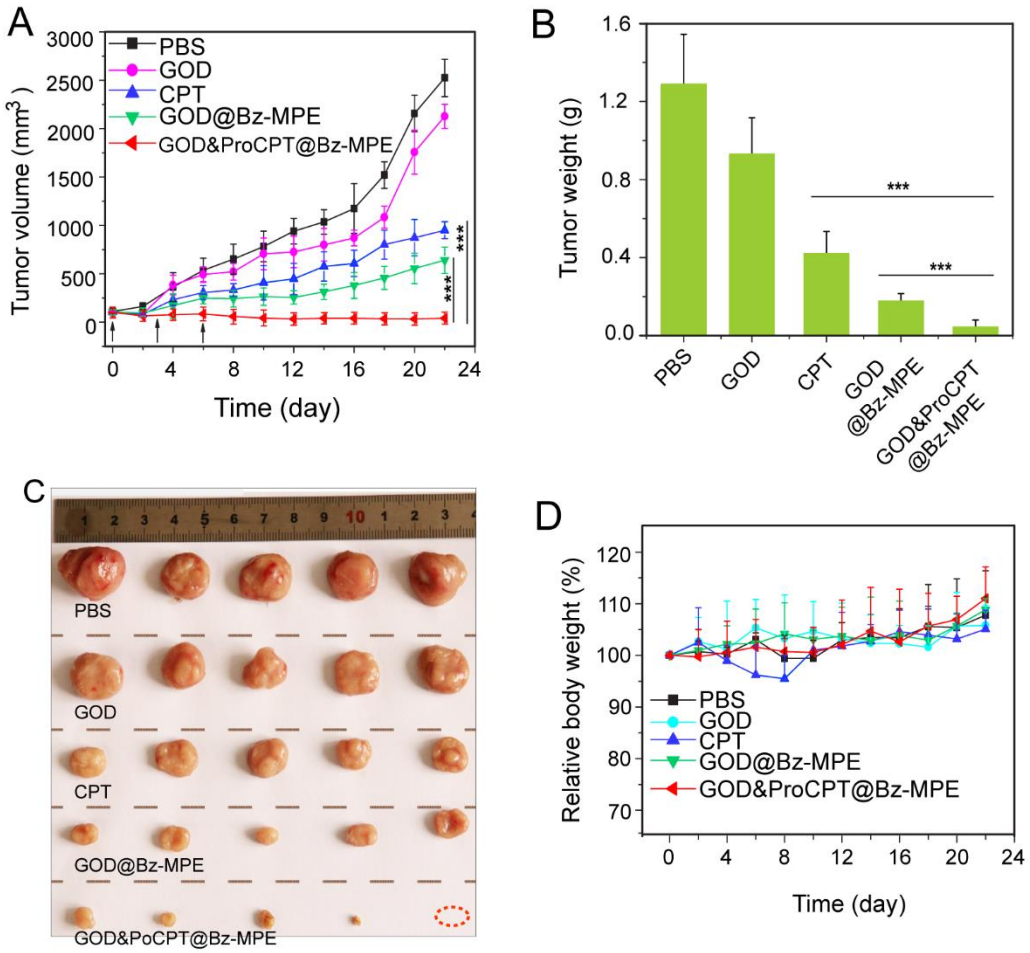

Figure 2. 24. Tumor growth profile and mice body weight change monitoring. **(A)** H22 tumor growth profiles of the mice treated with PBS, GOD, CPT, GOD@Bz-MPE, and GOD&ProCPT@Bz-MPE. The arrows indicate the injection time. (B) Average tumor weight at the end of treatment. **(C)** Tumor images at the end of treatment. Red circle indicates the completely eliminated tumor. **(D)** Body weight change of the mice treated with PBS, GOD, CPT, GOD@Bz-MPE, and GOD&ProCPT@Bz-MPE. Mean ± SD, n = 5. ***P< 0.005 (t-test).

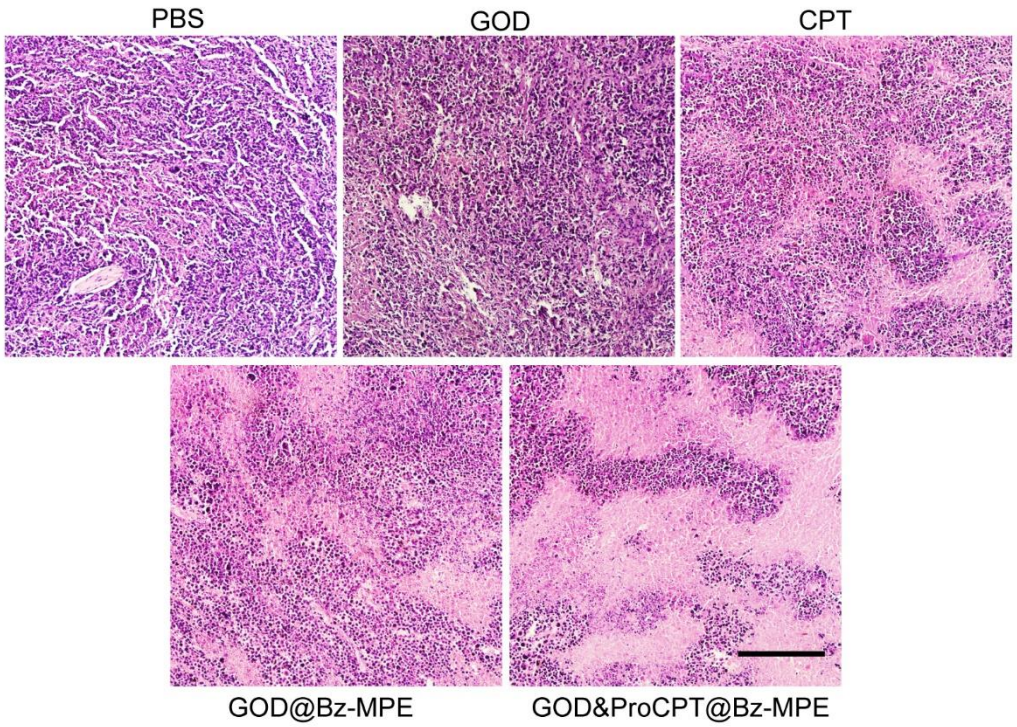

Figure 2. 25. H&E staining images of tumor tissues through histological analysis at the end of treatment. Scale bar = 200 μm.

2.4. Discussion

The application of conventional chemotherapeutic drugs for cancer treatment is often associated with awful short and long-term toxicities and side effects which severely limit its potential to achieve satisfactory therapeutic effect [63]. Consequently, there have been tremendous researches in the field focusing to address this issue by developing various new strategies to alleviate undesirable toxicities of chemotherapeutic drugs while enhancing the treatment effect especially by introducing nanotechnology into cancer therapy [64]. Among them, the application of prodrugs and activating enzymes for instance in the so-called enzyme prodrug therapy (EPT) has

considerably gained much attention due to its promising approach to control the drug activity such that it can mostly become active at the desired pathological site [65-67].

Nevertheless, the majority of EPT approaches so far reported are accomplished *via* a two-step method involving prior delivery of activating enzymes to the tumor region and consecutive systemic administration of prodrugs for activation in the presence of the enzymes, which alter and compromise their treatment efficiency mostly due to different bioavailability of both activating enzymes and prodrugs at the desired site of action, highly possible activation of prodrugs off-target, and short systemic circulation half-life of the small molecule prodrugs due to fast renal clearance [11, 12]. Recently, the development of therapeutic nanoreactors inspired by the sophisticated biosynthetic pathways from nature is acquiring growing attentiveness as a single nanoparticle with various integrated functionalities can be smartly engineered for a desired application in precise nanomedicine [2, 4]. Although there has been great effort directed toward the development of ideal therapeutic nanoreactors, it is still challenging to facilely generate a therapeutic nanoreactor with balanced key features of tunable selective membrane permeability and structural stability for prodrug delivery and activation in diseased tissues.

Herein we report a novel strategy to engineer a therapeutic nanoreactor that can coload both activating enzyme and prodrug with tunable and controllable membrane permeability based on PEG-*b*-P(BzMA-*co*-MPE) diblock copolymers self-assembled into well-defined polymersomes of ~200 nm diameter **(Figure 2.11 and Figure 2.12)**. The demonstrated engineering strategy shows feasibility to control the membrane permeability of the reaction vessels thereby readily adjusting the feeding ratios of the

environmental stimuli-responsive monomer and other used monomer during polymerization process **(Figure 2.14**A-D**)**.

According to polymersomes interesting features which allow for accommodating both hydrophilic and hydrophobic cargoes, we have successfully coloaded activating enzyme (GOD) in the reaction vessel interior part and a phenylboronic ester-caged CPT prodrug (ProCPT) in the membrane to get GOD&ProCPT@Bz-MPE therapeutic nanoreactors. The well-designed GOD&ProCPT@Bz-MPE therapeutic nanoreactors with an optimized 23.6% of ultra-pH responsive moiety (MPE) in their membrane proved to possess an indirect cascade reaction which can be induced by mild acidic environment (pH 6.5-6.8) for massively generation of cytotoxic H_2O_2 that can also serve as triggering agent to activate ProCPT prodrug and release cytotoxic chemotherapeutic CPT drug (**Figure 2.17**A, D).

In vitro study shows that our system has enhanced A549 cancer cells killing effect compared to any single treatment of GOD or CPT alone (**Figure 2.18** and **Figure 2.19**A, B). In particular, the determined CI values in the range of 0.5 and 0.2 indicated a strong synergism degree of GOD and CPT, which suggested that the enhanced cells killing efficacy of our designed GOD&ProCPT@Bz-MPE therapeutic nanoreactor was likely beneficial for the synergistic oxidation therapy and chemotherapy (**Figure 2.21**A). The *in vivo* applicability results of the engineered GOD&ProCPT@Bz-MPE therapeutic nanoreactor on H22 tumor-bearing mice show appreciable accumulation at the tumor site *via* EPR effect for a prolonged time of ~48 h (**Figure 2.22**). Additionally, the concentrations of cytotoxic massive H_2O_2 and active CPT drug were determined to be

much higher produced at tumor site as compared with other organs such as liver (**Figure 2.23**A-D). The *in vivo* antitumor results show that GOD&ProCPT@Bz-MPE therapeutic nanoreactor nearly ablated tumors and completely stopped tumor growth with low side effects (**Figure 2.24**A-D and **Figure 2.25**). In overall, the obtained results show that the well-devised GOD&ProCPT@Bz-MPE therapeutic nanoreactor achieved enhanced therapeutic effect against tumors with relatively low side effect.

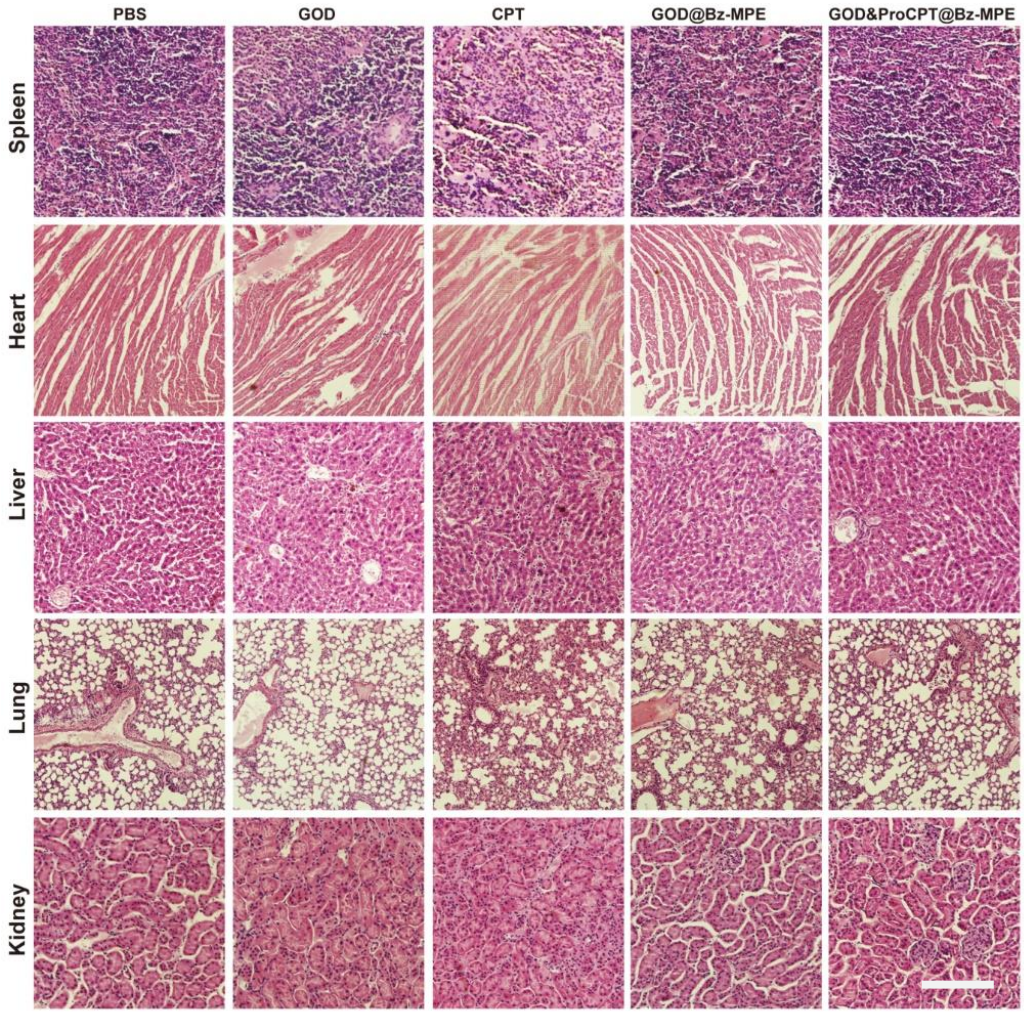

Figure 2. 26. H&E staining images of major organs (spleen, heart, liver, lung, and kidney) after treatment by different formulations. Scale bar = 100 μm.

2.5. Conclusions

In summary, we presented a nanoreactor, GOD&ProCPT@Bz-MPE, integrating enzymes and prodrugs into one delivery system with tunable membrane permeability for prodrug delivery and tumor-specific activation. The ultra pH-sensitive MPE segments in the membranes of the polymersome endow the tumor microenvironment-specific activation of GOD&ProCPT@Bz-MPE to initiate massive production of H_2O_2 and H_2O_2-triggered transformation of prodrugs into active drugs, which considerably enhanced tumor eradication efficiency by the combination of oxidation-chemotherapy. Moreover, the used prodrugs that were caged by phenylboronic ester can be facilely extended to all the anticancer drugs containing amine or hydroxyl groups. Therefore, the strategy presented in this work is expected to inspire the future development of therapeutic nanoreactors for prodrug delivery and activation thereby enhancing therapeutic efficacy and mitigating the adverse toxic effects.

2.6. References

[1] B.C. Buddingh', J.C.M. van Hest, Artificial Cells: Synthetic Compartments with Life-like Functionality and Adaptivity, Accounts of Chemical Research, 50 (2017) 769-777.

[2] T. Nishimura, K. Akiyoshi, Biotransporting Biocatalytic Reactors toward Therapeutic Nanofactories, Advanced Science, 5 (2018) 1800801.

[3] V. Balasubramanian, A. Correia, H. Zhang, F. Fontana, E. Mäkilä, J. Salonen, J. Hirvonen, H.A. Santos, Biomimetic Engineering Using Cancer Cell Membranes for Designing Compartmentalized Nanoreactors with Organelle-Like Functions, Advanced Materials, 29 (2017) 1605375.

[4] J.F. Mukerabigwi, Z. Ge, K. Kataoka, Therapeutic Nanoreactors as In Vivo Nanoplatforms for Cancer Therapy, Chemistry – A European Journal, 24 (2018) 15706-15724.

[5] P.R. LeDuc, M.S. Wong, P.M. Ferreira, R.E. Groff, K. Haslinger, M.P. Koonce, W.Y. Lee, J.C. Love, J.A. McCammon, N.A. Monteiro-Riviere, V.M. Rotello, G.W. Rubloff, R. Westervelt, M. Yoda, Towards an in vivo biologically inspired nanofactory, Nature Nanotechnology, 2 (2007) 3-7.

[6] A. Ranquin, W. Versées, W. Meier, J. Steyaert, P. Van Gelder, Therapeutic Nanoreactors: Combining Chemistry and Biology in a Novel Triblock Copolymer Drug Delivery System, Nano Letters, 5 (2005) 2220-2224.

[7] T. Nishimura, Y. Sasaki, K. Akiyoshi, Biotransporting Self-Assembled Nanofactories Using Polymer Vesicles with Molecular Permeability for Enzyme Prodrug Cancer Therapy, Advanced Materials, 29 (2017) 1702406.

[8] Y. Anraku, A. Kishimura, M. Kamiya, S. Tanaka, T. Nomoto, K. Toh, Y. Matsumoto, S. Fukushima, D. Sueyoshi, M.R. Kano, Y. Urano, N. Nishiyama, K. Kataoka, Systemically Injectable Enzyme-Loaded Polyion Complex Vesicles as In Vivo Nanoreactors Functioning in Tumors, Angewandte Chemie International Edition, 55 (2016) 560-565.

[9] W. Ke, J. Li, F. Mohammed, Y. Wang, K. Tou, X. Liu, P. Wen, H. Kinoh, Y. Anraku, H. Chen, K. Kataoka, Z. Ge, Therapeutic Polymersome Nanoreactors with Tumor-Specific Activable Cascade Reactions for Cooperative Cancer Therapy, ACS Nano, 13 (2019) 2357-2369.

[10] O. Onaca-Fischer, J. Liu, M. Inglin, C. G. Palivan, Polymeric Nanocarriers and Nanoreactors: A Survey of Possible Therapeutic Applications, Current Pharmaceutical Design, 18 (2012) 2622-2643.

[11] A. Scomparin, H.F. Florindo, G. Tiram, E.L. Ferguson, R. Satchi-Fainaro, Two-step Polymer- and Liposome-Enzyme Prodrug Therapies for Cancer: PDEPT and PELT Concepts and Future Perspectives, Advanced Drug Delivery Reviews, 118 (2017) 52-64.

[12] G. Xu, H.L. McLeod, Strategies for Enzyme/Prodrug Cancer Therapy, Clinical Cancer Research, 7 (2001) 3314-3324.

[13] Y. Zhu, B. Yang, S. Chen, J. Du, Polymer vesicles: Mechanism, preparation, application, and responsive behavior, Progress in Polymer Science, 64 (2017) 1-22.

[14] J.S. Lee, J. Feijen, Polymersomes for Drug Delivery: Design, Formation and Characterization, Journal of Controlled Release, 161 (2012) 473-483.

[15] Y. Mai, A. Eisenberg, Self-assembly of Block Copolymers, Chemical Society Reviews, 41 (2012) 5969-5985.

[16] R. Bleul, R. Thiermann, M. Maskos, Techniques To Control Polymersome Size, Macromolecules, 48 (2015) 7396-7409.

[17] A. Larrañaga, M. Lomora, J.R. Sarasua, C.G. Palivan, A. Pandit, Polymer Capsules as Micro-/nanoreactors for Therapeutic Applications: Current Strategies to Control Membrane Permeability, Progress in Materials Science, 90 (2017) 325-357.

[18] T. Einfalt, R. Goers, I.A. Dinu, A. Najer, M. Spulber, O. Onaca-Fischer, C.G. Palivan, Stimuli-Triggered Activity of Nanoreactors by Biomimetic Engineering Polymer Membranes, Nano Letters, 15 (2015) 7596-7603.

[19] T. Einfalt, D. Witzigmann, C. Edlinger, S. Sieber, R. Goers, A. Najer, M. Spulber, O. Onaca-Fischer, J. Huwyler, C.G. Palivan, Biomimetic Artificial Organelles with In itro and In vivo Activity Triggered by Reduction in Microenvironment, Nature Communications, 9 (2018) 1127.

[20] J. Li, Y. Li, Y. Wang, W. Ke, W. Chen, W. Wang, Z. Ge, Polymer Prodrug-Based Nanoreactors Activated by Tumor Acidity for Orchestrated Oxidation/Chemotherapy, Nano Letters, 17 (2017) 6983-6990.

[21] J. Gaitzsch, D. Appelhans, L. Wang, G. Battaglia, B. Voit, Synthetic Bio-nanoreactor: Mechanical and Chemical Control of Polymersome Membrane Permeability, Angewandte Chemie International Edition, 51 (2012) 4448-4451.

[22] J. Li, A. Dirisala, Z. Ge, Y. Wang, W. Yin, W. Ke, K. Toh, J. Xie, Y. Matsumoto, Y. Anraku, K. Osada, K. Kataoka, Therapeutic Vesicular Nanoreactors with Tumor-Specific Activation and Self-Destruction for Synergistic Tumor Ablation, Angewandte Chemie International Edition, 56 (2017) 14025-14030.

[23] Q. Yan, J. Wang, Y. Yin, J. Yuan, Breathing Polymersomes: CO2-Tuning Membrane Permeability for Size-Selective Release, Separation, and Reaction, Angewandte Chemie International Edition, 52 (2013) 5070-5073.

[24] K.T. Kim, J.J.L.M. Cornelissen, R.J.M. Nolte, J.C.M. van Hest, A Polymersome Nanoreactor with Controllable Permeability Induced by Stimuli-Responsive Block Copolymers, Advanced Materials, 21 (2009) 2787-2791.

[25] K. Zhou, H. Liu, S. Zhang, X. Huang, Y. Wang, G. Huang, B.D. Sumer, J. Gao, Multicolored pH-tunable and activatable fluorescence nanoplatform responsive to physiologic pH stimuli, J. Am. Chem. Soc., 134 (2012) 7803-7811.

[26] L. Shi, T.M. Chapman, E.J. Beckman, Poly(ethylene glycol)-block-poly(N-vinylformamide) Copolymers Synthesized by the RAFT Methodology, Macromolecules, 36 (2003) 2563-2567.

[27] Y. Liu, J. Du, M. Yan, M.Y. Lau, J. Hu, H. Han, O.O. Yang, S. Liang, W. Wei, H. Wang, J. Li, X. Zhu, L. Shi, W. Chen, C. Ji, Y. Lu, Biomimetic enzyme nanocomplexes and their use as antidotes and preventive measures for alcohol intoxication, Nature nanotechnology, 8 (2013) 187-192.

[28] M.-H. Lai, S. Lee, C.E. Smith, K. Kim, H. Kong, Tailoring Polymersome Bilayer Permeability Improves Enhanced Permeability and Retention Effect for Bioimaging, ACS Applied Materials & Interfaces, 6 (2014) 10821-10829.

[29] W. Ke, W. Yin, Z. Zha, J.F. Mukerabigwi, W. Chen, Y. Wang, C. He, Z. Ge, A robust strategy for preparation of sequential stimuli-responsive block copolymer

prodrugs via thiolactone chemistry to overcome multiple anticancer drug delivery barriers, Biomaterials, 154 (2018) 261-274.

[30] T.-C. Chou, Theoretical Basis, Experimental Design, and Computerized Simulation of Synergism and Antagonism in Drug Combination Studies, Pharmacological Reviews, 58 (2006) 621-681.

[31] B. Xiao, M. Zhang, E. Viennois, Y. Zhang, N. Wei, M.T. Baker, Y. Jung, D. Merlin, Inhibition of MDR1 Gene Expression and Enhancing Cellular Uptake for Effective Colon Cancer Treatment Using Dual-Surface-Functionalized Nanoparticles, Biomaterials, 48 (2015) 147-160.

[32] C. de Gracia Lux, S. Joshi-Barr, T. Nguyen, E. Mahmoud, E. Schopf, N. Fomina, A. Almutairi, Biocompatible Polymeric Nanoparticles Degrade and Release Cargo in Response to Biologically Relevant Levels of Hydrogen Peroxide, Journal of the American Chemical Society, 134 (2012) 15758-15764.

[33] A.P. Esser-Kahn, N.R. Sottos, S.R. White, J.S. Moore, Programmable Microcapsules from Self-Immolative Polymers, Journal of the American Chemical Society, 132 (2010) 10266-10268.

[34] W. Yin, J. Li, W. Ke, Z. Zha, Z. Ge, Integrated Nanoparticles To Synergistically Elevate Tumor Oxidative Stress and Suppress Antioxidative Capability for Amplified Oxidation Therapy, ACS Applied Materials & Interfaces, 9 (2017) 29538-29546.

[35] K.E. Broaders, S. Grandhe, J.M.J. Fréchet, A Biocompatible Oxidation-Triggered Carrier Polymer with Potential in Therapeutics, Journal of the American Chemical Society, 133 (2011) 756-758.

[36] A. Vila, H. Gill, O. McCallion, M.a.J. Alonso, Transport of PLA-PEG particles across the nasal mucosa: effect of particle size and PEG coating density, Journal of Controlled Release, 98 (2004) 231-244.

[37] X. Wang, J. Hu, G. Liu, J. Tian, H. Wang, M. Gong, S. Liu, Reversibly Switching Bilayer Permeability and Release Modules of Photochromic Polymersomes Stabilized by Cooperative Noncovalent Interactions, Journal of the American Chemical Society, 137 (2015) 15262-15275.

[38] P. Mi, H. Yanagie, N. Dewi, H.-C. Yen, X. Liu, M. Suzuki, Y. Sakurai, K. Ono, H. Takahashi, H. Cabral, K. Kataoka, N. Nishiyama, Block Copolymer-boron Cluster Conjugate for Effective Boron Neutron Capture Therapy of Solid Tumors, Journal of Controlled Release, 254 (2017) 1-9.

[39] S. Quader, X. Liu, Y. Chen, P. Mi, T. Chida, T. Ishii, Y. Miura, N. Nishiyama, H. Cabral, K. Kataoka, cRGD Peptide-installed Epirubicin-loaded Polymeric Micelles for Effective Targeted Therapy Against Brain Tumors, Journal of Controlled Release, 258 (2017) 56-66.

[40] M. Huang, K. Zhao, L. Wang, S. Lin, J. Li, J. Chen, C. Zhao, Z. Ge, Dual Stimuli-Responsive Polymer Prodrugs Quantitatively Loaded by Nanoparticles for Enhanced Cellular Internalization and Triggered Drug Release, ACS Applied Materials & Interfaces, 8 (2016) 11226-11236.

[41] A.F. Mason, B.C. Buddingh', D.S. Williams, J.C.M. van Hest, Hierarchical Self-Assembly of a Copolymer-Stabilized Coacervate Protocell, Journal of the American Chemical Society, 139 (2017) 17309-17312.

[42] A.V. Bazhin, P.P. Philippov, S. Karakhanova, Reactive Oxygen Species in Cancer Biology and Anticancer Therapy, Oxidative Medicine and Cellular Longevity, 2016 (2016) 4197815.

[43] U.E. Martinez-Outschoorn, M. Peiris-Pagés, R.G. Pestell, F. Sotgia, M.P. Lisanti, Cancer Metabolism: A Therapeutic Perspective, Nature Reviews Clinical Oncology, 14 (2016) 11.

[44] A. Grzelak, B. Rychlik, G. Bartosz, Light-dependent Generation of Reactive Oxygen Species in Cell Culture Media, Free Radical Biology and Medicine, 30 (2001) 1418-1425.

[45] Y. Cai, H. Shen, J. Zhan, M. Lin, L. Dai, C. Ren, Y. Shi, J. Liu, J. Gao, Z. Yang, Supramolecular "Trojan Horse" for Nuclear Delivery of Dual Anticancer Drugs, Journal of the American Chemical Society, 139 (2017) 2876-2879.

[46] T.-C. Chou, Drug Combination Studies and Their Synergy Quantification Using the Chou-Talalay Method, Cancer Research, 70 (2010) 440.

[47] A. Fadaka, B. Ajiboye, O. Ojo, O. Adewale, I. Olayide, R. Emuowhochere, Biology of Glucose Metabolization in Cancer Cells, Journal of Oncological Sciences, 3 (2017) 45-51.

[48] L.-H. Fu, C. Qi, J. Lin, P. Huang, Catalytic Chemistry of Glucose Oxidase in Cancer Diagnosis and Treatment, Chemical Society Reviews, (2018).

[49] L.K. Boroughs, R.J. DeBerardinis, Metabolic Pathways Promoting Cancer Cell Survival and Growth, Nature Cell Biology, 17 (2015) 351.

[50] K. Chang, Z. Liu, X. Fang, H. Chen, X. Men, Y. Yuan, K. Sun, X. Zhang, Z. Yuan, C. Wu, Enhanced Phototherapy by Nanoparticle-Enzyme via Generation and Photolysis of Hydrogen Peroxide, Nano Letters, 17 (2017) 4323-4329.

[51] S.-Y. Li, H. Cheng, B.-R. Xie, W.-X. Qiu, J.-Y. Zeng, C.-X. Li, S.-S. Wan, L. Zhang, W.-L. Liu, X.-Z. Zhang, Cancer Cell Membrane Camouflaged Cascade Bioreactor for Cancer Targeted Starvation and Photodynamic Therapy, ACS Nano, 11 (2017) 7006-7018.

[52] J. Zhou, M. Li, Y. Hou, Z. Luo, Q. Chen, H. Cao, R. Huo, C. Xue, L. Sutrisno, L. Hao, Y. Cao, H. Ran, L. Lu, K. Li, K. Cai, Engineering of a Nanosized Biocatalyst for Combined Tumor Starvation and Low-Temperature Photothermal Therapy, ACS Nano, 12 (2018) 2858-2872.

[53] W. Fan, N. Lu, P. Huang, Y. Liu, Z. Yang, S. Wang, G. Yu, Y. Liu, J. Hu, Q. He, J. Qu, T. Wang, X. Chen, Glucose-Responsive Sequential Generation of Hydrogen Peroxide and Nitric Oxide for Synergistic Cancer Starving-Like/Gas Therapy, Angewandte Chemie International Edition, 56 (2017) 1229-1233.

[54] R. Jin, Z. Liu, Y. Bai, Y. Zhou, X. Chen, Effective Control of Enzyme Activity Based on a Subtle Nanoreactor: A Promising Strategy for Biomedical Applications in the Future, ACS Applied Nano Materials, 1 (2018) 302-309.

[55] M. Huo, L. Wang, Y. Chen, J. Shi, Tumor-selective Catalytic Nanomedicine by Nanocatalyst Delivery, Nature Communications, 8 (2017) 357.

[56] Y. Zhang, Y. Yang, S. Jiang, F. Li, J. Lin, T. Wang, P. Huang, Degradable Silver-based Nanoplatform for Synergistic Cancer Starving-like/metal Ion Therapy, Materials Horizons, 6 (2019) 169-175.

[57] L. Feng, R. Xie, C. Wang, S. Gai, F. He, D. Yang, P. Yang, J. Lin, Magnetic Targeting, Tumor Microenvironment-Responsive Intelligent Nanocatalysts for Enhanced Tumor Ablation, ACS Nano, 12 (2018) 11000-11012.

[58] H. Cheng, X.-Y. Jiang, R.-R. Zheng, S.-J. Zuo, L.-P. Zhao, G.-L. Fan, B.-R. Xie, X.-Y. Yu, S.-Y. Li, X.-Z. Zhang, A Biomimetic Cascade Nanoreactor for Tumor Targeted Starvation Therapy-amplified Chemotherapy, Biomaterials, 195 (2019) 75-85.

[59] R. Zhang, L. Feng, Z. Dong, L. Wang, C. Liang, J. Chen, Q. Ma, R. Zhang, Q. Chen, Y. Wang, Z. Liu, Glucose & Oxygen Exhausting Liposomes for Combined Cancer Starvation and Hypoxia-activated Therapy, Biomaterials, 162 (2018) 123-131.

[60] L.F. Liu, S.D. Desai, T.-K. Li, Y. Mao, M. Sun, S.-P. Sim, Mechanism of Action of Camptothecin, Annals of the New York Academy of Sciences, 922 (2000) 1-10.

[61] P. Icard, S. Shulman, D. Farhat, J.-M. Steyaert, M. Alifano, H. Lincet, How the Warburg Effect Supports Aggressiveness and Drug Resistance of Cancer Cells?, Drug Resistance Updates, 38 (2018) 1-11.

[62] H. Maeda, Tumor-Selective Delivery of Macromolecular Drugs via the EPR Effect: Background and Future Prospects, Bioconjugate Chemistry, 21 (2010) 797-802.

[63] M.S. Nars, R. Kaneno, Immunomodulatory effects of low dose chemotherapy and perspectives of its combination with immunotherapy, International Journal of Cancer, 132 (2013) 2471-2478.

[64] J. Shi, P.W. Kantoff, R. Wooster, O.C. Farokhzad, Cancer nanomedicine: progress, challenges and opportunities, Nature Reviews Cancer, 17 (2016) 20-37.

[65] S.K. Sharma, K.D. Bagshawe, Antibody Directed Enzyme Prodrug Therapy (ADEPT): Trials and tribulations, Advanced Drug Delivery Reviews, 118 (2017) 2-7.

[66] B. Städler, A.N. Zelikin, Enzyme prodrug therapies and therapeutic enzymes, Advanced Drug Delivery Reviews, 118 (2017) 1-1.

[67] S.K. Sharma, K.D. Bagshawe, Translating antibody directed enzyme prodrug therapy (ADEPT) and prospects for combination, Expert Opinion on Biological Therapy, 17 (2017) 1-13.

Chapter III: Cisplatin Resistance Reversal of Lung Cancers by Tumor Acidity Activable Vesicular Nanoreactors *via* Tumor Oxidative Stress Amplification

3.1. Introduction

Cisplatin is one of potent platinum-based chemotherapeutic agents widely used in clinical practices for treatment of a broad spectrum of human malignant solid tumors including ovarian, prostate, lung, bladder, colorectal and esophageal cancers.[1, 2] In principal, cisplatin mediates its antitumor effects mainly by virtue of reaction with DNA in nuclei and mitochondria to induce DNA lesions which subsequently lead to cell death through DNA damage, mitochondria apoptosis, and activation of various signal transduction pathways.[3]

Although cisplatin is clinically proven and still one of the major chemotherapeutic drugs currently used in clinics to treat cancer, numerous clinical and preclinical studies showed that severe side effects such as nephrotoxicity, neurotoxicity, and ototoxicity are often associated with cisplatin application which consequently limit the amount of dose that can be administered.[4-6] Moreover, it was clinically evidenced that the cisplatin fair initial response is often followed by development of either acquired or intrinsic chemo-resistance in most of patients.[7, 8] Drug resistance is a critical challenge encountered in chemotherapy as it can promote tumor reoccurrence and consequently lead to therapeutic failure.[9, 10] Therefore, the poor prognosis and high recurrence rates are still the main barriers that strictly obstruct cisplatin successful application in clinic.[11, 12]

In view of the possible mechanism for cisplatin-resistance of cancer cells, the decreased cytoplasmic accumulation of cisplatin, increased altered DNA self-healing, and enhanced cellular detoxification were primarily revealed and reported as substantial factors that favor cancer cell survival against cisplatin cytotoxicity.[11, 13]

Currently, a variety of precise nanomedicine designs to reverse cisplatin resistance, such as cisplatin targeted delivery, depletion of intracellular glutathione (GSH) and metallothionein (MT) proteins, as well as the introduction of combination therapies have been explored as attractive approaches to enhance cisplatin chemosensitivity and achieve optimistic therapeutic effects.[14-20] In addition to DNA damage and mitochondrial apoptosis which are widely recognized as the major cell killing mechanisms of cisplatin, substantial evidences currently revealed that cisplatin can induce oxidative stress which also plays an essential role to its pronounced cytotoxicity though activation of intracellular pro-apoptotic pathways.[21-24] Interestingly, treatment with antioxidants has been demonstrated to modulate cisplatin-induced toxic adverse reactions,[5, 25] however, decreased antitumor effect was observed in most cases,[26, 27] which suggested the involvement of oxidative stress in the cisplatin mechanism of action to induce cell death.[24]

Moreover, recent investigations revealed that various reactive oxygen species (ROS) inducer agents such as shikonin, saikosaponins and bithionol can potentiate chemotherapeutic efficacy of cisplatin by amplification of intracellular ROS.[28-31] Considering the ROS paradoxical key roles in regulation of various cellular pathways including apoptosis, it is of great significance to design a pioneering therapeutic nanosystem which can exploit ROS as sensitizing agents to improve cisplatin chemo-sensitivity and overcome drug resistance.

Herein, a vesicular nanoreactor that can locally amplify intracellular oxidative stress to sensitize drug resistant cells toward cisplatin anti-cancer activity is developed. Briefly, polymeric vesicles engineered from diblock copolymers composed of poly(ethylene glycol) (PEG) and copolymerized segment of benzyl methacrylate (Bz) and 2-(piperidin-1-yl) ethyl methacrylate (PEMA) were used to build therapeutic nanoreactors that coencapsulate and deliver both chemotherapeutic drug cisplatin and glucose oxidase (GOD). Of note, GOD is a biocompatible oxido-reductase enzyme that can exert antitumor toxicities especially through activation of cellular oxidative stress and cell starvation *via* depletion of glucose as major cellular source of energy.[32]

The therapeutic nanoreactor denoted as Cis/GOD@Bz-V was rationally designed to stay impermeable during blood circulation. On the other hand, the tumor mild acidity (pH 6.5-6.8) can activate its molecular weight selective membrane permeability to small molecules, leading to the release of cisplatin locally and followed by the subsequent diffusion of small molecules such as oxygen and glucose across the selective permeable membrane of the Cis/GOD@Bz-V therapeutic nanoreactor to initiate a cascade reaction for *in situ* generation of superfluous amount of H_2O_2 that can induce cellular oxidative stress, which in turn reverses cisplatin drug resistance *via* activation of pro-apoptotic pathways to achieve enhanced detrimental effect against drug resistant tumor cells **(Figure 3.1)**.

Cisplatin-resistant human lung cancer tumor cell model (A549R) was used to test treatment efficacy of our designed nanosystem both *in vitro* and *in vivo*. The results showed that Cis/GOD@Bz-V therapeutic nanoreactor has effective killing potential against cisplatin-resistant A549R cells and can significantly inhibit tumor growth of cisplatin-resistant A549R tumor model without observable adverse effects.

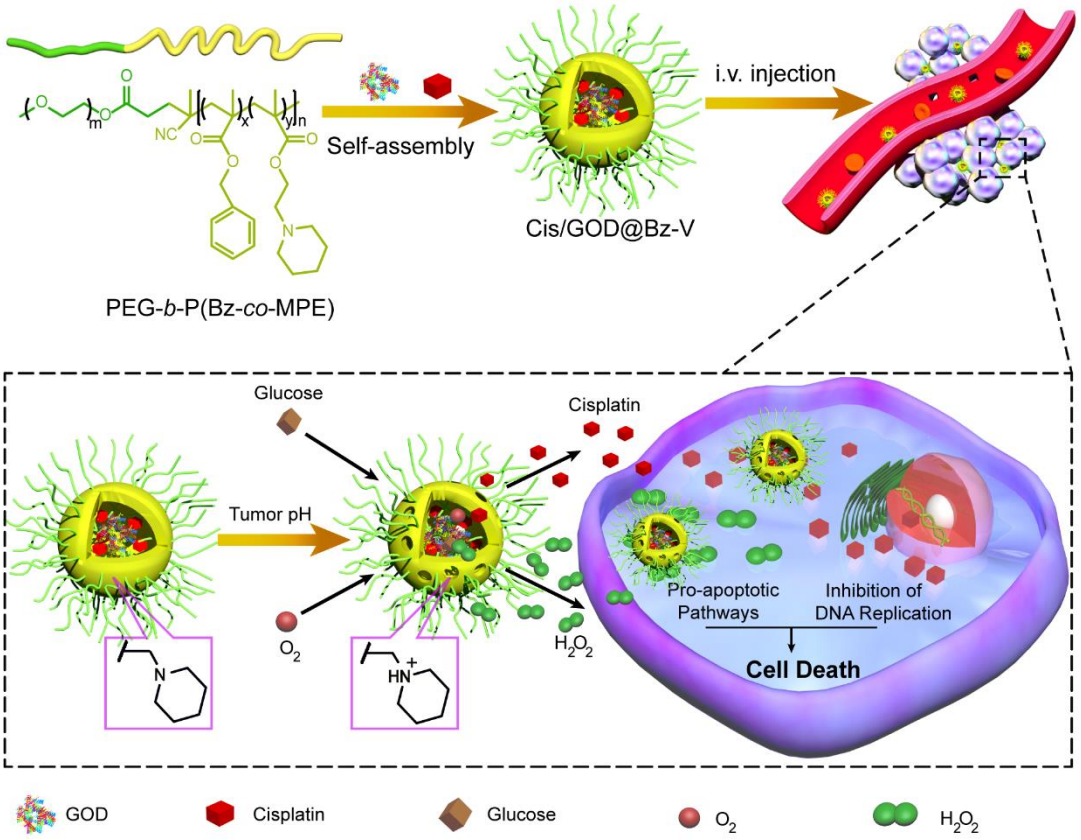

Figure 3. 1. Schematic illustration of preparation steps for Cis/GOD@Bz-V therapeutic nanoreactor. The tumor acidity (pH 6.5-6.8) can activate Cis/GOD@Bz-V nanoreactor membrane permeability to release cisplatin and allow diffusion of small molecules such as glucose and oxygen and initiate a cascade reaction for *in situ* generation of high amount of H_2O_2 ROS that can induce cellular oxidative stress to amplify cisplatin chemosensitivity against cisplatin-resistant A549R cells *via* activation of pro-apoptotic pathways.

3.2. Materials and Methods

3.2.1. Materials

Cisplatin (≥ 99%) was purchased from Shandong Platinum Source Chemical Co., Ltd. Glucose oxidase (GOD) from *Aspergillus niger* (200 U mg^{-1}) was obtained from Sigma-Aldrich and used as received. Horseradish peroxidase (HRP, 250 U mg^{-1}) was procured from Klamar® (Shanghai, China). *β*-D-Glucose was obtained from TCI Development Co.,Ltd., fluorescein isothiocyanate (FITC), 1-(3-dimethylaminopropyl)-3-ethylcarbodiimide hydrochloride (EDC, 98%), N-Hydroxysuccinimide (NHS, 4-dimethylaminopyridine (DMAP, 98%), and benzyl methacrylate (Bz, 98%) were supplied by Energy Chemical and passed through a silica column before use to remove the inhibitor. PEG-RAFT agent (M_n = 5000, M_n/M_w = 1.05), 2-(piperidin-1-yl) ethyl methacrylate (PEMA), and cypate were synthesized according to the previous reported methods.[33, 34] 3-(4,5-dimethylthiazol-2-yl)-2,5-diphenyltetrazolium bromide (MTT), propidium iodide (PI, 94%), fluorescein diacetate (FDA), Genomic DNA Mini Preparation Kit with Spin Column, reactive oxygen species (ROS) Assay Kit (2',7'-dichlorofluorescin diacetate, DCFH-DA), Caspase 3 Kit, and Annexin V-FITC Apoptosis Detection Kit were purchased from Beyotime Institute of Biotechnology (Shanghai, China). Fetal bovine serum (FBS), Roswell Park Memorial Institute (RPMI-1640) without glucose, and trypsin were purchased from GIBCO. The cisplatin-resistant human lung cancer cell line A549R and human lung cancer cell line A549 were obtained from Shanghai Fumengjiyin Biotechnology (FMGbio) Co. Ltd. Female BALB/c nude mice and female BALB/c mice with 4-Week-old were purchased from Beijing Vital River Laboratory Animal Technology Co., Ltd.

The animal studies were carried out according to the regulations for the administration of affairs concerning experimental animals (Hefei, revised in June 2015).

3.2.2. Synthesis of FITC or Cypate-labelled Glucose Oxidase (FITC-GOD and Cypate-GOD)

FITC or cypate-labelled glucose oxidase was synthesised as follows: For FITC-GOD preparation, FITC in DMSO (25 μL, 10 mg/mL) was dropped into the aqueous solutions of GOD (2 mL, 10 mg/mL containing 100 mM sodium carbonate) at 4°C. After 12 h reaction, the reaction mixture was dialyzed against deionized water in the dark and lyophilized. FITC number conjugated to GOD was determined to be 2.5 by the extinction coefficients of 44,100 M^{-1} cm^{-1} at 280 nm (GOD) and 81,000 M^{-1} cm^{-1}at 495 nm (FITC).

For Cypate-GOD conjugation, Cypate (0.1 g, 0.14 mmol), EDC (30 mg, 0.15 mmol), and NHS (19 mg, 0.15 mmol) were dissolved in dimethyl sulfoxide (DMSO) (500 μL) and stirred for 1 h at room temperature. Subsequently, cypate solution (25 μL) was added into GOD aqueous solutions (1 mL, 10 mg/mL). After reaction at 4°C for 12 h, the mixture solution was dialyzed against deionized water in the dark and lyophilized. Cypate number conjugated to GOD was determined to be 2.1 by the extinction coefficients of 44,100 M^{-1} cm^{-1} at 280 nm (GOD) and 224,000 M^{-1} cm^{-1} at 778 nm (cypate).

3.2.3. Synthesis of PEG-*b*-P(BzMA-*co*-PEMA) Block Copolymer

The PEG-*b*-P(BzMA-*co*-PEMA) block polymer was synthesized *via* reversible addition-fragment transfer (RAFT) to copolymerize benzyl methacrylate (BzMA) and 2-(piperidin-1-yl) ethyl methacrylate (PEMA) using PEG-RAFT agent as the polymeric macro-chain transfer agent. Briefly, PEG-RAFT agent (0.1 g, 0.02 mmol), BzMA (0.59 g, 3.33 mmol), PEMA (0.11 g, 1 mmol), 2′-azobisisobutyronitrile (AIBN) (0.28 mg, 1.7 μmol), and 1,4-dioxane (3 mL) were charged into a Schlenk flask. The reaction solution in flask was then degassed by three freeze-pump-thaw cycles and sealed under vacuum. After 12 h of polymerization in an oil bath at 80 °C, the reaction was quenched with liquid nitrogen before being exposed to air. Subsequently, the crude product was precipitated in diethyl ether solution followed by dissolving in dichloromethane (DCM) and precipitate two more times in diethyl ether. Then the product was collected by centrifugation and dried in a vacuum oven for 24 h to obtain pale yellow powder (0.52 g, Yield: 65%, $M_{n,GPC}$ = 30,000, M_w/M_n = 1.10). According to the ^{1}H NMR analysis in $CDCl_3$, the degree of polymerization (DP) of BzMA and PPEMA segment were determined to be 120 and 21, respectively (**Figure 3.2A**). Thus, the block copolymer was denoted as PEG_{113}-*b*-P($BzMA_{120}$-*co*-$PEMA_{21}$).

3.2.4. Preparation of Cisplatin and GOD Co-loaded Polymeric Nanoreactors

The diblock copolymer PEG_{113}-*b*-P($BzMA_{120}$-*co*-$PEMA_{21}$) (2 mg) was dissolved in 500 μL of THF/DMSO (4:1) co-solvent, followed by addition of 5 mL of PBS solution containing cisplatin (1 mg/mL) and GOD (1 mg/mL) at a constant rate of 1 mL h^{-1} using an injection pump. Unencapsulated cisplatin and organic solvents were

removed by dialysis method. The free GOD was removed by ultracentrifugation, then, the solution was concentrated to 4 mL. Cisplatin and GOD co-loaded PEG-*b*-P(BzMA-*co*-PEMA) polymeric nanoreactors were denoted as Cis/GOD@Bz-V. The cisplatin or GOD individually loaded into PEG-*b*-P(BzMA-*co*-PEMA) polymeric nanoreactors were also prepared according to the similar method and denoted as Cis@Bz-V or GOD@Bz-V, respectively. The concentration of cisplatin in each polymeric nanoreactors solution was determined by inductively coupled plasma mass spectrometry (ICP-MS). FITC-GOD was utilized to determine the concentration of GOD by fluorescence spectroscopy. Furthermore, PEG-*b*-P(BzMA-*co*-PEMA) polymeric vesicles loading cisplatin and cypate-GOD were also self-assembled for *in vivo* investigations with the same method. Drug loading capacities DLCs (%) = [(weight of loaded drug)/(weight of total nanoreactors)] × 100.

3.2.5. pH-Triggered Membrane Permeability Analyses

The pH-triggered membrane permeability of polymeric nanoreactors was evaluated according to enzyme cascade reaction. Typically, Cis/GOD@Bz-V solutions sealed in a dialysis bag (MWCO = 3500 Da) were incubated in PBS containing glucose (1 mg/mL), HRP (150 mU/mL), and TMB (100 μM) at pH 7.4 or pH 6.8. The absorbance of oxidative TMB at 370 nm was recorded at predetermined time intervals.

3.2.6. H_2O_2 Production and Cisplatin Release

H_2O_2 production and cisplatin release from Cis/GOD@Bz-V polymeric nanoreactors were measured by dialysis diffusion method. Briefly, Cis/GOD@Bz-V

was incubated with glucose (1 mg/mL) in dialysis bags (MWCO = 3500 Da) at pH 7.4 or 6.8. At predetermined time intervals, aliquot samples were collected and the same amount of PBS was added. The collected dialysis medium was subjected to cisplatin and H_2O_2 measurement. The cisplatin content was measured by ICP-MS and H_2O_2 concentration was quantified by dissolved oxygen (D.O.) meter in the presence of catalase (1000 units).

3.2.7. Cytotoxicity Evaluation

A549R or A549 cells (1×10^4 cells) were seeded into 96-well plates in 100 μL RPMI-1640 medium with 10% FBS under 5% CO_2 humidified atmosphere at 37 °C overnight. Then the cells were incubated with various concentrations of cisplatin, Cis@Bz-V, GOD@Bz-V, or Cis/GOD@Bz-V with glucose (1 mg/mL) at pH 7.6 or pH 6.8. After 48 h, the medium was replaced with 100 μL fresh medium and MTT solution (20 μL, 5 mg/mL) was added for another 4 h incubation. Next, the solution was removed and DMSO (150 μL) was added to dissolve the formed purple formazan crystals. After shaking the plates for 15 min, the absorbance at the wavelength of 490 nm and 570 nm was measured by a microplate reader.

For live and dead staining assay, A549R cells (5×10^5 cells) were incubated with cisplatin, Cis@Bz-V, GOD@Bz-V, or Cis/GOD@Bz-V with or without glucose (1 mg/mL) at pH 7.4 or pH 6.8 for 24 h. The equivalent cisplatin concentration was fixed to 1.5 μM or with equivalent GOD concentration of 91.4 mU/mL. Next, the medium was replaced with cold PBS containing FDA (10 μg/mL) and PI (20 μg/mL) solution.

After 20 min incubation, the cells were washed with PBS twice and fluorescence microscopy was used to observe the FDA and PI positive cells.

3.2.8. Cellular Uptake of Platinum and DNA Platination

To study the cellular uptake of platinum, A549R or A549 cells (5×10^5 cells) were seeded into 12-well plates in RPMI-1640 medium (500 μL) with 10% FBS under 5% CO_2 humidified atmosphere at 37 °C overnight. Then the cells were incubated with fresh medium containing cisplatin, Cis@Bz-V or Cis/GOD@Bz-V in the presence of glucose (1 mg/mL) at pH 6.8 for 6 h. The equivalent platinum concentration was fixed to 1.5 μM. Next, the cells were washed twice with PBS and harvested by trypsinization. The platinum contents in cells were measured by ICP-MS.

To study DNA platination, A549R or A549 cells were incubated with cisplatin, Cis@Bz-V or Cis/GOD@Bz-V in the presence of glucose (1 mg/mL) at pH 6.8 for 48 h. The equivalent platinum concentration was fixed to 1.5 μM. Next, DNA in cells was obtained by Genomic DNA Mini Preparation Kit and the platinum concentration in DNA solution was measured by ICP-MS.

3.2.9. Caspase 3 Activity Evaluation

For intracellular caspase 3 activity detection, A549R or A549 cells (3×10^5 cells) were seeded into 6-well plates in RPMI-1640 medium (2 mL) with 10% FBS at 37 °C under 5% CO_2 humidified atmosphere overnight. Next, the cells were incubated in fresh media containing of PBS, free cisplatin, Cis@Bz-V, GOD@Bz-V, or

Cis/GOD@Bz-V at the cisplatin-equivalent concentration of 1.5 μM or with equivalent GOD concentration of 91.4 mU/mL for 12 h in the presence of glucose (1 mg/mL) at pH 6.8. The cellular caspase 3 activity was measured by following the procedure from Caspase 3 activity detection Kit (beyotime).

3.2.10. *In Vitro* Intracellular ROS, Caspase 3 Activity and Apoptosis Rate Evaluation

For *in vitro* intracellular ROS detection, A549R cells (1×10^5 cells) were seeded into 12-well plates in RPMI-1640 medium (500 μL) with 10% FBS at 37 °C under 5% CO_2 humidified atmosphere overnight. The medium was replaced with fresh medium containing cisplatin, Cis@Bz-V, GOD@Bz-V, or Cis/GOD@Bz-V in the presence of glucose (1 mg/mL) at pH 6.8 for 12 h. The equivalent cisplatin concentration was fixed to 1.5 μM or with equivalent GOD concentration of 91.4 mU/mL. Next, the medium was substituted with PBS containing ROS probe (2',7'-dichlorofluorescin diacetate, DCFH-DA, 10 μM). After 20 min incubation, the cells were washed twice with PBS and imaged with CLSM (Ex: 488 nm, Em: 500 nm-540 nm). The ImageJ software was applied to analyze fluorescence intensity.

For apoptosis rate evaluation, A549R cells (1×10^5 cells) were seeded into 12-well plates in RPMI-1640 medium (500 μL) with 10% FBS at 37 °C under 5% CO_2 humidified atmosphere overnight. The medium was replaced with fresh medium containing cisplatin, Cis@Bz-V, GOD@Bz-V, or Cis/GOD@Bz-V in the presence of glucose (1 mg/mL) at pH 6.8 for 24 h. The equivalent cisplatin concentration was fixed to 1.5 μM or with equivalent GOD concentration of 91.4 mU/mL. Next, cells were

collected into 2 mL tubes by trypsinization and Annexin V/PI staining assay was conducted according to manufacturer's protocol. Finally, the apoptosis rate was quantified by flow cytometric analysis.

3.2.11. *In Vivo* Biodistribution and Intratumor ROS Level Evaluation

To detect the biodistribution of the polymeric nanoreactors, BALB/c mice with established 4T1 tumors (~ 50 mm^3) were used. Cisplatin and cypate-GOD co-loaded PEG-*b*-P(BzMA-*co*-PEMA) polymeric nanoreactors were intravenously injected into the mice at the cypate concentration of 7.5 mg/kg. At predetermined time intervals, the mice were anesthetized and observed by *in vivo* imaging system (IVIS).

To monitor the intratumor ROS level evaluation, DCFH-DA staining method was performed. Briefly, A549R tumor bearing BALB/c nude mice (~ 50 mm^3) tumor bearing were intravenously injected with PBS, cisplatin, Cis@Bz-V, GOD@Bz-V, or Cis/GOD@Bz-V at the platinum-equivalent dose of 3 mg/kg or GOD-equivalent dose of 2.39 U/kg. After 24 h post-injection, DCFH-DA was injected intratumorally. After further 30 min, the mice were sacrificed and the tumors were collected and sectioned into 5 μm slices for CLSM observation. The ImageJ software was applied to analyze fluorescence intensity.

3.2.12. *In Vivo* Antitumor Activity

A549R tumor-bearing BALB/c nude mice (~50 mm^3) were intravenously injected with PBS, cisplatin, Cis@Bz-V, GOD@Bz-V, or Cis/GOD@Bz-V formulations at day 0, 3, and 6. In each administration, the equivalent platinum concentration and

equivalent GOD dose were 3 mg/kg and 2.39 U/kg, respectively. Every two day, the tumor size was recorded with a digital Vernier caliper. The tumor volume (V) was calculated by the following equation: $V = 0.5\ (a \times b^2)/2$, where "a" and "b" are the longest and shortest distance of the tumor, respectively. At day 21, the mice were sacrificed. The major organs including heart, kidney, spleen, liver, and lung as well as tumors were collected and sliced into 10 μm slices for hematoxylin and eosin (H&E) staining.

3.2.13. Statistical Analysis

All the data obtained were presented as mean ± standard deviation (SD). Student's *t*-test was performed to analyze the difference between the study groups and *p*-values lower than 0.05 were considered statistically significant. $^{**}p < 0.05$, $^{***}p < 0.01$(*t*-test).

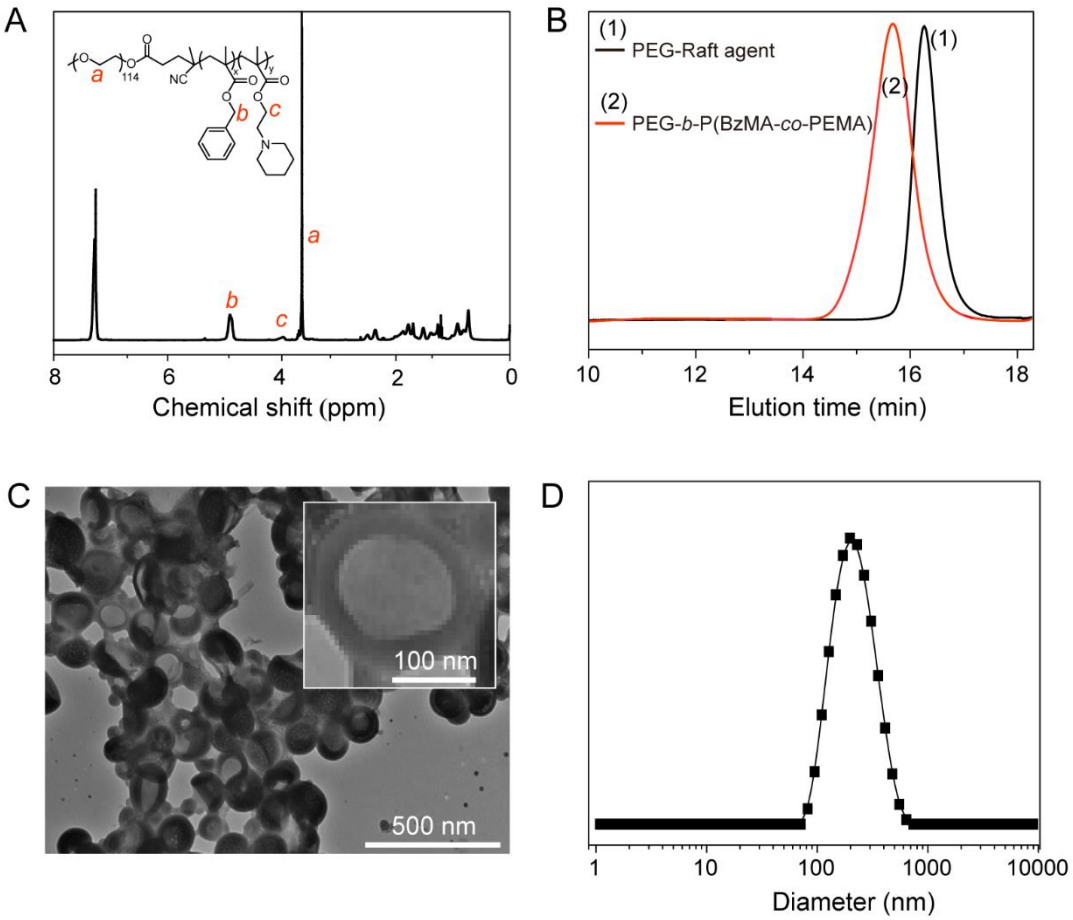

Figure 3. 2. Characterization images for PEG_{113}-*b*-P($BzMA_{120}$-*co*-$PEMA_{21}$). **(A)** ^1H NMR analysis of PEG_{113}-*b*-P($BzMA_{120}$-*co*-$PEMA_{21}$) polymer in $CDCl_3$. **(B)** GPC traces of macro-PEG_{113}-RAFT agent and PEG_{113}-*b*-P($BzMA_{120}$-*co*-$PEMA_{21}$) polymer. **(C)** TEM characterization image of Cis/GOD@Bz-V nanoreactor. **(D)** Size distribution test by DLS of cisplatin and GOD co-loaded PEG_{113}-*b*-P($BzMA_{120}$-*co*-$PEMA_{21}$) vesicle (Cis/GOD@Bz-V).

3.3. Results and Discussion

3.3.1. Preparation of Polymeric Nanoreactors

The diblock polymers, PEG-*b*-P(BzMA-*co*-PEMA), were synthesized *via*

reversible addition fragmentation chain transfer (RAFT) polymerization by using PEG_{113}-RAFT as macro-RAFT chain transfer agent. According to ^1H NMR analysis, the optimized degrees of polymerization (DP) for PBzMA and PPEMA segments were determined to be 120 and 21, respectively **(Figure 3.2A)**. Gel permeation chromatography (GPC) test results showed narrow molecular weight distributions with M_w/M_n of 1.10 **(Figure 3.2B).**

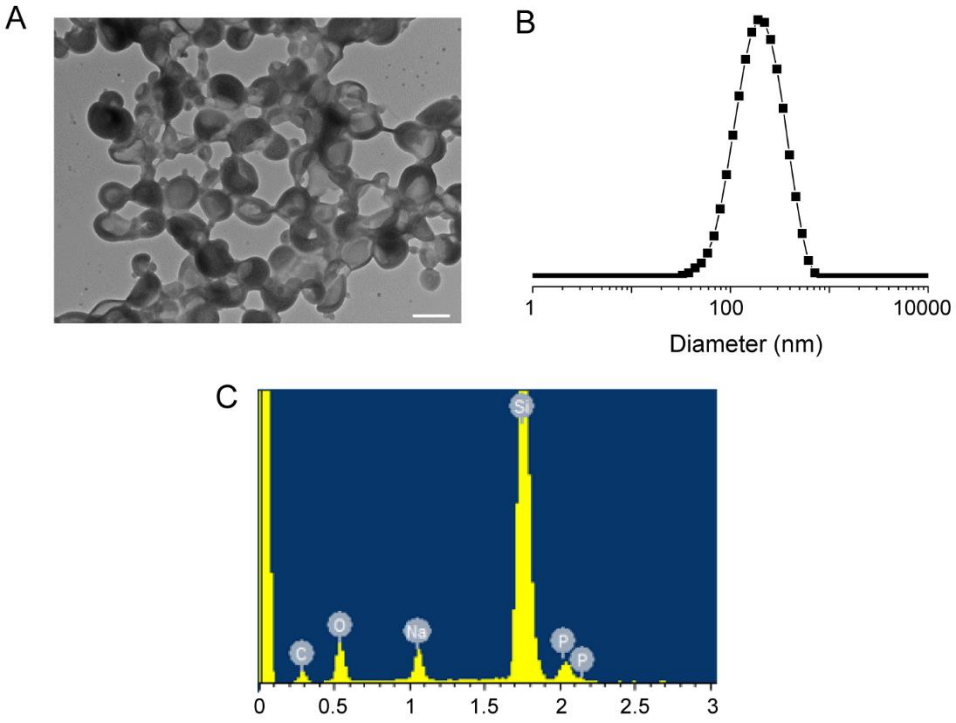

Figure 3. 3. (A) TEM image, **(B)** size distribution by DLS and **(C)** SEM element analysis of PEG_{113}-*b*-P($BzMA_{120}$-*co*-$PEMA_{21}$) vesicle. Scale bars represent 200 nm.

Amphiphilic diblock copolymer PEG_{113}-*b*-P($BzMA_{120}$-*co*-$PEMA_{21}$) can self-assemble into polymeric vesicles through solvent switch method upon addition of phosphate buffered saline (PBS, pH 7.4) into the solution made of polymer and

tetrahydrofuran/dimethyl sulfoxide (V/V = 4:1). According to transmission electron microscopy (TEM) images **(Figure 3.3A)**, the formed particles with a vesicular structure were found to have average diameter size of 170 ± 30 nm with membrane thickness of 30 nm ± 10 nm. Dynamic light scattering (DLS) test results showed that PEG_{113}-*b*-P($BzMA_{120}$-*co*-$PEMA_{21}$) polymeric vesicles have the diameter size of 190 nm and low polydispersity index (PDI) of 0.19 **(Figure 3.3B)**.

Cisplatin and GOD were encapsulated into the aqueous phase of PEG_{113}-*b*-P($BzMA_{120}$-*co*-$PEMA_{21}$) polymeric vesicles to engineer therapeutic nanoreactors which are denoted as Cis/GOD@Bz-V. The Cis/GOD@Bz-V nanoreactors loading capacity for cisplatin was determined to be 4.25 wt% by ICP-MS results. In addition, fluorescein isothiocyanate-labeled GOD (FITC-GOD) was used to detect the concentration of GOD in polymeric nanoreactors and the drug loading capacity (DLCs) was determined to be 2.39 wt% by UV-vis absorbance measurement. TEM characterization image for Cis/GOD@Bz-V nanoreactors presented spherical morphology with particle diameter size of 180 ± 20 nm and membrane thickness of 15 nm ± 10 nm **(Figure 3.2C).** DLS results showed particle size of 195 nm **(Figure 3.2D)**. Except the empty vesicle, Scanning electron microscope (SEM) element anlysisis appeared the singal of platinum, indicating effectively loading of cisplatin into the Cis/GOD@Bz-V nanoreators **(Figure 3.3C** and **3.4A)**. Moreover, the sole cisplatin-loaded vesicle was also prepared with DLCs of 4.0 wt% as a control and denoted as Cis@Bz-V.

Tertiary amine containing moieties have been widely used generate ultra-pH responsive nanoparticles.[33, 35] Due to the presence of PEMA segment in our prepared polymer, the pKa value of Cis/GOD@Bz-V polymeric nanoreactors was

determined to be 6.95 which is in the range of tumor microenvironment acidity and could be used to control the membrane permeability of Cis/GOD@Bz-V polymeric nanoreactors. Specifically, it is expected that the incubation of Cis/GOD@Bz-V in an environment with a pH slightly lower that its pKa value can subsequently induce PEMA segment phase transition and become soluble to generate permeable membrane of Cis/GOD@Bz-V while keeping the structure integrity of the nanoreactor.[36]

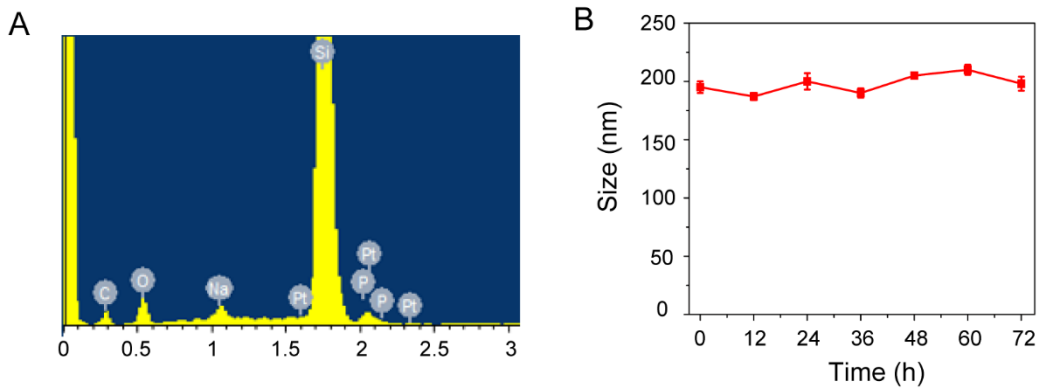

Figure 3. 4. Elemental analysis and stability assessment for Cis/GOD@Bz-V. **(A)** SEM element analysis of cisplatin and GOD co-loaded PEG_{113}-*b*-P($BzMA_{120}$-*co*-$PEMA_{21}$) vesicle (Cis/GOD@Bz-V). (**B**). The Cis/GOD@Bz-V nanoreactor size stability assessment by DLS at different time points, pH 6.8 and at 37 °C. Results = mean ± SD, $n = 3$.

As a proof of concept, we tested the pH-responsive permeability of Cis/GOD@Bz-V nanoreactor by a cascade reaction between GOD, glucose, 3,3',5,5'-tetramethylbenzidine (TMB) and horseradish peroxidase (HRP) at both pH 6.8 and pH 7.4. It is known that H_2O_2 can oxidize TMB under the catalysis of HRP, thus the

absorbance of oxidized TMB can be monitored to determine the permeability of the nanoreactors **(Figure 3.5A)**. Consistently, by incubating Cis/GOD@Bz-V polymeric nanoreactors in a solution of glucose, TMB, and HRP at pH 6.8 or pH 7.4, it was found that, the absorbance of oxidized TMB at 370 nm increased with time at pH 6.8 medium. However at pH 7.4, the absorbance of oxidized TMB showed no obvious increase **(Figure 3.5B).** Moreover, our engineered Cis/GOD@Bz-V polymeric nanoreactors proved stability with no obvious size change after incubation for 3 days at pH 6.8 which can be possibly explained by the fact that low content of PEMA was randomly distributed in the matrix of the nanoreactor membrane (**Figure 3.4B**). In overall, the results demonstrated the activation of membrane permeability for Cis/GOD@Bz-V nanoreactor when the pH was changed from 7.4 to 6.8, can selectively allow the transportation of small molecules (such as glucose, O_2, H_2O_2 and cisplatin) across the membrane while retaining the loaded GOD inside the reaction vessels.

Next, we monitored the H_2O_2 production from Cis/GOD@Bz-V in the presence of 1 mg/mL glucose at pH 7.4 or 6.8. As showed in **Figure 3.5C**, a large amount of H_2O_2 (over 100 μM) was generated in 60 minutes when the nanoreactor was incubated at pH 6.8 medium, on the other hand, negligible concentration of H_2O_2 was detectable even after 72 h of incubation, suggesting that tumor microenvironment acidity (~ pH 6.5-6.8) can trigger H_2O_2 production from Cis/GOD@Bz-V. Moreover, cisplatin drug release from Cis/GOD@Bz-V was investigated, and the result showed that about 90% cisplatin can be successfully released in less than one 1 h at pH 6.8, on the other hand, no more than 10% was released when Cis/GOD@Bz-V nanoreactors were incubated at pH 7.4 even up to 72 h of incubation **(Figure 3.5D).** Therefore, the engineered nanoreactors can be specifically activated at tumor pH for efficient H_2O_2 production

and used as cisplatin delivery nanocarriers for tumor-targeted drug release.

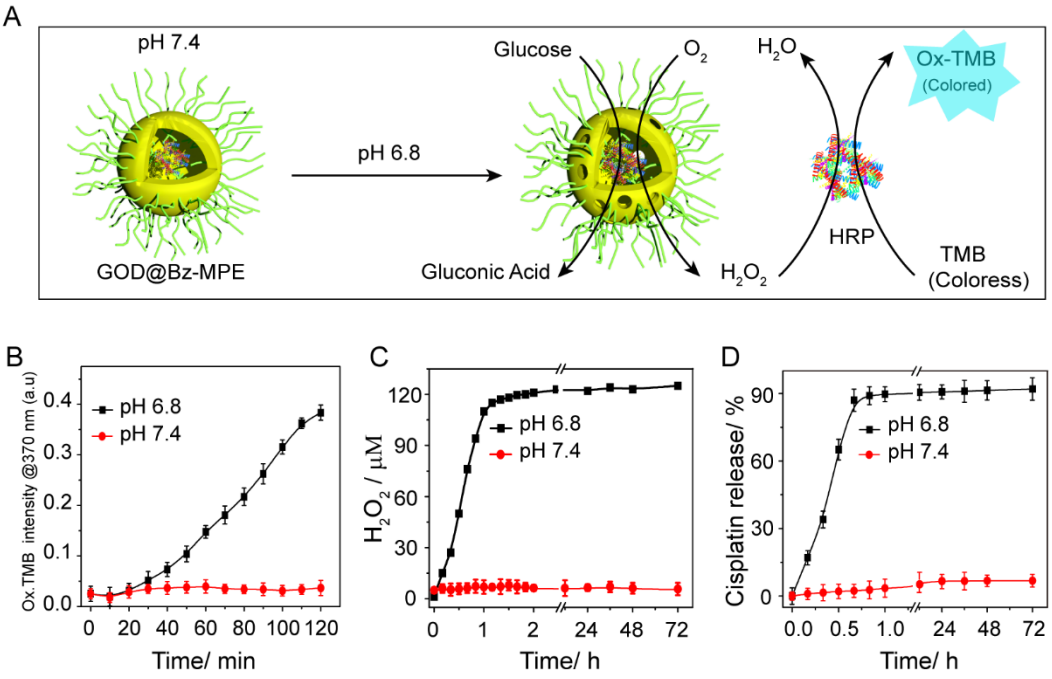

Figure 3. 5. Evaluation for Cis/GOD@Bz-V nanoreactor membrane permeability, H_2O_2 production and Cisplatin release. **(A)** Sketch for the methodology used to evaluate Cis/GOD@Bz-V nanoreactor membrane permeability behavior at both pH 7.4 or pH 6.8. **(B)** Time dependent oxidized TMB color absorbance intensity evaluation at 370 nm as the product of cascade reactions of Cis/GOD@Bz-V (GOD: 50 mU/mL) after being incubated in PBS solution in the presence of glucose (1 mg/mL), HRP (150 mU/mL), and TMB (100 μM) at pH 7.4 or pH 6.8. **(C)** Evaluation of H_2O_2 production for Cis/GOD@Bz-V (GOD: 50 mU/mL) in the presence of 1 mg/mL glucose at pH 7.4 or pH 6.8. **(D)** Cisplatin release profiles from Cis/GOD@Bz-V nanoreactors at pH 7.4 or pH 6.8. Results = mean ± SD, n = 3.

3.3.2. Cytotoxicity Evaluation

MTT assay was performed to test the cytotoxicity of our engineered therapeutic nanoreactor against cisplatin-resistant human lung cancer cell line (A549R) along with human lung cancer cell line (A549). Unlike A549 cell line, the free cisplatin exhibited negligible cytotoxicity against A549R even at high concentration of 5 μM as the cell viability was still higher than 90% at pH 6.8 **(Figure 3.6A-B)**. Surprisingly, the encapsulated cisplatin (Cis@Bz-V) showed moderate toxicity against A549R which was comparable to that of Cis@Bz-V against A549 with the half maximal inhibitory concentration (IC_{50}) value of 5.87 μM and 4.69 μM, respectively, at pH 6.8 **(Table 3.1).**

Table 3. 1. The calculated IC_{50} by treating A549 or A549R cell lines with various concentrations of free Cisplatin, Cis@Bz-V, GOD@Bz-V or Cis/GOD@Bz-V for 48 h at pH 6.8. Results = mean, $n = 4$.

Treatment group	A549		A549R	
	Cisplatin (μM)	GOD (mU/mL)	Cisplatin (μM)	GOD (mU/mL)
Free Cisplatin	5.13	-	-	-
Cis@Bz-V	4.69	-	5.87	-
GOD@Bz-V	-	215.03	-	249.34
Cis/GOD@Bz-V	1.39	84.06	1.46	88.99

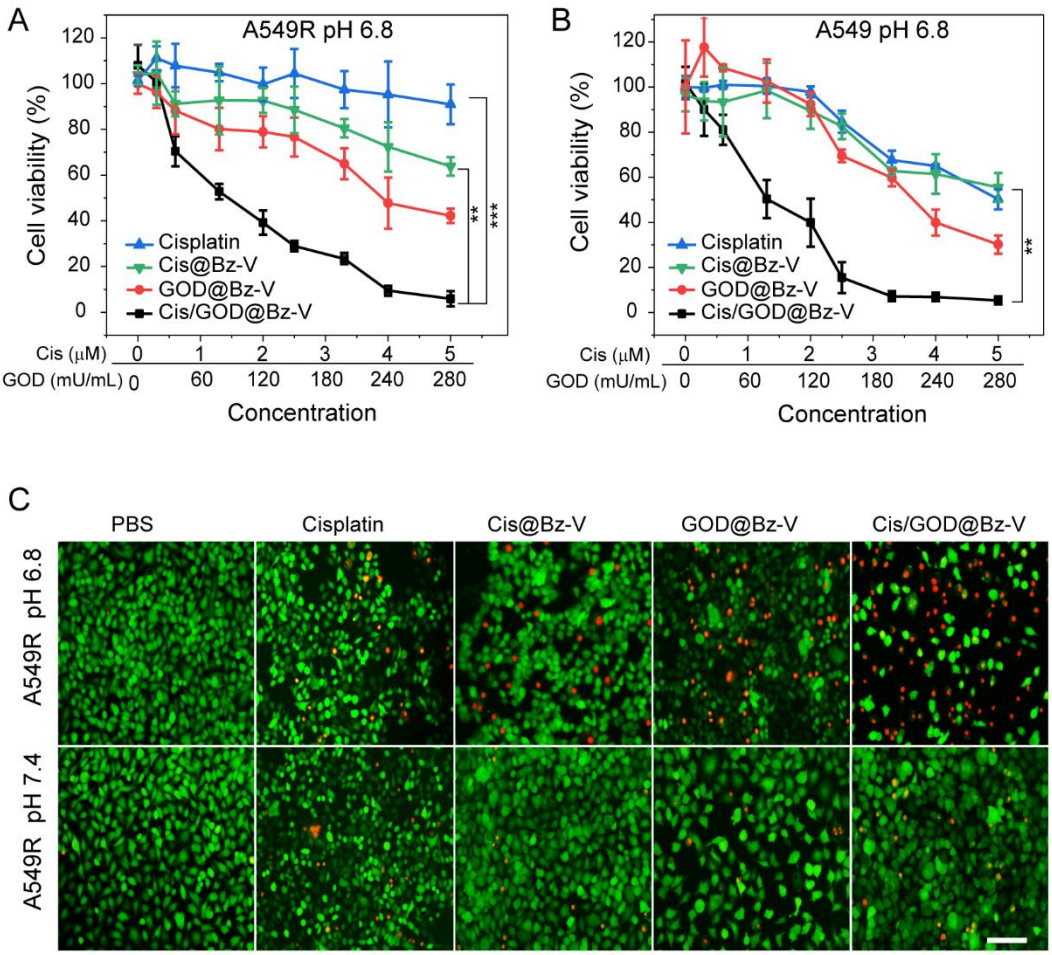

Figure 3. 6. Evaluation of *In vitro* cytotoxicity against A549R and A549 cell lines *via* MTT at pH 6.8 and live/dead assays. **(A)** The A549R cells viability after treatment with various concentration of free cisplatin, Cis@Bz-V, GOD@Bz-V, Cis/GOD@Bz-V for 48 h at pH 6.8 in the presence of glucose (1 mg/mL). Results = mean ± SD, $n = 4$. **(B)** The A549 cells viability after treatment with various concentrations of free cisplatin, Cis@Bz-V, GOD@Bz-V, or Cis/GOD@Bz-V for 48 h at pH 6.8 in the presence of glucose (1 mg/mL). Results = mean ± SD, $n = 4$. **(C)** Live/dead staining of A549R cells after different treatments at the equivalent cisplatin concentration of 1.5 μM or with equivalent GOD concentration of 91.4 mU/mL for 24 h and at pH 6.8 or 7.4 in the presence of glucose (1 mg/mL). Scale bars represent 20 μm.

The observed higher toxicity of Cis@Bz-V compared to free cisplatin can be possibly owing to the increased cellular uptake of cisplatin through endocytosis for nanoparticles such as Cis@Bz-V rather than Ctr1-mediated pathway for free cisplatin.[37] Moreover, at pH 6.8, the GOD@Bz-V showed identifiable cellular cytotoxicity against both A549R and A549 cell lines with IC_{50} value of 249.34 and 215.03 mU/mL (GOD concentration), respectively. In a sharp contrast, Cis/GOD@Bz-V showed the highest cytotoxicity against A549R and A549 cells with significantly reduced IC_{50} value of 1.46 μM (cisplatin) with corresponding 88.99 mU/mL (GOD), and 1.39 μM (cisplatin) with corresponding 84.06 mU/mL (GOD), respectively. The cytotoxicity of Cis/GOD@Bz-V was more than 4-folds higher against A549R compared to Cis@Bz-V cytotoxicity.

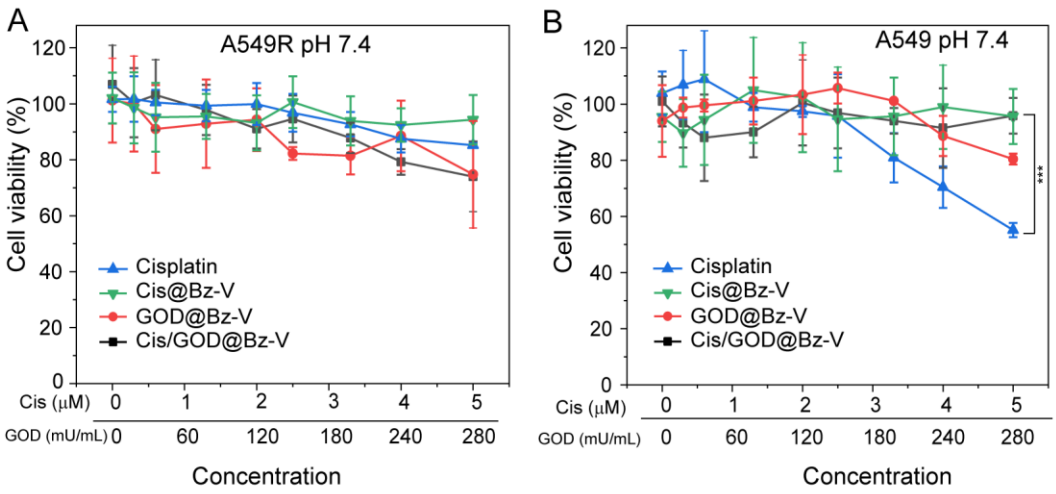

Figure 3. 7. Evaluation of *In vitro* cytotoxicity against A549R and A549 cell lines *via* MTT at pH 7.4. **(A)** A549R or **(B)** A549 cell line after treatment with various concentrations of free cisplatin, Cis@Bz-V, GOD@Bz-V or Cis/GOD@Bz-V for 48 h at pH 7.4. Results = mean ± SD, $n = 4$.

Moreover, at pH 7.4, except free cisplatin that showed normal cytotoxicity against A549 cell lines, other treatment formulations especially Cis@Bz-V, GOD@Bz-V, and Cis/GOD@Bz-V showed negligible cytotoxicity against A549R or A549 cell lines. The cell viability was still higher than 80% even at the highest cisplatin or GOD concentration of 5 μM or 280 mU/mL, respectively, which supported the predetermined pH controllable membrane permeability effect of PEG_{113}-*b*-P($BzMA_{120}$-*co*-$PEMA_{21}$) polymeric nanoreactor to initiate cytotoxic cascade reaction **(Figure 3.7)**.

Furthermore, the MTT results presented relatively low toxicity of empty PEG_{113}-*b*-P($BzMA_{120}$-*co*-$PEMA_{21}$) polymeric vesicles at high polymer concentration of 500 μg/mL at pH 7.8 or 6.8 against A549R cell line, which suggested the effective biocompatibility of the selected block copolymer to engineer the designed nanoreactors **(Figure 3.8)**.

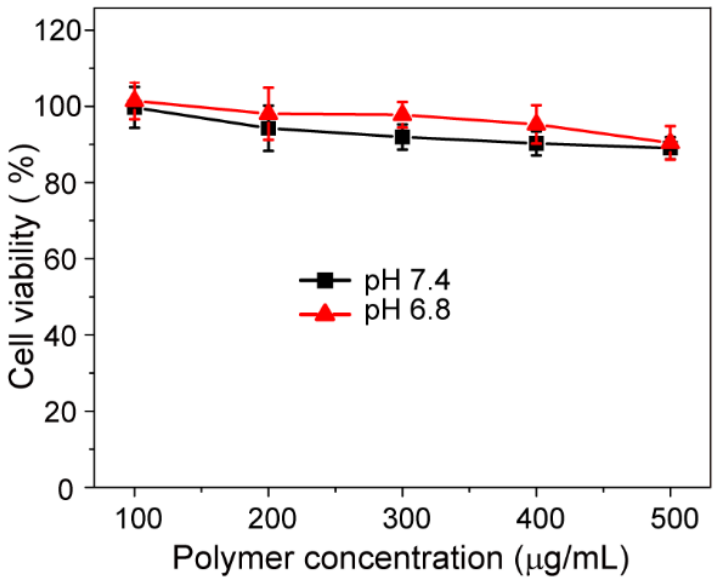

Figure 3. 8. Cell cytotoxicity evaluation of PEG_{113}-*b*-P($BzMA_{120}$-*co*-$PEMA_{21}$) polymer by against A549R cell line at pH 6.8 and 7.4 for 48 h. Results = mean ± SD, *n*

= 4.

Next, live/dead assay on A549R cells was further performed to stain live (green) and dead cells (red) by using fluorescein diacetate (FDA) and propidium iodide (PI), respectively. From the images presented in **Figure 3.6C**, it can be seen that few cells were PI-positive for free cisplatin treated group at pH 6.8 or pH 7.4. However, a moderate number of PI-positive cells can be observed for the Cis@Bz-V and GOD@Bz-V treated groups at pH 6.8. Obviously, it is remarked that Cis/GOD@Bz-V can induce much cytotoxicity as the treated cells are quantitatively PI positive at pH 6.8. On the other hand, negligible amount of PI positive cells that are comparable to PBS can be identified for the group treated with Cis@Bz-V, GOD@Bz-V, and Cis/GOD@Bz-V at pH 7.4. This test results are consistent with the observed cytotoxicity effects of free cisplatin, Cis@Bz-V, GOD@Bz-V, and Cis/GOD@Bz-V against A549R cell line at pH 6.8 or 7.4 according to MTT results.

3.3.3. Pt Cellular Uptake and Pt-DNA Adduct

To assess the involved mechanism to achieve the observed increased cytotoxicity of Cis/GOD@Bz-V against A549R or A549 cells, we first analyzed the cellular uptake of platinum and the content of Pt-DNA adducts by ICP-MS method after 4 h and 48 h incubation, respectively, with cisplatin, Cis@Bz-V or Cis/GOD@Bz-V at pH 6.8. In **Figure 3.9A**, it is remarkable that free cisplatin can be up-taken more than 2 times higher by A549 than A549R cells. This observation could be due to the fact it is well known that the copper transporter Ctr1 protein which plays an important role for cisplatin cellular uptake process is less expressed in cisplatin-resistant A549R cells than

in A549 cells, which could explain the observed impaired cellular uptake of free cisplatin by A549R cells.[38] Interestingly, the Cis@Bz-V or Cis/GOD@Bz-V treated groups showed much higher and analogous amount of internalized Pt into A549R or A549 cells, which was more than 3-folds, and 1.5-folds higher compared to that of free cisplatin treated A549R or A549 cells, respectively. This finding can likely be attributed to the change of cellular uptake pattern from copper transporter Ctr1-mediated pathway of free cisplatin to endocytosis pathway of nanoparticle such as Cis@Bz-V or Cis/GOD@Bz-V vesicles.[39] In line with the cellular uptake results, the analyzation of Pt-DNA adducts content by using Genomic DNA Mini Preparation Kit to extract DNA from the A549R cells after 48 h incubation with cisplatin, Cis@Bz-V or Cis/GOD@Bz-V.

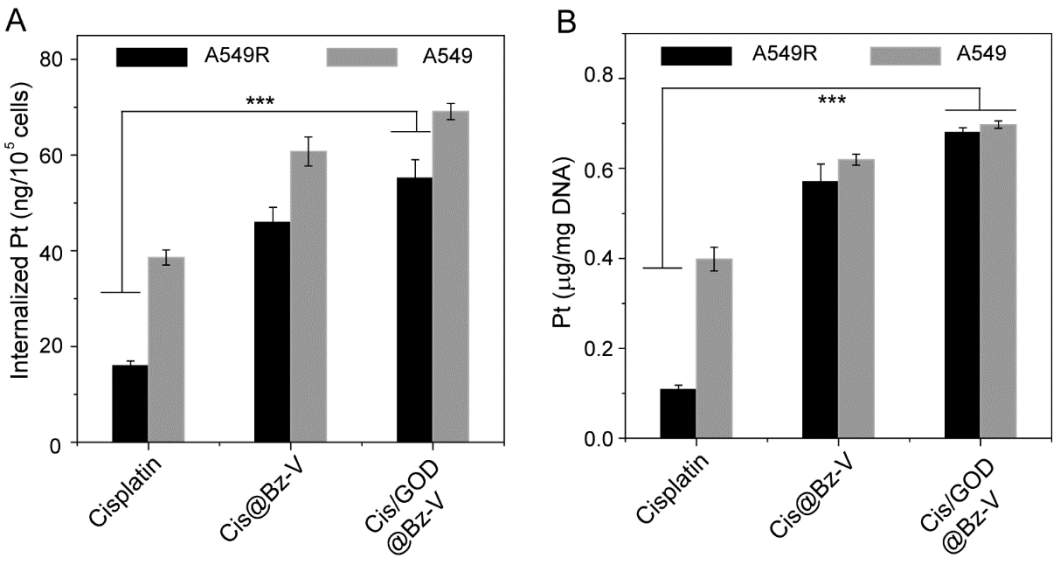

Figure 3. 9. Evaluation cellular platinum uptake and of DNA platination in A549R or A549 cell lines. **(A)** The platinum uptake measurements in A549R or A549 cell lines after 4 h treatment with cisplatin, Cis@Bz-V or Cis/GOD@Bz-V at pH 6.8 in the

presence of glucose (1 mg/mL) at the fixed platinum concentration of 1.5 μM. Results = mean ± SD, $n = 3$. **(B)** Evaluation of DNA platination in A549R or A549 cell lines after 48 h treatment with cisplatin, Cis@Bz-V, or Cis/GOD@Bz-V at pH 6.8 in the presence of glucose (1 mg/mL) at the fixed platinum concentration of 1.5 μM. Results = mean ± SD, $n = 3$. $^{**}p < 0.05$, $^{***}p < 0.01$(*t*-test).

Figure 3.9B showed that the incubation with Cis@Bz-V or Cis/GOD@Bz-V could raise the production of Pt-DNA adduct numbers more than 6 times and nearly 2 times higher compared to that of free cisplatin against A549R or A549 cells, respectively, which can be attributed to the observed increased cellular uptake of Cis@Bz-V or Cis/GOD@Bz-V by A549R or A549 cells. Therefore, the higher number of Pt-DNA adducts from Cis@Bz-V or Cis/GOD@Bz-V by A549R or A549 cells can reflect the more pronounced cisplatin induced DNA damage.[40]

3.3.4. *In Vitro* ROS, Caspase 3 Activity and Apoptosis

It is reported that cisplatin could induce ROS generation in cells, which can promote cellular oxidative stress to subsequently potentiate cisplatin-induced cell death through activation of intracellular pro-apoptotic pathways.[41]

To elucidate the possible mechanisms of Cis/GOD@Bz-V therapeutic nanoreactor to induce the observed higher toxicity in resistant cells of A549R at pH 6.8, we first analyzed intracellular ROS level as the key factor for higher cytotoxic parameter of Cis/GOD@Bz-V. From **Figure 3.10A**, Cis@Bz-V showed a slightly higher ROS fluorescence intensity compared to free cisplatin. In a sharp contrast, GOD@Bz-V or

Cis/GOD@Bz-V exhibited the strongest ROS fluorescence intensity. Quantitatively, flow cytometry results showed that Cis@Bz-V can generate nearly 2 and 1.5 times higher intracellular ROS level compared to the groups treated with PBS and free cisplatin, respectively. Apparently, the GOD@Bz-V and Cis/GOD@Bz-V-treated groups exhibited the highest and comparable generation of intracellular ROS that was more than 3 times higher than that of Cis@Bz-V **(Figure 3.10B-C)**. The dramatically increased intracellular ROS level was attributed to the activation of nanoreactor membrane at the tumor site where the confined GOD enzyme can catalyze the *in situ* generation of H_2O_2 in the presence of glucose and oxygen.[34]

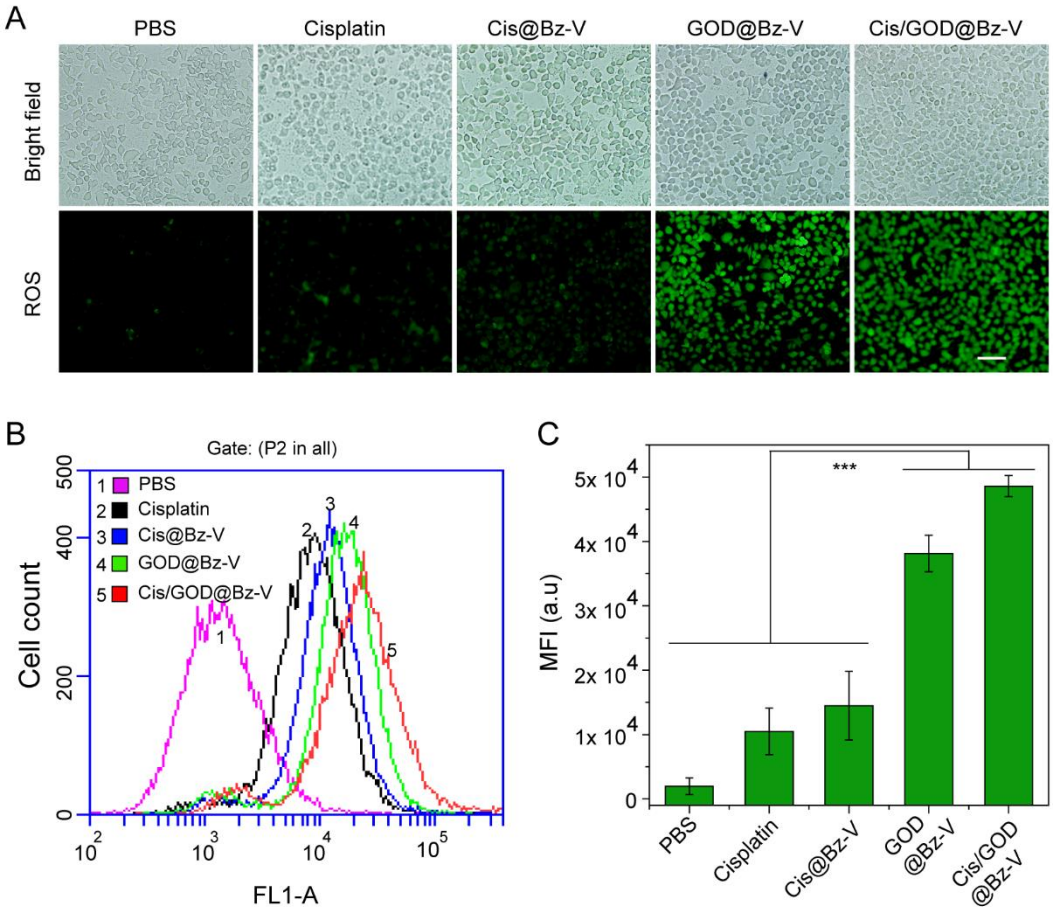

Figure 3. 10. Intracellular ROS level Evaluation. **(A)** *In vitro* evaluation of intracellular

ROS fluorescence intensity in A549R cells after treatments with PBS, free cisplatin, Cis@Bz-V, GOD@Bz-V, or Cis/GOD@Bz-V at the equivalent cisplatin concentration of 1.5 μM or with equivalent GOD concentration of 91.4 mU/mL in the presence of glucose (1 mg/mL) at pH 6.8 for 24 h. Scale bar = 20 μm **(B)** Flow cytometer evaluation of intracellular ROS fluorescence intensity level in A549R cells after treatments with PBS, free cisplatin, Cis@Bz-V, GOD@Bz-V, or Cis/GOD@Bz-V and **(C)** their corresponding mean fluorescence intensity (MFI) at the equivalent cisplatin concentration of 1.5 μM or with equivalent GOD concentration of 91.4 mU/mL for 24 h in the presence of glucose (1 mg/mL) at pH 6.8. Results = mean ± SD, n = 3.

Next, caspase-3 activity in A549R and A549 cells was measured after different treatments at pH 6.8. From **Figure 3.11A**, though there was no significant difference by treatment with free cisplatin, treatment with Cis@Bz-V showed two-fold increase of the caspase 3 activity in both A549R and A549 cells compared to PBS. Interestingly, incubation with GOD@Bz-V exhibited 2 times higher activation of caspase 3 activity compared to that of Cis@Bz-V, but slightly lower than that of Cis/GOD@Bz-V in both A549R and A549 cells. This high caspase 3 activation by Cis/GOD@Bz-V can be attributed to the observed high generation of cytotoxic intracellular ROS level.

It is well-known that caspase 3 is a key mediator of apoptosis in mammalian cells.[42] Next, we monitored the apoptosis rate by incubation of A549R cell line with PBS, free cisplatin, Cis@Bz-V, GOD@Bz-V, or Cis/GOD@Bz-V. According to the results presented in **Figure 3.11B-C**, treatment with Cis/GOD@Bz-V can induce 26.44% of apoptotic cells that is more than 1.6-fold higher than that of Cis@Bz-V and

GOD@Bz-V and more than 8 times higher than that of free cisplatin against A549R cell at pH 6.8. Therefore, the combined cytotoxic effect of cisplatin *via* DNA damage and the well-known GOD cell killing mechanism especially by activation of cellular oxidative stress and depletion of glucose for cell starvation can achieve the enhanced cytotoxic effect of Cis/GOD@Bz-V against A549R cell.[43-45] More importantly, the *in vitro* results of this study suggested that intracellular ROS generation can play a key role to increase chemo-sensitivity of cisplatin against A549R cells and overcome cisplatin drug resistance mainly through activation of cellular pro-apoptotic pathways such as caspase 3 and induce cellular apoptosis.[46]

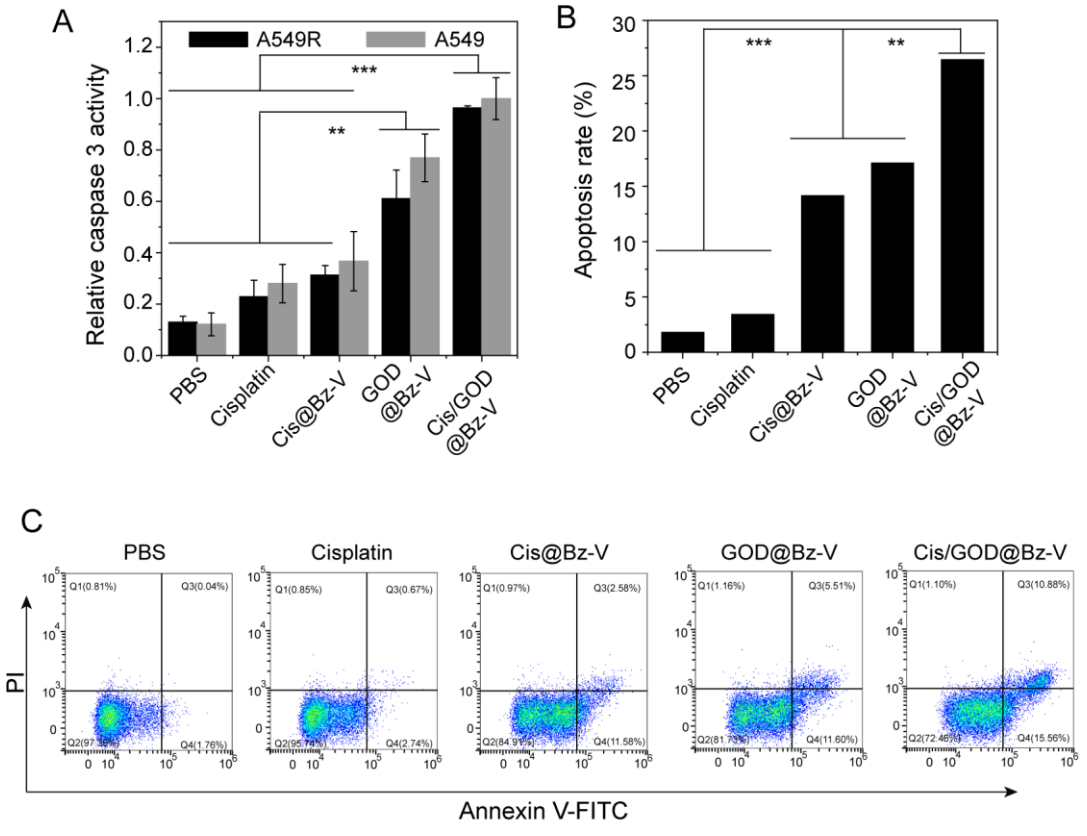

Figure 3. 11. Caspase-3 activity and apoptosis evaluation. **(A)** Caspase-3 activity

evaluation in A549R or A549 cell lines after incubation with PBS, free cisplatin, Cis@Bz-V, GOD@Bz-V, or Cis/GOD@Bz-V at the equivalent cisplatin concentration of 1.5 μM or with equivalent GOD concentration of 91.4 mU/mL for 12 h in the presence of glucose (1 mg/mL) at pH 6.8. Results = mean ± SD, n = 3. **(B** and **C)** Apoptosis rate quantification in A549R cells after treatments with PBS, free cisplatin, Cis@Bz-V, GOD@Bz-V, or Cis/GOD@Bz-V at the equivalent cisplatin concentration of 1.5 μM or with equivalent GOD concentration of 91.4 mU/mL for 24 h in the presence of glucose (1 mg/mL) at pH 6.8. $^{**}p < 0.05$, $^{***}p < 0.01$(*t*-test).

3.3.5. *In Vivo* Antitumor Efficacy against Cisplatin-Resistant Lung Tumor

To study the *in vivo* biodistribution and ROS generation level in tumor tissues, antitumor efficacy of Cis/GOD@Bz-V, six weeks old BALB/c mice bearing 4T1 tumor models with the tumor size of about 50 mm^3 were established. Firstly, Cis/GOD@Bz-V solution was intravenously injected into 4T1 tumor-bearing mice and observed by IVIS at predetermined time intervals.

As shown in **Figure 3.12A-B**, the vesicles can efficiently accumulate at the tumor sites after 24 h post injection. Next, the tumoral ROS level was monitored by DCFH-DA staining method after intravenously injection of PBS, cisplatin, Cis@Bz-V, GOD@Bz-V or Cis/GOD@Bz-V at the cisplatin and GOD concentration of 3 mg/Kg and 2.39 U/kg, respectively. From **Figure 3.12C-D,** the Cis/GOD@Bz-V group obviously showed the strongest tumor fluorescence intensity compared to cisplatin (by 5.34 times), Cis@Bz-V (by 2.79 times), or GOD@Bz-V (by 1.14 times), which was consistent with the cellular ROS generation results from *in vitro* experiments.

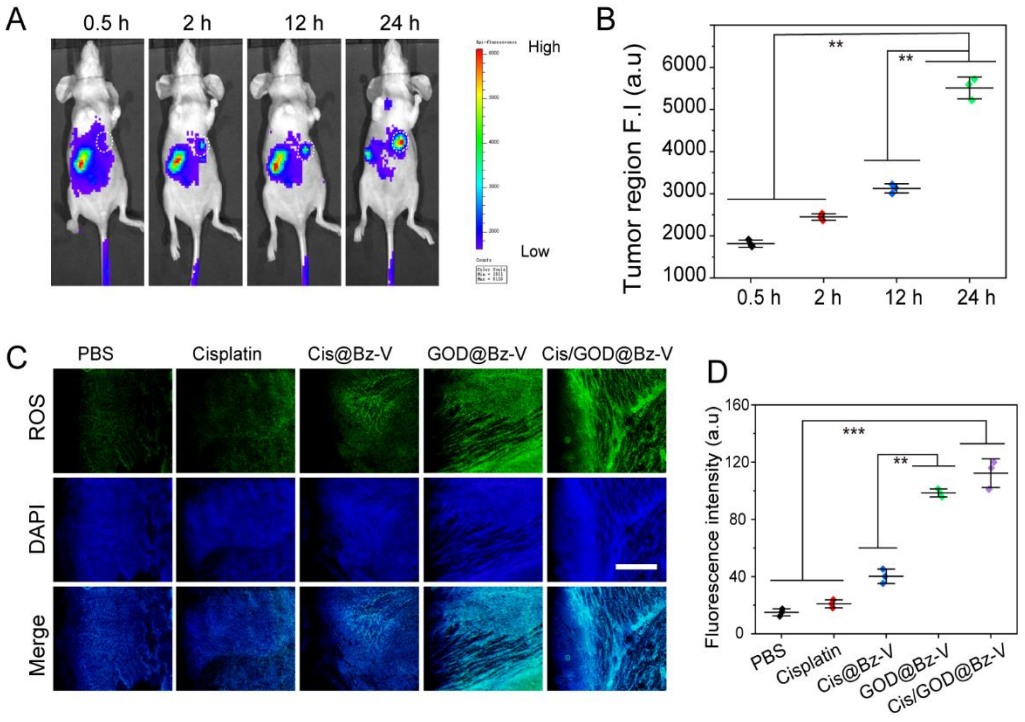

Figure 3. 12. *In vivo* nanoreactor biodistribution and Intratumor ROS level evaluation. **(A)** *In vivo* biodistribution of the nanoreactor at various time point post intravenous injection of PEG-*b*-P(BzMA-*co*-PEMA) vesicles loading both cisplatin and cypate-labeled GOD. **(B)** Time dependent quantification of cypate-GOD fluorescence intensity post intravenous injection of PEG-*b*-P(BzMA-*co*-PEMA) vesicles loading both cisplatin and cypate-labeled GOD at the tumor site (marked by white broken line cycle). **(C)** and **(D)** Fluorescent images for evaluation of intratumor ROS distribution in tumor tissues and their corresponding fluorescence intensity analyzed by ImageJ software, respectively, for different groups treated with PBS, free cisplatin, Cis@Bz-V, GOD@Bz-V, or Cis/GOD@Bz-V. The staining probe DCFH-DA was intratumorally injected at dose of 10 μM/kg and at 24 h post-injection. Results = mean ± SD, $n = 3$. $^{**}p < 0.05$, $^{***}p < 0.01$(*t*-test). Scale bar = 200μm.

This result suggested that Cis/GOD@Bz-V nanoreactors can effectively be accumulated at the tumor site *via* enhanced permeability and retention (EPR) effect.[47] Next, to evaluate the tumor growth suppression, 25 BALB/c nude mice bearing A549R tumor models were randomly divided into 5 groups and intravenously injected with PBS, cisplatin, Cis@Bz-V, GOD@Bz-V or Cis/GOD@Bz-V at cisplatin-equivalent dose of 3 mg/kg and GOD of 2.39 U/kg. From **Figure 3.13A-B**, treatment with free cisplatin could not inhibit the tumor growth with tumor size increased to 3.26 times of original at day 21 post-treatment possibly owing to the impaired cisplatin accumulation at the tumor site and the resistant properties of the A549R tumors.

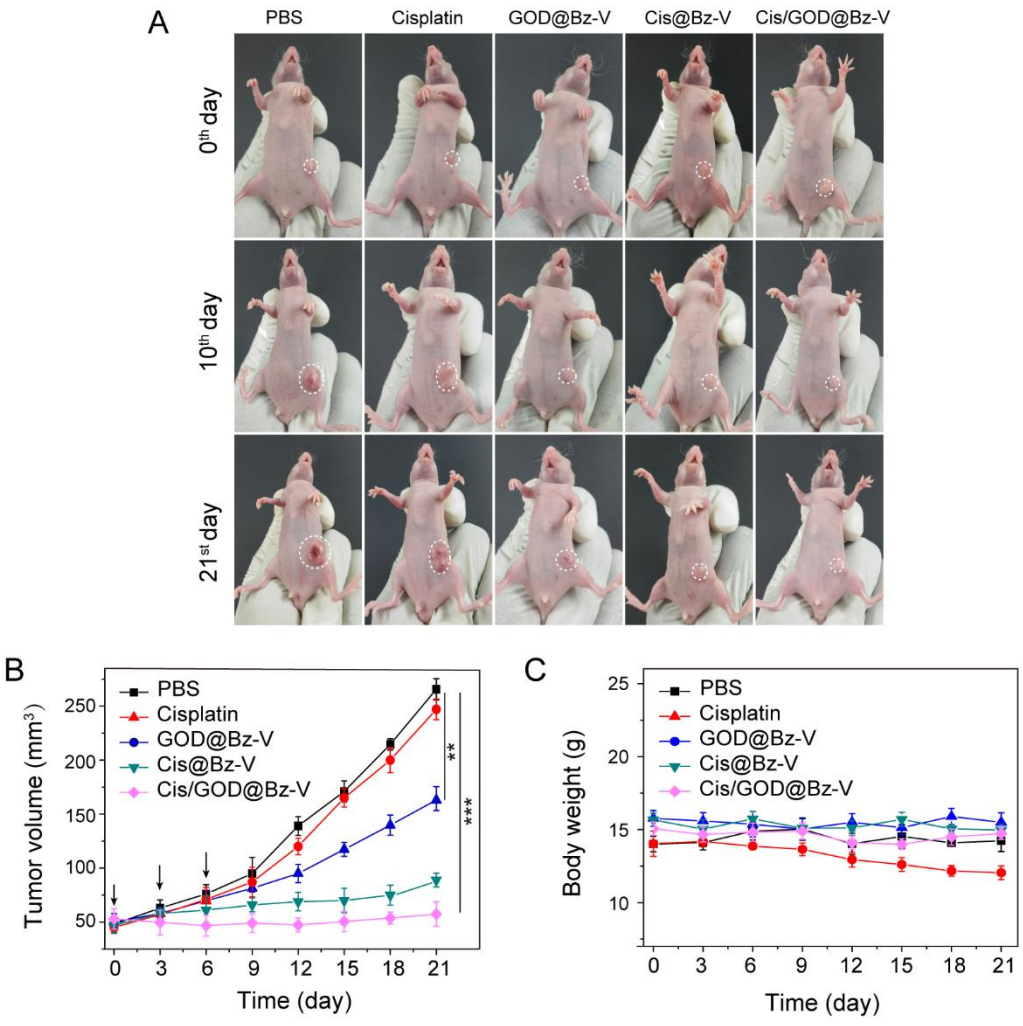

Figure 3. 13. Tumor growth profile and mice body change monitoring during treatment. Anti-tumor efficacy evaluation against A549R tumors after intravenous injection of PBS, free cisplatin, Cis@Bz-V, GOD@Bz-V, or Cis/GOD@Bz-V at the cisplatin equivalent dose of 3 mg/kg or GOD-equivalent dose of 2.39 U/kg. **(A)** Representative digital images of A549R tumor bearing BALBC/c nude mice at various time points after being treated with different formulations. **(B)** Time dependent A549R tumor growth profile. The injection time is shown by arrows. Results = mean ± SD, n = 5. **(C)** Time dependent mice body weight change monitoring during treatment. Results = mean ± SD, n = 5.

Moreover, GOD@Bz-V exhibited weak tumor growth suppression possibly due to the complex surviving strategies adapted by A549R resistant cells.[48] Interestingly, the Cis@Bz-V-treated group showed remarkable growth inhibition ability with the slight tumor volume increase likely owing to the enhanced Pt tumor cells as observed from *in vitro* cellular Pt uptake experiment. Significantly, Cis/GOD@Bz-V demonstrated efficient potentials to suppress tumor growth with no tumor size increment up to 21st day of treatment. In addition, the mice body weight change was also recorded during the treatment process **(Figure 3.13C)**. After three intravenous injection of free cisplatin, the body weight displayed a significant decrease, which was likely due to the toxic side effect caused by cisplatin. However, no obvious mice body weight loss was observed with the Cis/GOD@Bz-V treated group, suggesting that there was no systemic toxicity. Moreover, the main organs (heart, liver, spleen, lung, and kidney) and tumors were collected for H&E staining at the end of the treatment.

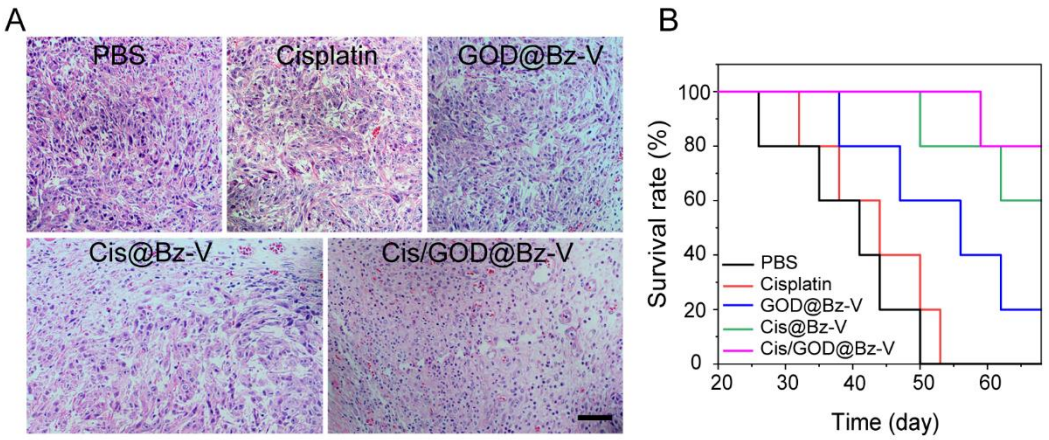

Figure 3. 14. (A) H&E staining of tumor tissues after treatments. Scale bar = 100 μm. **(B)** Survival rate profile during treatment $^{**}p < 0.05$, $^{***}p < 0.01$(*t*-test).

From **Figure 3.14A**, the tumor tissue of the group treated with Cis/GOD@Bz-V showed severe damage compared to other treatments groups. Intriguingly, treatment with Cis/GOD@Bz-V showed remarkably improved and increased survival rate compared to other groups **(Figure 3.14B)**. Furthermore, except the observed kidney tissue damage for the cisplatin-treated group, there was no other tissue damage observed for other treatments formulation **(Figure 3.15)**, which indicated the best therapeutic efficiency of Cis/GOD@Bz-V against A549R tumors without obvious adverse side effects.

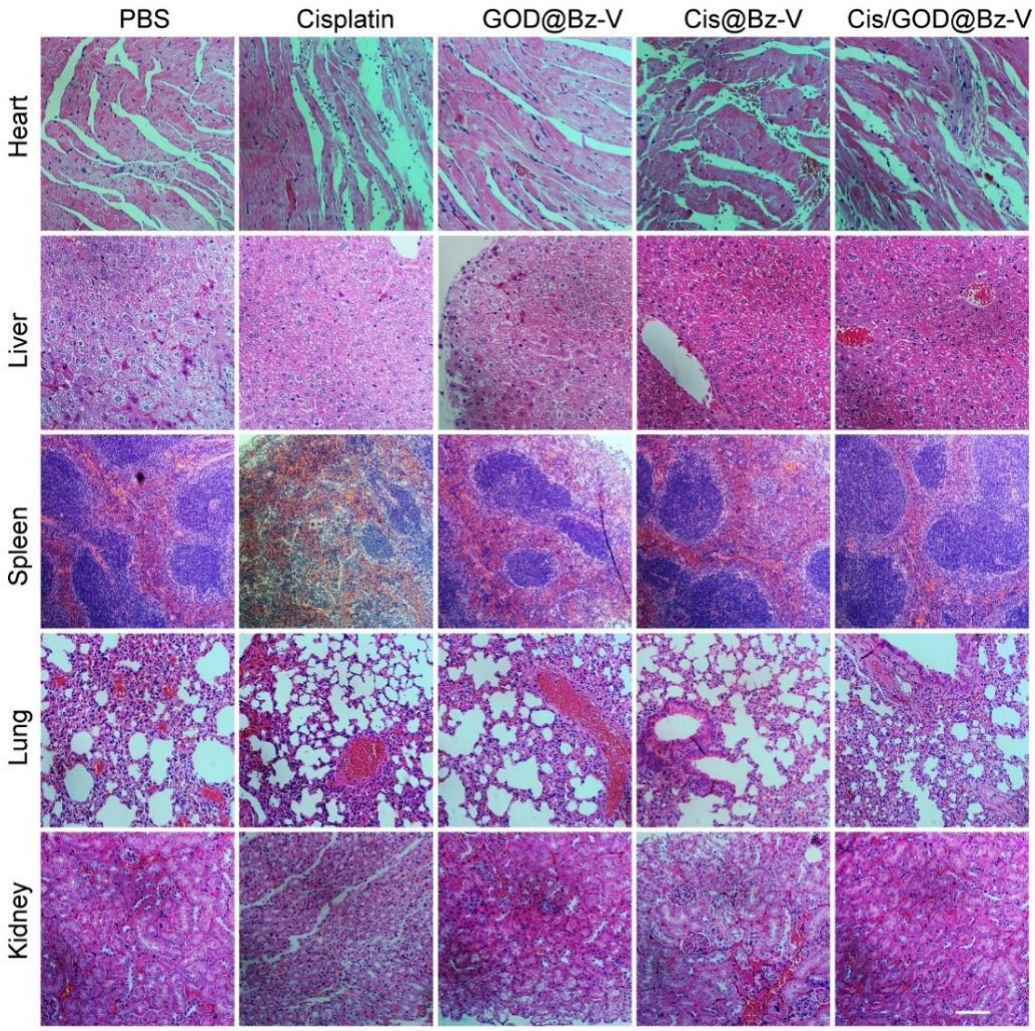

Figure 3. 15. Post-treatment H&E staining of heart, liver, spleen, lung, and kidney organs for the groups treated with PBS, free cisplatin, Cis@Bz-V, GOD@Bz-V or Cis/GOD@Bz-V formulation. Scale bar = 100 μm.

3.4. Conclusion

In summary, we have synthesized a diblock polymer PEG-*b*-P(BzMA-*co*-PEMA) and self-assembled into vesicles which were used to build a vesicular nanoreactor that

can coload deliver both GOD and cisplatin (Cis/GOD@Bz-V). The rationally designed tumor specific Cis/GOD@Bz-V nanoreactors showed exciting feasibility to enhance platinum cellular uptake *via* endocytotic pathway. Moreover, the subsequent generation of high amount of intracellular ROS showed remarkably improved cisplatin chemo-sensitivity against cisplatin-resistant A549R cells through activation of pro-apoptotic cellular pathways such as enhanced expression of caspase 3. Finally, Cis/GOD@Bz-V nanoreactors showed potential ability to inhibit drug resistant A549R tumor growth effectively without observable side effects. Therefore, the systematic exploitation of ROS as cellular oxidative stress precursor displays great potentials to enhance cisplatin therapeutic efficacy even in drug-resistant lung cancers.

3.5. Reference

[1] D.A. Fennell, Y. Summers, J. Cadranel, T. Benepal, D.C. Christoph, R. Lal, M. Das, F. Maxwell, C. Visseren-Grul, D. Ferry, Cisplatin in the modern era: The backbone of first-line chemotherapy for non-small cell lung cancer, Cancer Treatment Reviews, 44 (2016) 42-50.

[2] T.C. Johnstone, K. Suntharalingam, S.J. Lippard, The Next Generation of Platinum Drugs: Targeted Pt(II) Agents, Nanoparticle Delivery, and Pt(IV) Prodrugs, Chemical Reviews, 116 (2016) 3436-3486.

[3] L. Galluzzi, L. Senovilla, I. Vitale, J. Michels, I. Martins, O. Kepp, M. Castedo, G. Kroemer, Molecular mechanisms of cisplatin resistance, Oncogene, 31 (2011) 1869.

[4] A.M. Breglio, A.E. Rusheen, E.D. Shide, K.A. Fernandez, K.K. Spielbauer, K.M. McLachlin, M.D. Hall, L. Amable, L.L. Cunningham, Cisplatin is retained in the cochlea indefinitely following chemotherapy, Nature Communications, 8 (2017) 1654.

[5] S. Manohar, N. Leung, Cisplatin nephrotoxicity: a review of the literature, Journal of Nephrology, 31 (2018) 15-25.

[6] A. Yimit, O. Adebali, A. Sancar, Y. Jiang, Differential damage and repair of DNA-adducts induced by anti-cancer drug cisplatin across mouse organs, Nature Communications, 10 (2019) 1-11.

[7] L. Duan, R.E. Perez, P.D. Chastain, M.T. Mathew, D.R. Bijukumar, C.G. Maki, JMJD2 promotes acquired cisplatin resistance in non-small cell lung carcinoma cells, Oncogene, 38 (2019) 5643-5657.

[8] C. Nie, X. Qin, X. Li, B. Tian, Y. Zhao, Y. Jin, Y. Li, Q. Wang, D. Zeng, A. Hong, X. Chen, CACNA2D3 Enhances the Chemosensitivity of Esophageal Squamous Cell Carcinoma to Cisplatin via Inducing Ca2+-Mediated Apoptosis and Suppressing PI3K/Akt Pathways, Frontiers in Oncology, 9 (2019) 1-12.

[9] M. Nikolaou, A. Pavlopoulou, A.G. Georgakilas, E. Kyrodimos, The challenge of drug resistance in cancer treatment: a current overview, Clinical & Experimental Metastasis, 35 (2018) 309-318.

[10] I. Dagogo-Jack, A.T. Shaw, Tumour heterogeneity and resistance to cancer therapies, Nature Reviews Clinical Oncology, 15 (2017) 81.

[11] L. Amable, Cisplatin resistance and opportunities for precision medicine, Pharmacological Research, 106 (2016) 27-36.

[12] Z.H. Siddik, Cisplatin: mode of cytotoxic action and molecular basis of resistance, Oncogene, 22 (2003) 7265-7279.

[13] D.-W. Shen, L.M. Pouliot, M.D. Hall, M.M. Gottesman, Cisplatin resistance: a cellular self-defense mechanism resulting from multiple epigenetic and genetic changes, Pharmacol Rev, 64 (2012) 706-721.

[14] Y. Han, W. Yin, J. Li, H. Zhao, Z. Zha, W. Ke, Y. Wang, C. He, Z. Ge, Intracellular glutathione-depleting polymeric micelles for cisplatin prodrug delivery to overcome cisplatin resistance of cancers, Journal of Controlled Release, 273 (2018) 30-39.

[15] Y. Li, Y. Deng, X. Tian, H. Ke, M. Guo, A. Zhu, T. Yang, Z. Guo, Z. Ge, X. Yang, H. Chen, Multipronged Design of Light-Triggered Nanoparticles To Overcome Cisplatin Resistance for Efficient Ablation of Resistant Tumor, ACS Nano, 9 (2015) 9626-9637.

[16] J. Xu, Y. Kuang, R. Lv, P. Yang, C. Li, H. Bi, B. Liu, D. Yang, Y. Dai, S. Gai, F. He, B. Xing, J. Lin, Charge convertibility and near infrared photon co-enhanced cisplatin chemotherapy based on upconversion nanoplatform, Biomaterials, 130 (2017) 42-55.

[17] R. Zhang, X. Song, C. Liang, X. Yi, G. Song, Y. Chao, Y. Yang, K. Yang, L. Feng, Z. Liu, Catalase-loaded cisplatin-prodrug-constructed liposomes to overcome tumor hypoxia for enhanced chemo-radiotherapy of cancer, Biomaterials, 138 (2017) 13-21.

[18] P.a. Ma, H. Xiao, C. Yu, J. Liu, Z. Cheng, H. Song, X. Zhang, C. Li, J. Wang, Z. Gu, J. Lin, Enhanced Cisplatin Chemotherapy by Iron Oxide Nanocarrier-Mediated Generation of Highly Toxic Reactive Oxygen Species, Nano Letters, 17 (2017) 928-937.

[19] M.V. Babak, Y. Zhi, B. Czarny, T.B. Toh, L. Hooi, E.K.-H. Chow, W.H. Ang, D. Gibson, G. Pastorin, Dual-Targeting Dual-Action Platinum(IV) Platform for Enhanced

Anticancer Activity and Reduced Nephrotoxicity, Angewandte Chemie, 131 (2019) 8193-8198.

[20] Y. Zhang, Z. Liu, B.D. Thackray, Z. Bao, X. Yin, F. Shi, J. Wu, J. Ye, W. Di, Intraoperative Raman-Guided Chemo-Photothermal Synergistic Therapy of Advanced Disseminated Ovarian Cancers, Small, 14 (2018) 1801022.

[21] Y.-M. Choi, H.-K. Kim, W. Shim, M.A. Anwar, J.-W. Kwon, H.-K. Kwon, H.J. Kim, H. Jeong, H.M. Kim, D. Hwang, H.S. Kim, S. Choi, Mechanism of Cisplatin-Induced Cytotoxicity Is Correlated to Impaired Metabolism Due to Mitochondrial ROS Generation, PLOS ONE, 10 (2015) e0135083.

[22] H.-L. Huang, L.-W. Fang, S.-P. Lu, C.-K. Chou, T.-Y. Luh, M.-Z. Lai, DNA-damaging reagents induce apoptosis through reactive oxygen species-dependent Fas aggregation, Oncogene, 22 (2003) 8168-8177.

[23] M. Berndtsson, M. Hägg, T. Panaretakis, A.M. Havelka, M.C. Shoshan, S. Linder, Acute apoptosis by cisplatin requires induction of reactive oxygen species but is not associated with damage to nuclear DNA, International Journal of Cancer, 120 (2007) 175-180.

[24] A.S. Nerush, K.M. Shchukina, I.V. Balalaeva, A.G. Orlova, Hydrogen peroxide in the reactions of cancer cells to cisplatin, Biochimica et Biophysica Acta (BBA) - General Subjects, 1863 (2019) 692-702.

[25] R.K. Khurana, A. Jain, A. Jain, T. Sharma, B. Singh, P. Kesharwani, Administration of antioxidants in cancer: debate of the decade, Drug Discovery Today, 23 (2018) 763-770.

[26] N. Li, C. Sun, B. Zhou, H. Xing, D. Ma, G. Chen, D. Weng, Low Concentration of Quercetin Antagonizes the Cytotoxic Effects of Anti-Neoplastic Drugs in Ovarian Cancer, PLOS ONE, 9 (2014) e100314.

[27] M. Gosland, B. Lum, J. Schimmelpfennig, J. Baker, M. Doukas, Insights into Mechanisms of Cisplatin Resistance and Potential for Its Clinical Reversal, Pharmacotherapy: The Journal of Human Pharmacology and Drug Therapy, 16 (1996) 16-39.

[28] G. He, G. He, R. Zhou, Z. Pi, T. Zhu, L. Jiang, Y. Xie, Enhancement of cisplatin-induced colon cancer cells apoptosis by shikonin, a natural inducer of ROS in vitro and in vivo, Biochemical and Biophysical Research Communications, 469 (2016) 1075-1082.

[29] V.N. Ayyagari, T.-h.J. Hsieh, P.L. Diaz-Sylvester, L. Brard, Evaluation of the cytotoxicity of the Bithionol - cisplatin combination in a panel of human ovarian cancer cell lines, BMC Cancer, 17 (2017) 1-15.

[30] X. Wang, F. Zhang, X.-R. Wu, Inhibition of Pyruvate Kinase M2 Markedly Reduces Chemoresistance of Advanced Bladder Cancer to Cisplatin, Scientific Reports, 7 (2017) 45983.

[31] Q. Wang, X.-l. Zheng, L. Yang, F. Shi, L.-b. Gao, Y.-j. Zhong, H. Sun, F. He, Y. Lin, X. Wang, Reactive oxygen species-mediated apoptosis contributes to chemosensitization effect of saikosaponins on cisplatin-induced cytotoxicity in cancer cells, Journal of Experimental & Clinical Cancer Research, 29 (2010) 1-8.

[32] L.-H. Fu, C. Qi, J. Lin, P. Huang, Catalytic chemistry of glucose oxidase in cancer diagnosis and treatment, Chemical Society Reviews, 47 (2018) 6454-6472.

[33] J. Li, Y. Li, Y. Wang, W. Ke, W. Chen, W. Wang, Z. Ge, Polymer Prodrug-Based Nanoreactors Activated by Tumor Acidity for Orchestrated Oxidation/Chemotherapy, Nano Letters, 17 (2017) 6983-6990.

[34] J. Li, A. Dirisala, Z. Ge, Y. Wang, W. Yin, W. Ke, K. Toh, J. Xie, Y. Matsumoto, Y. Anraku, K. Osada, K. Kataoka, Therapeutic Vesicular Nanoreactors with Tumor-Specific Activation and Self-Destruction for Synergistic Tumor Ablation, Angewandte Chemie International Edition, 56 (2017) 14025-14030.

[35] K. Zhou, Y. Wang, X. Huang, K. Luby-Phelps, B.D. Sumer, J. Gao, Tunable, Ultrasensitive pH-Responsive Nanoparticles Targeting Specific Endocytic Organelles in Living Cells, Angewandte Chemie, 123 (2011) 6233-6238.

[36] J.F. Mukerabigwi, W. Yin, Z. Zha, W. Ke, Y. Wang, W. Chen, A.A.-W.M.M. Japir, Y. Wang, Z. Ge, Polymersome nanoreactors with tumor pH-triggered selective membrane permeability for prodrug delivery, activation, and combined oxidation-chemotherapy, Journal of Controlled Release, 303 (2019) 209-222.

[37] N.D. Eljack, H.-Y.M. Ma, J. Drucker, C. Shen, T.W. Hambley, E.J. New, T. Friedrich, R.J. Clarke, Mechanisms of cell uptake and toxicity of the anticancer drug cisplatin, Metallomics, 6 (2014) 2126-2133.

[38] Y. Min, C.-Q. Mao, S. Chen, G. Ma, J. Wang, Y. Liu, Combating the Drug Resistance of Cisplatin Using a Platinum Prodrug Based Delivery System, Angewandte Chemie International Edition, 51 (2012) 6742-6747.

[39] F. Arnesano, M.I. Nardella, G. Natile, Platinum drugs, copper transporters and copper chelators, Coordination Chemistry Reviews, 374 (2018) 254-260.

[40] C.W. Fong, Platinum anti-cancer drugs: Free radical mechanism of Pt-DNA adduct formation and anti-neoplastic effect, Free Radical Biology and Medicine, 95 (2016) 216-229.

[41] A. Brozovic, A. Ambriović-Ristov, M. Osmak, The relationship between cisplatin-induced reactive oxygen species, glutathione, and BCL-2 and resistance to cisplatin, Critical Reviews in Toxicology, 40 (2010) 347-359.

[42] C. Blanc, Q.L. Deveraux, S. Krajewski, R.U. Jänicke, A.G. Porter, J.C. Reed, R. Jaggi, A. Marti, Caspase-3 Is Essential for Procaspase-9 Processing and Cisplatin-induced Apoptosis of MCF-7 Breast Cancer Cells, Cancer Research, 60 (2000) 4386-4390.

[43] W. Fan, N. Lu, P. Huang, Y. Liu, Z. Yang, S. Wang, G. Yu, Y. Liu, J. Hu, Q. He, J. Qu, T. Wang, X. Chen, Glucose-Responsive Sequential Generation of Hydrogen Peroxide and Nitric Oxide for Synergistic Cancer Starving-Like/Gas Therapy, Angewandte Chemie International Edition, 56 (2017) 1229-1233.

[44] W. Ke, J. Li, F. Mohammed, Y. Wang, K. Tou, X. Liu, P. Wen, H. Kinoh, Y. Anraku, H. Chen, K. Kataoka, Z. Ge, Therapeutic Polymersome Nanoreactors with Tumor-Specific Activable Cascade Reactions for Cooperative Cancer Therapy, ACS Nano, 13 (2019) 2357-2369.

[45] J.F. Mukerabigwi, Z. Ge, K. Kataoka, Therapeutic Nanoreactors as In Vivo Nanoplatforms for Cancer Therapy, Chemistry – A European Journal, 24 (2018) 15706-15724.

[46] M.A. Fuertes, C. Alonso, J.M. Pérez, Biochemical Modulation of Cisplatin Mechanisms of Action: Enhancement of Antitumor Activity and Circumvention of Drug Resistance, Chemical Reviews, 103 (2003) 645-662.

[47] A.K. Iyer, G. Khaled, J. Fang, H. Maeda, Exploiting the enhanced permeability and retention effect for tumor targeting, Drug Discovery Today, 11 (2006) 812-818.

[48] L.K. Boroughs, R.J. DeBerardinis, Metabolic pathways promoting cancer cell survival and growth, Nature Cell Biology, 17 (2015) 351–359.

Chapter IV: Mitochondria Targeting Polymer Prodrug Nanoparticles to Overcome Multi-Drug Resistance Through Orchestrated Mitochondrial Oxidative Stress Amplification and DNA Damage

4.1. Introduction

Multidrug resistance (MDR) is one of the major threats that hinder chemotherapy success and often promote treatment poor prognosis over a wide range of cancer types.[1] It has been known for many decades that the overexpression of drug efflux pump transporters such as ATP-binding cassette (ABC) transporters is often linked to the enhanced anticancer drug efflux and causing chemotherapy failure. For example, the p-glycoproteins as one of ABC transporters, is the most extensively studied and identified as the major hall mark predominately responsible for most MDR against a wide array of anticancer drugs.[2, 3]

Nevertheless, despite continuous significant effort devoted for overcoming MDR through the inhibition and overruling multidrug transporters, the success has been little in cancer treatment.[4, 5] Fortunately, with the emerging of nanotechnology into cancer treatment, several reports suggested that nanoparticles can overcome the efflux pump mediated MDR mostly due to their distinctive cellular penetration mechanisms such as endocytosis compared to small molecular drug counterparts.[6, 7] However, it should be mentioned that cancer cells can inherently adapt altered metabolisms mostly driven by mitochondria signal transduction pathways thriving to survive under various stress even in the presence of nanoparticle treatment.

Mitochondria is semi-autonomous organelle that plays critical roles in physiology and pathology of eukaryotic cells.[8] At the cellular level, it is well known that mitochondria dynamically function as cellular central unit for energy production, programmed cell death, and regulation of several metabolic pathways including oxidative stress. Particularly in cancer cells, several studies demonstrated that the increased mitochondria dysfunction dramatically induces the overproduction of reactive oxygen species (ROS) that is around ten times higher compared to normal cells. Interestingly, although there is overexpression of ROS for cancer cell initiation and progression due to their unique adapted metabolic pathways, emerging researches widely proved that the excess ROS production can paradoxically induce cytotoxicity to cells through oxidative stress leading to apoptosis and necrosis.[9] This ROS overexpression in cancer cells has been receiving an intense focus by many researchers to develop various novel and effective treatment modalities against cancer.[10, 11]

In fact, altered metabolic pathways and redox aberrant are considered as the main causes for accentuated survival mechanisms of malignant cells to sustain proliferation, angiogenesis, and metastasis in the presence or absence of therapies.[12-14] As such, extensive studies revealed that although mitochondria are not the sole contributor to MDR of cancer cells, their potential role and versatile regulation of metabolic activities are contemplated to be the central causes that substantially promote the alteration of malignant cell phenotype leading to mitigated cell response to therapy.[15-18] Therefore, considering the correlation between mitochondria metabolic activities and the adaptation of drug resistant for cancer cells, we hypothesize that targeting mitochondria should be an effective approach to diverse the MDR and achieve an enhanced cancer treatment effect.

In light of well-defined distinctive features of mitochondria such as unique metabolic activities, the transmembrane potential ($\Delta\psi_m$), and possessing their own DNA sequence (mtDNA) compared to other organelles, various approaches to selectively deliver bioactive molecules to mitochondria have been reported.[19-21] Among them, the application of lipophilic cations such as tetraphenylphosphonium (TPP) can exclusively target and accumulate into mitochondria in proportion to electrochemical gradient compared to others organelles in the cytosol and mitochondria trans-membranes potential ($\Delta\psi_m$), respectively.[22]

Cinnamaldehyde is a bioactive compound that is commonly used in food industry as a flavor and additive agents. It has also been used as traditional medicine to treat several diseases caused by inflammation.[23] In addition, plenty of studies showed that cinnamaldehyde possess anticancer activities mainly through *in situ* amplification of mitochondria ROS production and alteration of mitochondria transduction pathways such as altered mitochondrial permeability transition leading the release of cytochrome *c* in the cytosol and induce apoptosis.[24, 25]

Nevertheless, the relatively short half-life of cinnamaldehyde especially during systemic circulation hindered its application for targeted delivery. To overcome this, the research group of Lee and colleagues developed a strategy to deliver cinnamaldehyde as a prodrug with promising cancer cell killing effect through the amplification of intracellular oxidative stress.[26, 27] More recently, Chen and coworkers reported a polymer conjugate comprising cinnamaldehyde moiety that can be used to induce amplified oxidative stress and boost antitumor immunity with promising therapeutic efficiency.[28]

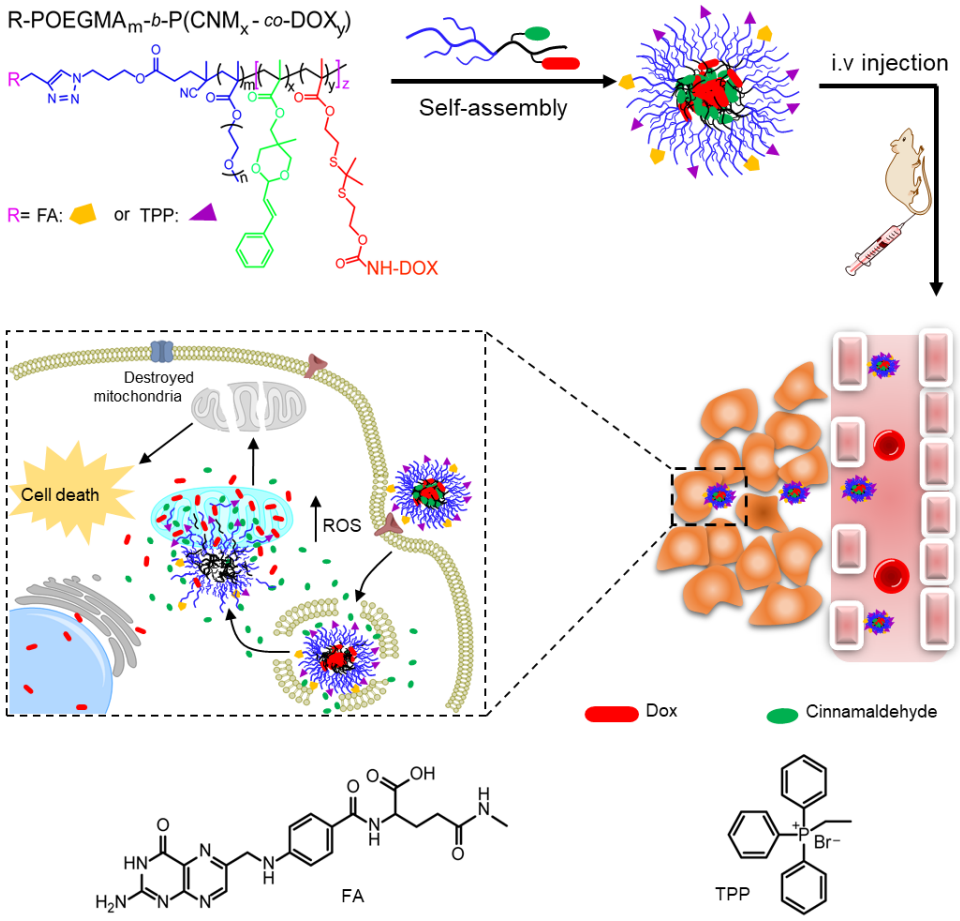

Figure 4. 1. Schematic representation of FA&TPP-PEOGMA$_m$-*b*-P(CNM$_x$-co-DOX$_y$) diblock copolymer used to prepare PCD micelle nanoparticles and their proposed mechanism of action to overcome multidrug resistance of a cancer cell.

Once PCD nanoparticles are accumulated into the cancer cell, the endosomal pH can induce the release of cinnamaldehyde (CNM) that can stimulate the mitochondria for overproduction of cytotoxic superfluous amount of ROS in the cell. Subsequently, this excessive ROS generation can induce the release of doxorubicin (DOX) in the mitochondria *via* cleavage of thioketal linker from the PCD polymer backbone. This treatment strategy can therefore achieve enhanced cytotoxicity through the

amplification of mitochondrial oxidative stress and DNA damage to overcome multi drug resistance.

Herein, novel dual targeting polymer prodrug nanoparticles that can simultaneously target cancer cells and mitochondria by folic acid (FA) and TPP targeting moiety, respectively, are rationally designed to overcome MDR through an orchestrated amplification of mitochondrial oxidative stress by cinnamaldehyde (CNM), and damage of either mtDNA or cellular DNA by doxorubicin (DOX). Briefly, FA&TPP-PEOGMA$_{18}$-*b*-P(CNM$_{17}$-*co*-DOX$_{15}$) block copolymer was synthesized and used to prepare PCD nanoparticles **(Figure 4.1)**.

Once PCD nanoparticles are accumulated into cancer cells, the relatively lower endosomal pH value (~pH 5–6.5) can trigger the release of CNM in the cell followed by amplification of intracellular ROS level that can subsequently trigger the release of DOX precisely in the mitochondria by the cleavage of thioketal linkage (TK) from the PCD polymer backbone **(Figure 4.22A)**.

In addition to the amplified oxidative stress induced by amplification of mitochondria ROS overproduction by cinnamaldehyde, the DOX release in the mitochondria can contribute the cell cytotoxicity through the damage of either mtDNA or cellular DNA.

Our proposed treatment strategy showed enhanced cell killing efficacy against DOX resistant MCF-7 ADR cells that was comparable to non-resistant MCF-7 cell lines *in vitro*. Moreover, PCD nanoparticles showed potential efficacy to inhibit the growth of MCF-7 ADR xenograft tumor model without observable side effect.

4.2. Material and Methods

4.2.1. Materials

Doxorubicin hydrochloride ~98% (DOX-HCl) was purchased from Hisun Pharmaceutical Co., Ltd (Hangzhou, China). Copper(I) bromide (CuBr), and Oligo ethylene glycol methacrylate (OEGMA, M_n= 500 g/mol) passed through silica column to remove MEHQ inhibitor before to use were both obtained from Sigma Aldrich (Shanghai, China). Folic acid (FA) was bought from Folic acid Fisher Bioreagents. Cinnamaldehyde, thioglycolic acid, sodium borohydride ($NaBH_4$), methacryloyl chloride, iodine (I_2), *N,N,N′,N″,N″*-pentamethyldiethylenetriamine (PMDETA), methacryloyl chloride, and nitrophenyl chloroformate were purchased from Energy Chemical Co., Ltd (Shanghai, China). Tris-(hydroxymethyl) ethane, *p*-toluenesulfonic acid, n-hydroxysuccinimide (NHS), 1-ethyl-3-(dimethylaminopropyl) carbodiimide (EDC), and propargylamine were procured from Sinopharm Chemical Reagent Co., Ltd (China). 2′-azobisisobutyronitrile (AIBN, Sigma Aldrich) was recrystallization twice from methanol prior to use. Other chemicals were obtained from Energy Chemical Co., Ltd (Shanghai, China). 3-(4,5-dimethylthiazol-2-yl)-2,5-diphenyltetrazolium bromide (MTT), propidium iodide (PI, 94%), fluorescein diacetate (FDA), Genomic DNA Mini Preparation Kit with Spin Column, reactive oxygen species (ROS) Assay Kit (2',7'-dichlorofluorescin diacetate, DCFH-DA), Caspase 3 Kit, DNA damage detection kit, and Annexin V-FITC Apoptosis Detection Kit were purchased from Beyotime Institute of Biotechnology (Shanghai, China). Fetal bovine serum (FBS), Roswell Park Memorial Institute (RPMI-1640), and trypsin were purchased from GIBCO. MCD-7 ADR and MCF-7 cell lines were bought from

Shanghai Fumengjiyin Biotechnology (FMGbio) Co. Ltd. 5-Week-old female BALB/c nude mice were purchased from Beijing Vital River Laboratory Animal Technology Co., Ltd. The animal studies were carried out according to the regulations for the administration of affairs concerning experimental animals (Hefei, revised in June 2015).

4.2.2. Instrumentation

^{1}H and ^{13}C NMR spectra of the synthesized chemicals were characterized by Bruker AV400 NMR 400 MHz spectrometer. Gel permeation chromatography (GPC) equipped with a G1310B Iso. pump, a G1316A PL gel column, and a G1362A differential refractive index detector, using DMF as eluent with 1 g/L LiBr at a flow rate of 1.0 mL/min, was used to determine the molecular weight (M_w) and molecular weight distribution (M_w/M_n) of the synthesized polymers compared to standards calibrated using a series of low-polydispersity PEG polymers. JEOL-2100F Transmission Electron Microscope (TEM) was used to examine the morphology and size of the prepared nanoparticles by dropping 5 μL of diluted sample on a copper grid placed on filter paper to remove excess solution, followed by drying process at room temperature. Zeta-potential analyzer with dynamic laser light scattering (DLS) equipped a Malvern Zetasizer Nano ZS90, a He-Ne laser (633 nm), and 173^{o} collecting optics was used to analyze the nanoparticle zeta potential and size distribution. Reversed-phase high performance liquid chromatography (RP-HPLC) analysis was conducted on a Shimadzu HPLC system equipped with a LC-20AP binary pump, a C18 column, and an SPD-20A UV-Vis detector. A Xenogen IVIS Spectrum optical imaging device (PerkinElmer) was used to study the sample bio-distribution *in vivo*. F-4600

Fluorescence Spectrophotometer (Hitachi, Japan) was used to detect sample fluorescence spectroscopy. Confocal laser scanning microscopy (CLSM) images were acquired using Leica TCS SP5 microscope (Germany). FTIR analysis was performed on shimadzu from a pellet prepared from a mixture of sample and Potassium bromide.

4.2.3. Compound 1 Synthesis

The ROS cleavable thioketal linker (TK) was synthesized according to the procedure published elsewhere. Briefly, anhydrous thioglycolic acid (20 g, 0.22 mol) and dry acetone (25 g) were charged into 500 mL three-necked flask and saturated hydrogen chloride atmosphere. After stirring for 2 h at room temperature, the reaction was quenched by placing the flask into a precooled ice-salt bath until the crystallization was complete. Followed by crystals filtration and washing several times using cold hexane and water alternatively. The collected crystals were dried under vacuum overnight to get snowy crystals product.

4.2.4. Synthesis of Thioketal Linker (TK)

The product carboxylic acid functional groups were hydrolyzed to hydroxyl groups as follow: compound 1 (7 g, 31 mmol) and sodium borohydride ($NaBH_4$) (5 g, 132 mmol) were discharged into three-necked flask filled with 140 mL dry tetrahydrofuran (THF) and cooled into ice bath. Subsequently, iodine (17.4 g, 67 mmol) dissolved into dry THF (80 mL) was dropwise added into the mixture *via* adding funnel while stirring in the presence of reflux condenser.

Thereafter, the reaction was heated to refluxed overnight. The reaction pot was

cooled down at room temperature and methanol (30 mL) was cautiously added into the flask until the solution turns clear and stirred for 30 min. Next, the solvent was removed under *vacuo* and the obtained white paste was further dissolved into 20% aqueous KOH solution (200 mL) and stirred for another 30 min followed by extraction with ethyl acetate. Finally, the organic layer was collected and dried over sodium sulfate before being concentrated in vacuo. The crude product was passed into column chromatography using ethyl acetate (EA) and petroleum ether (PE) (ratio 2:1, respectively) to get a colorless viscous solution mentioned as TK (5.14 g). $C_7H_{16}O_2S_2$: ^{1}H NMR (400 MHz, $CDCl_3$) δ 3.80 (t, *J* = 6.0 Hz, 4H), 2.89 (t, *J* = 6.1 Hz, 4H), 2.54 (s, 2H), 1.64 (s, 6H) **(Scheme 4.1** and **Figure 4.2)**.

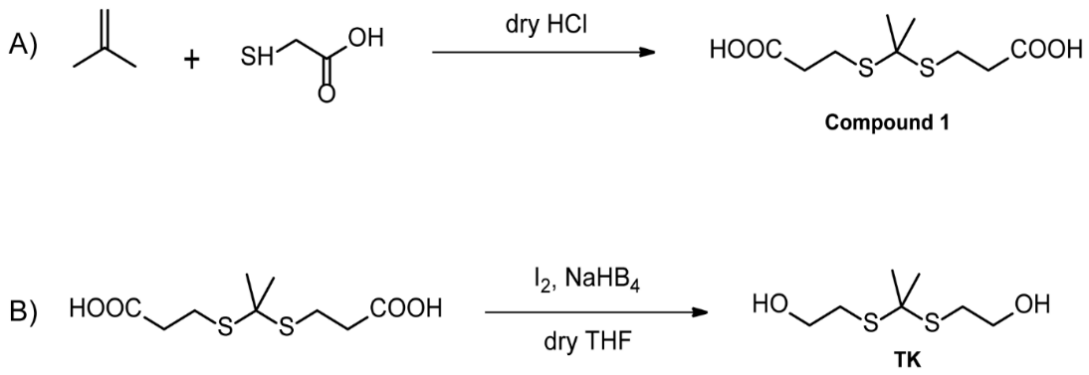

Scheme 4. 1. (A) Compound 1 and **(B)** Thioketal linker (TK) synthesis procedure.

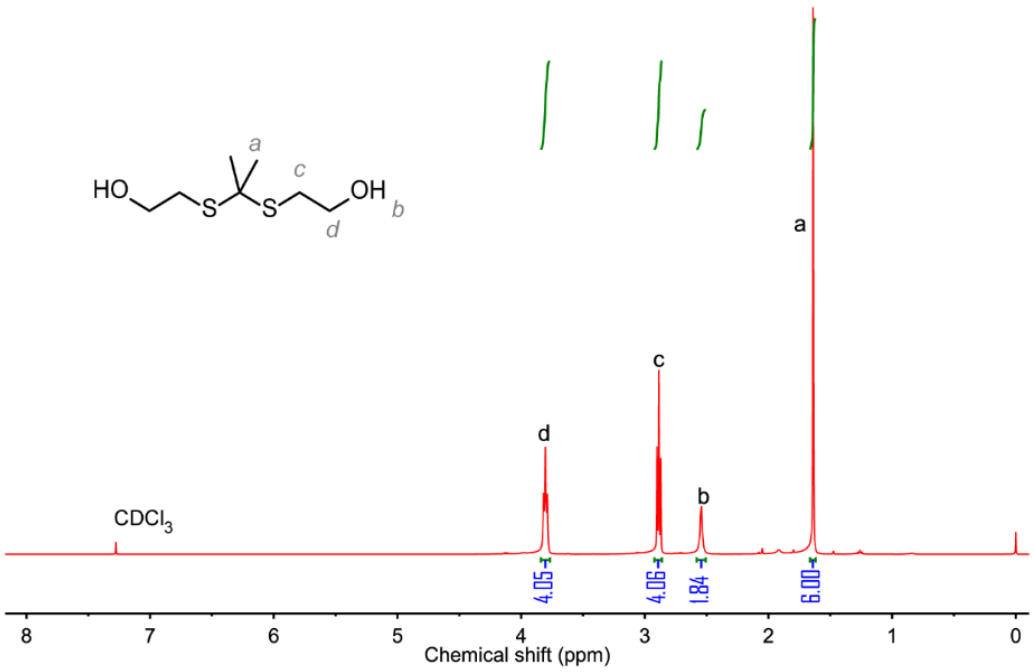

Figure 4. 2. TK ^{1}H-NMR spectra in $CDCl_3$.

4.2.5. Compound 2 Synthesis

TK-acrylic monomer was synthesized first. Briefly, TK (6.15 g, 31.3 mmol) and triethyl amine solution (TEA 3.17 g, 31.3 mmol) were dissolved into 40 mL dry THF and cooled into ice bath. Subsequently, 2-methyl-cryloyl chloride (3.27 g, 31.3 mmol) diluted into dry 10 mL dry THF was dropwise added using dropping funnel while stirring at 0^{o}C. After addition, the reaction was stirred at room temperature for 12 h. Finally, the solution was filtered and concentrated in vacuo and the TK-acrylic monomer (2.06 g) was obtained from column chromatography (PE/EA =2/1). $C_{11}H_{20}O_3S_2$: ^{1}H NMR (400 MHz, $CDCl_3$) δ 6.06 (s, 1H), 5.52 (s, 1H), 4.24 (t, J = 7.0 Hz, 2H), 3.71 (t, J = 6.3 Hz, 2H), 2.95 – 2.70 (m, 4H), 1.97 (s, 1H), 1.88 (s, 3H), 1.56 (s, 6H) **(Figure 4.3)**.

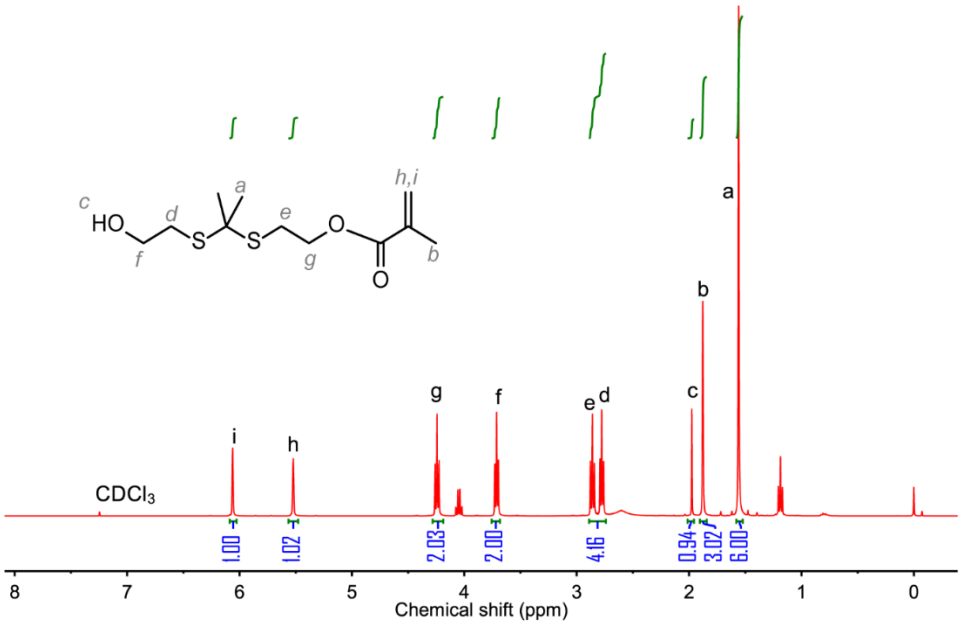

Figure 4. 3. TK-Acrylic (compound 1) ^{1}H-NMR spectra in $CDCl_3$.

4.2.6. Compound 3 Synthesis

The remaining hydroxyl functional group from TK-acrylic monomer was activated as follow: A mixture of compound 2 (2 g, 7.56 mmol), TEA (0.75 g, 7.56 mmol), and pyridine (20 µL) were dissolved into 20 mL dry THF and cooled at 0 °C in ice bath. Subsequently, nitrophenyl chloroformate (1.52 g, 7.56 mmol) diluted into dry 10 mL dry THF was dropwise added using dropping funnel while stirring at 0 °C. After addition, the reaction was stirred at room temperature for 24 h. Finally, the solution was filtered and concentrated in vacuo and the activated TK-acrylic monomer (2.1 g) was obtained from column chromatography (hexane/EA =2/1). $C_{18}H_{23}NO_7S_2$: ^{1}H NMR (400 MHz, $CDCl_3$) δ 8.30 (t, J = 12.5 Hz, 2H), 7.40 (d, J = 9.1 Hz, 2H), 6.13 (s, 1H), 5.59 (s, 1H), 4.53 – 4.23 (m, 4H), 3.10 – 2.85 (m, 4H), 1.95 (s, 3H), 1.64 (d, J = 10.5 Hz, 6H) **(Figure 4.4)**.

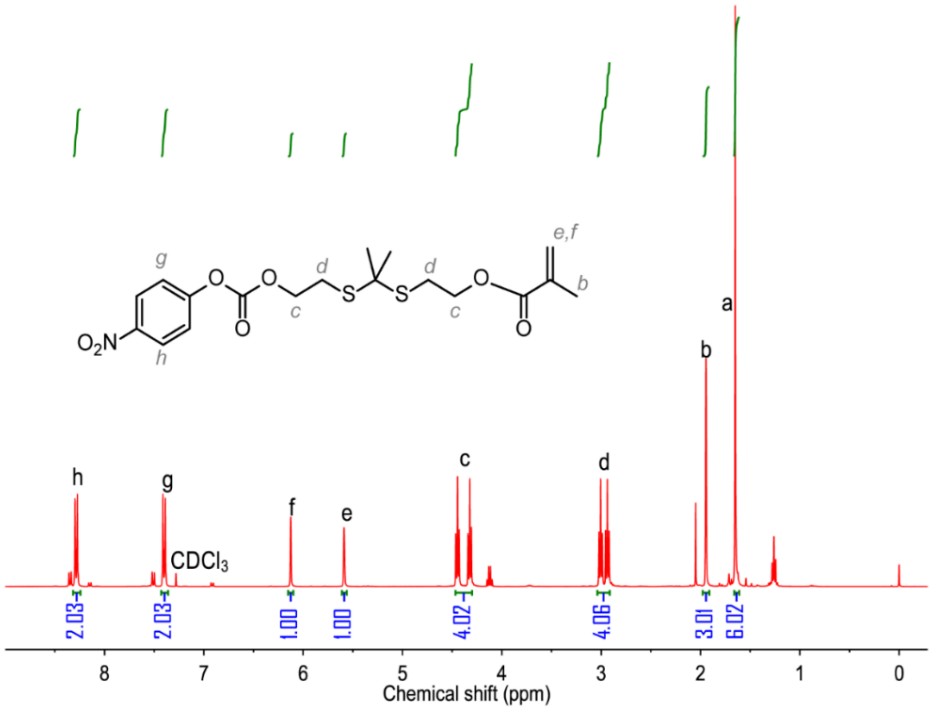

Figure 4. 4. Activated TK-Acrylic (compound 3) ^{1}H-NMR spectra in $CDCl_3$.

4.2.7. DOX Monomer Synthesis

Doxorubicin hydrochloride (DOX-HCl, 0.5 g, 0.9 mmol) was dissolved into 4 mL dimethylformamide (DMF) and TEA (0.14 g, 1.4 mmol) was added and allowed to react for 30 min at room temperature in dark **(Scheme 4.2)**. Subsequently, activated TK-acrylic monomer (compound 3: 0.6 g, 1.4 mmol) dissolved into 2 mL DMF was added to the solution and stirred for 24 h at room temperature. Thereafter, 50 mL toluene was repeatedly added and the mixture was evaporated under vacuo at 35 °C (3 times) The obtained dry powdered crude product was passed through a column chromatography (DCM/methanol = 13/1) to obtain DOX-monomer (0.36 g). $C_{39}H_{47}NO_{15}S_2$: ^{1}H NMR (400 MHz, $CDCl_3$) δ 13.94 (s, 1H), 13.22 (s, 1H), 8.07 (t, J = 12.6 Hz, 1H), 7.78 (dd, J = 16.6, 8.6 Hz, 1H), 7.61 (s, 1H), 7.39 (t, J = 7.1 Hz, 1H),

6.86 (d, *J* = 9.0 Hz, 2H), 6.12 (s, 1H), 5.59 (s, 1H), 5.51 (d, *J* = 2.5 Hz, 1H), 5.41 (d, *J* = 8.4 Hz, 1H), 5.36 – 5.23 (m, 1H), 4.76 (t, *J* = 7.5 Hz, 2H), 4.59 (s, 1H), 4.36 – 4.12 (m, 5H), 4.08 (s, 3H), 3.88 (d, *J* = 11.5 Hz, 1H), 3.69 (d, *J* = 4.9 Hz, 1H), 3.25 (t, *J* = 15.8 Hz, 1H), 3.12 – 2.75 (m, 3H), 2.35 (dt, *J* = 32.2, 13.2 Hz, 2H), 2.17 (dd, *J* = 14.7, 3.8 Hz, 1H), 1.94 (d, *J* = 7.8 Hz, 3H), 1.74 (d, *J* = 28.7 Hz, 4H), 1.59 (s, 6H), 1.30 (d, *J* = 6.5 Hz, 3H). ^{13}C NMR (101 MHz, $CDCl_3$) δ 215.15 – 212.90 (m), 188.10 – 185.43 (m), 166.58 (s), 163.31 – 159.87 (m), 157.20 – 153.75 (m), 142.59 – 139.78 (m), 136.47 – 134.65 (m), 133.27 (d, *J* = 50.7 Hz), 127.76 – 124.96 (m), 121.65 – 117.44 (m), 115.32 (d, *J* = 55.6 Hz), 112.10 – 109.71 (m), 100.30 (d, *J* = 87.4 Hz), 70.31 – 68.48 (m), 67.30 (d, *J* = 18.2 Hz), 65.21 (d, *J* = 64.6 Hz), 63.64 (t, *J* = 35.4 Hz), 62.37 – 61.32 (m), 58.08 – 55.06 (m), 46.85 (d, *J* = 63.1 Hz), 35.39 (d, *J* = 53.0 Hz), 33.80 (t, *J* = 13.7 Hz), 31.25 – 28.44 (m), 18.01 (d, *J* = 51.3 Hz), 16.58 (d, *J* = 57.2 Hz), -0.36 (d, *J* = 72.8 Hz).

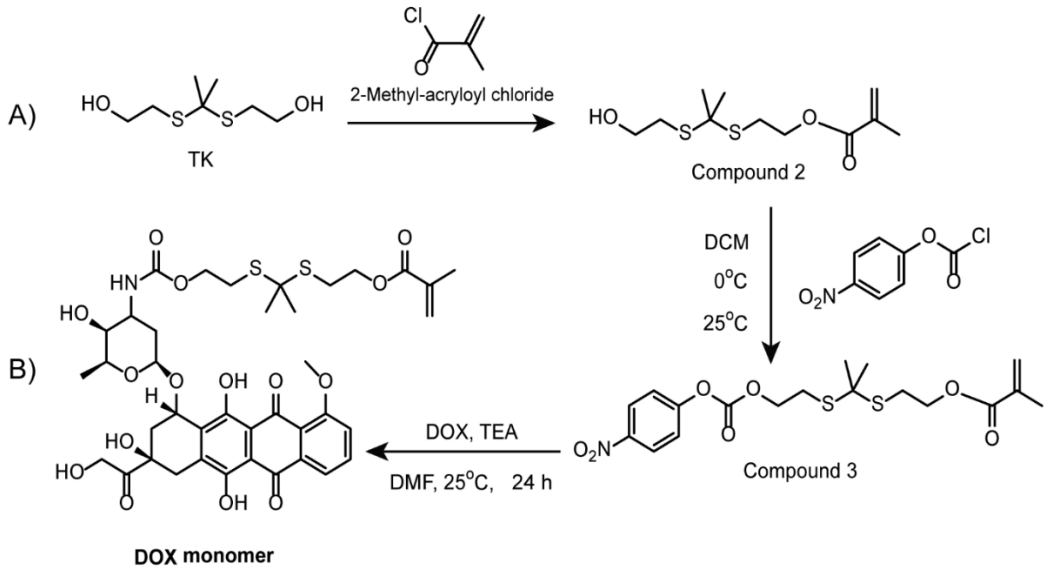

Scheme 4. 2. (A) Compound 1 and 2, and **(B)** Doxorubicin (DOX) monomer synthesis

procedure.

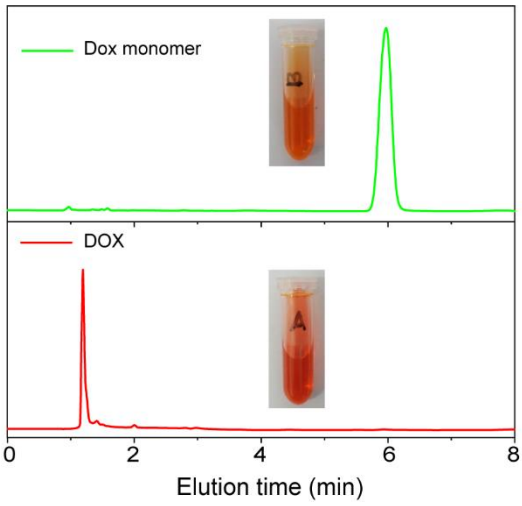

Figure 4. 5. DOX monomer and DOX HPLC analysis.

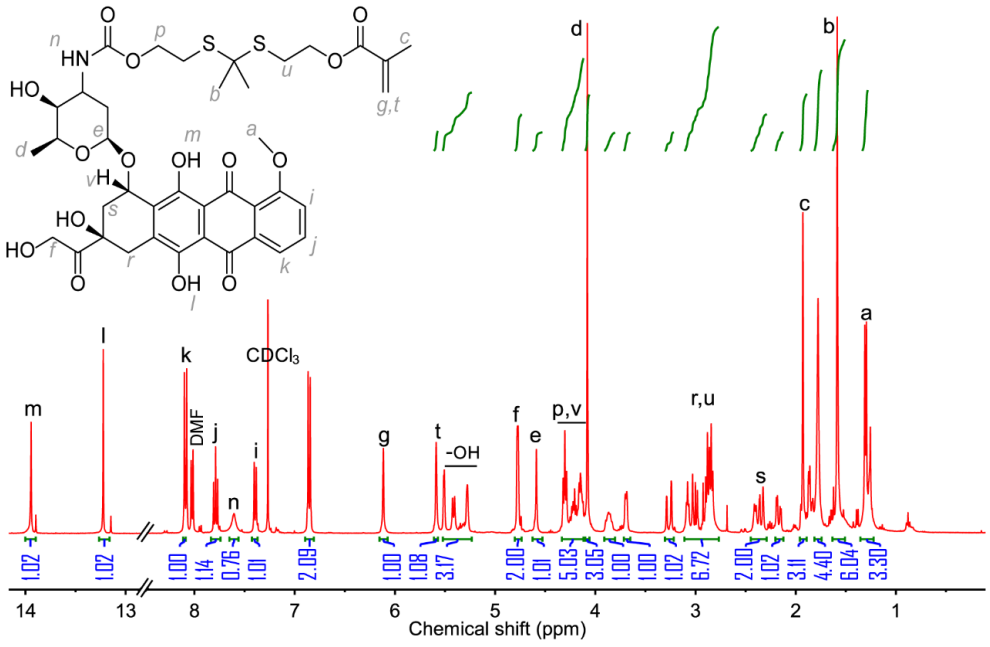

Figure 4. 6. DOX monomer ^{1}H-NMR spectra in $CDCl_3$.

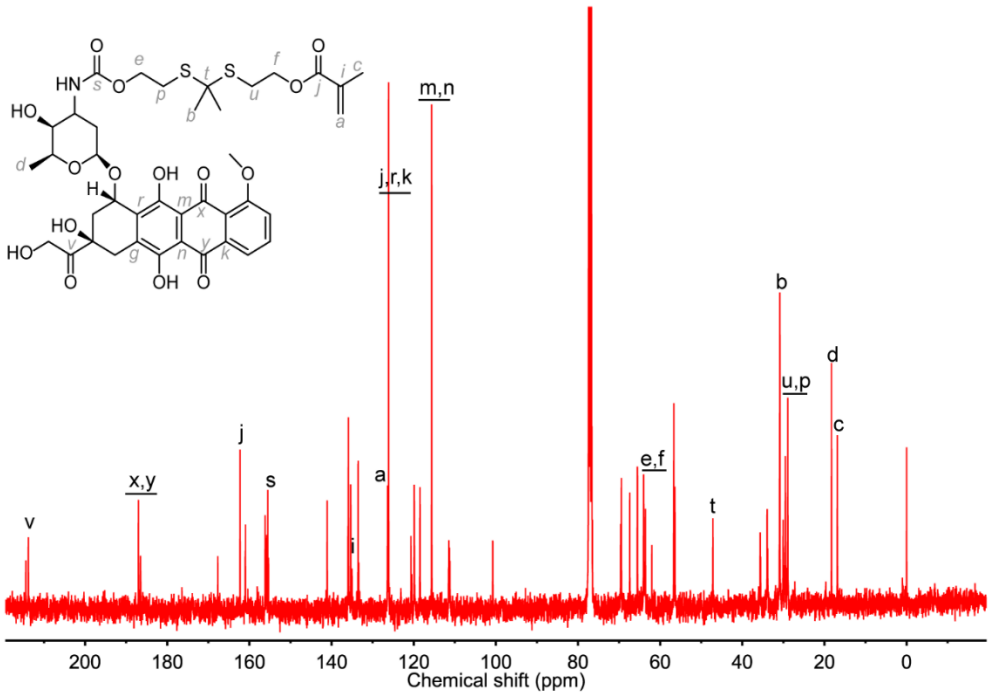

Figure 4. 7. DOX monomer ^{13}C-NMR spectra in $CDCl_3$.

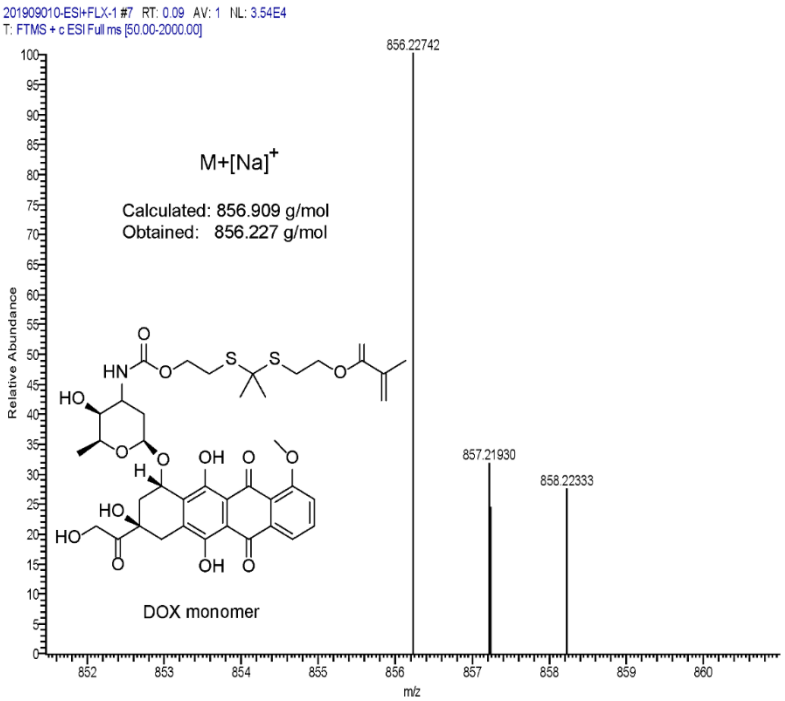

Figure 4. 8. DOX monomer mass analysis by ESI-MS.

4.2.8. Synthesis of Cinnamaldehyde Derivative

A mixture of cinnamaldehyde (10 g, 75 mmol), tris-(hydroxymethyl) ethane (8.41 g, 70 mmol), and *p*-toluenesulfonic acid (190 mg, 1 mmol) were added into two-neck flask equipped filled with 120 mL dry THF and immediately refluxed at 70 °C for 12 h. Thereafter, TEA (155 mg, 1.5 mmol) was added to terminate the reaction. The solvent was removed by vacuo and the product was obtained from column chromatography (PE/EA =3/1). $C_{14}H_{18}O_3$: ^{1}H NMR (400 MHz, $CDCl_3$) δ 7.46 – 7.20 (m, 5H), 6.78 (d, J = 16.2 Hz, 1H), 6.19 (dd, J = 16.2, 4.7 Hz, 1H), 5.08 (d, J = 4.7 Hz, 1H), 3.99 (d, J = 11.7 Hz, 2H), 3.85 (d, J = 5.4 Hz, 2H), 3.56 (d, J = 11.7 Hz, 2H), 1.80 (t, J = 5.4 Hz, 1H), 0.78 (s, 3H) **(Scheme 4.3A** and **Figure 4.9)**.

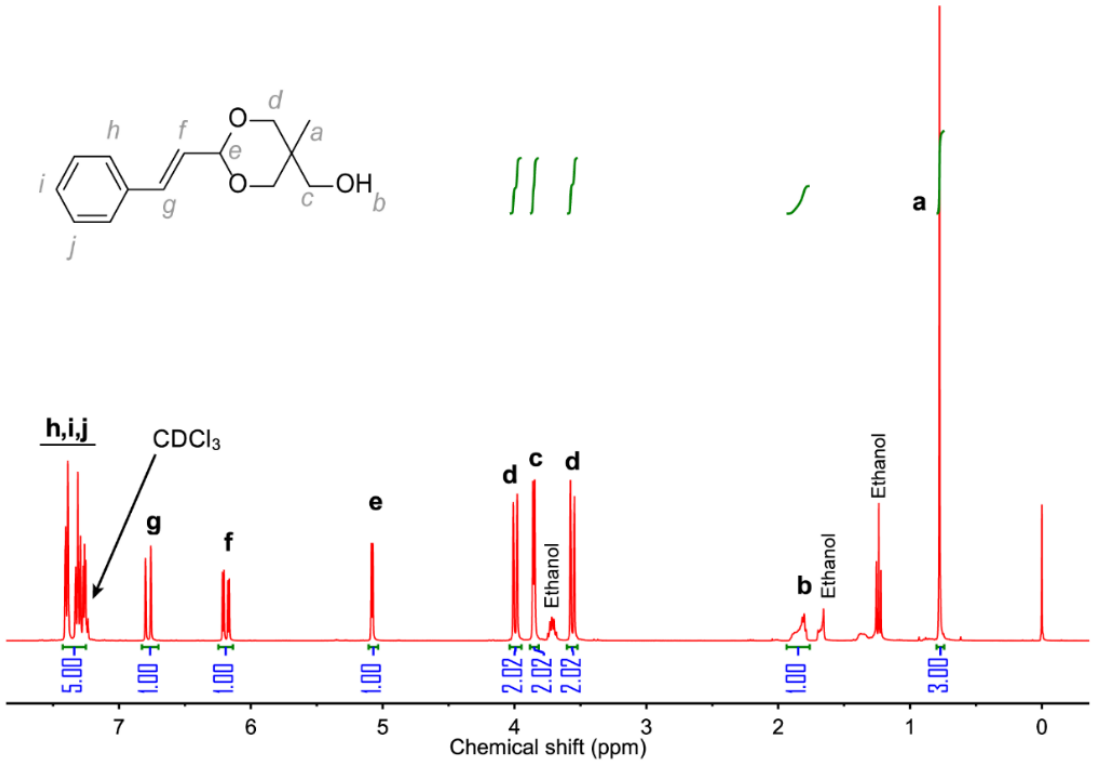

Figure 4. 9. CNM derivative ^{1}H-NMR spectra in $CDCl_3$.

4.2.9. Synthesis of Cinnamaldehyde Monomer (CNM)

To synthesize cinnamaldehyde monomer (CNM), cinnamaldehyde derivative (3 g, 13 mmol) and TEA (1.56 g, 15.3 mmol) were dissolved into 25 mL dry dichloromethane (DCM) and cooled into ice bath. Subsequently, 2-methyl-acryloyl chloride (1.6 g, 15.3 mmol) diluted into dry DCM was dropwise added by adding funnel at 0 °C. After addition, the reaction was stirred at room temperature for 12 h. Finally, the solution was filtered and concentrated in vacuo and the product (2.5 g) was obtained from column chromatography (PE/EA = 4/1). $C_{18}H_{22}O_4$: ^{1}H NMR (400 MHz, DMSO) δ 7.55 – 7.45 (m, 2H), 7.40 – 7.23 (m, 3H), 6.73 (d, *J* = 16.2 Hz, 1H), 6.24 (dd, *J* = 16.2, 4.7 Hz, 1H), 6.08 (dd, *J* = 1.4, 1.0 Hz, 1H), 5.76 – 5.65 (m, 1H), 5.13 (dd, *J* = 4.7, 0.8 Hz, 1H), 4.27 (s, 2H), 3.89 (t, *J* = 12.3 Hz, 2H), 3.61 (d, *J* = 11.7 Hz, 2H), 1.94 – 1.86 (m, 3H), 0.75 (d, *J* = 8.5 Hz, 3H). ^{13}C NMR (101 MHz, $CDCl_3$) δ 167.28 (s), 136.31 (s), 135.94 (d, *J* = 3.3 Hz), 133.79 (d, *J* = 6.2 Hz), 128.57 (s), 128.28 (s), 126.88 (s), 126.06 (s), 125.52 (s), 125.14 (d, *J* = 12.6 Hz), 101.13 (d, *J* = 14.1 Hz), 77.34 (d, *J* = 11.6 Hz), 77.08 (s), 76.76 (s), 73.31 (s), 73.01 (s), 67.71 (s), 66.75 (s), 34.14 (s), 33.86 (s), 18.90 (s), 18.37 (d, *J* = 5.2 Hz), 17.30 (s) (**Scheme 4.3B** and **Figure 4.10, 4.11,** and **4.12)**.

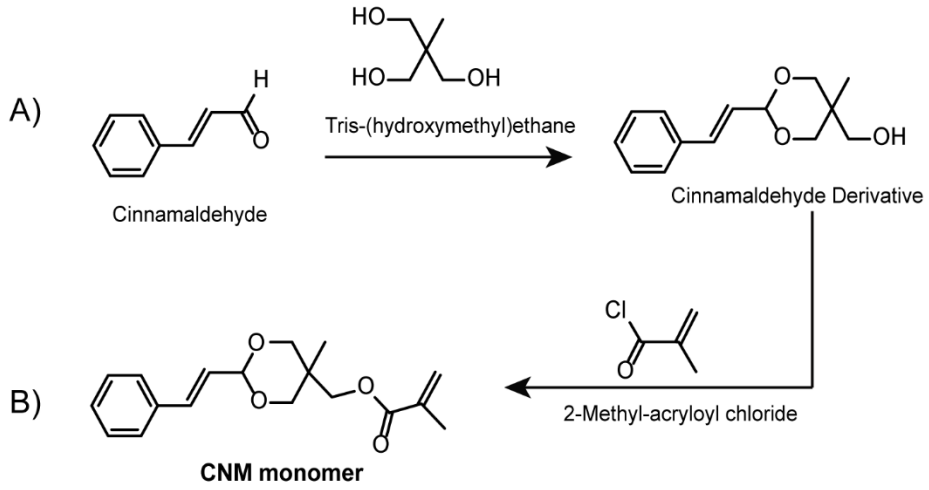

Scheme 4. 3. (A) Cinnamaldehyde derivative and **(B)** Cinnamaldehyde (CNM) monomer synthesis procedure.

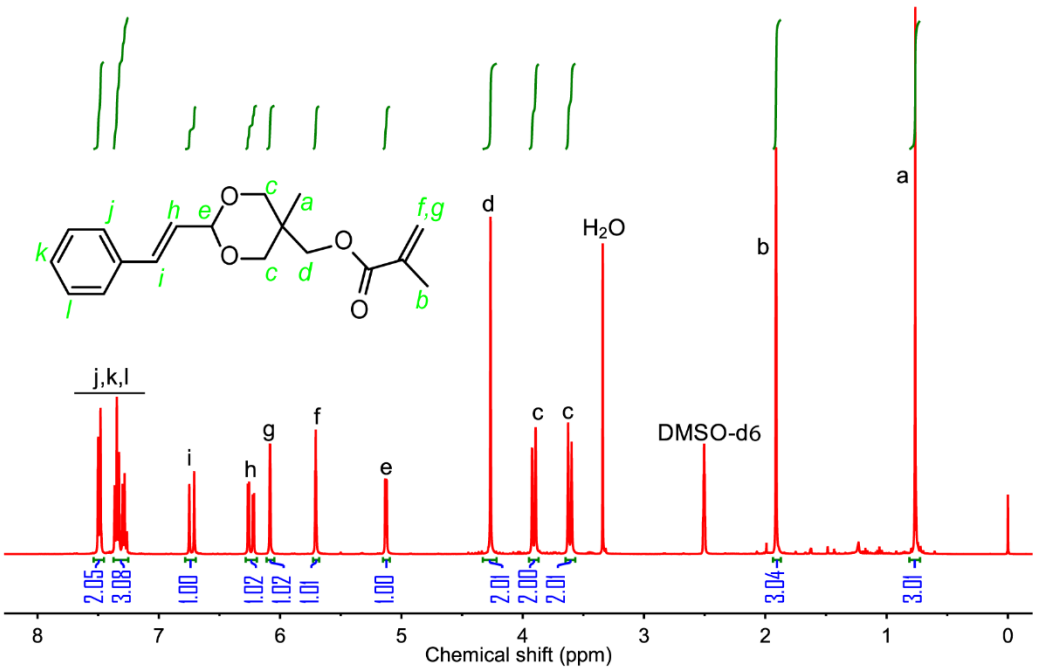

Figure 4. 10. CNM monomer ^{1}H-NMR spectra in DMSO-d6.

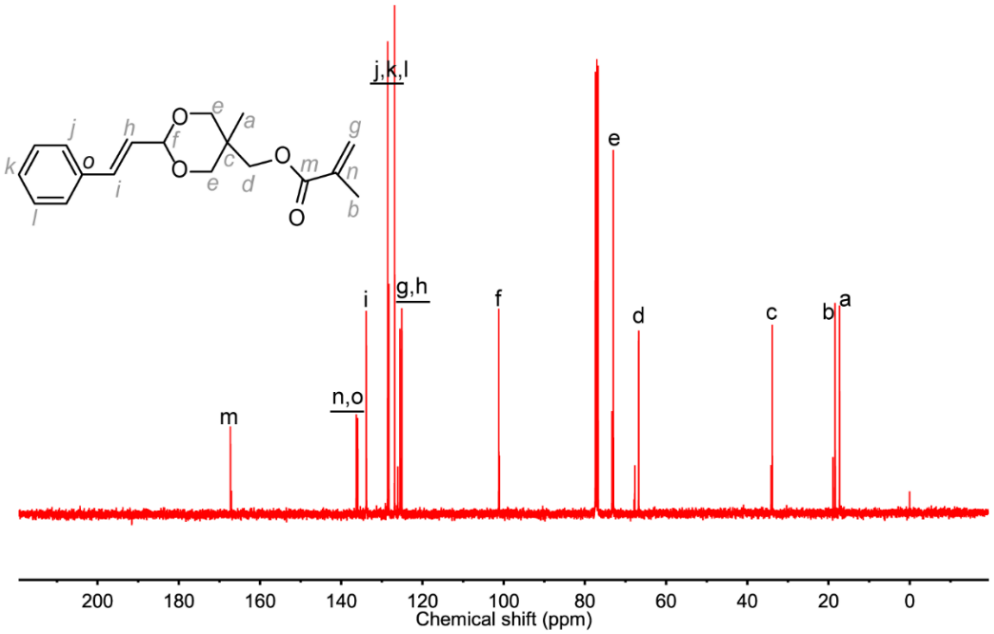

Figure 4. 11. CNM monomer ^{13}C-NMR spectra in $CDCl_3$.

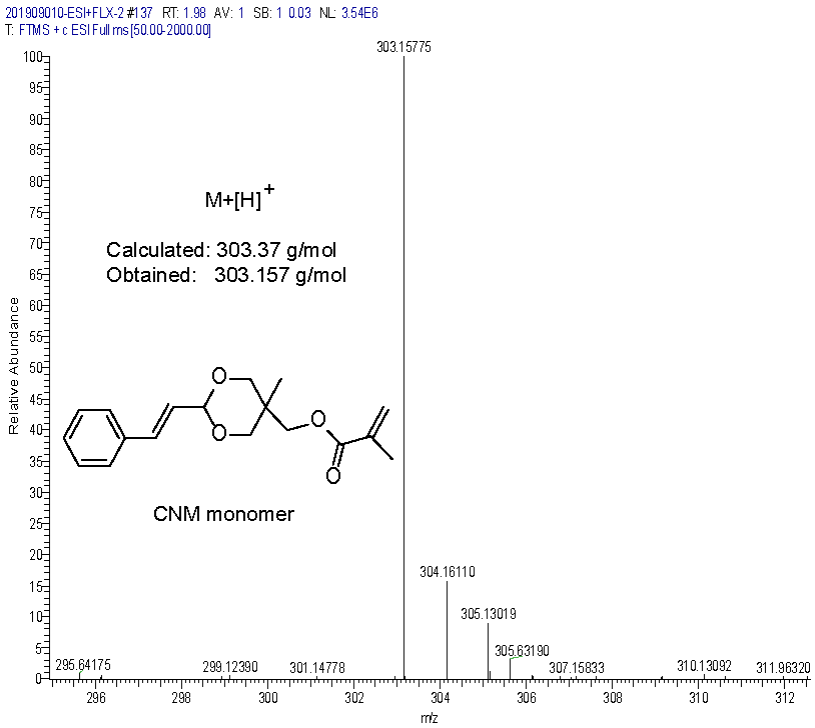

Figure 4. 12. CNM monomer mass analysis by ESI-MS.

4.2.10. Synthesis of FA-Alkyne

Folic acid (0.5 g, 1.13 mmol) was dissolved into 50 mL dry DMF and placed into a cooled water bath, followed by adding n-hydroxysuccinimide (NHS, 0.13 g, 1.3 mmol) and 1-ethyl-3-(dimethylaminopropyl) carbodiimide (EDC, 0.22 g, 1.25 mmol). The mixture was stirred at 5 °C for 30 min to form white precipitate. Subsequently, propargylamine (62 mg, 1.13 mmol) dissolved into 5 mL dry DMF was introduced into the reaction and the resultant mixture was warmed to 25 °C and reacted for another 24 h. Finally, 150 mL of distilled water was added into the reaction vessel and stirred for further 30 min to form precipitate. The obtained yellowish precipitate was filtered and washed 3 times with acetone and dried in a vacuum oven overnight to yield (0.48 g). $C_{22}H_{22}N_8O_5$: ^{1}H NMR (400 MHz, DMSO) δ 12.31 (s, 1H), 11.42 (s, 1H), 8.65 (s, 1H), 8.14 (d, *J* = 7.7 Hz, 1H), 7.63 (dd, *J* = 18.0, 8.6 Hz, 2H), 6.95 (t, *J* = 6.0 Hz, 2H), 6.61 (t, *J* = 19.8 Hz, 2H), 4.49 (d, *J* = 5.9 Hz, 2H), 4.33 (ddd, *J* = 9.8, 7.8, 4.9 Hz, 1H), 2.32 (t, *J* = 7.4 Hz, 2H), 2.12 – 1.83 (m, 2H), 1.23 (s, 1H) (**Scheme 4.4** and **Figure 4.15)**.

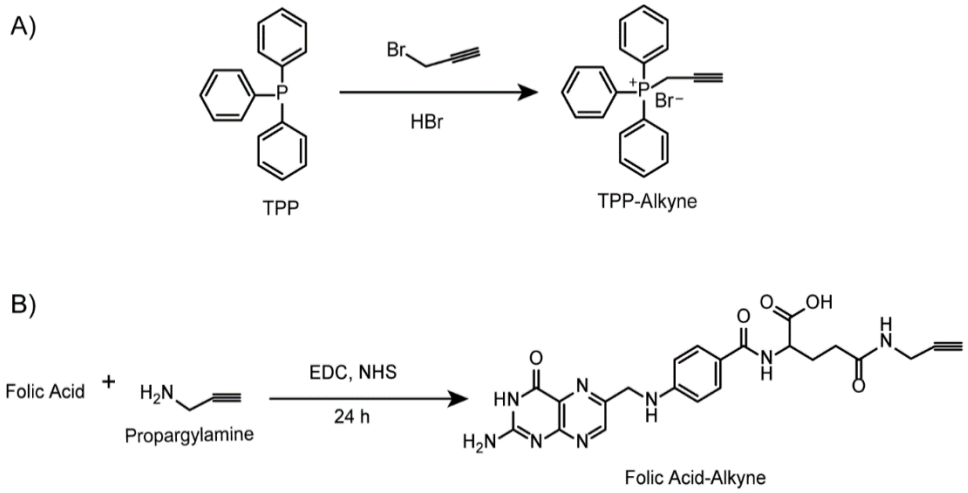

Scheme 4. 4. (A) Tetraphenylphosphonium (TPP)-Alkyne and **(B)** Folic acid-alkyne

synthesis procedure.

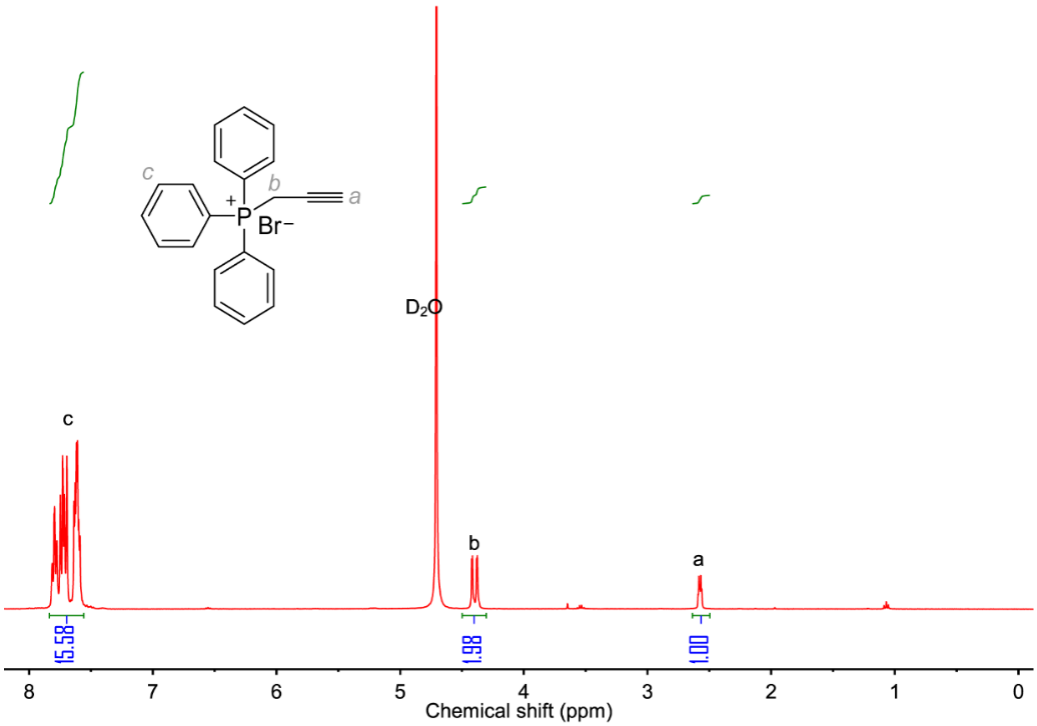

Figure 4. 13. TPP-Alkyne ^{1}H-NMR spectra in $CDCl_3$.

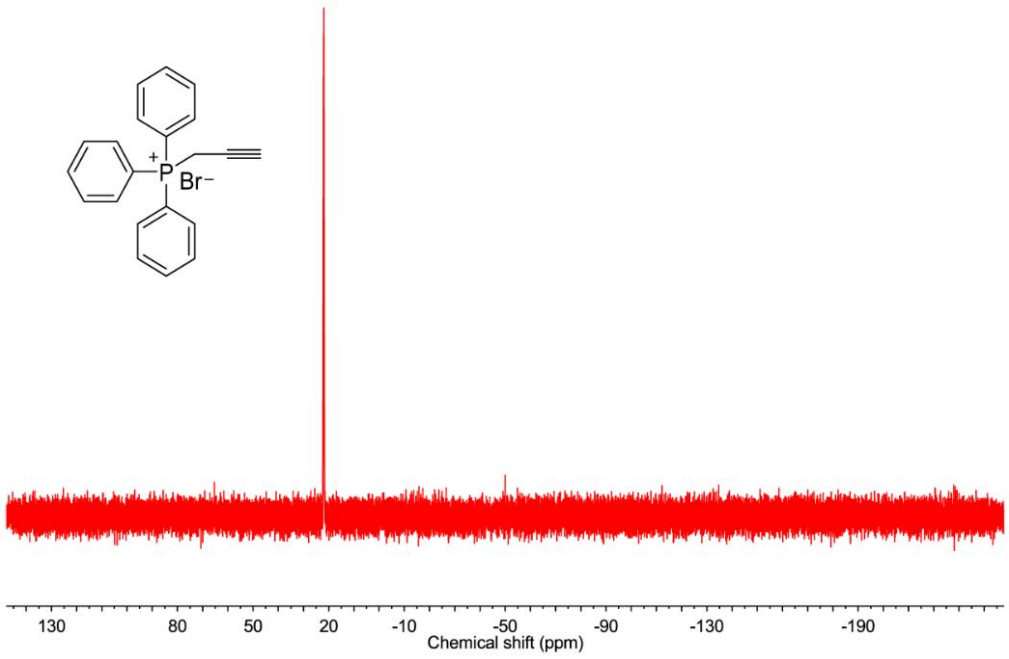

Figure 4. 14. TPP-Alkyne ^{31}P-NMR spectra in $CDCl_3$.

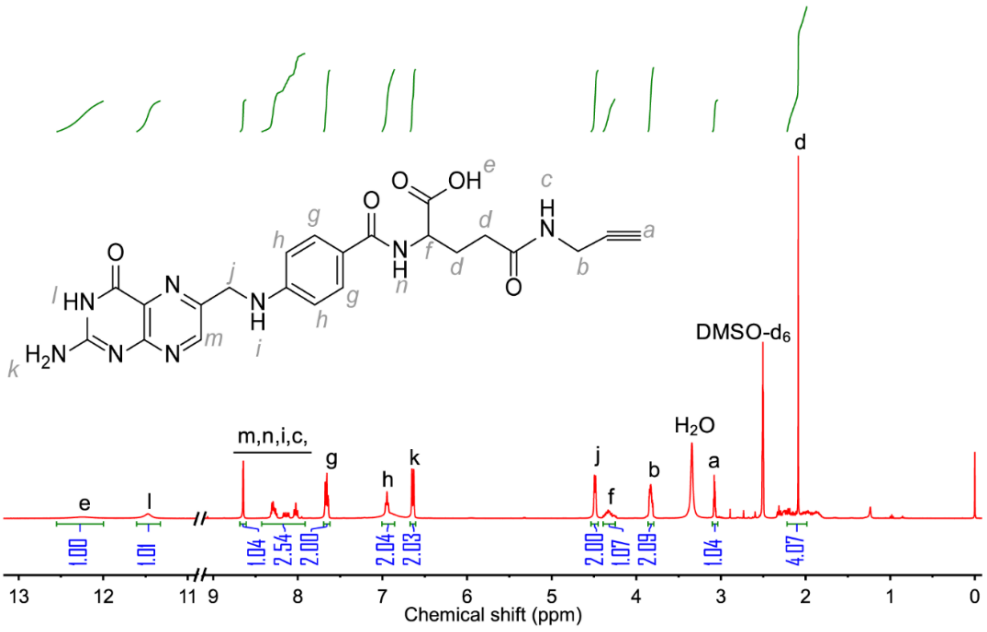

Figure 4. 15. Folic Acid-Alkyne ^{1}H-NMR spectra in $CDCl_3$.

4.2.11. Synthesis of N_3-PEOGMA

N_3-PEOGMA macro-RAFT chain transfer agent was synthesized using reversible addition-fragment transfer (RAFT) polymerization technique. Briefly, a mixture of OEGMA (M_n= 500 g/mol, 3 g, 6 mmol), N_3-CTA (126.7 mg, 0.3 mmol), and 2′-azobisisobutyronitrile (AIBN) (4.9 mg, 30 µmol) dissolved into 5 mL 1,4-dioxane were transferred into 10 mL polymerization tube. Subsequently, the tube was degassed by three freeze-pump-thaw cycles and sealed under vacuum. The mixture was polymerized into preheated oil bath at 80 °C for 4 h. Thereafter, the tube was dipped into liquid nitrogen followed by exposing the reaction to air. The resultant mixture was diluted by 5 mL DCM and the product was collected by precipitation and centrifugation into diethyl ether/hexane cosolvent (ratio: 1/1) three times. Finally, the obtained

yellowish viscous polymer denoted as N_3-PEOGMA was dried into oven under vacuum overnight. Product (2.95 g), ^{1}H-NMR analysis showed that the degree of polymerization (DP) for OEGMA 18 and the GPC test result shows $M_{n,GPC}$ = 10096 g/mol, and M_w/M_n = 1.02 (**Scheme 4.5, Figure 4.16** and **4.17)**.

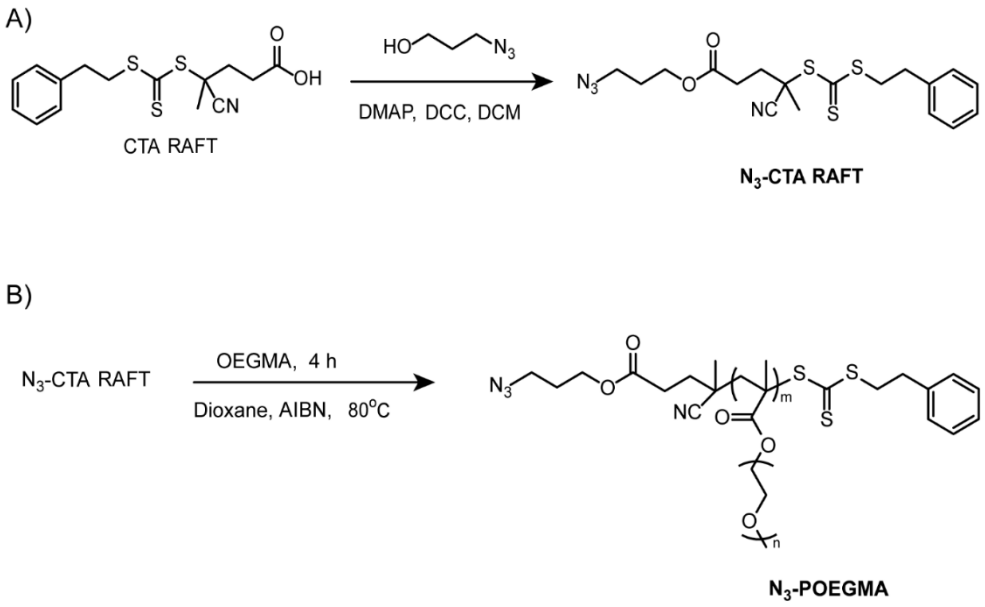

Scheme 4. 5. (A) N_3-CTA RAFT chain transfer agent and **(B)** N_3-PEOGMA synthesis procedure.

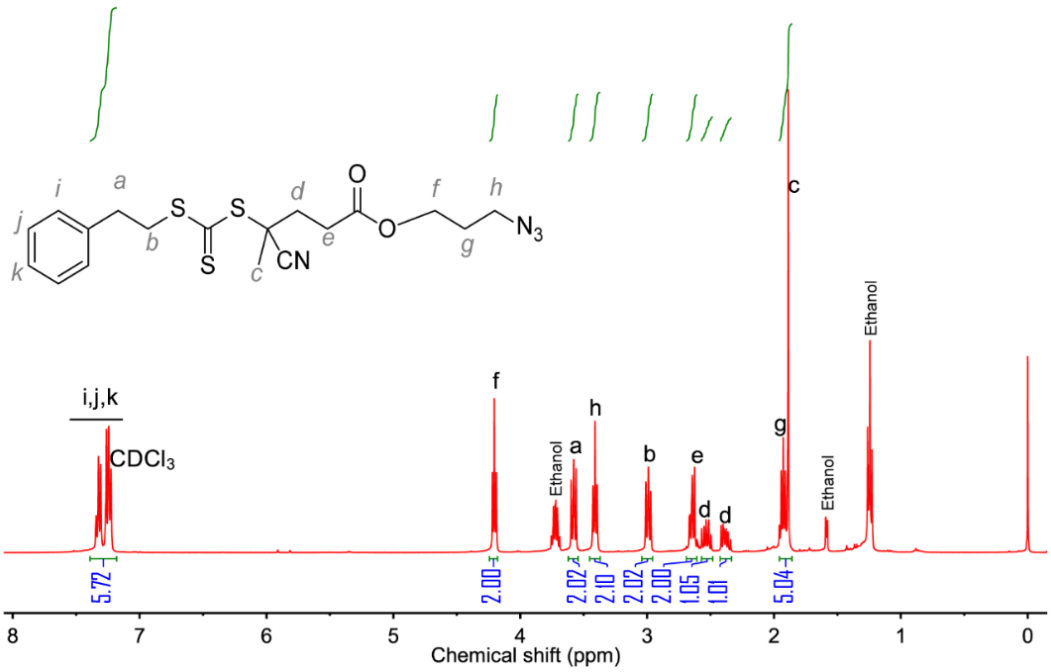

Figure 4. 16. N_3-CTA-RAFT ^{1}H-NMR spectra in $CDCl_3$.

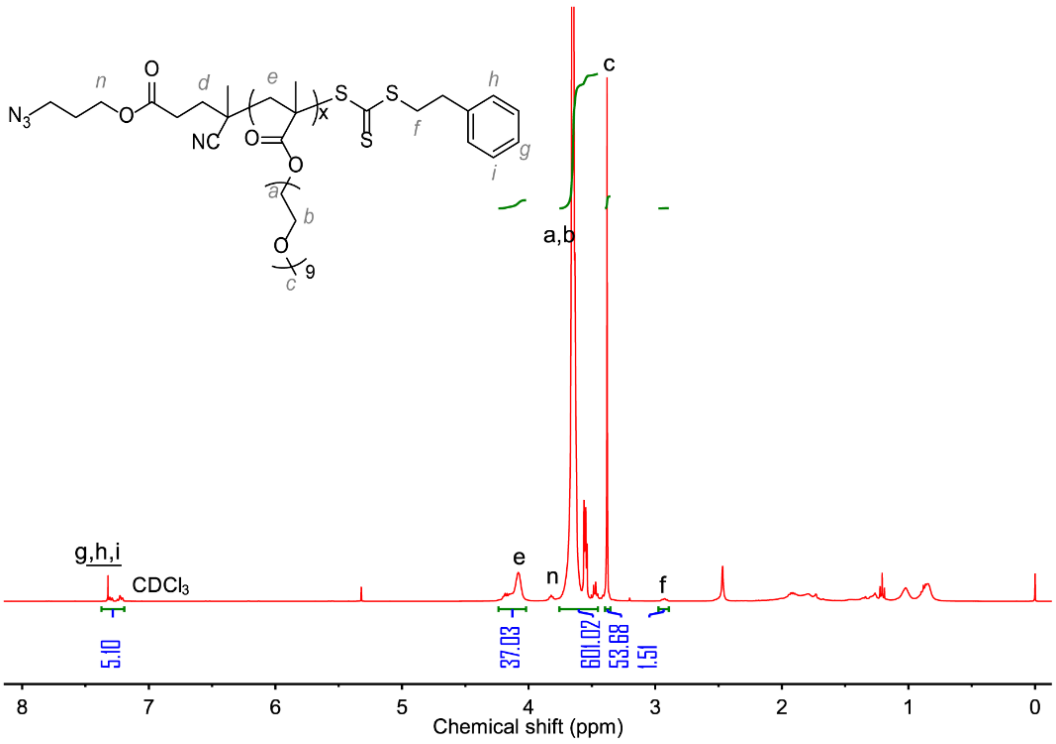

Figure 4. 17. N_3-PEOGMA-RAFT ^{1}H-NMR spectra in $CDCl_3$.

4.2.12. Determination of Critical Micelle Concentration (CMC)

The critical micelle concentration (CMC) of PCD nanoparticles was determined by pyrene fluorescence probe procedure. Typically, a series of 5 mL PCD nanoparticle solution was prepared by dilution from 1 to 10^{-6} mg/mL. Subsequently, a solution of pyrene dissolved in acetone (50 μL, 1.21 x10^{-2} mg/mL) was added to each prepared dilution of PCD nanoparticle solution, followed by sonication at room temperature for 2 h. Thereafter, the resulting mixture mixtures were left in opened tube under mild stirring overnight to evaporate acetone. Each sample excitation intensity was tested by fluorescence spectrophotometer set at the fluorescence emission of 374 nm and scanning in the wavelength range of 290-370 nm. The CMC value was determined by plotting excitation intensity ratio at a wavelength 340 nm and 325 nm (I_{340}/I_{325}) against the concentration of PCD nanoparticle solution.

4.2.13. Synthesis of N_3-PEOGMA$_m$-*b*-P(CNM$_x$-co-DOX$_y$) Polymer

N_3-PEOGMA$_m$-*b*-P(CNM$_x$-co-DOX$_y$) block copolymer was synthesized using RAFT polymerization technique by copolymerization of CNM and DOX monomer in the presence of N_3-PEOGMA as macro-RAFT chain transfer agent **(Scheme 4.5,** and **4.6)**. Briefly, a mixture of MCN monomer (134.7 mg, 0.45 mmol), DOX monomer (206.7 mg, 0.25 mmol), N_3-PEOGMA (100 mg, 9.9 μmol), and AIBN (0.14 mg, 0.99 μmol) dissolved into 3 mL 1,4-dioxane were transferred into 5 mL polymerization tube. Subsequently, the tube was degassed by three freeze-pump-thaw cycles and sealed under vacuum. The mixture was polymerized into preheated oil bath at 80 °C for 24 h. Thereafter, the tube was dipped into liquid nitrogen followed by exposing the reaction

to air. The resultant mixture was diluted by 2 mL DCM and the product was collected by precipitation and centrifugation into diethyl ether three times. Finally, the obtained polymer was dried into oven under vacuum overnight. Product (236.87 g), ^{1}H-NMR analysis showed that the degree of polymerization (DP) for DOX and CNM monomer were 17 and 15, respectively. The GPC test result shows $M_{n,GPC}$ = 28,145 g/mol with M_w/M_n = 1.12. The polymer was denoted as N_3-PEOGMA$_{18}$-*b*-P(CNM$_{17}$-*co*-DOX$_{15}$) **(Figure 4.18)**. The polymer N_3-PEOGMA$_{18}$-*b*-P(CNM)$_{47}$ *i.e.* prepared without DOX monomer ($M_{n,GPC}$ = 23,632 g/mol) and N_3-PEOGMA$_{18}$-*b*-P(DOX)$_{18}$ *i.e.* prepared without CNM monomer ($M_{n,GPC}$ = 23,615 g/mol) were synthesized using the same procedure as described above.

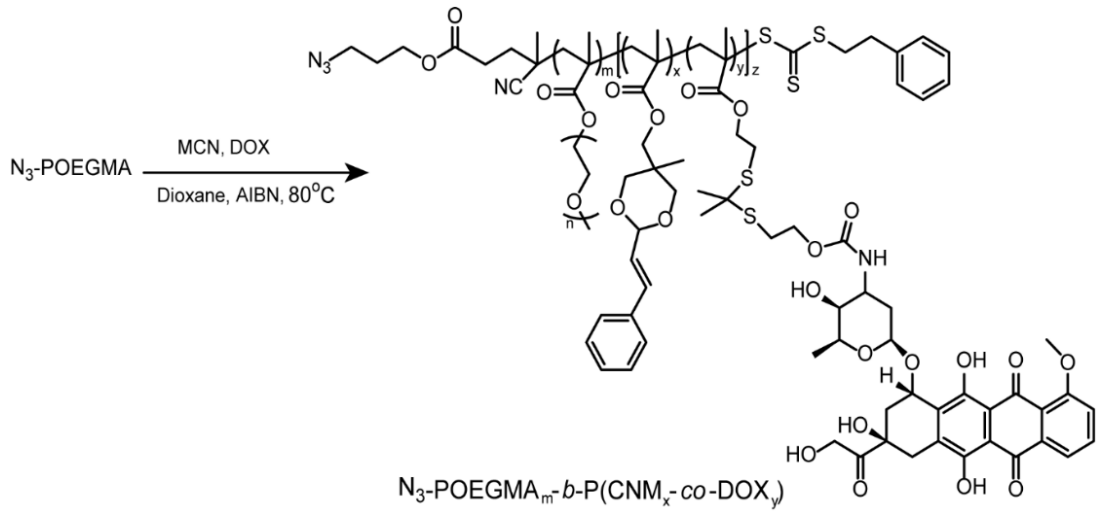

Scheme 4. 6. N_3-PEOGMA$_m$-*b*-P(CNM$_x$-*co*-DOX$_y$) polymer denoted as "PCD polymer" synthesis procedure.

4.2.14. Synthesis of TPP or FA-terminated-PEOGMA$_m$-*b*-P(CNM$_x$-co-DOX$_y$) Polymers

TPP-PEOGMA$_{18}$-*b*-P(CNM$_{17}$-*co*-DOX$_{15}$) copolymer was synthesized by copper(I)-catalyzed azide-alkyne 1,3-dipolar cycloaddition (CuAAC). Typically, a mixture of N$_3$-PEOGMA$_{18}$-*b*-P(CNM$_{17}$-*co*-DOX$_{15}$) copolymer (250 g, 8.9 μmol), TPP-alkyne (10.15 mg, 26.7 μmol), and *N,N,N′,N″,N″*-pentamethyldiethylenetriamine (PMDETA, 200 mg, 1.12 mmol) dissolved into 3 mL DMSO were transferred into a reaction tube and alternatively purged with nitrogen and degassed by three freeze-pump-thaw cycles. Subsequently, a long neck funnel was used to quickly transfer Copper(I) bromide CuBr (42 mg, 0.29 μmol) under nitrogen atmosphere and the tube was sealed under vacuum. The reaction was carried out at 40 °C under stirring for 24 h. Thereafter, the tube was immersed into liquid nitrogen and the mixture was exposed to air and passed through a short column of neutral alumina. The obtained product was subjected into a dialyzing bag with a molecular weight cutoff (MWCO) 1000 Da and dialyzed against DMSO then distilled water. Finally, the product denoted as TPP-PEOGMA$_{18}$-*b*-P(CNM$_{17}$-*co*-DOX$_{15}$) was collected by lyophilization. By replacing TPP-alkyne with FA-alkyne, similar procedure was used to synthesize FA-PEOGMA$_{18}$-*b*-P(CNM$_{17}$-*co*-DOX$_{15}$) polymer **(Figure 4.21)**.

4.2.15. Self-Assembly and Nanoparticle Stability Evaluation

A mixture of TPP-PEOGMA$_{18}$-*b*-P(CNM$_{17}$-*co*-DOX$_{15}$) and FA-PEOGMA$_{18}$-*b*-P(CNM$_{17}$-*co*-DOX$_{15}$) copolymers (ratio: 4:1, respectively, 5 mg) dissolved into 1 mL THF solvent was quickly transferred into a vial containing 5 mL phosphate buffer solution (PBS, pH 7.4) under vigorous stirring at room temperature to form micelles.

The resultant mixture was stirred for 2 h for nanoparticle stabilization, followed by removing organic solvent by dialysis (dialyzing bag MWCO = 3500 Da) against PBS. The obtained nanoparticle solution was denoted as PCD and the DOX encapsulation capacity was quantified to be 28.31 wt% according to ^{1}H-NMR analysis. Similar procedure was used to prepare n-PCD nanoparticles that are nanoparticle with both CNM and DOX segments but without TPP and FA targeting moieties. Moreover, TPP&FA-PEOGMA$_{18}$-*b*-P(CNM)$_{47}$ copolymers or TPP&FA-PEOGMA$_{18}$-*b*-P(DOX)$_{18}$ copolymers were used to prepared nanoparticles named PC or PD, respectively, that are nanoparticles decorated with both TPP and FA targeting moieties but without DOX segment for PC nanoparticles and CNM segment for PD nanoparticles.

To analyze nanoparticle stability under various solution conditions, PCD nanoparticle solution (1 mg/mL) incubated either in RPMI 1640 media containing 10% FBS or PBS pH 7.4 at 37 °C and with mild stirring for 5 days. Meanwhile, the nanoparticle size and particle distribution (PDI) were monitored every 24 h by DLS.

4.2.16. DOX Release Evaluation

The *in vitro* Dox release profile was studied in a simulated tumor microenvironment reactive oxygen species (ROS) environment. Briefly, PCD nanoparticle solution (1 mL, 1 mg/mL) was sealed in dialyzing bag (MWCO = 3500 Da) and incubated into 9 mL PBS at pH 5.5 or 6.8 in the presence of various concentration of H_2O_2 (0 μM, 100 μM, or 1 mM) and $FeSO_4$ (1.0 μM) at 37 °C under mild stirring. At predetermined time intervals, 500 μL dialysate aliquot was withdrawn and replace with similar solution. The dialysate was freeze-dried and redissolved in

acetonitrile for monitoring the released DOX concentration by UV-vis RP-HPLC using H_2O/Acetonitrile (7:3, v/v) as mobile phase at a constant pump rate of 1 mL/min, and at detection-wavelength of 234 nm.

4.2.17. Cell Viability and Live/Dead Assays

Cell viability was assessed by MTT assay on MCF-7 ADR or MCF-7 cell line. Briefly, respective cell line was cultured on 96-well plate (1×10^4 cells per well) in 100 μL RMPI-1640 medium supplemented with 10% FBS, 1% penicillin and streptomycin antibiotics, and with (for MCF-7 ADR) or without (for MCF-7) 900 ng/mL DOX. The plates were incubated in 5% CO_2 humidified atmosphere at 37 °C for 24 h. Thereafter, the solution was aspirated and replaced by 90 μL fresh RMPI-1640 medium, followed by adding 10 μL of desired concentrations of free DOX, free CNM, n-PCD, PD, or PCD and incubated for another 48 h. Next, the solution was aspirated and replaced by 100 μL fresh medium followed by addition of MTT solution (20 μL, 5 mg/mL) and incubation of 4 h. Finally, the solution was replaced by adding 200 μL DMSO and placed on shaking bed for 15 min in dark before being put into microplate reader to measure the absorbance at the wavelength of 570 nm.

To evaluate the dead and live cells, PI/FDA cell staining assay was conducted. Typically, MCF-7 ADR cell line was cultured into 12 well plate (1×10^5 cells/well) in RMPI-1640 medium with free PBS, DOX, n-PCD, PD, or PCD at the equivalent DOX concentration of 1.5 μg/mL and incubated for another 24 h. Subsequently, the solution was aspirated and replaced by 500 μL cold PBS containing FDA (10 μg/mL) and PI (20 μg/mL) solution to stain live and dead cells, respectively, and incubated for 10 min

at 37 °C. Finally, cells were gently washed 2 times with cold PBS and examined by fluorescence microscopy.

4.2.18. Mitochondria Drug-Targeting Localization

MCF7-ADR or MCF-7 cells were cultured in a special glass-bottom culture plate at a density of 1×10^3 cells for 24 h. Thereafter, cells were treated with DOX, n-PCD, PD, or PCD at DOX equivalent dose of 1.5 μg/mL and incubated for 12 h. Next, cells were gently washed with cold PBS and treated with Mito-tracker green first followed by staining with Hoechst 33342 to stain mitochondria and nucleus, respectively, according to the manufacturer's protocol, followed by imaging with CLSM.

4.2.19. *In Vitro* Intracellular ROS Evaluation

ROS detection kit assay was performed. Briefly, MCF7-ADR or MCF-7 cells were cultured at a density of (1×10^5 cells) into 12 well plates for 24 h. Next, cells were treated with free PBS, PC, DOX, n-PCD, PD, or PCD at the equivalent DOX concentration of 1.5 μg/mL and incubated for another 24 h. Therefore, the culture was gently washed twice with cold PBS and subsequently add 2',7'-dichlorofluorescin diacetate (DCFH-DA) solution in cold PBS (200 mL, 10 μM) followed by 20 min incubation. Finally, the cells were washed twice with cold PBS and imaged by fluorescence microscopy.

4.2.20. *In Vivo* Antitumor Activity and Histological Analysis

For antitumor activity study, MCF-7 ADR tumor model was established into the right limb armpits of 6-week-old female Balb/c nude mice and when the tumor size reached ~80 mm^3, mice were blindly distributed into 5 treatment groups made of 6 mice each group and initiate treatment experiments. At day 0, 3, 6, and 9, PBS, free DOX, n-PCD, PD, or PCD was intravenously injected into mice at the DOX equivalent dose of 5 mg/kg. Meanwhile, mice body weight change and tumor size were periodically monitored each three days since the first injection till day 21. To calculate the tumor volume, the following equation: $V = A \times B^2/2$, where "A" is the longest and "B" is the shortest side of the tumor was used. For histological analysis study, at day 10, one mouse for each treatment group was sacrificed and tumor and the major organs were harvested and sliced into 10 μm thick section stained for H&E staining and imaging.

4.2.21. Statistical analysis

The results were presented as mean ± standard deviation (SD). The Student's t-test was used to analyze the significance of the results and data were statistically judged significant when the two-tailed P-Value is < 0.05.

4.3. Results and Discussion

4.3.1. Synthesis and Characterization of Monomers and Polymers

Initially, the DOX monomer was prepared by connecting doxorubicin and methacrylate monomer *via* ROS cleavable thioketal (TK) linker **(Scheme 4.1,** and **4.2)**. Based on the synthesized cinnamaldehyde derivative compound, cinnamaldehyde monomer denoted as CNM was prepared by esterification reaction **(Scheme 4.3)**. The ^{1}H & ^{13}C-NMR and ESI-MS as well as HPLC characterizations confirmed the successful preparation of both DOX and CNM monomers **(Figure 4.5, 4.6, 4.7, 4.8, 4.10, 4.11,** and **4.12)**.

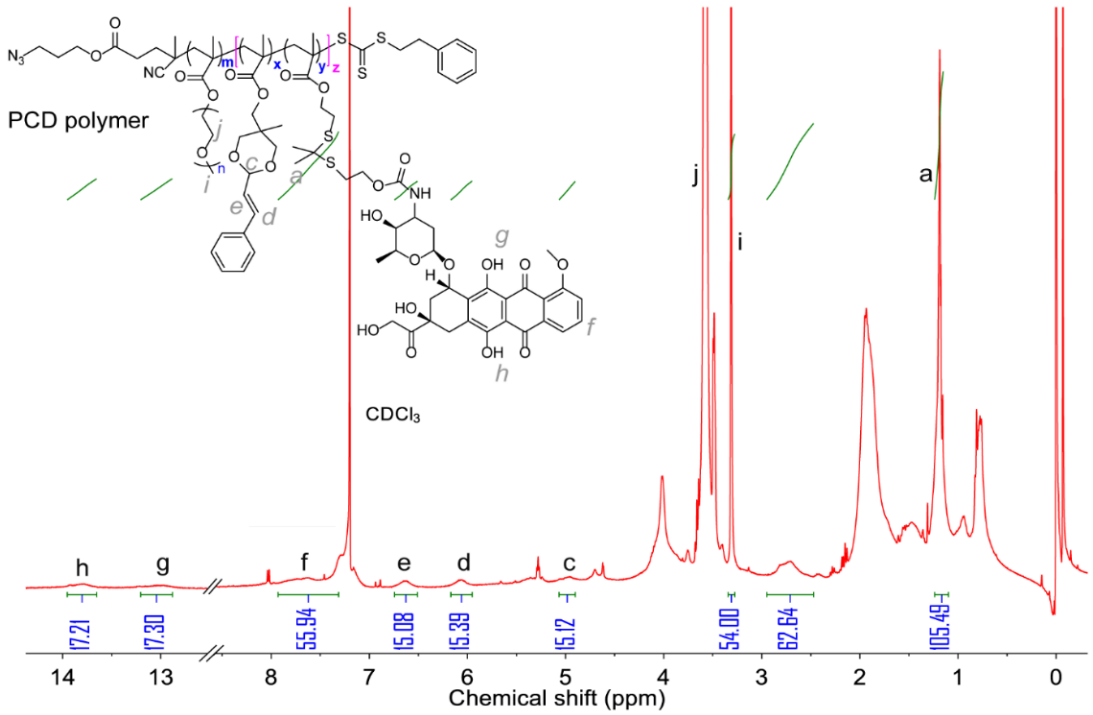

Figure 4. 18. PCD polymers ^{1}H-NMR spectra in $CDCl_3$.

For N_3-PEOGMA$_m$-*b*-P(CNM$_x$-*co*-DOX$_y$) polymer synthesis, a reversible

addition fragmentation chain transfer (RAFT) polymerization technique was chosen using N_3-PEOGMA$_{18}$-RAFT as macro-RAFT chain transfer agent **(Scheme 4.5,** and **4.6)**. The CNM and DOX monomer polymerization degree were adjusted to 15 and 17, respectively, as confirmed by ^{1}H-NMR analysis and the synthesized diblock copolymer was denoted as N_3-PEOGMA$_{18}$-*b*-P(CNM$_{15}$-*co*-DOX$_{17}$) **(Figure 4.18)**. GPC characterization result showed that N_3-PEOGMA$_{18}$-*b*-P(CNM$_{15}$-*co*-DOX$_{17}$) diblock copolymer has molecular weight of M_n = 28,145 g/mol with a relatively low molecular weight distribution of M_w/M_n = 1.12 **(Figure 4.22B)**.

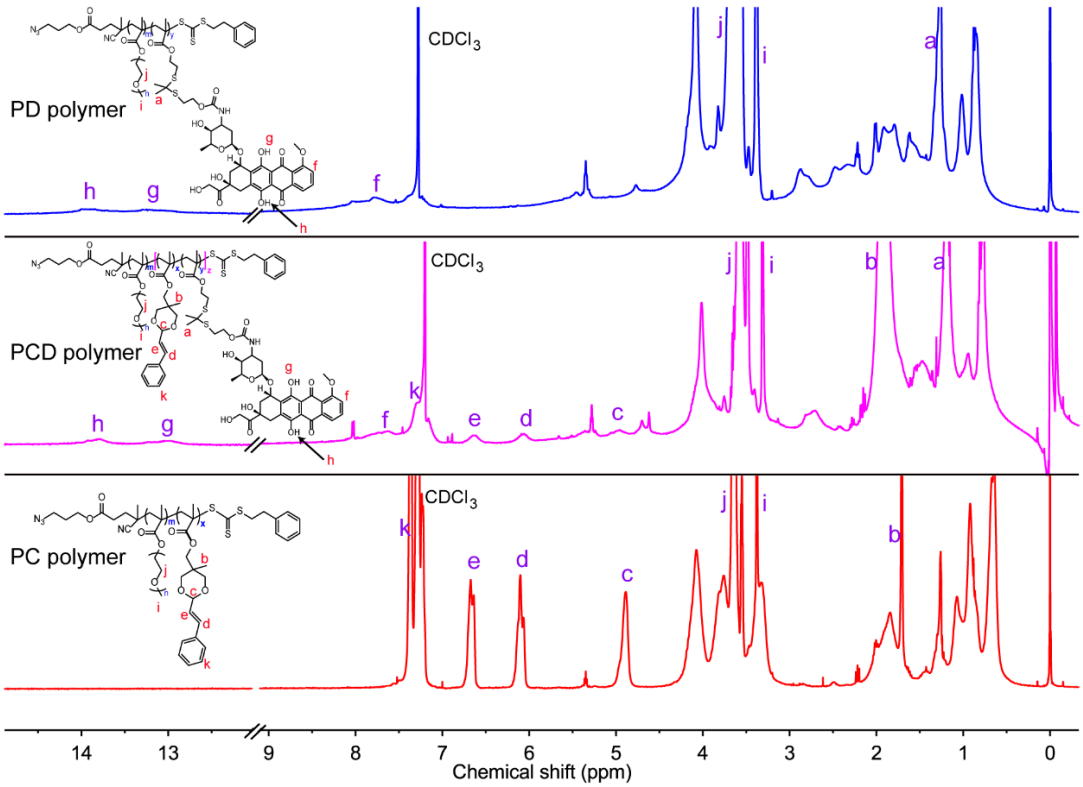

Figure 4. 19. ^{1}H-NMR spectra in $CDCl_3$ for PD, PCD and PC polymers.

By using the same procedure, the polymer N_3-PEOGMA$_{18}$-*b*-P(CNM)$_{47}$ *i.e.* prepared without DOX monomer ($M_{n,GPC}$ = 23,632 g/mol) and N_3-PEOGMA$_{18}$-*b*-P(DOX)$_{18}$ *i.e.* prepared without CNM monomer ($M_{n,GPC}$ = 23,615 g/mol) were synthesized **(Figure 4.19** and **4.20)**.

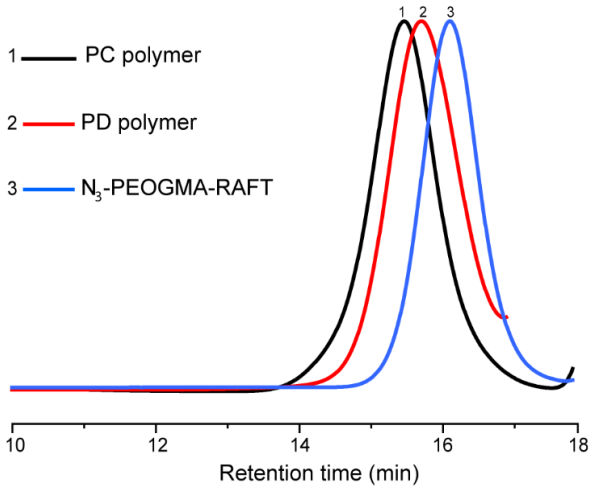

Figure 4. 20. PC, PD and PEOGMA-RAFT polymers analysis by GPC.

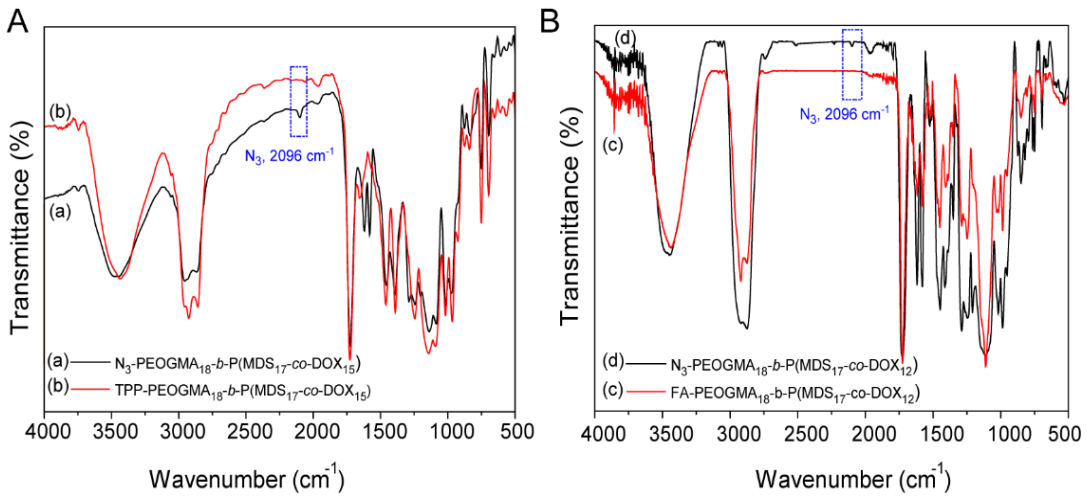

Figure 4. 21. (A) TPP-PCD and **(B)** FA-PCD polymers FTIR characterization after CuAAC click reaction.

Next TPP-alkyne or FA-alkyne were separately conjugated to the prepared polymers through click chemistry between alkyne and azide end-functional groups by copper(I)-catalyzed azide-alkyne 1,3-dipolar cycloaddition (CuAAC) mechanism to get TPP or FA-PEOGMA$_{18}$-*b*-P(CNM$_{15}$-*co*-DOX$_{17}$) diblock copolymers as an example **(Figure 4.13, 4.14,** and **4.15)**. After the click reaction, the FT-IR analysis spectrum showed a complete disappearance of characteristic peak at 2096 cm^{-1} attributed to azide functional group before the reaction suggested that TPP or FA was successfully attached to the polymers **(Figure 4.21)**.

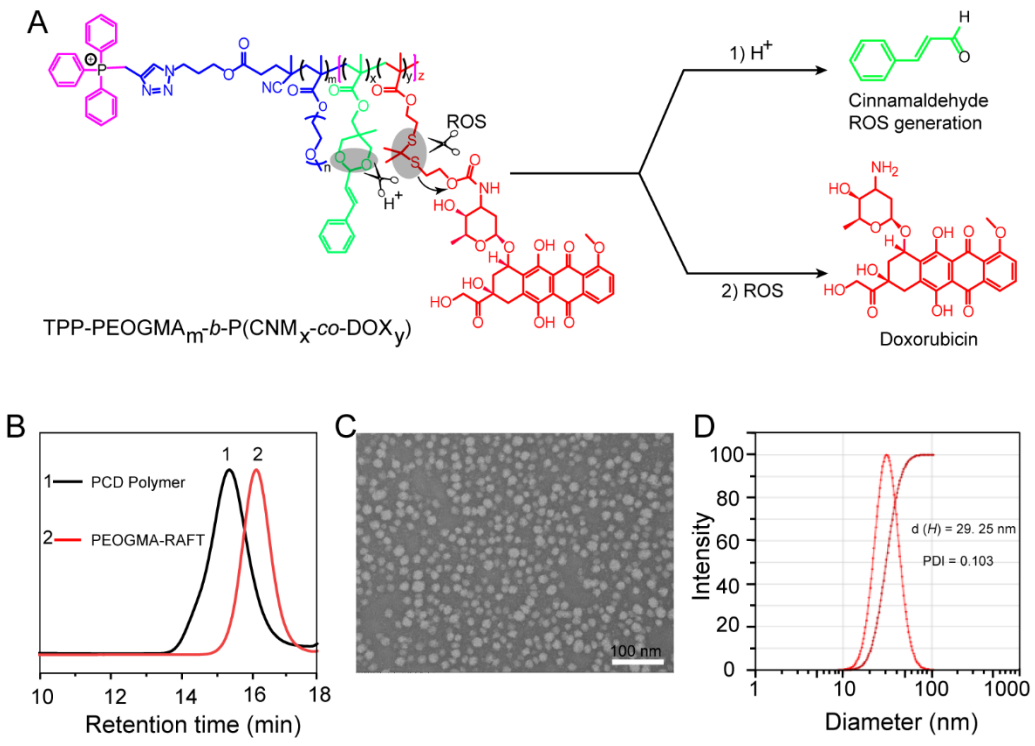

Figure 4. 22. PCD polymer proposed mechanism of action and characterization. **(A)** Schematic representation of the proposed mechanism for PCD polymer to release the cinnamaldehyde and doxorubicin in the cytosol and mitochondria in the cancer cell,

respectively, *via* cascade reaction events stimulated by endosomal acidic pH to release cinnamaldehyde and ROS to release doxorubicin. **(B)** PCD polymer retention time analysis by GPC. **(C)** TEM image for PCD nanoparticles. (D) PCD nanoparticle size characterization by DLS.

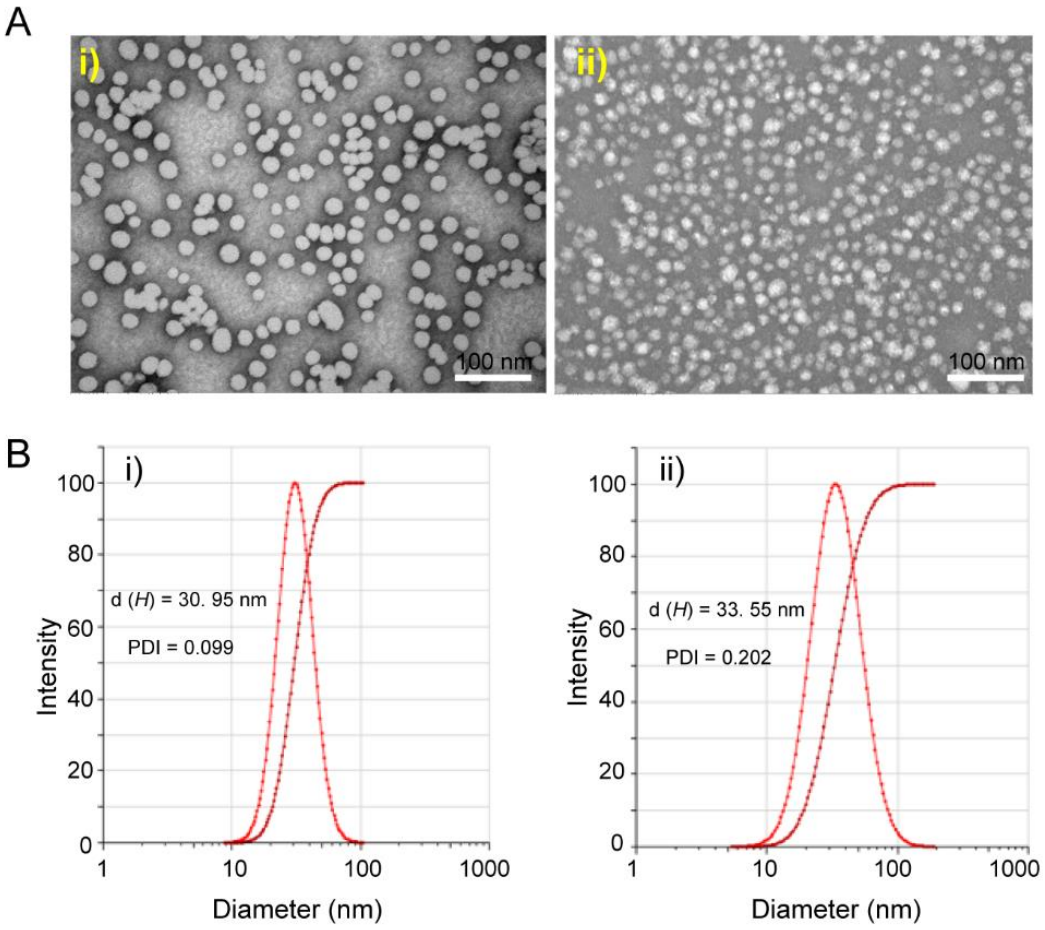

Figure 4. 23. (A) TEM image for PC (i) and PD nanoparticles (ii). **(B)** DLS size characterization for PC (i) and PD nanoparticles (ii).

4.3.2. Nanoparticle Preparation, Stability and Drug Release Studies

Due to amphiphilicity feature of our prepared diblock copolymers, they can self-assembly into micelle nanoparticles through the solvent replacement approach. For example, a mixture of TPP-PEOGMA$_{18}$-*b*-P(CNM$_{17}$-*co*-DOX$_{15}$) and FA-PEOGMA$_{18}$-*b*-P(CNM$_{17}$-*co*-DOX$_{15}$) diblock copolymers (ratio: 4:1, respectively) was used to prepare micelle denoted as PCD nanoparticles decorated with both FA and TPP as targeting species for cancer cells and mitochondria, respectively.[29, 30]

Table 4. 1. List of synthesized PCD, PC, PD and n-PCD polymers, "R" stands for TPP or FA.

N^o	Polymer name	Polymer abbreviation	M_n (g/mol)	DOX encapsulation capacity (wt%)
1	R-PEOGMA$_{18}$-*b*-P(CNM$_{15}$-*co*-DOX$_{17}$)	PCD	28 145	28.31
2	R-PEOGMA$_{18}$-*b*-P(CNM)$_{47}$	PC	23 632	-
3	R-PEOGMA$_{18}$-*b*-P(DOX)$_{18}$	PD	23 615	41.75
4	PEOGMA$_{18}$-*b*-P(CNM$_{15}$-*co*-DOX$_{17}$)	n-PCD	28 145	28.31

TEM image analysis showed uniform round shaped morphology particles with diameter size of 25.17 nm for PCD nanoparticles **(Figure 4.22C)**. This result was in consistent with DLS characterization as PCD nanoparticles have an average hydrodynamic diameter (d(*H*)) of 29.25 nm with a relatively lower polydispersity index (PDI) of 0.103 **(Figure 4.22D)**.

Using similar methods, PEOGMA$_{18}$-*b*-P(CNM$_{17}$-*co*-DOX$_{15}$) diblock copolymer was used to prepare nanoparticles without any targeting moiety and denoted as n-PCD nanoparticles **(Table 4.1)**.

Moreover, TPP&FA-PEOGMA$_{18}$-*b*-P(CNM)$_{47}$ or TPP&FA-PEOGMA$_{18}$-*b*-P(DOX)$_{18}$ diblock copolymers were used to prepared nanoparticles named PC or PD, respectively, that are nanoparticles decorated with both TPP and FA targeting moieties but without DOX segment for PC nanoparticles, and CNM segment for PD nanoparticles **(Figure 4.23)**.

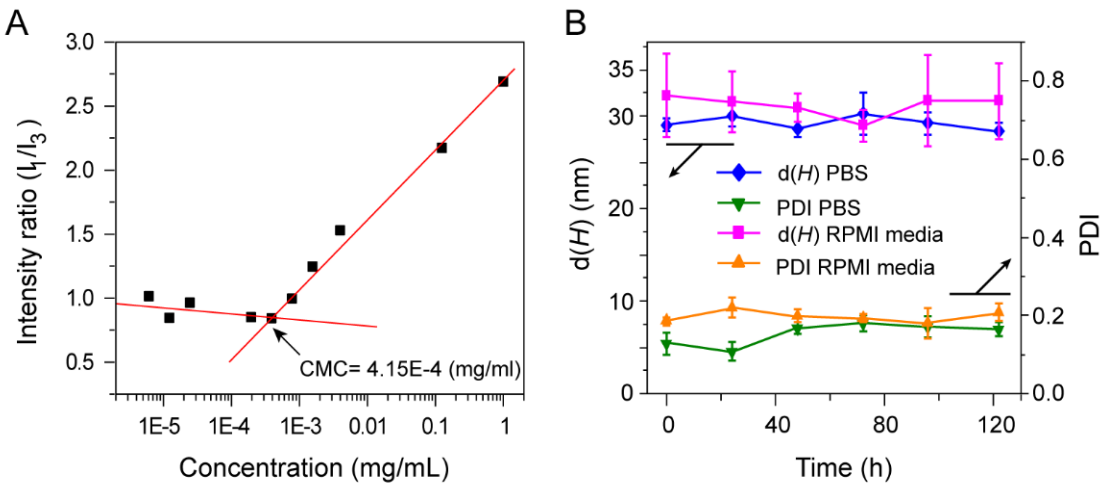

Figure 4. 24. Critical micelle concentration and stability analysis for PCD nanoparticle. **(A)** Critical micelle concentration analysis for PCD nanoparticle. **(B)** PCD nanoparticle stability study in PBS or RPMI 1600 cell culture medium containing 10% FBS over a period of 5 days.

The stability is among the critical factors that determine an ideal nanoparticle designed for *in vivo* studies. The critical micelle concentration (CMC) analysis showed

a relatively lower number of 4.15 $\times 10^{-4}$ mg/mL which suggested enhanced stability of PCD nanoparticles under low concentration **(Figure 4.24A)**. Moreover, PCD nanoparticles proved to be stable under various solution conditions such as in RPMI 1640 media containing 10% FBS or PBS pH 7.4 at 37 °C even up to 5 days of incubation without obvious observable change of d(*H*) and PDI as confirmed by DLS study **(Figure 4.24B)**.

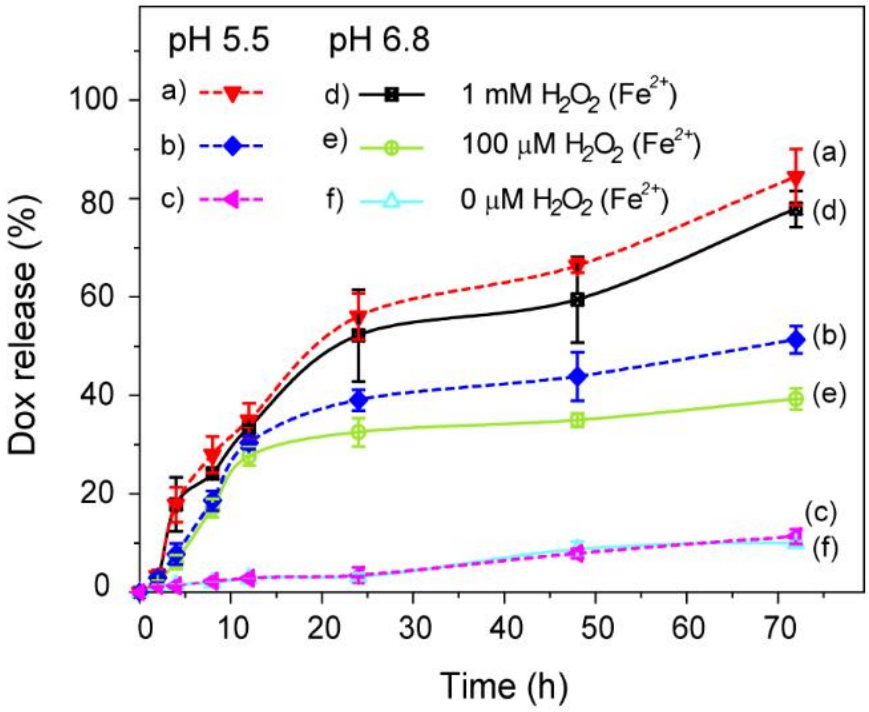

Figure 4. 25. Time dependent DOX release profile for PCD nanoparticle in aqueous solution containing H_2O_2 and Fe^{2+} at pH 5.5 or 6.8.

The application of polymer prodrug with programmable drug release in drug delivery is recently accumulating much interest due to their fascinating advantages such as high drug loading capacity with no premature drug leakage during systemic

circulation.[31] The PCD nanoparticles drug loading capacity was found to be as high as 28.31wt% for doxorubicin based on ^{1}H-NMR analysis. Given the fact that TK linker was used to covalently conjugate DOX segment to the backbone of the hydrophobic block of the PCD diblock polymers used to prepare PCD nanoparticles, this TK bond that can be cleaved by ROS and be used as programmable means to specifically release parent DOX in the mitochondria of the cancer cells after the amplification of intracellular ROS by cinnamaldehyde.[32]

The *in vitro* DOX release profile was monitored by Uv-vis HPLC in a simulated tumor microenvironment in the presence of various concentration of H_2O_2 (0 μM, 100 μM, or 1 mM) and $FeSO_4$ (1.0 μM) at 37 °C and at pH 5.5 or 6.8. The incubation of PCD nanoparticles at pH 5.5 or 6.8 into H_2O_2 free medium showed that a negligible amount of DOX that is less than 10% can be released up to 72 h either at pH 5.5 or 6.8, which suggested that the acidity has a little effect on the release of DOX. On the other hand, a relatively moderate and time dependent DOX release of 39% and 52% was observed when the 100 μM H_2O_2 was added at 72 h and at the pH 6.8 or 5.5 medium, respectively. In a sharp contrast, the addition of 1 mM H_2O_2 into the incubation medium at pH 6.8 or 5.5 showed enhanced and comparable DOX release capacity of ~80% in sustainable and time dependent fashion up to 72 h **(Figure 4.25)**.

4.3.3. Cell viability and Live and Dead evaluation results

The cytotoxicity effect of our prepared nanoparticles was evaluated by MTT assay against DOX resistant MCF7-ADR or nonresistant MCF-7 cell lines by treatment with DOX, n-PCD, PD, or PCD formulations.

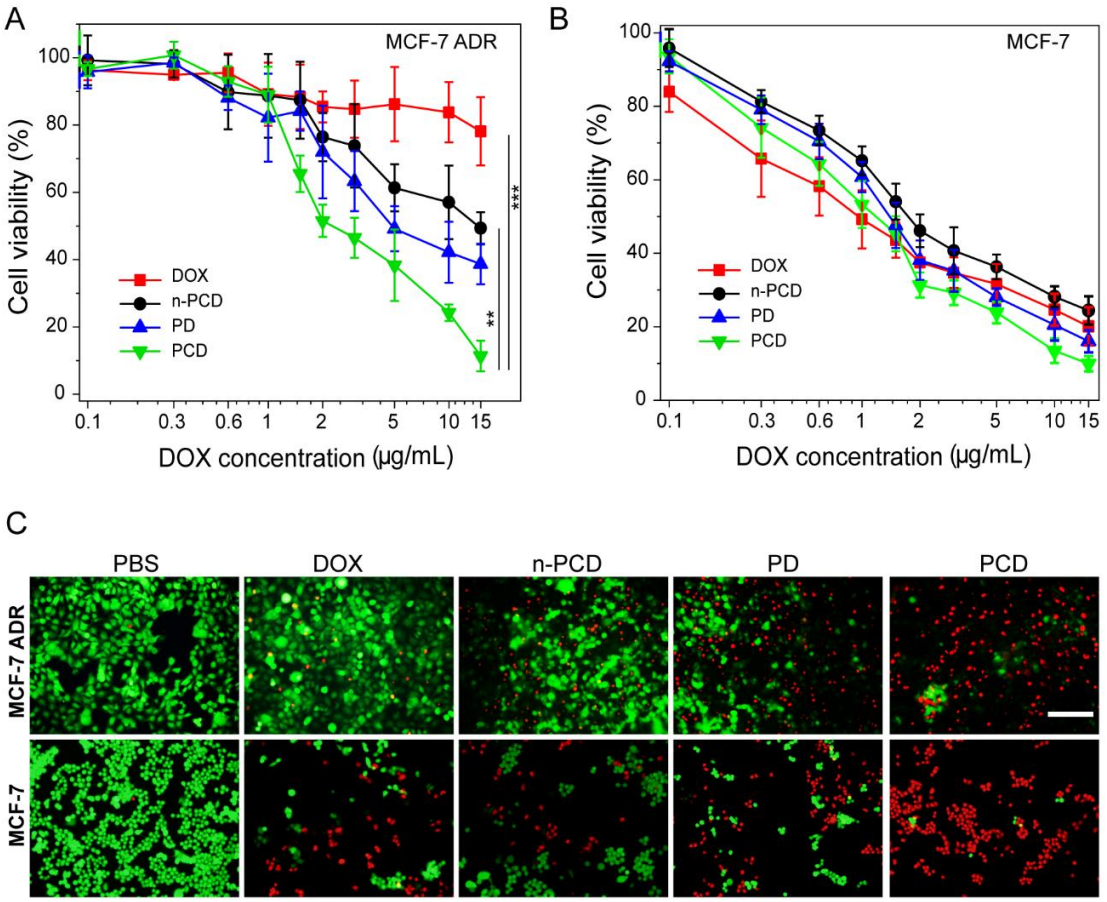

Figure 4. 26. Cell viability assay for DOX, n-PCD, PD, and PCD formulations against **(A)** MCF-7 ADR and **(B)** MCF-7 cell lines for 48 h. Results= mean ±SD, *n* = 4. **(C)** Live and Dead assay for MCF-7 ADR or MCF-7 cell lines treated DOX, n-PCD, PD, and PCD formulations at DOX equivalent treatment dose of 1.5 μg/mL for 24 h. *n* = 3. Scale bar = 50 μm.

As presented from **Figure 4.26A**, it is observed that treatment with free DOX has a negligible cytotoxicity effect against MCF7-ADR cells as the viable cell was still more than 80% up to the high concentration of 15 μg/mL. Moreover, n-PCD nanoparticles showed a moderate MCF7-ADR cell cytotoxicity with the half maximal inhibitory concentration (IC_{50}) value of 12.08 μg/mL. On the other hand, PD

nanoparticles exhibited an improved MCF7-AD cell killing efficacy with IC_{50} value of 5.35 μg/mL. In a contrast, the group treated with PCD nanoparticles showed a significantly enhanced cytotoxicity against MCF7-AD cell line with IC_{50} value of 2.07 μg/mL that is around 6-fold and 2-fold lower than that of n-PCD and PD nanoparticles, respectively **(Table 4.2)**.

Table 4. 2. The calculated IC_{50} by treating MCF-7 ADR or MCF-7 cell lines with various concentrations of free DOX, n-PCD, PD, and PCD formulations for 48 h. Results = mean, $n = 4$.

Treatment Formulation	MCF-7 ADR (μg/mL)	MCF-7 (μg/mL)
DOX	---	0.951
n-PCD	12.08	1.87
PD	5.35	1.40
PCD	2.07	1.09

Expectedly, the treatment with free DOX showed high response with remarkably enhanced cytotoxicity against MCF-7cell line with the relatively lowest calculated IC_{50} value of 0.951 μg/mL. Intriguingly, the treatment with n-PCD and PD formulation showed comparable cytotoxicity effect against MCF-7 cell line with the IC_{50} value of 1.87 μg/mL and 1.40 μg/mL, respectively. Although, treatment with PCD nanoparticles showed a comparable cytotoxicity with the IC_{50} value of 1.09 μg/mL

compared to free DOX cytotoxicity profile against MCF-7cell line, it was remarked that the higher dose >2 μg/mL of PCD nanoparticles performed much better in killing MCF-7cell line compared to bare DOX formulation at the same doses. (**Figure 4.26B, Table 4.2**).

Next, after treating MCF-7 ADR cell line with the live and dead assay revealed that DOX, n-PCD, PD, and PCD formulations at DOX equivalent treatment dose of 1.5 μg/mL for 24 h, the live and dead assay using FDA (green stain) and PI (red stain) to stain live and dead cells, respectively after treatment, revealed that DOX has a negligible cytotoxic effect as almost all cell were found to be stained greed (live cells). Treatment with n-PCD and PD nanoparticles showed moderate cytotoxicity against MCF-7 ADR cell line as a fraction of cells were stained red positive (dead cells). In a sharp contrast, PCD nanoparticles showed enhanced cytotoxicity against MCF-7 ADR cell line as the majority of cells were found to be PI positive (**Figure 4.26C)**.

The treatment of MCF-7 cell line with both DOX, n-PCD and PD formulations showed comparable cytotoxic effect and it was observed that PCD nanoparticles has efficacious cytotoxicity against MCF-7 cell line compared to other formulations tested (**Figure 4.26C)**. This live and dead assay result is found to be in a good agreement with the cell cytotoxicity evaluation results presented in **Figure 4.26A,B**.

4.3.4. Mitochondria Targeting Localization

As our prepared PCD nanoparticles were designed to target mitochondria within the cells, their mitochondria targeting properties were examined by CLSM on MCF7-ADR or MCF-7 using mito-tracker green as common probe to stain mitochondria and

Hoechst 33342 (blue) to stain the nucleus as well as the intrinsic natural red fluorescence of DOX.

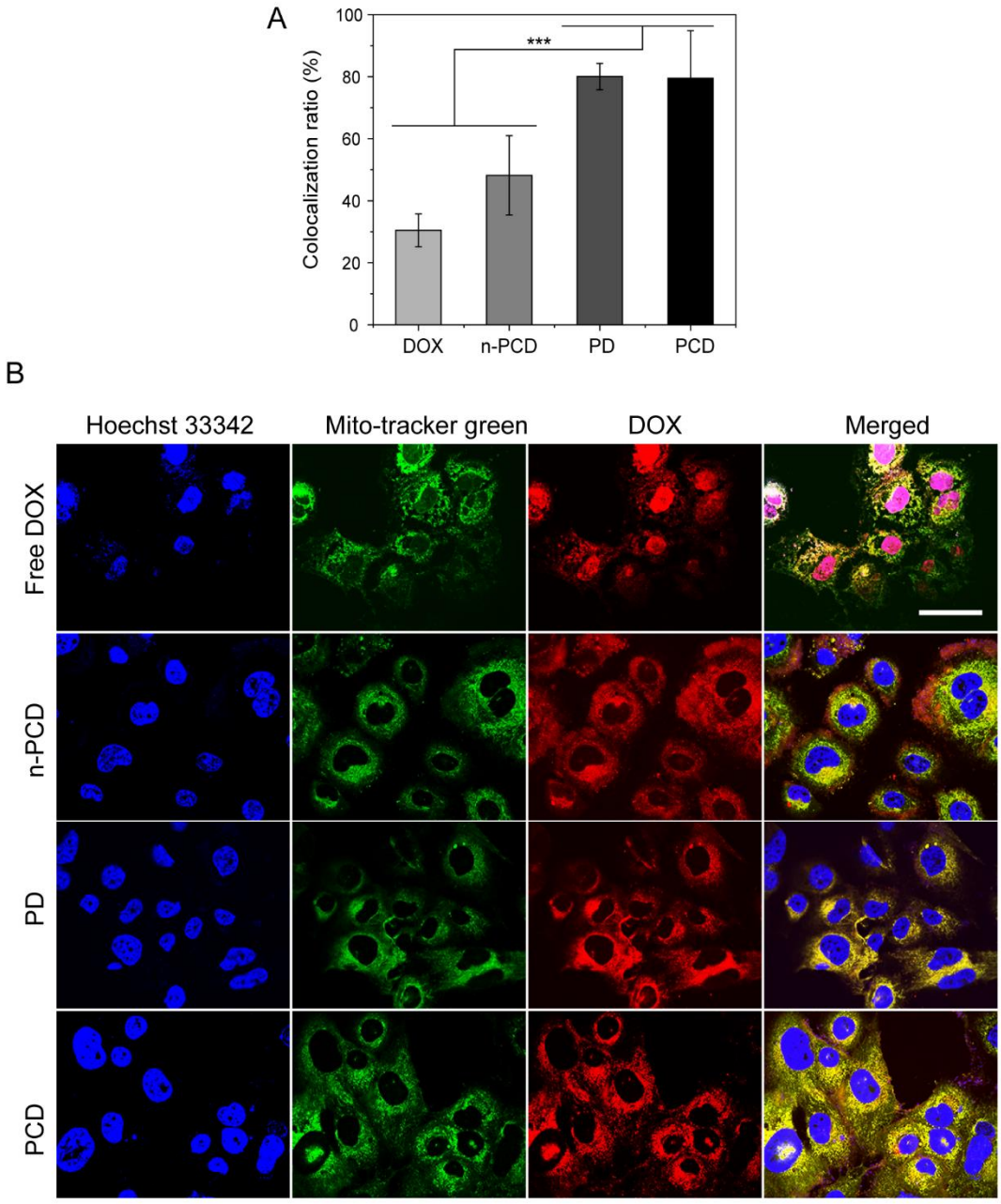

Figure 4. 27. Mitochondria localization and cell viability assay for MCF-7 ADR cell line. **(A** and **B)** CLMS images for the evaluation of drug cellular accumulation and

mitochondria localization in MCF-7 ADR cell line with DOX, n-PCD, PD, and PCD formulations at DOX equivalent treatment dose of 1.5 μg/mL for 12 h, by staining nucleus by Hoechst 33342 (blue), mitochondria by mito-tracker green, intrinsic red fluorescence for DOX and their respective calculated colocalization ratio by ImageJ software between red (DOX) and green (Mitochondria) fluorescence region to generate yellowish color. Scale bar = 5 μm.

From **Figure 4.27A-B**, after treatment of MCF7-ADR cell line treatment with DOX, n-PCD, PD, or PCD at DOX equivalent dose of 1.5 μg/mL and incubated for 12 h, it was observed that much of DOX can be found in the nucleus compared to mitochondria for DOX treated group with mitochondria colocalization that is less than 30%. Expectedly, treatment with n-PCD that is nanoparticle without any targeting species showed poor mitochondria targeting property with colocalization ratio of less than 50%. Moreover, CLSM merged image clearly showed that much red fluorescence intensity was surrounding green fluorescence within the cytoplasm which suggested a slow cellular penetration mechanism of n-PCD nanoparticles.

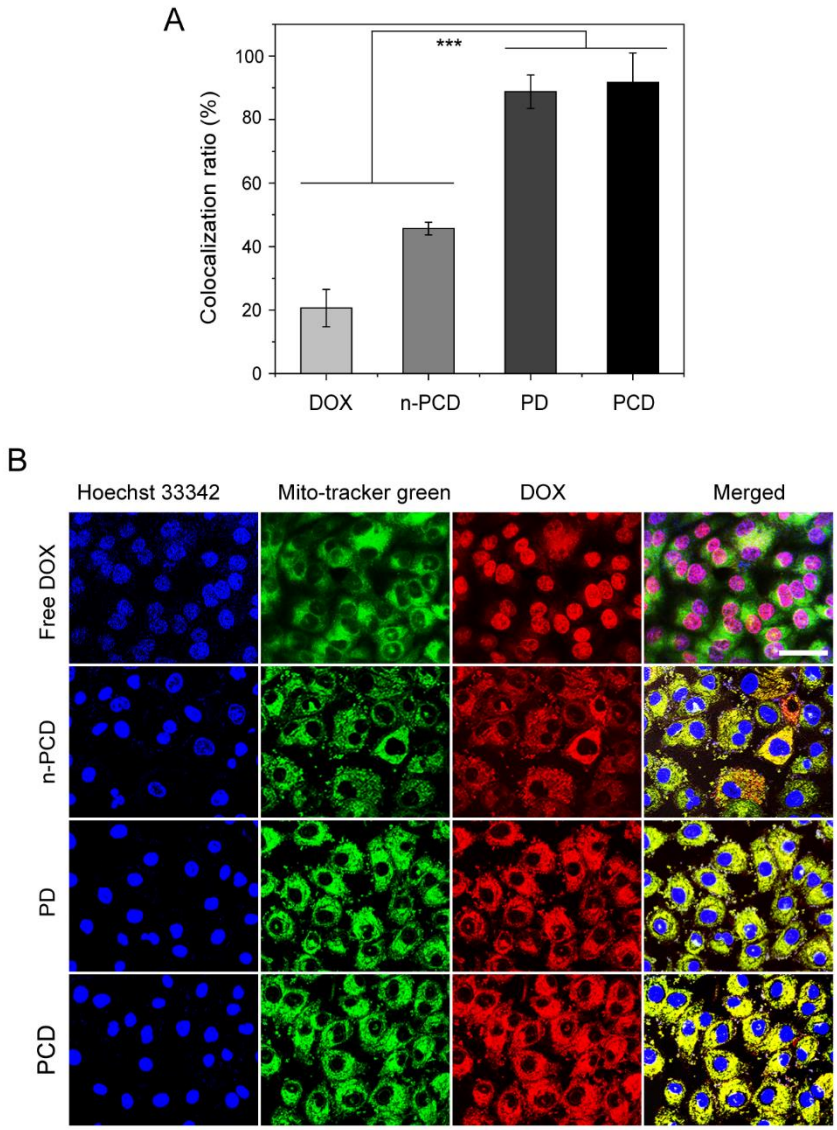

Figure 4. 28. Mitochondria localization and cell viability assay for MCF-7 cell line. **(A** and **B)** CLMS images for the evaluation of drug cellular accumulation and mitochondria localization in MCF-7 cell line with DOX, n-PCD, PD, and PCD formulations at DOX equivalent treatment dose of 1.5 µg/mL for 12 h, by staining nucleus by Hoechst 33342 (blue), mitochondria by mito-tracker green, intrinsic red fluorescence for DOX and their respective calculated colocalization ratio by ImageJ software between red (DOX) and green (Mitochondria) fluorescence region to generate yellowish color. Scale bar = 5 µm.

In a sharp contrast, the treatment with PD or PCD that are nanoparticles functionalized with both FA and TPP, showed enhanced potential to target mitochondria as confirmed by increased yellowish color showed by the merged images as a result of comparable green (mitochondria) and red (DOX) fluorescence colors colocalization ratio of ~85%. Interestingly, similar colocalization ratio trend was observed by treating MCF-7 with DOX, n-PCD, PD, or PCD, which suggested that PCD nanoparticles can extensively be accumulated and target mitochondria in both resistant MCF7-ADR or nonresistant MCF-7 cell lines at a comparable extent **(Figure 4.28A-B)**.

4.3.5. Intracellular ROS level evaluation results

After treating MCF7-ADR or MCF-7 cells with free PBS, PC, DOX, n-PCD, PD, or PCD at the equivalent DOX concentration of 1.5 μg/mL for 24 h, the intracellular ROS level was monitored by staining cells with DCFH-DA according to the manufacturer protocol (beyotime). As it is clearly observed from **Figure 4.29**, treatment with DOX or PD against MCF7-ADR showed negligible ROS generation that is comparable to the negative control group treated with PBS. In contrast, treatment with PC, n-PCD and PCD nanoparticles against MCF7-ADR showed remarkable and comparable capacity to induce the intracellular ROS generation as evidenced by the relatively strong green fluorescence. This could be possibly explained by the fact that all of these nanoreactors contain cinnamaldehyde moiety which is known to induce an increase the intracellular ROS generation in cancer cells. Interestingly, similar intracellular ROS generation trend by treating MCF-7 cells with free PBS, PC, DOX,

n-PCD, PD, or PCD was observed **(Figure 4.30)**.

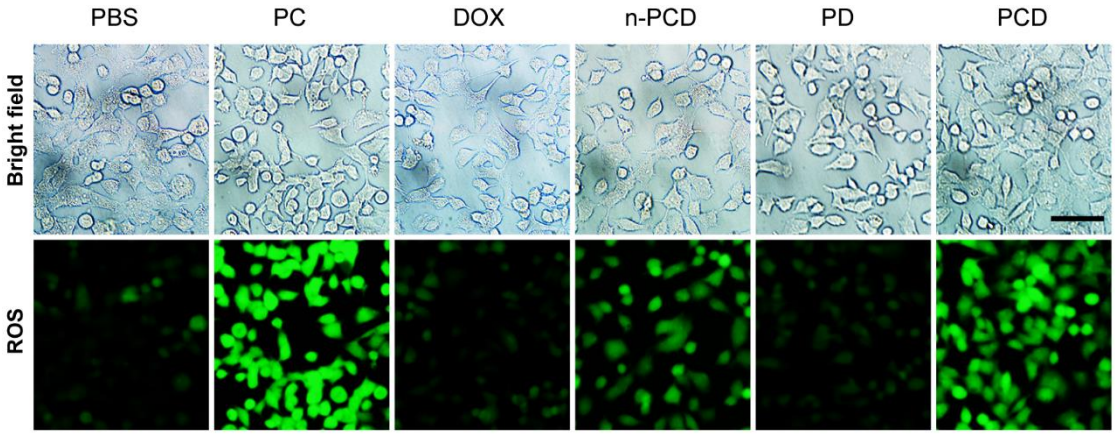

Figure 4. 29. Intracellular ROS level MCF-7 ADR cell line treated with free PBS, PC, DOX, n-PCD, PD, or PCD at the equivalent DOX concentration of 1.5 μg/mL for 24 h. n = 4. Scale bar = 10 μm.

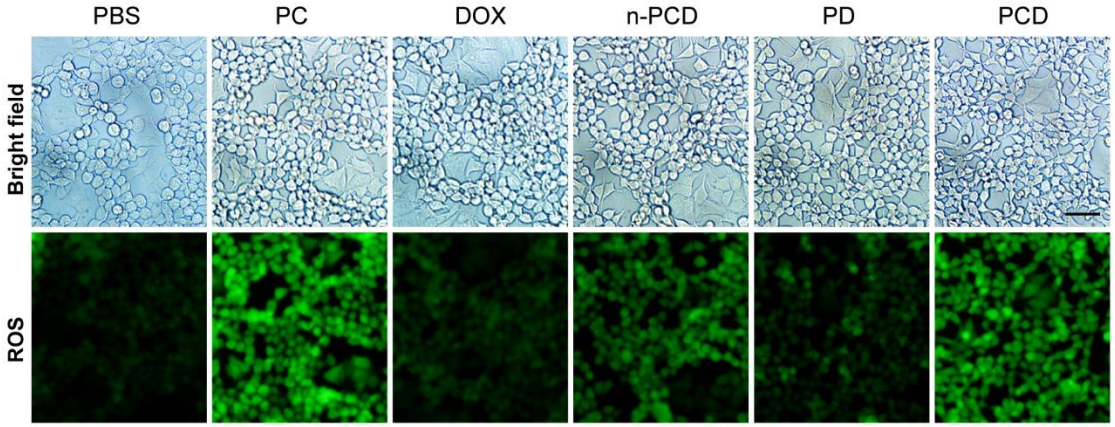

Figure 4. 30. Intracellular ROS level MCF-7 cell line treated with free PBS, PC, DOX, n-PCD, PD, or PCD at the equivalent DOX concentration of 1.5 μg/mL for 24 h. n = 4. Scale bar = 10 μm.

4.3.6. Antitumor Efficacy

To test antitumor effect of our prepared nanoparticles, 5 weeks-old Balb/c nude mice bearing MCF-7 ADR tumor model with the size around 80 mm^3 were randomly divided into 5 groups and intravenously injected with PBS, DOX, n-PCD, PD, or PCD formulations at the DOX equivalent dose of 5 mg/kg four times at an interval of 3 days. The tumor growth profile was then monitored every and each 3 days since the first injection to the day 21.

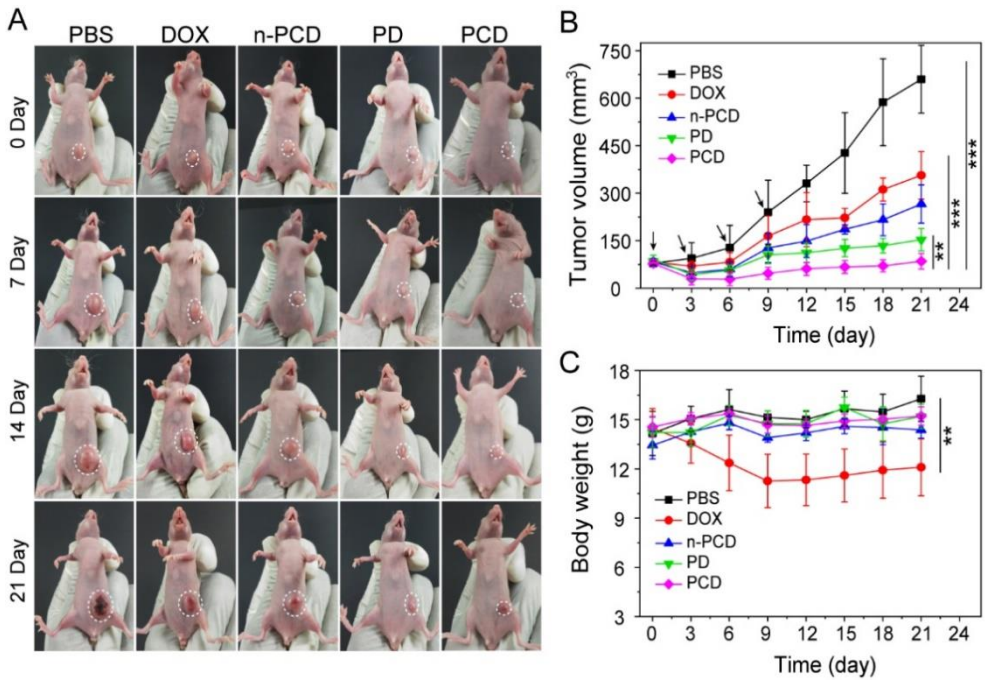

Figure 4. 31. Tumor growth profile and mice body weight monitoring during treatment. **(A)** Digital images showing the tumor treatment progress for MCF-7 ADR tumor bearing mice by PBS, DOX, n-PCD, PD, or PCD formulation at DOX equivalent dose of 5 mg/kg at different time interval. **(B)** MCF-7 ADR tumor growth profile under treatment for 21 days. The arrows show the injection time (n=5). **(C)** Mice body weight change monitoring trend during treatment (*n* =5).

From **Figure 4.31A-B**, it is clearly observed that the tumor was rapidly growing for the control group treated with PBS as the tumor size reached to around 700 mm^3 at day 21. Although DOX treated group showed a relatively reduced tumor growth profile of 357 mm_3 tumor size at day 21 that is almost two times smaller compared to PBS treated group, this should also be explained to the fact that the body weight of the DOX treated group was heavily affect during treatment which can also have effect on its tumor growth profile against MCF-7 ADR tumor model. On the other hand, treatment with n-PCD formulation showed a moderate tumor growth suppression extent as the tumor size reached to 265 mm^3 at day 21.

An increased tumor growth inhibition was observed by treating mice with PD formulation as the tumor size was calculated to be 146 mm^3. Intriguingly, PCD nanoparticles showed a relatively enhanced tumor growth inhibition profile against MCF-7 ADR tumor model that is exactly 1.8-fold, 3.2-fold, 4.2-fold effectiveness compared to PD, n-PCD, and DOX treatment formulations, respectively. Moreover, the monitoring of mice body weight during treatment showed that the treatment with n-PCD, PD, or PCD formulations showed no unusual body weight change. However, in addition to the noticed diarrhea during treatment, each mouse treated with DOX showed a tremendously body weight loss of almost 36% during the entire treatment course up to day 21 **Figure 4.31C**.

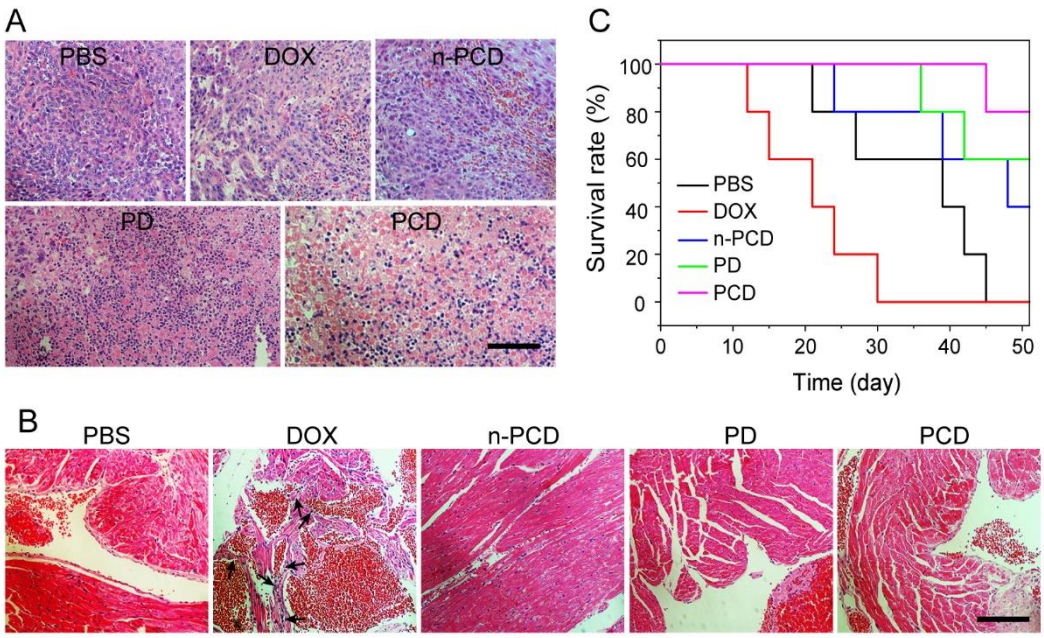

Figure 4. 32. (A) and **(B)** H&E staining images for tumor and heart tissue for histological analysis at day 10 of treatment, respectively. **(C)** Treatment survival rate evaluation (n=5). Scale bar = 100 µm.

At day 10 during treatment, a mouse from each group treated with PBS, DOX, n-PCD, PD, or PCD formulations was randomly selected and sacrificed for histological analysis of tumor tissues and tissues of major organs such as heart, kidney, spleen, lung, and liver. From **Figure 4.32A,** the H&E staining images of tumor tissue for the mice treated with PD showed clearly remarkable tissue damage compared to DOX and n-PCD formulations which showed a lesser and comparable tumor tissue damage extent. In a sharp contrast, PCD nanoparticles showed enhanced potential to extensively damage tumor tissue. Moreover, treatment with n-PCD, PD, or PCD formulations showed no tissue damage for major organs that are heart, kidney, spleen, lung, and liver **(Figure 4.33)**. However, the heart tissues of the group treated with DOX showed major

tissue lesion and damage as mentioned by arrows which is the common side effect of doxorubicin chemotherapy (**Figure 4.32B)**.[33, 34] Finally, the survival experiment result showed that our synthesized PCD nanoparticles cannot only inhibit the tumor growth but also remarkably increase the mice patient survival rate **(Figure 4.32C)**.

4.4. Conclusion

In summary, we have successfully synthesized a polymer prodrug that is FA&TPP-PEOGMA$_{18}$-*b*-P(CNM$_{17}$-*co*-DOX$_{15}$) that can be used to prepare PCD micelle nanoparticles. The designed dual targeting PCD nanoparticles decorated with FA and TPP to target cancer cell and mitochondria, respectively, showed potential to be used as tumor specific polymer prodrug-based nanoparticles to reverse multi-drug resistance in cancer treatment and achieve enhanced therapeutic effect. The *in vitro* results showed that PCD nanoparticles can effectively kill DOX resistant MCF-7 ADR cell line comparatively to nonresistant MCF cell line mainly through the amplification of mitochondria oxidative stress and DNA damage. Moreover, the in vivo results showed that PCD nanoparticles have enhanced potential to inhibit the growth of MCF-7 ADR xenograft tumor model and can enhance the patient survival rate without observable side effect. In overall, the obtained results suggested that targeting mitochondria organelle in cancer cell can not only achieve enhanced treatment efficacy but also to overcome MDR in cancer treatment.

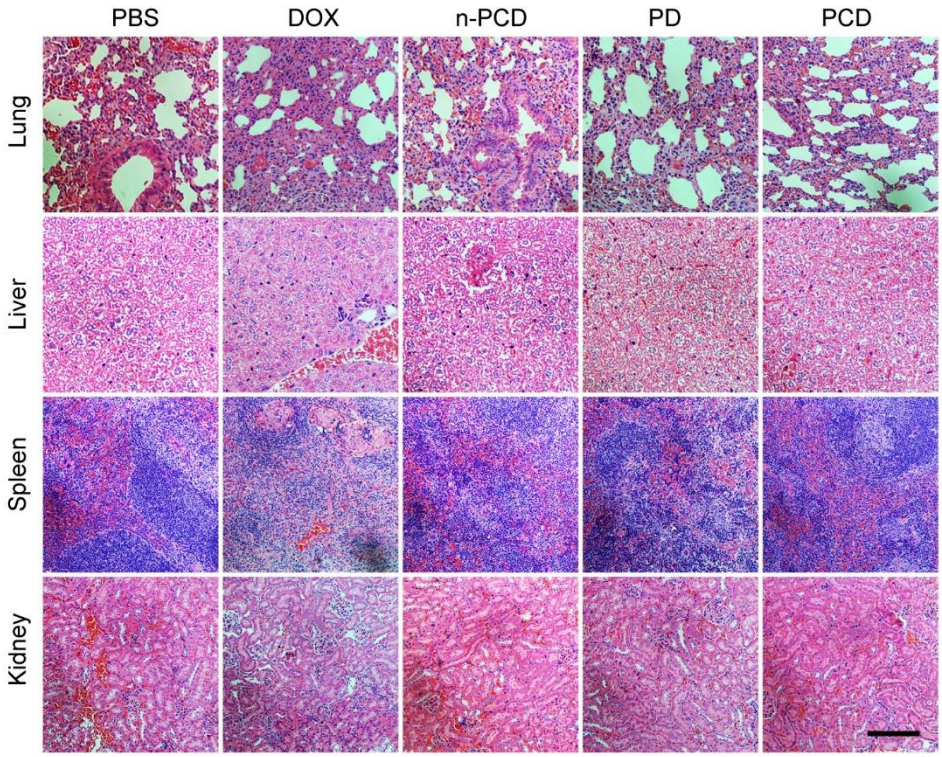

Figure 4. 33. H&E staining images for kidney, spleen liver and lung organ tissues at 10th day of treatment with various formulations that are PBS, DOX, n-PCD, PD, and PCD. Scale bar = 100 µm.

4.5. Reference

[1] Y.G. Assaraf, A. Brozovic, A.C. Gonçalves, D. Jurkovicova, A. Linē, M. Machuqueiro, S. Saponara, A.B. Sarmento-Ribeiro, C.P.R. Xavier, M.H. Vasconcelos, The multi-factorial nature of clinical multidrug resistance in cancer, Drug Resistance Updates, 46 (2019) 100645.

[2] C.F. Higgins, Multiple molecular mechanisms for multidrug resistance transporters, Nature, 446 (2007) 749-757.

[3] W. Li, H. Zhang, Y.G. Assaraf, K. Zhao, X. Xu, J. Xie, D.-H. Yang, Z.-S. Chen, Overcoming ABC transporter-mediated multidrug resistance: Molecular mechanisms and novel therapeutic drug strategies, Drug Resistance Updates, 27 (2016) 14-29.

[4] A.K. Nanayakkara, C.A. Follit, G. Chen, N.S. Williams, P.D. Vogel, J.G. Wise, Targeted inhibitors of P-glycoprotein increase chemotherapeutic-induced mortality of multidrug resistant tumor cells, Scientific Reports, 8 (2018) 1-18.

[5] G. Szakács, J.K. Paterson, J.A. Ludwig, C. Booth-Genthe, M.M. Gottesman, Targeting multidrug resistance in cancer, Nature Reviews Drug Discovery, 5 (2006) 219-234.

[6] Z. Gao, L. Zhang, Y. Sun, Nanotechnology applied to overcome tumor drug resistance, Journal of Controlled Release, 162 (2012) 45-55.

[7] M. Kumarasamy, A. Sosnik, Chapter 11 - Overcoming efflux transporter-mediated resistance in cancer by using nanomedicines, in: A. Sosnik, R. Bendayan (Eds.) Drug Efflux Pumps in Cancer Resistance Pathways: From Molecular Recognition and Characterization to Possible Inhibition Strategies in Chemotherapy, Academic Press, 2020, pp. 337-369.

[8] M. Picard, D.C. Wallace, Y. Burelle, The rise of mitochondria in medicine, Mitochondrion, 30 (2016) 105-116.

[9] Z. Zou, H. Chang, H. Li, S. Wang, Induction of reactive oxygen species: an emerging approach for cancer therapy, Apoptosis, 22 (2017) 1321-1335.

[10] K. Wang, J. Jiang, Y. Lei, S. Zhou, Y. Wei, C. Huang, Targeting Metabolic–Redox Circuits for Cancer Therapy, Trends in Biochemical Sciences, 44 (2019) 401-414.

[11] L. Raj, T. Ide, A.U. Gurkar, M. Foley, M. Schenone, X. Li, N.J. Tolliday, T.R. Golub, S.A. Carr, A.F. Shamji, A.M. Stern, A. Mandinova, S.L. Schreiber, S.W. Lee,

Selective killing of cancer cells by a small molecule targeting the stress response to ROS, Nature, 475 (2011) 231-234.

[12] C. Bosc, M.A. Selak, J.-E. Sarry, Resistance Is Futile: Targeting Mitochondrial Energetics and Metabolism to Overcome Drug Resistance in Cancer Treatment, Cell Metabolism, 26 (2017) 705-707.

[13] E.M. Kuntz, P. Baquero, A.M. Michie, K. Dunn, S. Tardito, T.L. Holyoake, G.V. Helgason, E. Gottlieb, Targeting mitochondrial oxidative phosphorylation eradicates therapy-resistant chronic myeloid leukemia stem cells, Nature Medicine, 23 (2017) 1234-1240.

[14] M.G. Vander Heiden, R.J. DeBerardinis, Understanding the Intersections between Metabolism and Cancer Biology, Cell, 168 (2017) 657-669.

[15] H. Wang, Z. Gao, X. Liu, P. Agarwal, S. Zhao, D.W. Conroy, G. Ji, J. Yu, C.P. Jaroniec, Z. Liu, X. Lu, X. Li, X. He, Targeted production of reactive oxygen species in mitochondria to overcome cancer drug resistance, Nature Communications, 9 (2018) 1-16.

[16] B. Kalyanaraman, G. Cheng, M. Hardy, O. Ouari, M. Lopez, J. Joseph, J. Zielonka, M.B. Dwinell, A review of the basics of mitochondrial bioenergetics, metabolism, and related signaling pathways in cancer cells: Therapeutic targeting of tumor mitochondria with lipophilic cationic compounds, Redox Biology, 14 (2018) 316-327.

[17] P.E. Porporato, N. Filigheddu, J.M.B.-S. Pedro, G. Kroemer, L. Galluzzi, Mitochondrial metabolism and cancer, Cell Research, 28 (2018) 265-280.

[18] P. Tsvetkov, A. Detappe, K. Cai, H.R. Keys, Z. Brune, W. Ying, P. Thiru, M. Reidy, G. Kugener, J. Rossen, M. Kocak, N. Kory, A. Tsherniak, S. Santagata, L. Whitesell, I.M. Ghobrial, J.L. Markley, S. Lindquist, T.R. Golub, Mitochondrial

metabolism promotes adaptation to proteotoxic stress, Nature Chemical Biology, 15 (2019) 681-689.

[19] W. Zhang, X. Hu, Q. Shen, D. Xing, Mitochondria-specific drug release and reactive oxygen species burst induced by polyprodrug nanoreactors can enhance chemotherapy, Nature Communications, 10 (2019) 1-14.

[20] Z. Liu, H. Pei, L. Zhang, Y. Tian, Mitochondria-Targeted DNA Nanoprobe for Real-Time Imaging and Simultaneous Quantification of Ca2+ and pH in Neurons, ACS Nano, 12 (2018) 12357-12368.

[21] Z. Ye, L. Wei, X. Geng, X. Wang, Z. Li, L. Xiao, Mitochondrion-Specific Blinking Fluorescent Bioprobe for Nanoscopic Monitoring of Mitophagy, ACS Nano, 13 (2019) 11593-11602.

[22] J. Zielonka, J. Joseph, A. Sikora, M. Hardy, O. Ouari, J. Vasquez-Vivar, G. Cheng, M. Lopez, B. Kalyanaraman, Mitochondria-Targeted Triphenylphosphonium-Based Compounds: Syntheses, Mechanisms of Action, and Therapeutic and Diagnostic Applications, Chemical Reviews, 117 (2017) 10043-10120.

[23] H. Ka, H.-J. Park, H.-J. Jung, J.-W. Choi, K.-S. Cho, J. Ha, K.-T. Lee, Cinnamaldehyde induces apoptosis by ROS-mediated mitochondrial permeability transition in human promyelocytic leukemia HL-60 cells, Cancer Letters, 196 (2003) 143-152.

[24] S.-H. Hong, I.A. Ismail, S.-M. Kang, D.C. Han, B.-M. Kwon, Cinnamaldehydes in Cancer Chemotherapy, Phytotherapy Research, 30 (2016) 754-767.

[25] C.-e. Wu, Y.-w. Zhuang, J.-y. Zhou, S.-l. Liu, R.-p. Wang, P. Shu, Cinnamaldehyde enhances apoptotic effect of oxaliplatin and reverses epithelial-

mesenchymal transition and stemnness in hypoxic colorectal cancer cells, Experimental Cell Research, 383 (2019) 1-11.

[26] J. Noh, B. Kwon, E. Han, M. Park, W. Yang, W. Cho, W. Yoo, G. Khang, D. Lee, Amplification of oxidative stress by a dual stimuli-responsive hybrid drug enhances cancer cell death, Nature Communications, 6 (2015) 1-9.

[27] E. Han, B. Kwon, D. Yoo, C. Kang, G. Khang, D. Lee, Dual Stimuli-Activatable Oxidative Stress Amplifying Agent as a Hybrid Anticancer Prodrug, Bioconjugate Chemistry, 28 (2017) 968-978.

[28] S. Ma, W. Song, Y. Xu, X. Si, S. Lv, Y. Zhang, Z. Tang, X. Chen, Rationally Designed Polymer Conjugate for Tumor-Specific Amplification of Oxidative Stress and Boosting Antitumor Immunity, Nano Letters, 4 (2020) 2514–2521.

[29] Y. Wen, C.L. Schreiber, B.D. Smith, Dual-Targeted Phototherapeutic Agents as Magic Bullets for Cancer, Bioconjugate Chemistry, 3 (2020) 474–482.

[30] L. Wang, X. Niu, Q. Song, J. Jia, Y. Hao, C. Zheng, K. Ding, H. Xiao, X. Liu, Z. Zhang, Y. Zhang, A two-step precise targeting nanoplatform for tumor therapy via the alkyl radicals activated by the microenvironment of organelles, Journal of Controlled Release, 318 (2020) 197-209.

[31] D. Dutta, W. Ke, L. Xi, W. Yin, M. Zhou, Z. Ge, Block copolymer prodrugs: Synthesis, self-assembly, and applications for cancer therapy, WIREs Nanomedicine and Nanobiotechnology, 12 (2020) 1-19.

[32] S. Wang, G. Yu, Z. Wang, O. Jacobson, L.-S. Lin, W. Yang, H. Deng, Z. He, Y. Liu, Z.-Y. Chen, X. Chen, Enhanced Antitumor Efficacy by a Cascade of Reactive Oxygen Species Generation and Drug Release, Angewandte Chemie International Edition, 58 (2019) 14758-14763.

[33] J.V. McGowan, R. Chung, A. Maulik, I. Piotrowska, J.M. Walker, D.M. Yellon, Anthracycline Chemotherapy and Cardiotoxicity, Cardiovascular Drugs and Therapy, 31 (2017) 63-75.

[34] B. Kalyanaraman, Teaching the basics of the mechanism of doxorubicin-induced cardiotoxicity: Have we been barking up the wrong tree?, Redox Biology, 29 (2020) 1-9.

Chapter V: General Conclusion and Future Perspectives

5.1. General conclusion

In summary, the rising interest into exploitation of therapeutic nanoreactors towards cancer treatment suggests a promising approach to achieve versatile treatment strategies such as the application of exogenous activating and therapeutic enzymes that are rarely found at the desired treatment sites to achieve tremendously enhanced therapeutic effects with extensively mitigated adverse side effects. In this thesis, we have successively developed a strategy to fast-forward engineer a therapeutic nanoreactor with both tunable membrane permeability and structural stability after activation. Our therapeutic nanoreactor denoted as GOD&ProCPT@Bz-MPE showed additional interesting features such as the ability to deliver both the prodrug (ProCPT or ProPTX) and its activating enzyme (GOD) at the pathological site, as well as the tumor specific activation. The presented strategy can also be exploited to achieve a single step enzyme prodrug therapy that is advantageous to enhance the prodrug and activating enzyme bioavailability at the treatment site thus an improved therapeutic effect. Moreover, similar strategy were used and successfully synthesized a therapeutic nanoreactor denoted as Cis/GOD@Bz-V that showed exciting feasibility to enhance platinum cellular uptake *via* endocytotic pathway and the reversal of cisplatin resistance in A549R cells through the generation of enhanced intratumor ROS production and activation of pro-apoptotic cellular pathways such as enhanced expression of caspase 3.

Furthermore, we have successfully developed a novel strategy to reverse multidrug resistance in cancer therapy simply through the targeting of mitochondria

metabolic activities. Our synthesized polymer prodrug that is FA&TPP-PEOGMA$_{18}$-*b*-P(CNM$_{17}$-*co*-DOX$_{15}$) and used to prepare PCD nanoparticles showed that they can effectively kill DOX resistant MCF-7 ADR cell line comparatively to nonresistant MCF cell line mainly through the amplification of mitochondria oxidative stress and DNA damage. Interestingly, given the fact that our developed dual targeting PCD nanoparticles were prepared using polymer prodrug block copolymers, it is feasible to achieve high drug loading capacity without premature drug leakage which are advantageous to achieve improved systemic circulation half-life and enhanced tumor accumulation during treatment.

Collectively, the study conducted in this thesis is expected to contribute to the existing literature especially through the inspiring the next generation of researchers to develop advanced therapeutic nanoreactor and with novel treatment approaches to achieve enhanced therapeutic effect and with remarkably minimized adverse effect as well as to overcome multi-drug resistance and ready for clinical translation in cancer therapy.

5.2. Future outlooks

Although we successfully presented a representative strategy to engineer a therapeutic nanoreactor that is GOD&ProCPT@Bz-MPE to achieve a single step enzyme prodrug therapy for cancer treatment, it is seemingly that less options can be feasible about which type of enzymes and prodrugs that can be paired and coloaded into the same nanoplatform and remain inactive during the delivery process until they reach the favorable conditions to activate the nanoreactor at the desired pathological site. Moreover, Given the big size of macromolecular biomaterials such as most of the

enzymes particularly GOD with molecular weight of around 160 kDa, it is found that only relatively less amount of GOD can be encapsulated in the aqueous section of the used polymersomes to engineer our developed therapeutic nanoreactor. To solve the latter limitation, the future works need to develop novel strategies to engineer nanoreactor with high encapsulation efficiency of bio-macromolecular fragile materials by also preserving their activities and protecting them from various denaturants while working under harsh environment.

Furthermore, despite the impressive rapidly evolving progress and interest about the application of therapeutic nanoreactors for cancer therapy, further effort is still needed to clarify various related vital aspects such as the modulation strategies for enzymatic activities in therapeutic nanoreactors thereby optimizing the loading efficiency and loading capacity, as well as the regulation of the efflux rate for the substrates and products across the reaction vessel membrane. Moreover, the development of tangible strategy to immobilize multiple enzymes into a single nanocompartment or into a single nanoreactor with multiple nanocompartments is highly recommended to enhance the effectiveness and applicability of these therapeutic nanoreactors into cancer therapy.

The role of mitochondria organelle into the promotion of diseased tissue multi-drug resistance has been extensively studied elsewhere from the literature. Although our developed PCD nanoparticles showed a remarkably enhanced therapeutic efficacy to reverse multi-drug resistance such as against DOX resistant MCF-7 ADR cell line according to the obtained both *in vitro* and *in vivo* experimental results, the involved mechanisms of action for PCD nanoparticles to effectively reverse multi-drug resistance still need to be further and deeply explored, which is also taken as limitation of the study presented in chapter 4 of this thesis.

Acknowledgements

First and foremost, I express sincere gratitude to my supervisor **Prof. Dr. Zhishen Ge** who gave me the great opportunity to join his research group. The completion of this research could not have been realized without his precious time and expertise guidance provided.

In the same lines, I acknowledge the **University of Science and Technology of China (USTC)** for providing a pleasant learning environment. It is of immense pleasure to thank **all respectful Teachers from USTC** who contributed in one way or another for the success of my studies at USCT. I would also like to extend my appreciation to the **CAS-TWAS Presidential Fellowship** for financial support provided. I take also this time to thank my working institution that is **University of Rwanda** which provided a study leave permit for me to pursue PhD studies at USTC since the past four years to date (2020).

I am deeply grateful to **all my labmates** especially: Dr. Junjie Li, Dr. Han Yu, Dr. Wei Yin, Dr. Zhengshi Zha, Zhang Ping, Wendong Ke, Yuheng Wang, Xiang Li, Longchang Xi, Qinghao Zhou, Jingbo Wang, Shuang Zhang, Abd Al-Wali Mohammed M. Japir, Fathelrahman Mohammed, Alhadi Ibrahim, Dutta Debabrata and Etienne Twizeyimana for their incredible willingness and helpfulness in providing the useful information during all the time spent together in laboratory. Similarly, I am thankful to **everyone** who provided any kind of help and support while I was living in Hefei city.

Last but not least, It is of great pleasure for me to express my gratitude **all my friends** and **family members** especially my wife **Ingabire Claudine**, my son **Ethan M. Ngabo**, both my **parents**, my **sisters** and **brothers** for their overwhelming love and moral support showed to me when it was needed the most. Above all, I thank my **God** to protect and guide me through all till to day.

Thank you all.

Jean Felix Mukerabigwi

1st, June, 2020.

List of Publications

1. **J.F. Mukerabigwi**, **Z. Ge***, K. Kataoka*, Therapeutic Nanoreactors as In Vivo Nanoplatforms for Cancer Therapy, Chemistry – A European Journal, 24 (2018) 15706-15724.
2. **J.F. Mukerabigwi**, W. Yin, Z. Zha, W. Ke, Y. Wang, W. Chen, A.A.-W.M.M. Japir, Y. Wang, **Z. Ge***, Polymersome nanoreactors with tumor pH-triggered selective membrane permeability for prodrug delivery, activation, and combined oxidation-chemotherapy, Journal of Controlled Release, 303 (2019) 209-222.
3. **J.F. Mukerabigwi**, Y. Han, N. Lu, W. Ke, Y. Wang, L. Xi, Q. Zhou, F. Mohammed, A. Ibrahim, **Z. Ge***, Cisplatin Resistance Reversal of Lung Cancers by Tumor Acidity Activable Vesicular Nanoreactors via Tumor Oxidative Stress Amplification, **(Prepared Manuscript).**
4. **J.F. Mukerabigwi**, L. Xi, N. Lu, W. Ke, Abd Al-Wali M. M. Japir, Y. Wang, Q. Zhou, F. Mohammed, X. Li, **Z. Ge***, Mitochondria Targeting Polymer Prodrug Nanoparticles to Overcome Multi-Drug Resistance Through Orchestrated Mitochondrial Oxidative Stress Amplification and DNA Damage, **(Manuscript under preparation).**
5. F. Mohammed, W. Ke, **J.F. Mukerabigwi**, A.A.-W.M. M. Japir, A. Ibrahim, Y. Wang, Z. Zha, N. Lu, M. Zhou, **Z. Ge***, ROS-Responsive Polymeric Nanocarriers with Photoinduced Exposure of Cell-Penetrating Moieties for Specific Intracellular Drug Delivery, ACS Applied Materials & Interfaces, 11 (2019) 31681-31692.
6. A. Ibrahim, E. Twizeyimana, N. Lu, W. Ke, **J.F. Mukerabigwi**, F. Mohammed,

A.A.-W.M.M. Japir, **Z. Ge***, Reduction-Responsive Polymer Prodrug Micelles with Enhanced Endosomal Escape Capability for Efficient Intracellular Translocation and Drug Release, ACS Applied Bio Materials, 2 (2019) 5099-5109.

7. W. Yin, W. Ke, W. Chen, L. Xi, Q. Zhou, **J.F. Mukerabigwi**, Z. Ge*, Integrated block copolymer prodrug nanoparticles for combination of tumor oxidative stress amplification and ROS-responsive drug release, Biomaterials, 195 (2019) 63-74.
8. W. Yin, M. Qiang, W. Ke, Y. Han, **J.F. Mukerabigwi**, **Z. Ge***, Hypoxia-responsive block copolymer radiosensitizers as anticancer drug nanocarriers for enhanced chemoradiotherapy of bulky solid tumors, Biomaterials, 181 (2018) 360-371.
9. W. Ke, W. Yin, Z. Zha, **J.F. Mukerabigwi**, W. Chen, Y. Wang, C. He, **Z. Ge***, A robust strategy for preparation of sequential stimuli-responsive block copolymer prodrugs via thiolactone chemistry to overcome multiple anticancer drug delivery barriers, Biomaterials, 154 (2018) 261-274.
10. Z. Zha, Y. Hu, **J.F. Mukerabigwi**, W. Chen, Y. Wang, C. He, **Z. Ge***, Thiolactone Chemistry-Based Combinatorial Methodology to Construct Multifunctional Polymers for Efficacious Gene Delivery, Bioconjugate Chemistry, 29 (2018) 23-28.
11. W. Ke, Z. Zha, **J.F. Mukerabigwi**, W. Chen, Y. Wang, C. He, **Z. Ge***, Matrix Metalloproteinase-Responsive Multifunctional Peptide-Linked Amphiphilic Block Copolymers for Intelligent Systemic Anticancer Drug Delivery, Bioconjugate Chemistry, 28 (2017) 2190-2198.